UNIVERSITE MONTPELLIER II
SCIENCES ET TECHNIQUES DU LANGUEDOC

THESE

pour obtenir le grade de
DOCTEUR DE L'UNIVERSITE MONTPELLIER II

Discipline : Géophysique Interne
Formation Doctorale: Structure et Evolution de la Lithosphère
Ecole Doctorale: Systèmes Intégrés en Biologie, Agronomie, Géosciences, Hydrosciences, Environnement

présentée et soutenue publiquement
par

ANDREAS WÜSTEFELD

le 27 Septembre 2007

TITRE

Methods and applications of shear wave splitting: The East European Craton

Methods et applications des ondes des cisaillement : Le Craton de l'Europe de l'Est

JURY

Marc DAIGNIERES	President
Götz BOKELMANN	Directeur de Thèse
Jean-Paul MONTAGNER	Rapporteur
Paul SILVER	Rapporteur
Alain VAUCHEZ	Examinateur
Martin SCHIMMEL	Examinateur

Table of Contents:

0. Résumé en français

Les ondes sismiques représentent indiscutablement la source d'information la plus complète pour étudier l'intérieur de la terre. Sensible aux changements physiques et chimiques qu'elle va rencontrer sur son chemin, une onde sismique arrivant à une station d'enregistrement contient quantité d'informations concernant sa genèse à la source sismique et son trajet à travers la terre. Le mécanisme d'un tremblement de terre peut être déterminé, et permet ainsi de gagner des informations sur la région de la source.

Une onde sismique est également sensible aux propriétés élastiques le long du trajet parcouru. En conséquence l'inversion des propriétés observée d'une onde (onde de volume, onde de surface oscillation propre) permet des interprétations sur la structure interne de la terre.

Une des nombreuses propriétés physiques affectant les ondes sismiques est l'anisotropie. L'identification de l'orientation de l'anisotropie sismique et par la suite l'interprétation de ses origines par comparaison avec les structures en surface, aide à comprendre les grands processus tectoniques du globe terrestre.

L'anisotropie sismique dépend de la vitesse de propagation des ondes selon la direction considérée. Une telle anisotropie peut être induit par des variations structurales telle qu'une alternance de couches minces ayant des propriétés élastiques différentes [Backus, 1962], ou la présence de fissures orientées par la contrainte et remplies de fluide [Crampin, 1984; Kendall et al., 2006] ou bien par l'orientation préférentielle de minéraux anisotropes [par exemple, Nicolas et Christensen, 1987] lors de la déformation plastique du milieu. Il est admis que l'olivine joue un rôle majeur dans l'anisotropie du manteau supérieur car elle représente la phase minéralogique dominante. Elle peut s'y déformer de façon plastique et développer de fortes orientations préférentielles de ses axes cristallographiques. Elle est enfin caractérisée par une forte anisotropie intrinsèque qui est en outre de symétrie relativement simple, orthorhombique.

Un des effets de l'anisotropie sismique est le déphasage des ondes de cisaillement, par l'effet de la biréfringence du milieu. Lorsqu'une onde de cisaillement pénètre dans un milieu anisotrope, elle se sépare en deux ondes quasi-S polarisées perpendiculairement et se propageant à des vitesses différentes. Au fur et à mesure de leur propagation dans le milieu anisotrope, ces deux ondes vont donc être déphasées et un délai δt se crée entre les temps d'arrivée des deux ondes que l'on peut enregistrer à la surface de la Terre. La direction du plan de polarisation de l'onde rapide est dénommée Φ et ce sont ces deux paramètres, Φ et dt, que l'on peut physiquement mesurer dans le signal sismologique pour caractériser l'anisotropie du milieu traversé. Le délai est fonction de l'épaisseur de la couche anisotrope, de la force de l'anisotropie intrinsèque du milieu, et de la cohérence de la déformation verticale.

Le déphasage des ondes de cisaillement est étudié depuis deux décennies. Au commencement limité aux ondes S issues des événements locaux [Ando et Ishikawa, 1982], la technique est maintenant largement adoptée pour l'étude des phases issues du noyau, telles que SKS, SKKS, PKS [par exemple, Vinnik et al., 1984; Silver et Chan, 1991]. Pendant les dernières deux décennies la méthode de mesure de déphasage des ondes de cisaillement a été largement appliquée à de nombreux contextes géodynamiques: Zones de subduction [par exemple, Margheriti et al., 2003 ;Levin et al., 2004 ; Nakajima et Hasegawa, 2004], dorsales océaniques [par exemple Kendall, 1994; Gao et al., 1997; Wolfe & Solomon, 1998; Walker et al., 2004; Kendall, 2005], points chauds [Barruol et Granet, 2002; Walker et al., 2001; 2005], îles océaniques [Behn et al, 2004; Fontaine et al., 2007] et orogénies [par exemple, Barruol et al., 1998 ; Flesch et al., 2005].

L'utilisation des phases télésismiques permet d'effectuer des mesures d'anisotropie sous une station à des grandes distances des régions sismiquement actives. Cette technique permet en particulier, d'aborder l'étude de la déformation du manteau sous les cratons qui représentent les lithosphères épaisses et stables des continents et qui ne sont généralement pas des régions sismiquement actives. De par leur épaisseur par rapport aux lithosphères avoisinantes et de leur stabilité dans le temps, les racines des craton peuvent agir en tant qu'obstacle au flux de manteau environnant [Fouch et al., 2000]. L'analyse de l'anisotropie sur et autour des cratons peut aider à distinguer cette déformation actuelle, liée au mouvement de plaques, de la déformation fossile. Plusieurs études ont analysé l'anisotropie sous divers cratons comme le craton Nord-Américain, le craton du Sao Francisco en Amérique du sud ou celui du Kaapvaal en Afrique du Sud [Fouch et al., 2000; Heintz et Kennett, 2005; Fouch et Rondenay, 2006; Assumpção et al. 2006]. Notre étude se concentre sur l'anisotropie sous le Craton Est Européen (CEE) qui est peu connue.

En Europe centrale, des études régionales semblent indiquer un flux de manteau dominant proche de la direction du mouvement de la lithosphère européenne. Ajouter des informations d'anisotropie sous le Craton Est Européen permet de préciser d'une part les

structures intimes du craton mais également les interactions du mouvement de plaques et du flux mantellique sous-jacent.

Structure de la thèse

Dans cette thèse j'effectuerai tout d'abord des rappels sur la physique fondamentale de la propagation des ondes sismiques, avec un regard particulier sur les milieux anisotropes [chapitre 2]. En chapitre 3, j'exposerai les différentes origines possibles de l'anisotropie. Généralement l'anisotropie peut être divisée en deux classes: anisotropie cristalline (de petite échelle puisque étant fondamentalement issue de l'anisotropie intrinsèque de chaque cristal) et anisotropie structurale (à grande échelle puisque étant liée à des structures comme par exemple des litages compositionnels).

L'anisotropie cristalline est caractérisée par la différence de vitesse de propagation d'une onde dans un monocristal (d'olivine pour le manteau supérieur) en fonction des ses axes cristallographiques. En considérant que le pourcentage d'anisotropie est donné par la formule $k_s = (V_{max} - V_{min}) / V_{moy}$, on mesure une anisotropie de propagation de 26% pour les ondes P, et une anisotropie de polarisation de 19% pour les ondes S. Ces valeurs étant importantes, on peut raisonnablement penser qu'une roche composée de tels minéraux anisotropes devrait elle aussi être anisotrope à l'échelle de l'agrégat décimétrique et si la structure est suffisamment homogène à l'échelle (pluri)kilométrique. Ce passage de différentes échelles n'est vérifié que si les axes cristallographiques des minéraux qui composent la roche sont orientés de façon non aléatoire et si la structure intime de la roche (foliation, linéation) est orientée spatialement de façon homogène. Les cristaux ont alors développé une orientation préférentielle de réseau (OPR en français, ou en anglais "lattice preferred orientations", LPO), induite par la déformation. Les profondeurs possibles où l'anisotropie peut se produire sont discutées comme les effets de différents arrangements tectoniques.

Les aspects techniques de mesure de déphasage des ondes de cisaillement sont présentés en chapitre 4. Différentes méthodes existent pour inverser l'effet de déphasage. La technique de Rotation/Corrélation [Bowman & Ando, 1987] se base sur le fait que les ondes polarisées ont théoriquement la même forme d'onde, mais sont simplement polarisées perpendiculairement entre elles et sont décalées d'un délai temporel δt. On va donc chercher, par des rotations successives, l'angle pour lequel les deux composantes ont la même forme d'ondes, c'est à dire lorsque leur corrélation est maximale.

La deuxième technique est basée sur la minimisation de l'énergie sur la composante transverse d'une onde de type SKS [Silver et Chan, 1991]. Dans une Terre isotrope, une onde SKS émergeant du noyau liquide est en effet purement radiale. Si l'onde traverse un

milieu anisotrope elle subit le phénomène de déphasage, et une certaine énergie est transférée sur la composante transverse de la phase considérée, en plus de la composante radiale. La minimisation de cette énergie est obtenue par un balayage de toutes les directions Φ possibles et des décalages dt. Cette méthode est très sensible au bruit sur la composante transverse. Elle est donc bien adaptée à l'analyse des ondes SKS, qui ont souvent un bon rapport signal / bruit.

0.1. SplitLab

L'application simultanée des différentes techniques de déphasage des ondes S est exécutée dans un nouvel environnement SplitLab (chapitre 4.3). Cet environnement graphique englobe le processus entier, depuis la requête de données jusqu'à l'interprétation des résultats. Contrairement à une technique entièrement automatisée, nous présentons une approche semi-automatique qui permet un contrôle continu de l'utilisateur durant l'ensemble du traitement. L'environnement de SplitLab est optimisé pour réitérer un grand nombre de processus tout en permettant à l'utilisateur de se concentrer sur le contrôle de la qualité et par la suite l'interprétation des résultats. Les modules de pré-traitement de SplitLab créent une base de données des événements et lient les sismogrammes correspondants. L'outil de visualisation des séismogrammes utilise cette base de données pour effectuer la mesure de façon interactive. Le post-traitement des résultats combinés d'un tel projet inclut une option de visualisation et d'exportation. Les interfaces utilisateur graphiques (GUIs) rendent l'utilisation intuitive (Figure A).

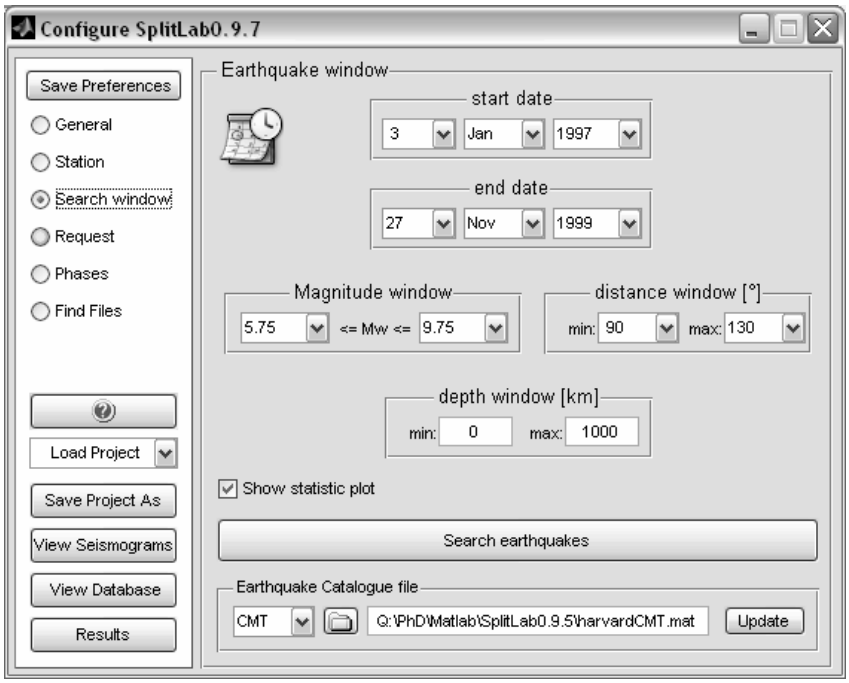

Figure A: La configuration de SplitLab est paramétrée interactivement. Ici par exemple, le panneau de choix de fenêtre de tremblement de terre.

SplitLab est fournis avec un exemple de données de la station ATD (Arta Cave, Djibouti) du réseau GEOSCOPE (Figure C). Le choix de cette station a été guidé par la qualité des données que l'on y trouve, la clarté de la direction anisotrope rapide, l'amplitude du déphasage temporel, et le consensus existant sur les paramètres de déphasage obtenu à partir de diverses études d'anisotropie publiées à cette station [Vinnik et al., 1989 ; Barruol et Hoffmann, 1999].

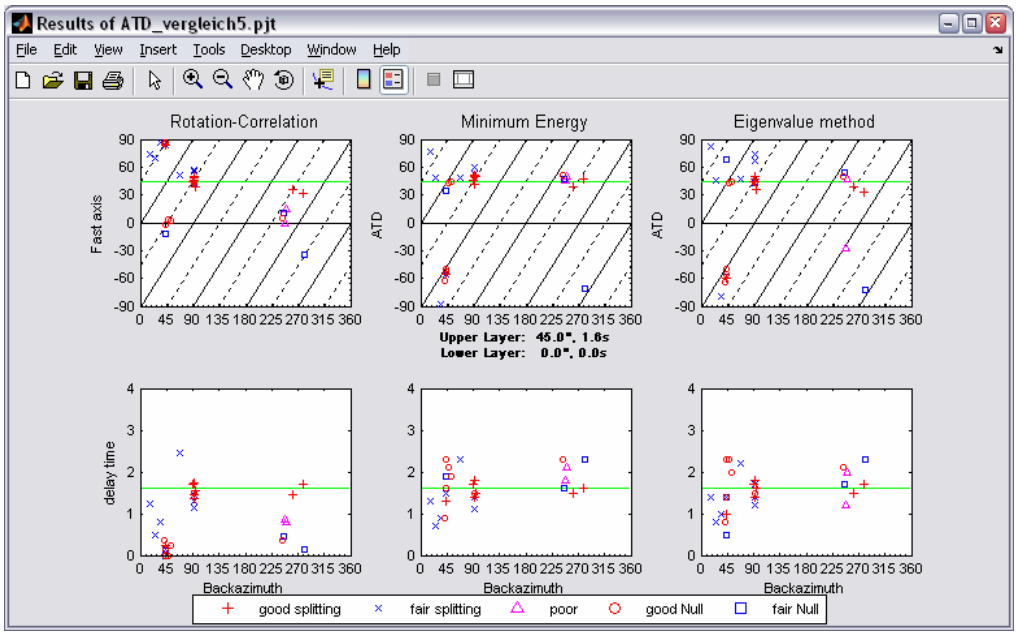

Figure B: Les résultats de la station ATD avec SplitLab. La comparaison des trois techniques différentes est possible très facilement

0.2. Critère de “Null”

Lors des mesures de déphasage d'ondes de cisaillement, de nombreux événements ne présentent pas de déphasage, l'énergie des ondes sismiques étant concentrée sur la composante radiale. Ce type de mesure est généralement caractérisé de "null" dans la littérature mais représente en fait une information importante. Je présenterai un nouveau critère pour distinguer sûrement des événements « Nulls » (chapitre 4.4). Ce critère est basé sur la comparaison des deux techniques indépendantes de mesure de déphasages des ondes S. Un test avec des sismogrammes synthétiques montre que un différence caractéristique entre la technique « *Rotation-Correlation* » [RC, Bowman et Ando, 1997] and « *energie minimal sur la composant transverse* » [SC, Silver et Chan, 1991].

Les deux techniques donnent des valeurs correctes si les backazimuths sont suffisamment loin des axes rapides (ou lents). Près de ces directions "Nulls", il y a des déviations caractéristiques, particulièrement pour la technique « Rotation-Correlation ». Les valeurs du δt_{RC} diminuent systématiquement, alors que Φ_{RC} montre des déviations d’environ 45° par rapport aux directions nulles (Figure C). De façon étonnante, le Φ_{RC} se trouve le long des lignes qui indiquent le backazimuth ±45°. Ceci est dû aux recherches de RC-technique

pour avoir une corrélation maximale entre les deux composants horizontaux Q (radial) et T (transversal). Je montrerai que cette technique faillit en cas des Nulls car le signal sur T est minimal. La technique trouve la meilleure corrélation à 45°, ou le maximum d'énergie de la composante Q est “copié” vers la composante T.

Les différences caractéristiques des résultats issus de ces deux techniques ne permettent pas seulement de différencier les Nulls des non-Nulls mais également d'assigner une qualité objective à une mesure individuelle. Cette quantification pourrait par la suite permettre de comparer différentes études. Ces critères sont appliqués à la station LVZ en Scandinavie où les résultats sont définis avec une plus grande certitude qu'auparavant, malgré une couverture backazimuthale très faible.

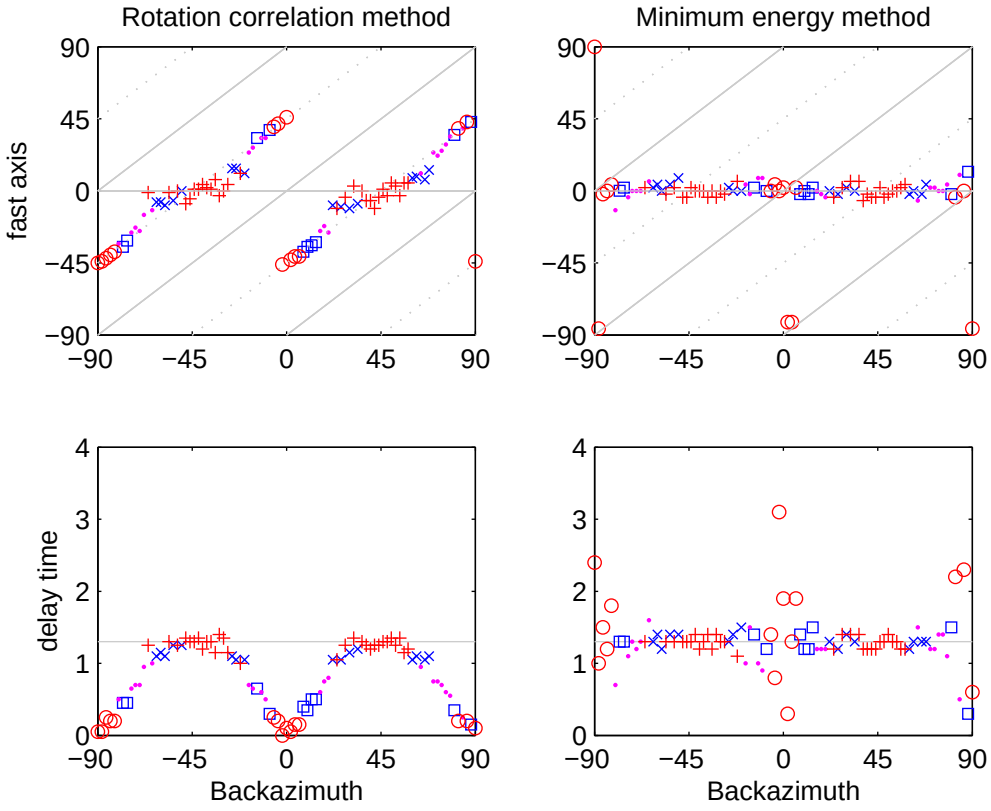

Figure A: Test synthétique à SNR_R = 15 pour la technique de Rotation-Corrélation (RC, gauche) et la technique minimum d'énergie (SC, droite). Les panneaux supérieurs montrent les haches rapides résultantes à différents backazimuths, expositions inférieures de panneaux que résulter retardent des évaluations de temps. Les valeurs d'entrée (Φ_{in} = 0° et dt_{in} = 1.3sec) sont indiquées par les traits horizontaux. La technique de SC rapporte des évaluations stables pour un éventail de backazimuths. Pour SNR_R inférieur et/ou plus petit retarder les périodes (voir le supplément électronique) que la RC-technique diffère encore plus des valeurs d'entrée. Bon Nulls détecté automatiquement sont marqué comme cercles, proche Nulls comme carres. De bons résultats sont marqués comme plus des signes, et des résultats proches comme croix. Des résultats pauvres sont indiqués comme points.

Finalement, des perspectives comme la possibilité d'automatiser complètement le processus de déphasage des ondes S à une station sismique sont présentées en chapitre 4.5.

0.3. Base des données de « shear wave splitting »

Le nombre de plus en plus important des études de déphasage des ondes S a été une motivation pour centraliser les données (chapitre 4.6) de déphasage des ondes de cisaillement publiées dans la littérature. Basée sur une collection statique commencée par Derek Schutt et Matt Fouch, cette base de données interactive permet l'accès par l'intermédiaire d'un web browser. Les chercheurs peuvent ainsi saisir leurs propres donnés et augmenter la base de données. L'interaction avec GoogleEarth, un outil employé couramment des SIG 3D, fournit une visualisation rapide avec différents ensembles de données.

Montagner et al. [2000] ont présente une méthode a calculer les paramètres théorétique a partir des résultats de la tomographie des ondes de surface. En utilisant le model global de Debayle et al [2005] une comparaison des paramètres théorétique avec la base des donnes montre une corrélation général de les deux methodes.

0.4. L'anisotropie du Craton Est Européen

Le chapitre 5 est focalisé sur l'anisotropie dans des régions cratoniques. D'abord, une vue d'ensemble générale sur la structure et l'évolution des cratons est présentée (chapitre 5.1), suivi d'un rappel des études de déphasage des ondes S sur des cratons (chapitre 5.2). Le chapitre 5.3 reprend l'évolution et les propriétés géophysiques du craton Est Européen et je présente dans la section 5.4 les mesures de déphasage effectuées dans cette thèse avec les techniques et outils précédemment présentés.

Le craton de l'Europe de l'Est (CEE) se compose de trois segments de croûte principaux: Fennoscandia, Sarmatia et Volgo-Uralia. Aujourd'hui, le CEE est largement recouvert par des sédiments du Phanerozoic. Seuls les boucliers de Fennoscandia et les parties sud du Bouclier Ukrainien et du Massif de Voronezh offrent à l'affleurement des roches protérozoïques et plus anciennes [Gorbatschev et Bogdanova 1993 ; Bogdanova, 1996].

Entre 2.1Ga et 2.0, le domaine océanique, qui séparait Sarmatia de Volgo-Uralia, s'est fermé. Simultanément, la subduction commencée sur le bord (actuel) nordique de Sarmatia se finit à environ 1.8Ga à la collision avec Fennoscandia. La réunion des deux blocs a eu lieu à environ 1.75Ga et est accompagnée d'« underplating ».

Un total de 16 stations sismologiques distribuées sur les multiples unités tectoniques du CEE sont analysées dans cette étude. Les axes rapides montrent de fortes variations pour chaque unité tectonique, suggérant une anisotropie « gelée » dans la lithosphère.

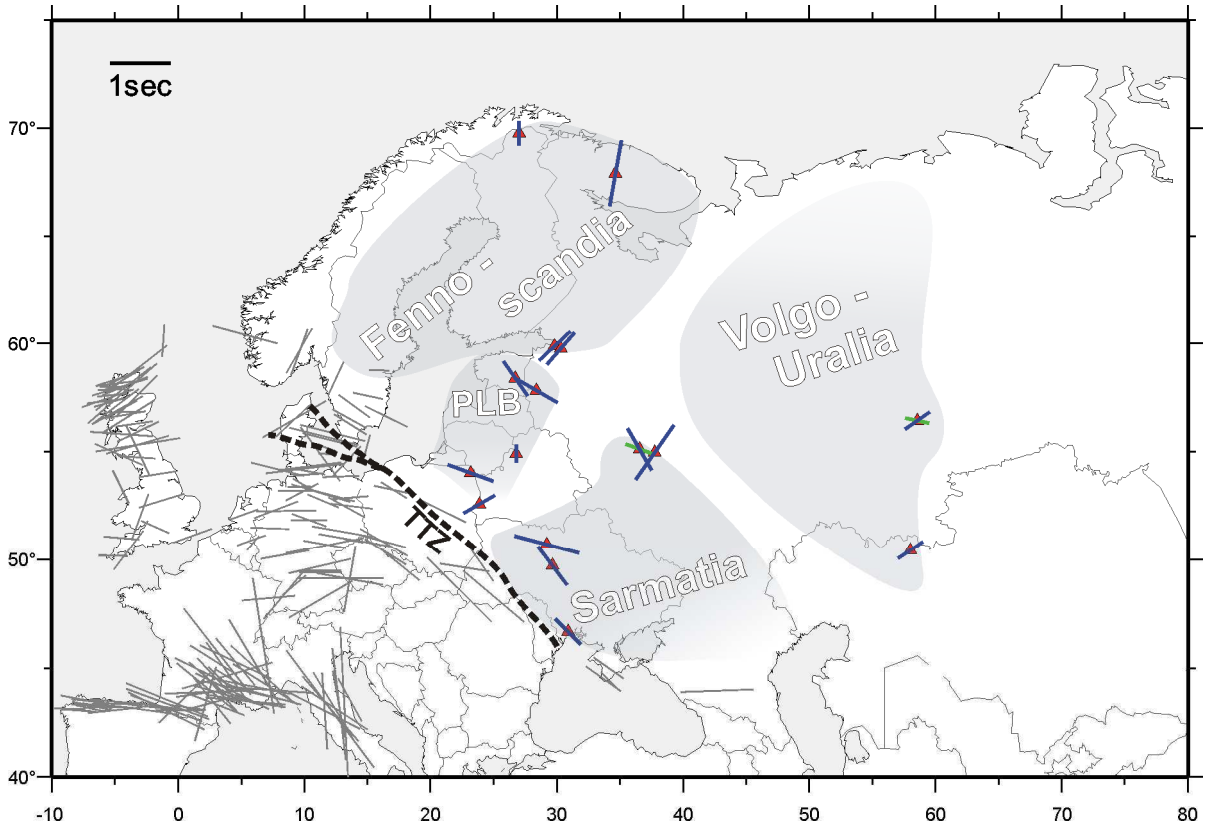

Figure D: Mesures de déphasages des ondes S en Europe. Les marqueurs gris représentent des mesures de la base de données SKS. Les marqueurs bleus et verts sont issus de cette étude, et représentent (lorsqu'elles semblent présentes), les couches anisotropes supérieure et inférieure respectivement. PLB="terrane" Polonais-Lituanien-Bélarus ; TTZ=Tesseyre-Tornquist zone

Une telle interprétation est soutenue par une corrélation variable des axes rapides avec la direction de mouvement de la plaque, qui ne montre pas de parallélisme systématique et qui ne semble pas refléter les processus asthénosphériques actuels à grande échelle.

En Fennoscandia, les axes rapides montrent des directions NS dans le bloc Karélien au nord, et NE-SW dans Svecofennia près de St. Petersburg. C'est en accord avec les résultats obtenus en Finlande [Plomerova et al., 2005]. La corrélation faible avec la direction de mouvement de la plaque Eurasie suggère des origines lithosphériques plutôt qu'asthénosphériques.

Les axes rapides des stations localisées sur les "terrane" Polonais-Lituanien-Bélarus montrent un alignement avec les unités géologiques mais également avec les linéations magnétiques, ce qui favorise encore l'hypothèse d'origine lithosphérique de l'anisotropie.

Les stations proches de l'Oural montrent des orientations d'axes rapides perpendiculaires à la direction générale de cette chaîne de montagne. Ceci pourrait contredire l'hypothèse de la déformation cohérente verticale décrite dans la littérature. Etant donné que les deux stations ARU et AKTK sont plutôt dans les parties externes de la chaîne de montagne, elles pourraient être protégées de l'influence des processus de la formation de la chaîne de montagne que l'on pourrait observer dans ses zones internes. Les directions observées

reflèteraient donc plutôt des directions anciennes de mouvement de la plaque pendant la subduction de Volgo-Uralia dans cette région.

Dans Samartia, les stations ne rapportent aucune orientation rapide logique d'axes rapides. Dans le NE, les deux stations OBN et MHV semblent indiquer une superposition complexe de cas d'hétérogénéité et de deux-couche d'anisotropie, provenant du massif de Voronezh et de la dorsale de Pachelma. À l'ouest, la station KIEV montre beaucoup de "Nulls" avec une gamme étendue de backazimuths. Ceci pourrait indiquer la présence de deux couches anisotropes mutuellement perpendiculaires ou bien l'absence d'anisotropie sous la station. Pour KIEV, il semble probable que la superposition de plusieurs événements tectoniques a finalement effacé les orientations préférentielles existantes des minéraux. Ceci expliquera le grand nombre des Nulls de un grande gamme des backazimuths.

Les orientations des axes rapides observées aux stations le long de la zone de suture de Tesseyre-Tornquist (TTZ) s'alignent avec les axes raides en Europe centrale. Ceci peut indiquer que les mêmes processus sont responsables de l'anisotropie de chaque côté de la zone de suture. Un processus possible pourrait être un flux de manteau, guidé et dévié par la lithosphère plus épaisse du CEE. Les études tomographiques indiquent en effet que l'augmentation de l'épaisseur lithosphérique coïncide avec le TTZ.

1. Thesis Motivation

Seismic waves are arguably the most powerful geophysical tools to investigate the Earth's deep interior. Sensitive to compositional changes and sharp contrasts, a seismic wave arriving at a recording station contains the whole suite of information acquired along its travel path. Source mechanisms can be studied at stations far away from the earthquakes, which gives information about the source region. A seismic wave is furthermore sensible to the elastic varying properties along its travel path. Consequently, the inversion of a seismic wave (body wave, surface wave, free oscillations) permits interpretations of the Earth's inner structure.

One of the many material properties affecting seismic waves is anisotropy. Identifying the orientation of seismic anisotropy and eventually interpreting its origins by comparison with surface tectonic features is aimed at understanding tectonic processes acting within the Earth.

Seismic anisotropy is the dependence of wave speed on direction. Such anisotropy can be caused by structural variability such as thin layers of alternating elastic properties [Backus, 1962] or fluid filled cracks [Crampin, 1984; Kendall et al., 2006]. A second origin of anisotropy is the preferred orientation of anisotropic minerals by strain [e.g., Nicolas & Christensen, 1987]. It is widely accepted, that the preferred orientations of olivine minerals play a major role in the anisotropy of the Earth's mantle.

Perhaps the best indicator of seismic anisotropy are split shear-waves. A seismic shear-wave passing through an anisotropic medium is split in two waves, polarized parallel to the anisotropic directions and travelling at different velocities. At the surface, they thus arrive separated by a certain delay time. In optics this effect is know as bifringence. Seismic shear-wave splitting has been studied for decades. Initially limited to direct S waves from local events [Ando & Ishikawa, 1982], the technique is now widly adopted for core-transiting phases such as SKS, SKKS, PKS [e.g., Vinnik et al., 1984, Silver and Chan, 1991]. Over the past two decades the method of shear-wave splitting has been

widely applied in several geologic settings: Subduction zones [e.g., Levin et al., 2004; Margheriti et al., 2003; Nakajima & Hasegawa, 2004], rifts [Kendall, 1994; Gao et al., 1997; Walker et al., 2004; Kendall, 2005], hotspots [Barruol & Granet, 2002; Walker et al., 2001; 2005], oceanic islands [Behn et al., 1999; Fontaine et al., 2007] and orogens [e.g., Barruol et al., 1998; Flesch et al., 2005].

Using teleseismic phases allows measurements at large distances from seismically active regions such as cratons. Cratons form the thick, stable interiors of the continents and their roots may act as obstacles to mantle flow [Fouch et al., 2000]. Analyzing anisotropy in such environments may help to distinguish this present day deformation, associated with plate motion, from fossil deformation. Several studies analyzed anisotropy beneath the various cratons [Fouch et al., 2000; Heintz & Kennett, 2005; Fouch & Rondenay, 2006; Assumpção et al. 2006].

Ever larger temporary arrays (e.g. USarray) and long running permanent stations make the available datasets grow fast. Shear wave splitting has thus become over last decade a quasi standard technique to perform at a seismic broad band station. This evokes the need for a splitting environment which is efficient and easy-to-use while still flexible enough to be applied to several problems.

The aim of this study was to develop such a shear-wave splitting environment, SplitLab, which is then applied to stations on the East European Craton. Matlab was chosen as the underlying code since it provides a great flexibility in operating systems and its scripting language can be readily adapted to specific problems. Furthermore, the possibilities to incorporate Graphical User Interfaces (GUIs) make SplitLab a modern, user-friendly and effective environment. SplitLab is intended to undertake the repetitive processing steps while enabling the user to focus on quality control and eventually the interpretation of the results.

The powerful possibilities of SplitLab are applied to stations on the East European Craton (EEC) for several reasons: first, from a geological point of view the Platform as a whole has yet not been investigated. Some of these stations have already been processed independently or within another framework [Silver & Chan, 1991; Makeyeva et al. 1992; Helffrich et al., 1994; Dricker et al, 1999]. A regional analysis of upper mantle anisotropy is an important link to the growing geological interest in this region in western literature after the fall of the Former Soviet Union [e.g., Gorbatschev & Bogdanova, 1993; Thybo et al, 2003; Bogdanova, 2005; Artemieva, 2006]. Second, the EEC is technically challenging due to its low delay times (<1sec) for most stations. The simultaneous comparison of three splitting techniques allows determining the anisotropy beneath a station with higher certainty. Third, seismograms are distributed over several data centers operated by GEOPHONE, IRIS or NARS. Being able to handle these formats efficiently is a challenge

to every code. And finally, a broad range of recording times (e.g., 15 years for KIEV and 18 month for NE53) and varying data quality provide a good synopsis of the generally accounted situations during shear wave splitting.

1.1. Thesis outline

This thesis will first point out the fundamental physics of seismic wave propagation, with a particular focus on anisotropic media [Chapter 2]. In Chapter 3, the different origins of anisotropy will be discussed. In general, anisotropy can be divided into to classes: (small-scale) crystalline anisotropy and (large-scale) structural anisotropy. The possible depths where anisotropy can occur are discussed as well as the effects of different tectonic settings.

The technical aspects of shear-wave splitting are presented in Chapter 4. The simultaneous application of the different splitting techniques is performed using the newly developed splitting environment SplitLab (Chapter 4.3). This graphical environment encompasses the whole splitting process from earthquake selection to seismogram request to data processing and finally results overview. Several graphical user interfaces (GUIs) make the usage intuitive.

I will present a novel criterion to reliably distinguish splitting events from so-called Nulls (Chapter 4.4). This criterion is based on the comparison of two genuinely different splitting techniques. Characteristic differences in their results allow not only to differentiate Nulls from non-Nulls but also to assign an objective quality to an individual measurement. This objectiveness might eventually enhance comparability between different studies.

A short outlook of how to possibly automate the whole splitting procedure of a seismic station is presented in Chapter 4.5.

The growing number of shear-wave splitting studies motivated to create a central collection of splitting data (Chapter 4.6). Based on a static text-file collection started by Derek Schutt and Matt Fouch, the Interactive Shear-Wave Splitting Database allows access via a web-browser. Most important, researchers can enter their own data so that at each time the newest studies are available. Interaction with GoogleEarth, a widely used 3D GIS tool, allows for fast visual comparison with different datasets.

Finally, Chapter 5 discusses anisotropy in cratonic regions. First, a general overview on the structure and evolution of cratons is presented (Chapter 5.1), followed by a short review of shear-wave splitting studies on cratons (Chapter 5.2). Chapter 5.3 resumes the evolution and the geophysical properties of the East European Craton. This is followed in Chapter 5.4 with the results of shear-wave splitting measurements performed in this thesis. A total of 16 stations distributed on the several tectonic units of the EEC permit the

analysis of coherence within and variability between these units. It is proposed to compare the (lithospheric) anisotropy with aeromagnetic data. Aeromagnetic data allow the detection of crustal structural trends and compositional changes in regions, whose geologies are only poorly constrained or covered by sediments.

2. Linear elasticity and wave propagation

Whenever a force is applied to a continuum, every point of this continuum is influenced by the force. Internal forces are commonly referred to as *body forces* while external forces are denoted *contact forces*. The most common example for a body force is acceleration due to gravity. Body forces are proportional to volume and density of the medium they are applied to. Contact forces depend on the area they are acting on.

In general, any external force applied to a continuum will deform the medium in size and shape. Internal forces try to resist this deformation. As a consequence the medium will return to its initial shape and volume once the external forces are removed. If this recovery of the original shape is perfect the medium is called elastic. The constitutive law relating the applied force with the resulting deformation is *Hooke's Law*, named after the 17th century physicist Robert Hooke (1635–1703). It is defined in terms of stress and strain. Many books have been written about this topic. This chapter is mainly based on Ranalli [1995] and Turcotte & Schubert [2002] for the stress/strain parts, and Stein & Wysession [2003], Lay & Wallace [1995] and Shearer [1999] for the seismic anisotropy. A detailed theory of wave propagation in anisotropic media is given for example by Tsvankin [2001].

To quantify the state of stress at a point P resulting from a force $\vec{F}$, P is imagined as an infinitesimal small cube, each side having an infinitesimal small surface δS. The traction $\vec{T}$ acting can be decomposed into its stress components normal (σ_h and tangential (σ_h) to this surface. The latter can be further decomposed into components parallel to the coordinate axes (Figure 1).

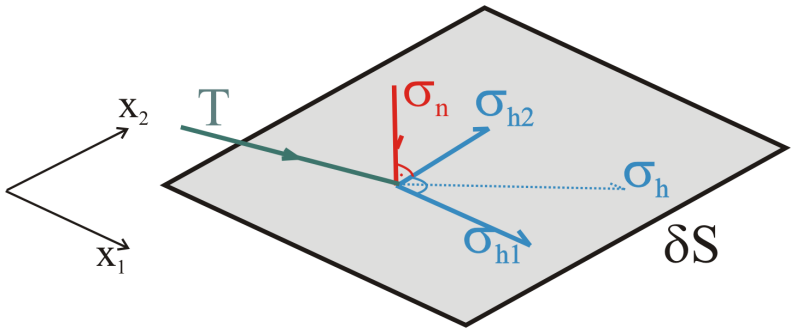

Figure 1: Components of stress acting on a surface. Any traction can be divided into its components normal and tangential to the surface. The latter can be further decomposed into two components parallel to the coordinate axes.

A stress σ_{ij} is defined as acting on the i-plane and being oriented in j-direction. Consequently, the components with repeating indices are normal stresses, while different indices indicate shear stresses (Figure 2). If the medium is in static equilibrium the sum of all stress components act in the 1, 2, and 3 directions as well as the total moment is zero. This symmetry is expressed as:

$$\sigma_{ij} = \sigma_{ji}$$

Thus, six independent parameters of the stress tensor σ_{ij} completely describe the state of stress at any point P of this continuum:

$$\sigma_{ij} = \begin{pmatrix} \sigma_{11} & \sigma_{12} & \sigma_{13} \\ \sigma_{21} & \sigma_{22} & \sigma_{23} \\ \sigma_{31} & \sigma_{23} & \sigma_{33} \end{pmatrix} = \begin{pmatrix} \sigma_{11} & \sigma_{12} & \sigma_{13} \\ \sigma_{12} & \sigma_{22} & \sigma_{23} \\ \sigma_{13} & \sigma_{32} & \sigma_{33} \end{pmatrix}, \qquad \text{with i, j = 1, 2, 3}$$

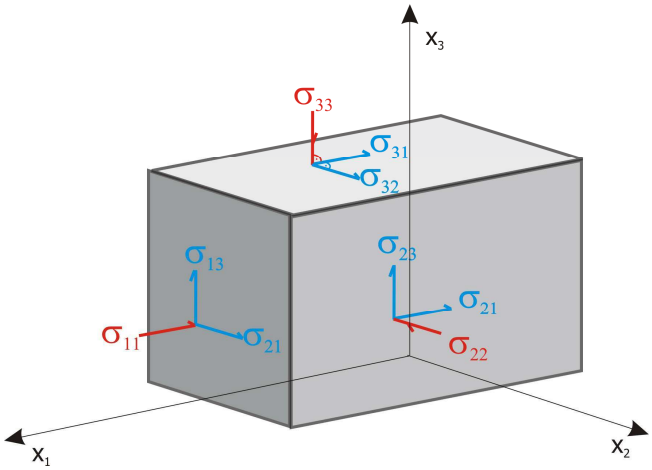

Figure 2: Complete representation of stresses acting on a block. Normal stresses are identified with repeating indices, whereas tangential stresses have different indices.

As mentioned above, an elastic body subjected to stress deforms. By definition, this deformation is called the strain ε. It is the (dimensionless) relative change in dimension of a body. In the three-dimensional case with deformations sufficiently small this is described by the infinitesimal strain tensor

$$\varepsilon_{ij} = \begin{pmatrix} \varepsilon_{11} & \varepsilon_{12} & \varepsilon_{13} \\ \varepsilon_{21} & \varepsilon_{22} & \varepsilon_{23} \\ \varepsilon_{31} & \varepsilon_{23} & \varepsilon_{33} \end{pmatrix} = \begin{pmatrix} \varepsilon_{11} & \varepsilon_{12} & \varepsilon_{13} \\ \varepsilon_{12} & \varepsilon_{22} & \varepsilon_{23} \\ \varepsilon_{13} & \varepsilon_{32} & \varepsilon_{33} \end{pmatrix}, \qquad \text{with i, j = 1, 2, 3}$$

where the same symmetry considerations as for the stress tensor reduce the number of independent components to six:

$$\varepsilon_{ij} = \varepsilon_{ji}$$

2.1. Hooke's Law

Stress and strain are related to each other by Hooke's Law, which assumes the strains to be sufficiently small and that stress and strain depend linearly on each other. Such a medium is called *linear elastic*. In its general form it can be written as

$$\sigma_{ij} = C_{ijkl}\varepsilon_{kl}, \qquad \text{with i, j, k, l = 1, 2, 3}$$

The fourth-order tensor C_{ijkl} is called the stiffness tensor, which consists of 81 entries and describes the elastic properties of a medium. This tensor actually links the applied stress to the resulting deformation of the medium. In general Hooke's Law can lead to complicated relations, but symmetry considerations remarkably simplify the equations by reducing the number of independent parameters from 81 to 36:

$$C_{ijkl} = C_{jikl} = C_{ijlk} = C_{jilk}$$

Moreover, general thermodynamics [e.g., Nye, 1972] requires the existence of a unique strain energy potential, and therefore:

$$C_{ijkl} = C_{klij}$$

which reduces the number of independent entries in the stiffness tensor to 21. These 21 parameters are necessary to fully describe the stress-strain relationship of an elastic body in its most general form. These parameters may vary with direction, in which case the medium is called *anisotropic*. In contrast, the properties of an *isotropic* medium are the same in every direction. There are seven unique symmetry systems, each representing a specific number of elastic parameters. The most complex and least symmetry is triclinic which needs the whole 21 elastic parameters to be fully described. In order of increasing symmetry the other six systems are (number of elastic parameters in brackets): monoclinic (13), orthorhombic (9), tetragonal (7, 6), trigonal (7, 6), hexagonal (5), cubic (3) and isotropic (2).

2.2. Isotropic media

In the case of isotropy, C_{ijkl} is invariant with respect to rotation, the number of independent parameters reduce to two:

$$C_{ijkl} = \lambda\delta_{ij}\delta_{kl} + \mu(\delta_{ik}\delta_{jl} + \delta_{il}\delta_{jk})$$

where λ and μ are called the Lamé parameters and δ_{il} is the Kronecker delta. μ also denotes the shear modulus, and describes the resistance to shearing of the medium according to

$$\sigma_{ij} = 2\mu\varepsilon_{ij}\,, \qquad \text{with } i \neq j$$

The bulk modulus K is defined as the ratio of applied isostatic stress to the fractional volumetric change:

$$\tfrac{1}{3}\sigma_{ij} = K\varepsilon_{ij}$$

In the case of uniaxial stress ($\sigma_{11} \neq 0 = \sigma_{22} = \sigma_{33}$), Young's Modulus E relates the stress to the strain in the same direction:

$$\sigma_{ij} = E\varepsilon_{ii} .$$

Finally, the (dimensionless) Poisson's ratio υ is also defined for uniaxial stress and relates the lateral strain to the axial strain:

$$\upsilon = -\frac{\varepsilon_{jj}}{\varepsilon_{ii}}$$

Note that here the Einstein sum convention is not applied. Note also that υ varies only between 0 and 0.5 with the upper limit representing a fluid ($\mu = 0$).

In the case of an isotropic, linear elastic material, the bulk modulus, the shear modulus and the density ρ define the compressive and shear velocities V_P and $V_{S,}$ respectively:

$$V_P = \sqrt{\frac{K + \frac{4}{3}\mu}{\rho}}$$

$$V_S = \sqrt{\frac{\mu}{\rho}}$$

In the following considerations it is convenient to use Voigt's representation of the stiffness tensor C_{ijkl}, which transfers the 3x3x3x3 tensor to a 6x6 matrix

$$c_{mn} = \begin{pmatrix} C_{1111} & C_{1122} & C_{1133} & C_{1123} & C_{1113} & C_{1112} \\ C_{2211} & C_{2222} & C_{2233} & C_{2223} & C_{2213} & C_{2212} \\ C_{3311} & C_{3322} & C_{3333} & C_{3323} & C_{3313} & C_{3312} \\ C_{2311} & C_{2322} & C_{2333} & C_{2323} & C_{2313} & C_{2312} \\ C_{1311} & C_{1322} & C_{1333} & C_{1323} & C_{1313} & C_{1312} \\ C_{1211} & C_{1222} & C_{1233} & C_{1223} & C_{1213} & C_{1212} \end{pmatrix} = \begin{pmatrix} c_{11} & c_{12} & c_{13} & c_{14} & c_{15} & c_{16} \\ c_{21} & c_{22} & c_{23} & c_{24} & c_{25} & c_{26} \\ c_{31} & c_{32} & c_{33} & c_{34} & c_{35} & c_{36} \\ c_{41} & c_{42} & c_{43} & c_{44} & c_{45} & c_{46} \\ c_{51} & c_{52} & c_{53} & c_{54} & c_{55} & c_{56} \\ c_{61} & c_{62} & c_{63} & c_{64} & c_{65} & c_{66} \end{pmatrix}$$

For isotropic material, the stiffness matrix can be represented by only two parameters, the so-called Lamé parameters λ and μ is

$$c_{mn} = \begin{pmatrix} \lambda+2\mu & \lambda & \lambda & 0 & 0 & 0 \\ \lambda & \lambda+2\mu & \lambda & 0 & 0 & 0 \\ \lambda & \lambda & \lambda+2\mu & 0 & 0 & 0 \\ 0 & 0 & 0 & \mu & 0 & 0 \\ 0 & 0 & 0 & 0 & \mu & 0 \\ 0 & 0 & 0 & 0 & 0 & \mu \end{pmatrix}$$

2.3. Anisotropic media

The more general anisotropic formulation describes the elastic properties of a material, if the variation of parameters with direction is allowed. Anisotropy may be due to crystal structure (Chapter 3.1) or other microscopic and macroscopic effects, e.g. layering; Chapter 3.2. Generally, either orthorhombic or hexagonal symmetry is assumed when analyzing the earth.

Hexagonal anisotropic media are characterized by a single plane of isotropy and one single axis of rotational symmetry. It can be caused either by intrinsic anisotropy of the dominant mineral (e.g. mica, clay, serpentine) or by periodic layering of materials with different elastic properties. The layers have to be thin in comparison to the seismic wavelength (Figure 3a). Hexagonal anisotropy is fully characterized by five independent elastic parameters. If we assume that the axis of symmetry is x_3 the stiffness matrix has the form

$$c_{mn}^{trans} = \begin{pmatrix} c_{11} & c_{11}-2c_{66} & c_{13} & 0 & 0 & 0 \\ c_{11}-2c_{66} & c_{11} & c_{13} & 0 & 0 & 0 \\ c_{13} & c_{13} & c_{33} & 0 & 0 & 0 \\ 0 & 0 & 0 & c_{55} & 0 & 0 \\ 0 & 0 & 0 & 0 & c_{55} & 0 \\ 0 & 0 & 0 & 0 & 0 & c_{66} \end{pmatrix}$$

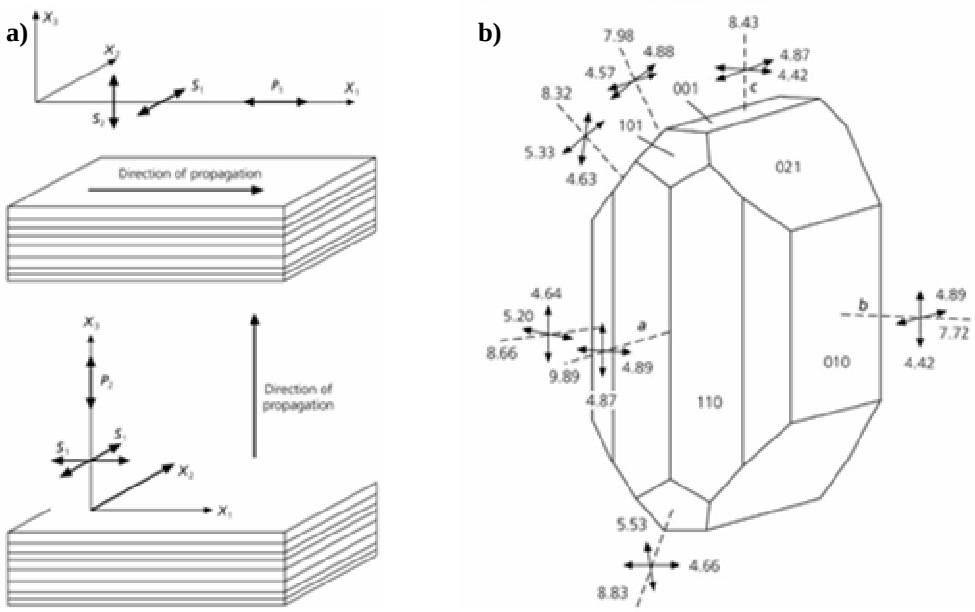

Figure 3: Possible origins of anisotropy (after Shearer [1999]): a) thin layered material results in hexagonal symmetry anisotropy. b) Minerals like olivine have an intrinsic anisotropy.

Orthorhombic media are characterized by three mutually orthogonal axes of symmetry. One of the most abundant mineral in the Earth's mantle, olivine, belongs to this class (Figure 3b). If the coordinate axes coincide with the symmetry axes the stiffness matrix of the orthorhombic system has nine independent entries and has the form

$$c_{mn}^{ortho} = \begin{pmatrix} c_{11} & c_{12} & c_{13} & 0 & 0 & 0 \\ c_{12} & c_{22} & c_{23} & 0 & 0 & 0 \\ c_{13} & c_{23} & c_{33} & 0 & 0 & 0 \\ 0 & 0 & 0 & c_{44} & 0 & 0 \\ 0 & 0 & 0 & 0 & c_{55} & 0 \\ 0 & 0 & 0 & 0 & 0 & c_{66} \end{pmatrix}$$

Olivine is an anisotropic mineral and a main composite of the (upper) mantle. It has a density of 3.311 kg/m^3. The elastic tensor (in GPa) of this orthorhombic mineral is [Kumazawa & Anderson, 1969]:

$$c_{ij} = \begin{pmatrix} 323.7 & 66.4 & 71.6 & 0 & 0 & 0 \\ 66.4 & 197.6 & 75.6 & 0 & 0 & 0 \\ 71.6 & 75.6 & 235.1 & 0 & 0 & 0 \\ 0 & 0 & 0 & 64.6 & 0 & 0 \\ 0 & 0 & 0 & 0 & 78.7 & 0 \\ 0 & 0 & 0 & 0 & 0 & 79.0 \end{pmatrix}$$

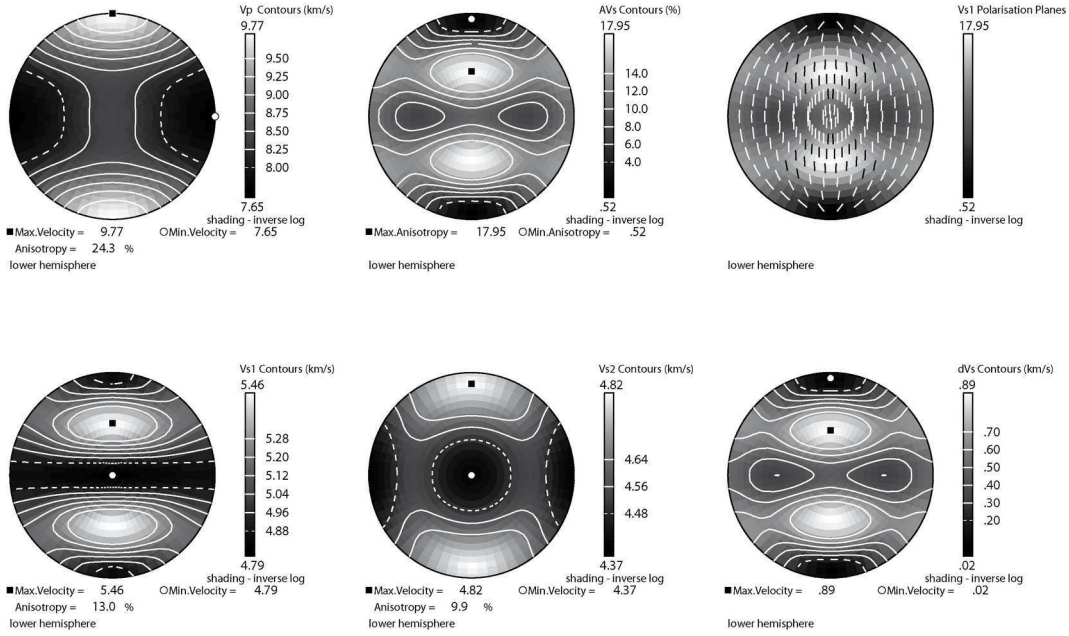

Figure 4: velocities of olivine in the lower hemisphere.

2.4. Plane wave propagation

Plane waves play an essential part in understanding wave propagation. Here, the displacement only varies in the direction of wave propagation. The displacement $\vec{u}$ at position vector $\vec{x}$ may be expressed as

$$\vec{u}(\vec{x},t) = \vec{f}(t - \vec{s}\vec{x}),$$

where $\vec{s} = \hat{n}/V$ is the slowness vector, whose magnitude is reciprocal to the velocity V, $\hat{n}$ is an unit vector, t is time and $\vec{f}$ is an arbitrary function representing the wave form. A harmonic plain wave with angular frequency ω is represented by

$$\vec{u}(\vec{x},t) = \vec{A}(\omega)e^{-i\omega(\hat{n}\vec{x}/V-t)}$$

The (elastic) wave propagation is governed by Hooke's Law. Written as a differential equation, the plane wave is described as

$$\rho\frac{\partial^2 u_i}{\partial t^2} - C_{ijkl}\frac{\partial^2 u_k}{\partial x_j \partial x_l} = 0$$

where ρ is the density of the medium, u_i is the displacement vector, and x_i are the Cartesian coordinates. Summation over repeated indices is implied. Note that anisotropy enters the equation via the stiffness tensor C_{ijkl}. Inserting this Ansatz in this differential equation gives the *Christoffel equation*, named after the German mathematician Elwin Bruno Christoffel (1829–1900)

$$(M_{ik} - \rho V^2\delta_{ik})E_k = 0$$

M_{ij} is the *Christoffel matrix*, which is a function of the material properties and direction of wave propagation:

$$M_{ij} = C_{ijkl}n_j n_i$$

The Christoffel equations describes a standard eigenvalue (ρV^2) – eigenvector (E_i) problem, where the eigenvalues are determined by

$$\det(M_{ij} - \rho V^2\delta_{ij}) = 0$$

The solution of this cubic equation yields three possible values of the squared velocity V, namely one P-wave and two S-wave velocities (e.g., S_H and S_V). As shown before (Chapter 2.2), the two S wave velocities are identical in isotropic media and we get

$$\alpha = V_P^{iso} = \sqrt{\frac{\lambda + 2\mu}{\rho}}; \quad \beta = V_S^{iso} = \sqrt{\frac{\mu}{\rho}}$$

For any specific direction n_i in an anisotropic medium, these are represented by the three eigenvalues. The three eigenvectors specify the polarization of the wave, namely the quasi-P, the fast S-wave, and slow S-wave. Backus [1965] showed that for weak anisotropy the velocities in dependence on azimuth θ can be approximated to first order as

$$\begin{aligned} V_P^2 &= A + B_c \cos 2\theta + B_s \sin 2\theta + C_c \cos 4\theta + C_c \sin 4\theta \\ V_{S\parallel}^2 &= D + E_c \cos 4\theta + E_s \sin 4\theta \\ V_{S\perp}^2 &= F + G_c \cos 2\theta + G_s \sin 2\theta \end{aligned}$$

where V_P is the P-wave velocity, $V_{S\parallel}$ and $V_{S\perp}$ are the S-wave velocity parallel and perpendicular to symmetry plane, respectively. The coefficients depend on the elastic constants:

$$\begin{aligned} A &= \tfrac{3}{8}(C_{1111} + c_{2222}) + \tfrac{1}{4}(C_{1122} + 2C_{1212}) \\ B_c &= \tfrac{1}{2}(C_{1111} - C_{2222}), \quad B_s = (C_{2111} + C_{1222}), \\ C_c &= \tfrac{1}{8}(C_{1111} + c_{2222}) - \tfrac{1}{4}(C_{1122} + 2C_{1212}) \\ C_s &= \tfrac{1}{2}(C_{2111} - C_{1222}) \\ D &= \tfrac{1}{8}(C_{1111} + c_{2222}) - \tfrac{1}{4}(C_{1122} - 2C_{1212}) \\ E_c &= -C_c, \quad E_s = -C_s \\ F &= \tfrac{1}{2}(C_{1313} + C_{2323}) \\ G_c &= \tfrac{1}{2}(C_{1313} - C_{2323}), \quad G_s = C_{2313} \end{aligned}$$

where the indices *c* and *s* indicate cosine and sine terms, respectively.

2.5. Seismological detection of anisotropy

2.5.1. P-waves

Early measurements of Pn velocities as a function of azimuth in the oceans revealed higher velocities perpendicular to the mid ocean ridges [e.g., Morris et al., 1969]. These measurements showed a strong 2θ dependency, as described before [Backus, 1965].

More general, the arrival of P-waves depends on azimuth and incident angle (Figure 4). The depth integral along all ray paths yields the delay time variations (Figure 5). Therefore, the study of teleseismic P delays reveals the anisotropic structure beneath a station. Bokelmann [2002a, 2002b] uses this technique to determine the 3D orientation of anisotropy beneath North America. Babuska & Plomerova [1996] propose a joint inversion of P-wave and Shear wave splitting (see below).

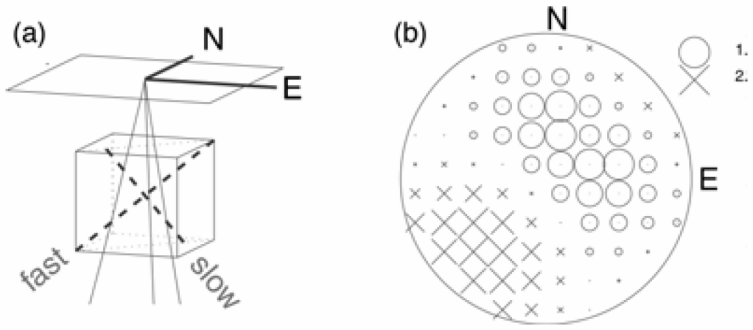

Figure 5: a) Ray geometry through an anisotropic block of dipping anisotropy. The fast axis is dipping 30° to the SW, the intermediate axis is dipping 60° to the NE, and the slow axis is horizontal. b) The lower hemisphere shows predicted fast/slow delays (crosses and circles respectively; given in sec) for a propagation through a 150 km anisotropic layer defined in a). [after Bokelmann, 2002b]

The analysis of polarizations of quasi-P waves has also proposed by Bokelmann [1995] and Schulte-Pelkum et al. [2001; 2003]. The horizontal polarization of the initial P particle motion can deviate by >10° from the predicted azimuth along a great circle from station to source. They showed that stations within regional distances of each other show consistent azimuthal deviation patterns, while the deviations seem to be independent of source depth and near-source structure.

2.5.2. Shear wave splitting

When a shear wave arrives at an anisotropic medium, the shear wave is split into two separate waves traveling at different velocities. Analyzing these split shear waves at

surface stations by recovering their original polarization gives information about the anisotropic medium. This is the subject of this thesis.

Montagner et al. [2000] present a derivation of this phenomenon. These equations have been described before by Vinnik et al. [1989] and Silver & Chan [1991]. Let us consider now the simplest case: a vertically propagating S-wave within an isotropic medium. The associated displacements in wave coordinate system (Radial, Transverse, and Vertical) are then

$$u_{iso}(z,t) = \begin{cases} u_R = a_0 \exp(i\omega(t - \frac{z-z_0}{Vs_0})) \\ u_T = 0 \\ u_z = 0 \end{cases}$$

where $Vs_0(z)$ is the S-wave velocity in the isotropic medium. In a geographic coordinate system the displacements are

$$u_{iso}(z,t) = \begin{cases} u_E = a_0 \cos\Psi \exp(i\omega(t - \frac{z-z_0}{Vs_0})) \\ u_N = a_0 \sin\Psi \exp(i\omega(t - \frac{z-z_0}{Vs_0})) \\ u_z = 0 \end{cases}$$

where Ψ is the backazimuth. Now assume, that at depth $z = z_0$ the wave enters an anisotropic medium with horizontal (fast and slow) symmetry axes. This reduces the problem to two dimensions, since the vertical axis is identical to all appearing systems. Let Ψ_A be the angle between North and the orientation of the fast S-wave polarization plane (Φ). Then

$$u_{aniso}(z,t) = \begin{bmatrix} u_f \\ u_s \end{bmatrix} = \exp(i\omega t) \begin{bmatrix} e^{i+} & 0 \\ 0 & e^{i-} \end{bmatrix} \times \begin{bmatrix} \cos\psi_A & \sin\psi_A \\ -\sin\psi_A & \cos\psi_A \end{bmatrix} \begin{bmatrix} a_N \\ a_E \end{bmatrix}$$

where $e^{i+} = \exp(-i\omega \frac{z-z_0}{Vs_0 + \delta Vs/2})$ and $e^{i-} = \exp(-i\omega \frac{z-z_0}{Vs_0 - \delta Vs/2})$. In other words, within the anisotropic layer the wave is split into two waves, traveling at velocities of $Vs_0 + \frac{\delta V}{2}$ and

$Vs_0 - \frac{\delta V}{2}$ and thus accumulating a delay. This is expressed in the "dephasing matrix" $H = \begin{bmatrix} e^{i+} & 0 \\ 0 & e^{i-} \end{bmatrix}$, whose elements $e^{i\pm}$ can be rewritten as

$$e^{i\pm} = e^{-i\omega\left(z-z_0 / Vs_0\right)} e^{\mp i\omega\left((z-z_0)\delta V / 2V_{S0}^2\right)}.$$

The second exponential term can be developed into a Taylor Series if $\omega(z-z_0)(\delta V/2V^2 s_0) << 1$. This is achieved for signal periods $T=2\pi/\omega$ larger than approximately 3s, assuming an anisotropy of 5% ($\delta V/Vs_0=0.05$), an average S-wave velocity of $Vs_0 = 4$km/s and a thickness of the anisotropic layer of 100km. Therefore, a first order approximation is valid for small anisotropies and body waves of long periods (T>10s). SKS waves are ideal for this analysis, since their dominant period is usually approximately 8 seconds, and their arrival is well separated from other phases.

A rotation of the displacement vector from the anisotropic system (f-s) into the wave coordinate system (R-T) yields

$$u_{aniso}(z,t) = \begin{bmatrix} u_R \\ u_T \end{bmatrix} = \begin{bmatrix} \cos^2 \psi'_A e^{i+} + \sin^2 \psi'_A e^{i-} \\ \frac{1}{2}\sin^2 \psi'_A \left(e^{i+} + e^{i-}\right) \end{bmatrix} a_0 e^{i\omega t}$$

$$u_R = a_0 e^{i\omega\left(t - \frac{z-z_0}{Vs_0}\right)} \left(\cos\frac{\omega(z-z_0)\delta V}{2Vs_0^2} + i\cos 2\psi'_A \sin\frac{\omega(z-z_0)\delta V}{2Vs_0^2}\right)$$

$$u_T = a_0 e^{i\omega\left(t - \frac{z-z_0}{Vs_0}\right)} \sin 2\psi'_A \sin\frac{\omega(z-z_0)\delta V}{2Vs_0^2}$$

where $\psi'_A = \psi_A - \psi$ is the angle between fast axes and North. Reordering and taking advantage of the fact that if $\omega(z-z_0)(\delta V/2V^2 s_0) << 1$ the components of displacement after the anisotropic layer in wave coordinate system are

$$u_R(t) = e^{i\omega t}(1 + i\omega\delta t \cos 2\psi'_A) u_R^0$$
$$u_T(t) = e^{i\omega t} \tfrac{1}{2}\delta t \sin 2\psi'_A \dot{u}_R^0$$

where $\delta t = (z\text{-}z_0)(\delta V/2V^2 s_0)$ is the accumulated delay time, and $\dot{u}_R^0 = \partial u_R^0 / \partial t = i\omega u_R^0$ is the time derivative of the waveform before the anisotropic layer ($u_T^0 = 0$).

2.5.3. Surface waves

In isotropic, laterally homogeneous media two types of surface waves exist (Figure 6): Love waves have rectilinear particle motion in a horizontal plane perpendicular to propagation direction. Rayleigh waves show elliptical particle motion in a vertical plane along propagation direction.

Surface waves propagate parallel to the surface of the earth. The penetration depth is proportional to their wavelength. For this reason, different modes of a surface wave travel at different velocities (reflecting the velocity structure of the Earth), leading to a dispersion of the signal. This can in turn be used to study the depth structure of the Earth. However, the long wave lengths limit the lateral resolution (~400km; [Debayle et al., 2005])

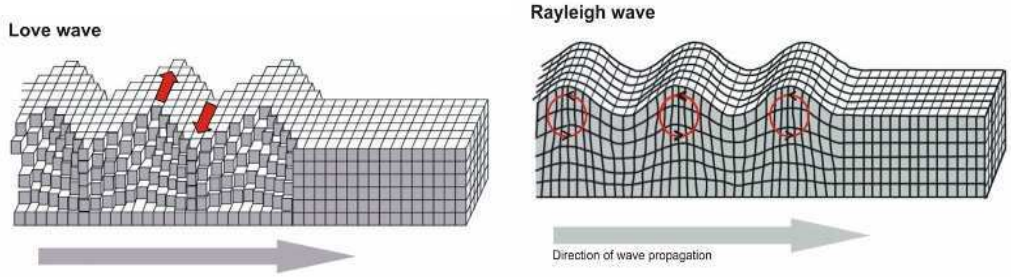

Figure 6: Sketch of the particle motion of Love and Rayleigh waves (after Lay & Wallace, 1995)

Discrepancies in dispersion curves of Love and Rayleigh waves can be well explained by hexagonal anisotropy with a vertical axis of symetry. Smith & Dahlen [1973] showed that the equation of azimuthal phase-velocity variations for Love and Rayleigh waves at a given period has a form similar to (quasi-) P waves:

$$V_{Love}(\theta) \approx V_{Rayleigh}(\theta) = A_1 + A_2 \cos 2\theta + A_3 \sin 2\theta + A_4 \cos 4\theta + A_5 \sin 4\theta$$

The application of these phenomena in seismology will be discuss in more detail in Chapter 4.6.2 .

3. Origins of seismic anisotropy

Seismic anisotropy is the directional variation of seismic wave speed. The cause of seismic anisotropy in the crust and in the mantle is still under debate. A seismic wave is an (transient) elastic deformation and thus experiences any elastic anisotropy. The speed at which the wave travels is directly linked to the elastic tensor and the directional variation of seismic wave speed (i.e. seismic anisotropy) is thus a measure of strength of anisotropy.

Seismic anisotropy is generally reported as the percentage difference between the velocities corresponding to the fastest and slowest orientations:

$$A = (V_{max} - V_{min})/V_{average}$$

where V is either the P- or S-wave velocity.

Seismic anisotropy occurs at many different scales from kilometers to single-crystal (grain) scales (Chapter 3.1). This broad range of spatial scales complicates the imaging efforts of band-limited data. The signal generated by earthquakes has a dominant period which is too long to be sensitive to only the single-crystal anisotropy. Furthermore, the Fresnel Zones associated with these dominant periods can sometimes be wider than the characteristic scale of type of anisotropy. Seismic waves within these Fresnel zones therefore experience an average of the different anisotropies, or “bulk” anisotropy. It is thus an indicator of long range order in a material, where features smaller than the seismic wavelength (e.g., crystals, cracks, pores, layers or inclusions) have a dominant alignment.

One cause of anisotropy might be alternating isotropic layers with different elastic properties [Backus, 1962]. However, the two primary candidate theories suggest that lithospheric and asthenospheric seismic anisotropy is either dominated by crystalline anisotropy [e.g., Nicolas and Christensen, 1987] or by fluid- or melt-filled cracks or dikes

[Crampin, 1991; Kendall, 1994]. Both candidates may also explain lower mantle anisotropy [Lay et al., 1998: Garneo, 2000; Kendall, 2000].

This chapter will present the mineralogical and geological aspects of anisotropy. A brief description of anisotropy in single-crystals (Chapter 3.1) is followed by the discussion of (large-scale) structural origins of anisotropy (Chapter 3.2). Both have different implications for geodynamic and tectonic interpretations, which are presented in Chapter 3.3 and 3.4.

3.1. Lattice-preferred orientation (Crystalline anisotropy)

The elastic properties of any material are described by a 4th-order tensor, C_{ijkl}, with 81 independent components. However, symmetry considerations simplify the tensor and thus reduce the number of independent components. All possible crystals belong to one of nine possible symmetry systems. The more complicated the symmetry, the more independent constants are needed to completely describe the tensor. In Geosciences, mostly orthorhombic (olivine; eight constants) and hexagonal (quartz; five constants) are considered. An orthorhombic symmetry (Figure 7a) has different velocities along three mutually perpendicular symmetry axes, whereas a hexagonal symmetry (Figure 7b) has different velocities parallel and perpendicular to its cylindrical symmetry axis. The complicated triclinic structure of feldspars is usually neglected.

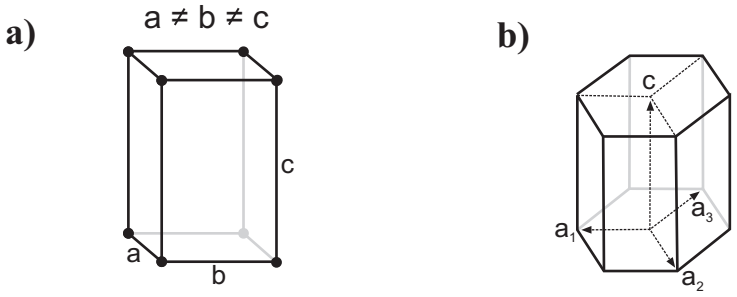

Figure 7: The two most common crystallographic symmetry systems are a) orthorhombic and b) hexagonal

Olivine is the most abundant mineral in the upper mantle. Its seismic velocities are strongly anisotropic (25% V_P and 12% V_S) [Nicolas & Christensen, 1987; Crampin, 1991; ben Ismaïl & Mainprice, 1998]. While initially oriented at random, deformation leads to a preferred orientation of the minerals under certain temperature and pressure conditions [Nicolas & Christensen, 1987]. Laboratory experiments with dunite (a rock comprised mainly of olivine and minor pyroxene), shows that progressive simple shear will encourage the development of lattice preferred orientations (LPO) of the olivine minerals such that the *a*-axis will rotate towards the direction of shear (Figure 8). The main mechanism is dislocation creep within the mineral, i.e. intercystalline slip of atoms

[Nicolas & Christensen, 1987]. Similarly, if the dunite is subjected to uniaxial strain (compressive or extensive), an LPO can also develop. In this case, the *a*-axis is rotated towards the direction of elongation.

A change in stress regime (and thus deformation type and direction) erases any asthenospheric LPO relatively quick by recrystallisation [Nicolas et al., 1973; Mainprice & Silver, 1993]. Therefore, any anisotropy in the lithosphere is assumed to reflect the last active deformation. In stable tectonic regimes, this last active deformation is then "frozen" in the anisotropy of the lithospheric rocks during post-tectonic thermal relaxation [Vauchez & Nicolas, 1991; James & Assumpção, 1996; Barruol et al., 1997; Barruol et al., 1998; Heintz & Kennett, 2006].

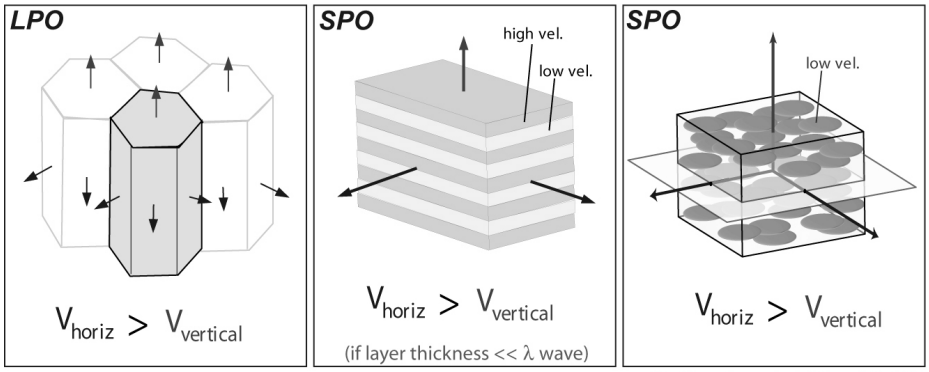

Figure 8: Different origins of anisotropy [after Moore et al., 2004]. LPO results from the intrinsic anisotropy of aligned minerals, whereas SP can be either due to repeated thin layering or to oriented, melt-filled cracks

3.2. Shape-preferred orientation (alignment of structures)

A preferred orientation of cracks, faults, fractures or compositional lamellae makes an otherwise homogeneous medium effectively anisotropic for wavelengths much larger than the spacing interval of the structure [Backus, 1962; Figure 8]. Such shape preferred orientations (SPO) result in an effective fast and slow orientation of seismic wave propagation, with the fast S-wave polarised along the strike of the cracks.

In the lower crust, SPO anisotropy is mainly due to fluid-filled cracks (e.g., Crampin, 1984; Crampin, 1991). In the mantle mainly melt-filled cracks or lenses, or compositional lamellae are the sources of SPO anisotropy [Mainprice, 1997; Kendall, 1994, 2000; Vauchez et al., 2000; Walker et al., 2004].

SPO is thought to be a significant cause of seismic anisotropy beneath mid-ocean ridges and perhaps some portions of subduction systems. Similarly, continental rift zones contain a range of evidence suggesting that SPO due to decompression melting plays an important

role in the development of seismic anisotropy. Beneath stable continental interiors with thick lithospheres, however, SPO is usually perceived as a local crustal phenomenon with less broad-scale influence on most seismic anisotropy observations.

3.3. Depth of anisotropy

Analyzing the anisotropic properties of the Earth improves knowledge of the present and past geodynamic processes. At different depth levels, different mechanisms provoke seismic anisotropy. Also, various geochemical and geophysical techniques allow to infer the distribution of minerals with various intrinsic anisotropies, which dominate in different depth levels [Figure 9; see Mainprice et al., 2000 for a review]. Global tomography models [e.g., Montagner & Tanimoto, 1990; Debayle et al., 2005) show significant radial anisotropy variations with depth of radial anisotropy. Montagner [1998] concluded that the strain, caused by a convecting mantle and responsible for orienting minerals, concentrate at boundary layers, where in turn anisotropy is strongest.

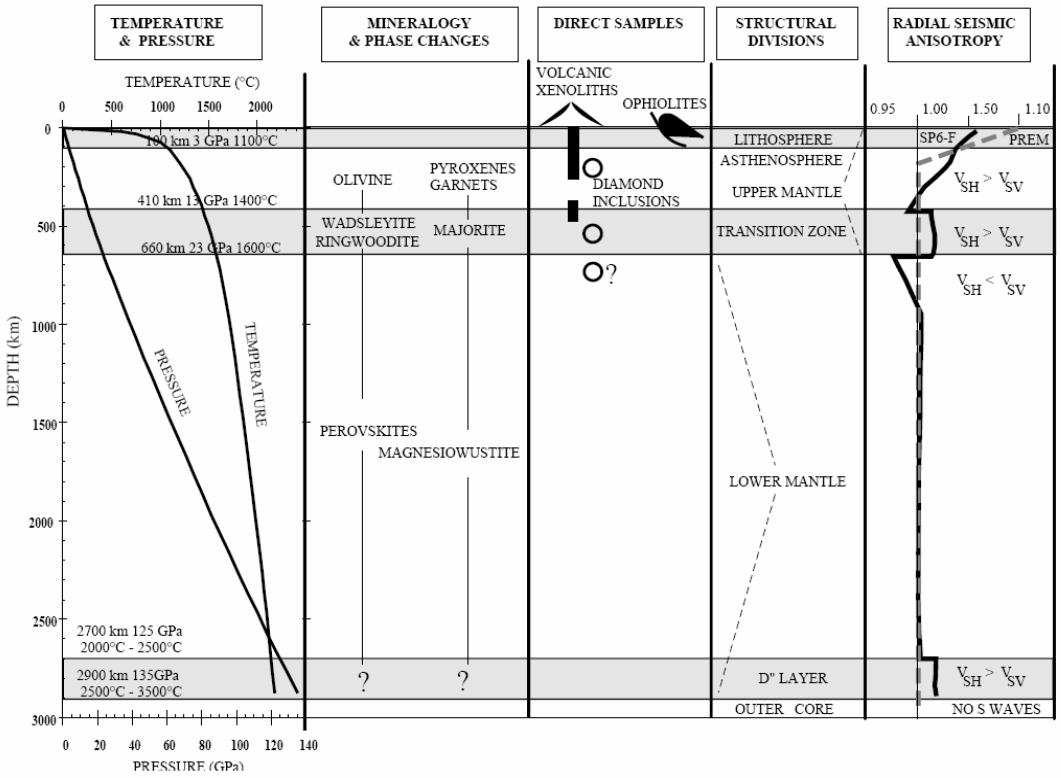

Figure 9: The major physical and chemical variations in the Earth's mantle which control seismic anisotropy [after Mainprice et al., 2000]. The seismic model SP6-F comes from Montagner and Kennett (1996).

It is an interesting feature in global seismology, that beneath continents primarily the Lehmann discontinuity is observed [Shearer, 1990; Gu et al., 2001]. Under oceans the much shallower Gutenberg discontinuity is often reported. If both Lehmann and Gutenberg discontinuity mark a transition from anisotropy to isotropy [Leven et al., 1981],

these can be interpreted as the bottom of a mechanical coherent lithosphere (or 'tectosphere' as proposed by Jordan [1978; 1981]). Gung et al. [2003] link those observations with similar results from surface wave anisotropy observations and conclude in regions where those discontinuities are horizontal, and thus anisotropy has a significant horizontal component, a relatively weak anisotropic lithosphere is underlain by relatively strong anisotropic asthenosphere.

In a more recent study Conrad et al. [2007] inferred the global pattern of anisotropic fabric from viscous mantle flow models. The results explain well oceanic anisotropy, but the fit is less well in continental areas. The authors conclude that both asthenosphere and lithosphere contribute to shear wave splitting, but the thicker lithosphere dominates for continents. In comparison, oceanic lithosphere is thinner, younger and less deformed and has thus a smaller contribution than the asthenosphere. This is in good agreement with previous studies of Barruol et al. [1997] and Tommasi [1998]

3.3.1. Anisotropy in the crust

Microfractures are generally oriented at random. However, oriented openings tend to close perpendicular to the maximum principal stress direction σ_1. These crack-systems are filled with other materials, in general fluids. The repeating variation of elastic parameters results in seismic anisotropy and a splitting of shear-waves. The fast S-wave spolarisation plane orientation Φ would be parallel to the current maximum horizontal stress component σ_H [e.g., Crampin & Chastin, 1999]. The magnitude of anisotropy scales with crack size and amount of cracks. This is the dominant source of anisotropy for the upper (~10km) part of the crust [Barruol & Kern, 1996], since below all cracks are closed. The contribution of crustal anisotropic rock minerals developing a LPO is assumed to be a few 0.1% [Barruol & Kern, 1996; A. Vauchez, pers. comm. 2007]

Anisotropy in the lower crust is dominated by finely layered horizontal strata due to the interactions of reflections and transmissions through thin layers [Backus, 1962; Chapter 3.2]. It is also characteristic to many shales, clays and mudstones, where the anisotropy is caused by horizontal intergranular platelets of mica and other minerals [see Crampin & Chastin, 2003].

Both of these cases result in hexagonal anisotropy (Figure 7, Figure 8), whereby the axis of symmetry is normal to the cracks or the layering, respectively. In crack-dominated crust, Φ generally renders the σ_H direction [e.g., Crampin & Chastin, 2003]. The accumulated delay time total is however small (~0.2 sec, Barruol and Kern [1996]) due to the minor thickness of the crust. Thus, crustal anisotropy is often neglected in studies focusing on mantle anisotropy. However, changes in crustal anisotropy direction have been successfully applied to relate stress changes with earthquake ruptures [Gamar &

Bernard, 1997] and volcanic eruptions [Gerst & Savage, 2004] which might be a useful forecasting tool.

3.3.2. Anisotropy in the lithosphere

If crust and subcontinental mantle deform coherently during tectonically active episodes (Figure 10), this is called *Vertically Coherent Deformation* (VCD) [Bormann et al., 1993; Silver, 1996]. Such deformation leads to the development of a LPO of olivine crystals (see Chapter 3.1). Thermal cooling of the lithosphere freezes the LPO to the lithosphere. Therefore, spatial variations in splitting parameters should track geologic variations and the measured Φs should, in the simplest case, follow the general tectonic trend. In the case of multiple episodes of deformation, only the last significant active episode prevails. See Chapter 3.4 for a more detailed discussion.

The three major categories of deformation that would be encountered are: transcurrent, collisional, and extensional regimes. In fact, pure collisions are rarely observed, and there is almost always a significant transcurrent component. See Chapter 3.4 for further discussions on this topic.

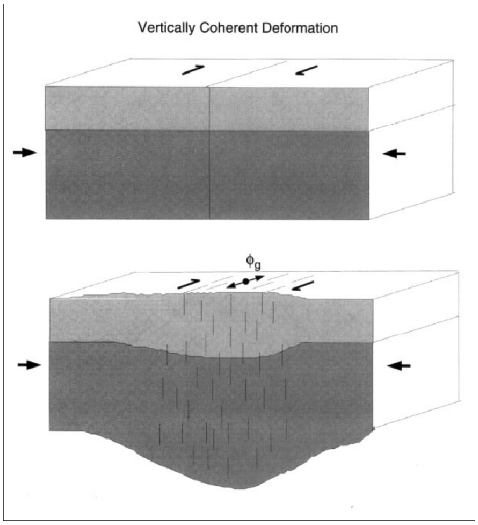

Figure 10: Vertically coherent deformation of crust and lithosphere [after Silver, 1996].

3.3.3. Anisotropy in the asthenosphere

In the case of asthenospheric anisotropy, the asthenosphere serves as a decoupling zone of the differential motion between the tectonic plate and the mantle. This model is referred to as *Simple Asthenospheric Flow* [Vinnik et al 1984; Bormann et al. 1993, 1996; Silver, 1996; Figure 11]. A special case of this model arises, if we assume the sub-asthenospheric mantle as stationary. Then, the lineation is oriented along the absolute plate motion (APM) direction of the plate. There is however growing evidence, that the mantle is moving in a

hotpot reference frame [Steinberger & O'Connell, 1998; Silver & Holt, 2002; Tarduno et al., 2003; Andrews et al., 2006; see also Chapter 5.4.1].

The mantle flow can be deviated by obstacles like lithospheric keels [Bormann et al., 1996; Fouch et al., 2000; 2006], cratons [e.g., Assumpção et al., 2006; Heintz & Kennett, 2006] or subduction slabs [e.g., Margheriti et al., 2003; Levin et al., 2004]. See Chapter 3.4.2 for further discussion on this subject.

To completely reorient olivine aggregates strains of order unity suffice [Nicolas et al., 1973; Mainprice & Silver, 1993; Chastel et al., 1993]. For tectonic plate speeds in the order of 1-10cm/yr and asthenospheric thickness of order 100 km such strains would be produced in only a few million years. Silver [1996] thus remarks that the memory of asthenospheric flow direction is short.

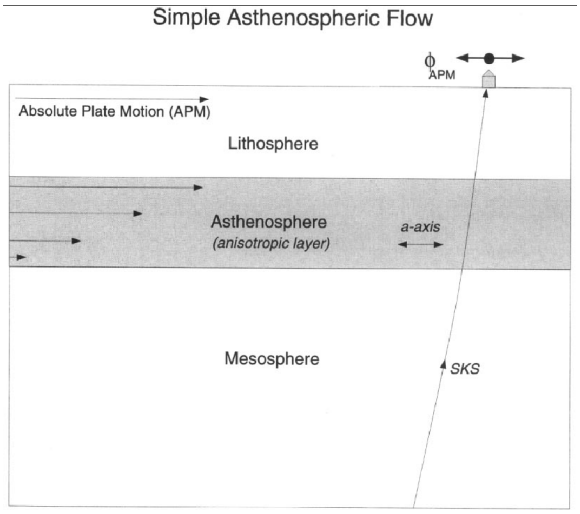

Figure 11: Simple asthenospheric flow aligns minerals "from below" [after Silver, 1996]

It is still a major question in geodynamics if absolute plate motion (APM) is caused or accommodated by asthenospheric motion [Forsyth & Uyeda, 1975; Bokelmann, 2002]. If the main driving force for plate motion originates from the side by subducting plates (slab pull) and from mid-ocean ridges (ridge push), the asthenosphere mainly accommodates the strain. If however the plate motion is caused from below by mantle convection, the plates are dragged in the direction of mantle flow (basal drag).

Topography of the base of the lithosphere may distort the correlation with plate motion vector. But generally it is assumed that if the anisotropy directions do not coincide with APM direction but correlate with surface geological trends, then lithospheric origins of anisotropy are implied. Shear-wave splitting alone cannot resolve the depth of anisotropy (it integrates the anisotropy along the travel path), but reliably determines the orientation and magnitude of anisotropy. Furthermore, some studies suggest a two-layer model

combining both hypotheses. Thus, the comparison of anisotropy directions with other geophysical and geological datasets gives an unique opportunity to improve the conceptual understanding of deformation processes in the earth and their causing forces.

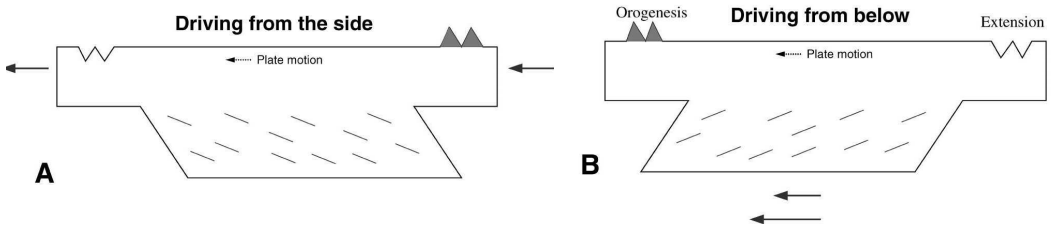

Figure 12: Sketch of the sense of shear within tectonic plate. Plate-mantle interaction leads to preferred mineral orientation in portions of thick lithosphere. Seismic fast axes are shown schematically by diagonal dashes. Dip direction of fast axes is indicative of driving mechanism. a) If plate is driven from side and mantle resists motion, fast axes dip away from plate-motion direction. b) Conversely, if plate is driven by faster-moving deeper mantle, fast axes dip toward absolute-plate-motion direction. [after Bokelmann, 2002]

3.3.4. Anisotropy in the transition zone

The upper mantle consists mostly of olivine, beside pyroxene, spinel, and garnet. In the transition zone between the 410 km and 660 km depth discontinuity, olivine is not stable and is replaced by high pressure polymorphs (β- and γ-spinel) with approximately the same composition. The dominant mineral in the transition zone is however wadsleyite At transition zone conditions, a wadsleysite crystal shows ~12% of anisotropy and capable of the evolution of CPOs, but characteristic orientations of symmetry axes lead to a weak bulk seismic anisotropy [Tommasi et al., 2004]. Horizontal shearing results in faster P_H and S_H waves, as observed by Seismic tomography [Montagner & Kennett, 1996]. In contrast such medium will appear isotropic for vertically propagating shear-waves (e.g. SKS) and will thus not produce any splitting.

3.3.5. Anisotropy in the lower mantle

It appears that the lower mantle is isotropic, with the exception of the D'' layer just above the core-mantle-boundary. However, still little is known on this depth interval. Restivo & Helffrich [2006] inferred from differences in splitting parameters of SKS and SKKS phases anisotropy in this layer. Their findings may support earlier speculations of a heterogeneous D'' layer with different anisotropic domains. These domains might be related to the remains of paleo-subduction slabs [e.g. Kendall & Silver, 1996; Lay et al., 1998]. Similar to the lithosphere, the anisotropy in the D'' layer is assumed to originate from melt inclusions and/or preferred crystal orientations [see Kendall, 2000].

3.4. Seismic anisotropy and plate tectonics

Data from surface waves and body waves indicate that anisotropy in the oceanic upper mantle appears to be relatively uniform [e.g. Montagner, 2002; Behn et al., 2004] while anisotropy in continental lithosphere changes over short length scales [Helffrich et al., 1994; Montagner et al., 2000; Conrad et al. 2007].

Seismic anisotropy reflects deformation processes. In the asthenosphere this deformation is due to relative motion between mantle and overlying plate. In the lithosphere the main deformation occurs at plate boundaries. The following chapters will present the effects of certain tectonic boundaries on the anisotropy. Detecting anisotropy in stable continental areas can help to interpret for ancient processes and the influence of obstacles to present mantle flow. This topic will be discussed in detail in Chapter 5 of this thesis.

3.4.1. Rifting

A continental rift is an elongated topographic depression overlying a lithosphere which has been significantly modified by extension. The mechanism of continental rifts can be separated into two end-member cases: active and passive rifting. For passive rifting we would expect that if the entire lithosphere extends, the crystallographic fast axis (and therefore splitting directions) would align in the direction of rift opening [Vachez et al. 2000, 2005]. Active rifting involves erosion of the lower lithosphere by mantle convection, causing an elevated asthenosphere beneath the rift zone. Kendall et al. [2006] propose a suite of different causes of anisotropy beneath the East African rift system (EARS, Figure 13). The main cause of anisotropy is attributed to thin melt pockets directly beneath the rift zone, oriented parallel to the rift axis. Away from the rift, the lithospheric LPO is due to pre-existing fabric, while beneath the lithosphere the LPO is due to viscous coupling between the base of the lithosphere and large-scale mantle upwelling. This model explains the rift-parallel Φ in the rift valley.

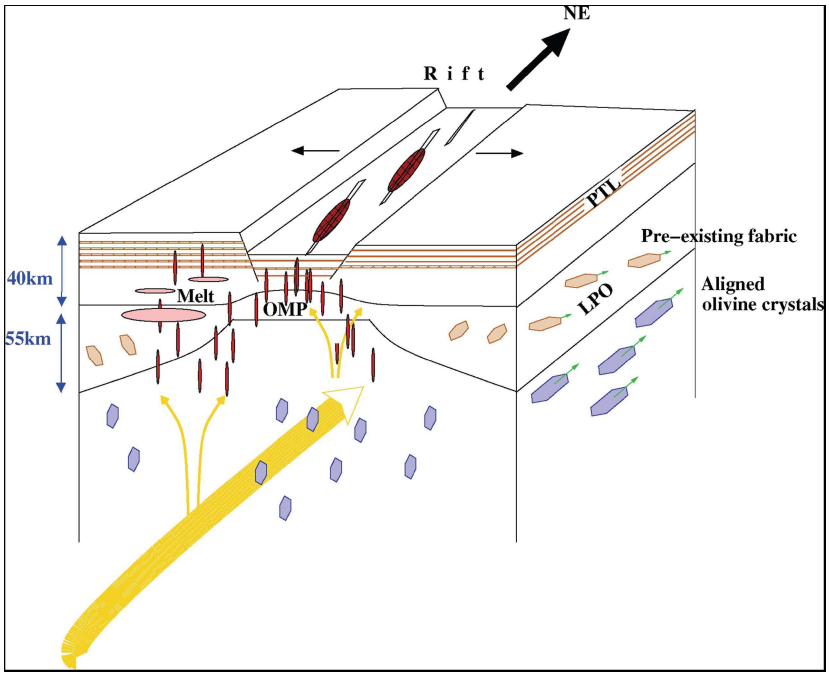

Figure 13: Model of seismic anisotropy beneath the East African Rift System [after Kendall et al., 2006]. A range of mechanisms is responsible for anisotropy, including periodic thin layering of contrasting materials, oriented pockets of melt, and the lattice-preferred orientation (LPO) of olivine crystals.

Gao et al. [1997] compare the variation of spitting parameters across rifts. They also relate their results of the East African Rift and the Rio Grande Rift to melt-filled cracks where Φ apparently followed a recent rotation of stress and thus re-organized the orientation of cracks. Both rifts are characterized by a relatively hot mantle probably above solidus. In contrast, the Baikal Rift shows cooler mantle that might be capable of generating a rift-perpendicular fabric away from the central rift valley. But in local patches of hot mantle, magmatic crack could cause rift parallel anisotropy (Figure 14).

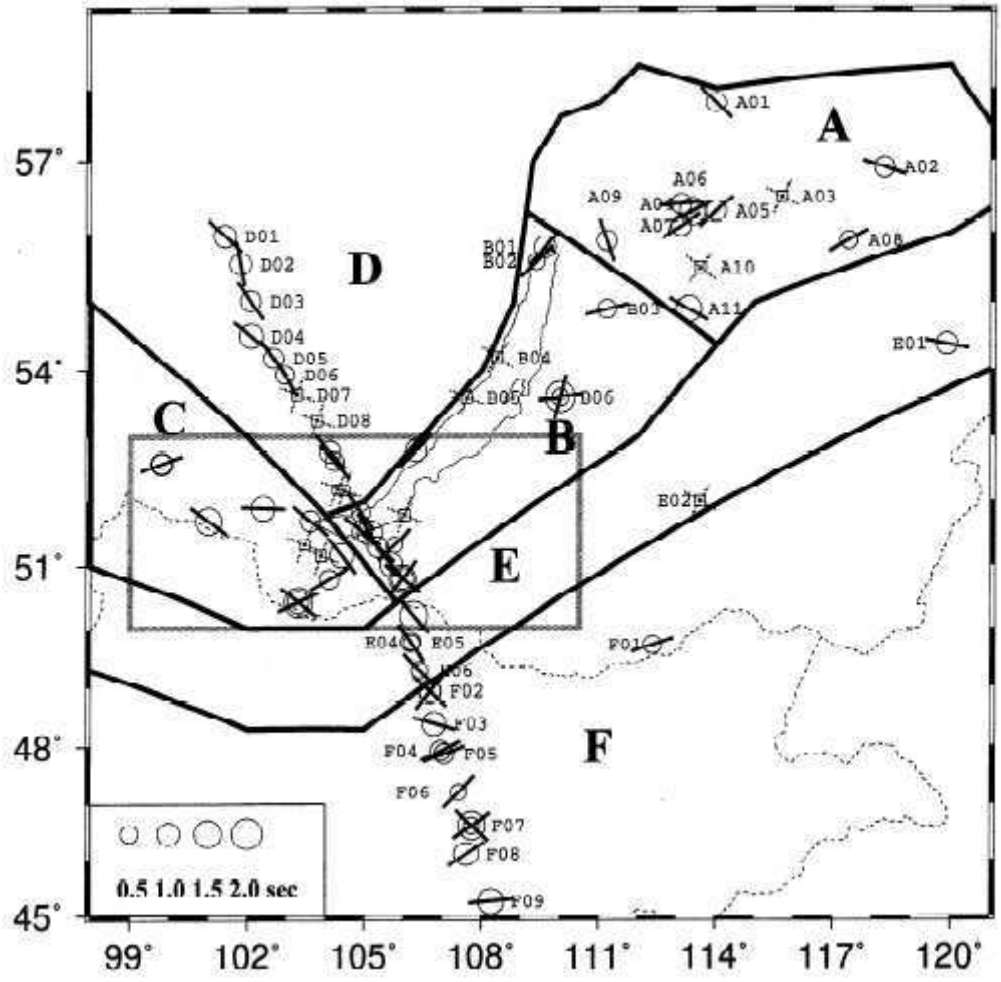

Figure 14: Splitting parameter variations across the Baikal Rift [after Gao et al., 1997]. North of the rift the observed Φs are rift perpendicular, while in the rift center they tend to be rift parallel. South of the rift Φ is again rift-perpendicular, though at even greater distances Φ again rotates rift parallel.

3.4.2. Subduction

Subduction zones exhibit a complex 3D pattern of mantle flow, especially at the corners of the slab. Complexity is possibly added by slab rollback, which may cause torroidal mantle flow beneath the backarc region [Hall et al., 2000]. The anisotropic fabric developed in such environments results in seemingly discrepant shear-wave splitting observations and interpretations for different (oceanic) subduction zones. Trench-parallel splitting directions are found for example for the Andean Subduction [e.g., Russo & Silver, 1994; Polet et al., 2000; Anderson et al., 2004], the Aleutian Islands [Yang et al., 1995], and in New Zealand [e.g., Audoine et al., 2004; Duclos et al., 2005]. Trench-normal splitting directions are found for the Philippine Subduction [Fouch & Fisher, 1998] and in Japan [e.g., Nakajima & Hasegawa, 2004]. A corner flow model has been used to explain splitting observations in Kamchatka [Levin et al., 2004] and the Apennines in Italy [Margheriti et al., 2003; Baccheschi et al., 2007].

Jung and Karato [2001] argue that the introduction of water to the olivine, the relation between flow geometry and seismic anisotropy undergoes marked changes. Under high-stress, high water content conditions, the anisotropic *b*-axes are oriented parallel to strain orientation. Lassak et al. [2006] model a synthetic seismic profile over a subduction zone. They find that a transition between anhydrous and hydrous mantle may cause a rotation of Φ from trench normal to trench parallel over short distances, accompanied by variations in delay times. These findings show the importance of the station setup for any future seismic experiment aimed to investigate anisotropy in subduction zones.

3.4.3. Orogens

Mountain chains are the surface expression of the collision of tectonic units. The depth dependence of rheology controls the style deformation. An important, but poorly constrained property is the strength of the lithosphere. A commonly accepted model for the strength of the lithosphere assumes a brittle upper crust, followed by a ductile lower crust and a strong upper mantle [Molnar & Lyon-Caen, 1988].

Knowing the extent of kinematic coupling between crust and upper mantle is important when comparing surface features with anisotropy orientations [Flesch et al., 2005]. A minimum in strength of the lower crust would result in a decoupling between upper mantle and crust. On the other hand, strong coupling implies vertically coherent deformation of crust and upper mantle [e.g. Silver, 1996].

Christensen & Crosson [1968] argued that if the deformation is in the form of uniaxial compression, the (slow) b-axis is aligned with the direction of compression. In consequence, the (fast) a-axis is then parallel to the trend of mountain chain. This relation is consistent with the direction of shortening in the upper mantle of active compressional belts [Makeyeva et al., 1992]. Alternatively, Vauchez & Nicolas [1991] interpret these (fast) orientations parallel to the mountain belt in terms of shear flow in the mantle along the strike of the belt.

Flesch et al. [2005] compared the Central Asian surface deformation field inferred from GPS and fault slip rate data with mantle deformation inferred from SKS splitting. Their data indicate a complete decoupling between crust and mantle in the Yunnan Province, whereas in Tibet a coupled, vertically coherent deformation is proposed. Lev et al. [2006] found a pronounced shift from NS direction in the Sichuan province and mostly EW directions in Yunnan. They suggest a fundamental change in deformation regime throughout the study area, which is consistent with Flesch et al. [2005].

In the Appalachians the splitting directions follow the geologic trend, indicating lithospheric origins of anisotropy, with small asthenospheric contributions.[Barruol et al., 1997]. Anomalous trends in the central part of the Appalachians are explained by frozen-in anisotropy as a consequence of a broad upper mantle strike-slip zone, which cause

vertical foliations. The authors point out, that a decoupling between crust and mantle is required for such model.

3.4.4. Oceans

Analyzing anisotropy beneath oceanic plates constrains fundamental ideas of plate tectonics by mapping mantle flow. Oceanic plates are relatively young (<200Ma) and thus largely undisturbed. That makes the comparison with plate motion directions straight-forward. Forsyth [1975] was the first to observe azimuthal anisotropy in surface wave data of the Pacific Ocean. These findings have been confirmed and refined by others for various oceans: the Indian Ocean [e.g., Montagner, 1986; Lévêque et al., 1997] and in a recent study Montagner [2002] analyzed the 3D structure of anisotropy beneath the Pacific Plate. The simultaneous inversion for Love and Rayleigh waves allows to detect both azimuthal and radial anisotropy and thus infer 3D orientation of anisotropy. The correlation with plate motion direction is generally good at depth between 100 and 200km, with notable exceptions close to hotspots: La Réunion and Mauritius [Lévêque et al. 1997] as well as Hawaii and Polynesia [Montagner, 2002]. This can be explained by a decoupling between plate and asthenosphere.

The lack of permanent ocean bottom seismometers (OBS) make representative analysis of shear wave splitting at the current stage impossible. Wolfe & Solomon [1998] evaluated a set of temporary OBS across the East Pacific Rise. They found ridge axis perpendicular splitting orientations, which is in agreement with spreading related mantle flow. Recent splitting studies on oceanic islands around Africa [Behn et al., 2004], the Galapagos Islands [Fontaine et al, 2005] and Polynesia [Fontaine et al., 2007] by and large confirm the correlation with plate motion, although individual stations show complex splitting patterns or no splitting (Null stations). This might reflect multi-layer anisotropy, the dominance of specific fabric of olivine ([011] fibre CPO) or local heterogeneities caused by plume activities.

4. Shear-wave splitting

Shear-wave splitting has become a widely used technique to analyse anisotropy at depth. It provides an exceptional possibility to study the Earth in otherwise inaccessible depths. The asthenosphere and the lower lithosphere are usually out of reach for methods other than seismology. By studying split shear waves anisotropic regions can be identified. Almost vertical ray paths of core refracted phases (SKS, SKKS, PKS; Figure 15) enable an integrated view of anisotropy directly beneath a station, without having to consider lateral heterogeneities. The interpretation of such anisotropy leads ultimately to a better knowledge of the Earths' deep interior and understanding of geodynamic processes.

4.1. Overview

A seismic shear-wave, which passes through an anisotropic region, experiences the phenomenon of birefringence. The incident shear-wave is split in two orthogonal components travelling at different velocities: the component polarized parallel to the orientations of the fast S-wave polarisation plane begins to lead the orthogonal component. The delay between those two components is proportional to the thickness of the anisotropic layer and/or strength of anisotropy. This results in two effects at a station at the surface:

- The two waveforms are separated by a time delay dt, which depends on both the thickness of the anisotropic layer and the strength of anisotropy
- The polarization is rotated in respect to the initial polarization of the wave.

By measuring this splitting of the S-wave it is possible to determine the two anisotropy parameters *orientation of the fast S-wave polarisation plane* Φ and *delay time* dt. One crucial factor for this is the knowledge of the initial polarisation of the wave. In teleseismic studies this problem can be addressed by using teleseismic core-refracted

phases (SKS, SKKS, PKS, …) or core-reflected phases (ScS, PcS, …). Figure 15 shows the travel paths of some of the most commonly used phases.

These phases have the advantage that their initial polarisation corresponds to the backazimuth (i.e. station-earthquake azimuth). For core refracted phases, all source side shear information is usually lost at the S-to-P conversion at the core-mantle boundary. It travels as P-waves in the (fluid) outer core, eliminating any possible source-side anisotropy contamination of the wave. At the P-to-S conversion, on leaving the outer core, the SKS wave is polarised parallel to the backazimuth.

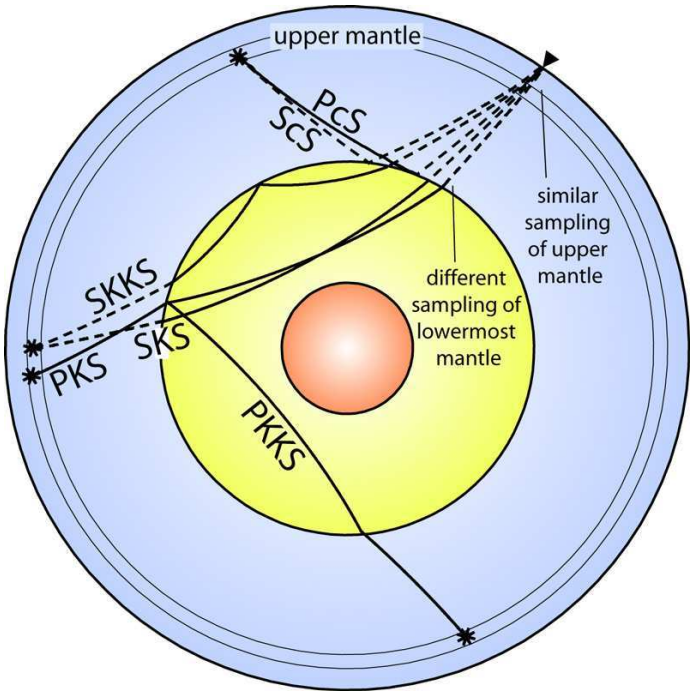

Figure 15: Travel paths of generally used seismic phases. These phases arrive at the station at relatively steep angles. Similar parts of the upper mantle is sampled while the waves pass through different regions close to the Core-Mantle-boundary [image courtesy of E. Garnero]

Each of these phases has characteristic source-receiver distances, at which they can be recorded. For SKS phases this is at distances between 85º and 140º. At other distances the arrival is either superposed by other phases or the phase is non-existent (Figure 16).

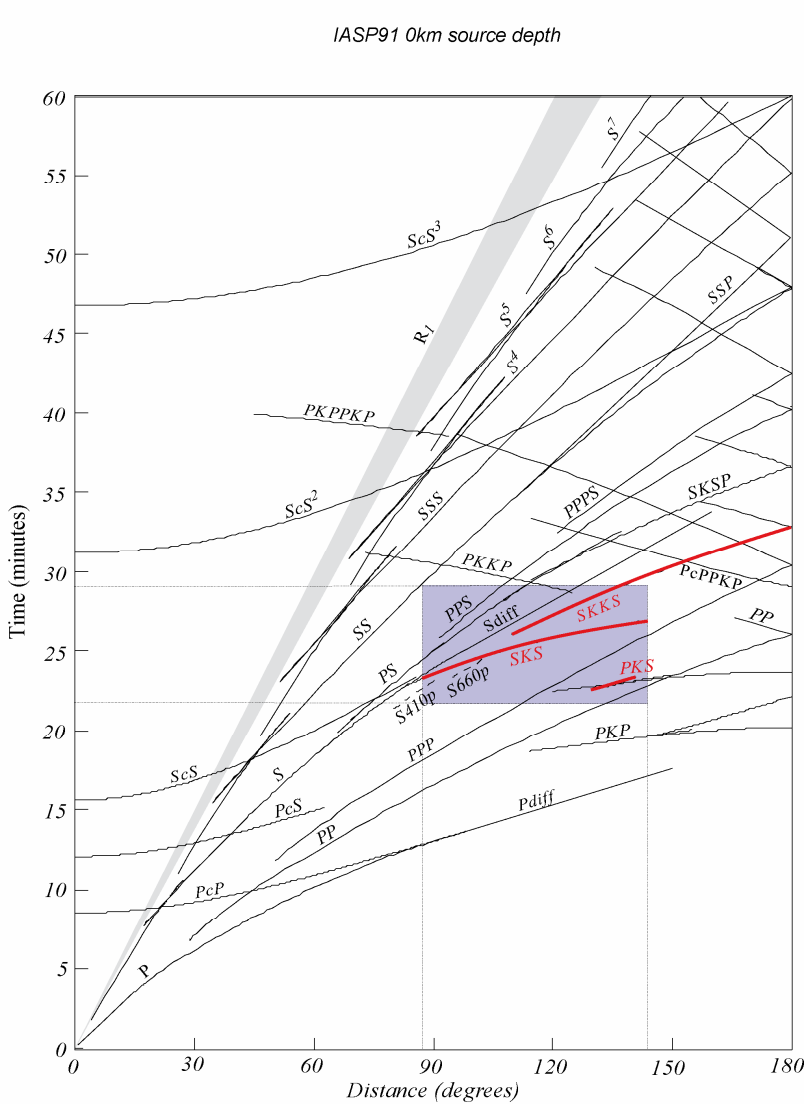

Figure 16: Theoretical phase plot. Core refracted shear-phases used for shear-wave splitting occur at distances between 90º and 145º. Mostly these are well separated from other phases, which could otherwise contaminate the signal of the phase of interest.

4.2. Inversion techniques

Two complementary types of techniques exist for estimating the splitting parameters Φ and *dt*, with each type having two main branches (Figure 17). The first type (multi-event technique) analyse simultaneously a set of records coming from different azimuths. Kosarev et al. [1984] and Vinnik et al. [1989] propose to stack the transverse components with weights depending on azimuths. However, this method lacks the possibility to constrain measurement errors. Chevrot [2000] projects the amplitudes of transverse components to the amplitudes of the time derivatives of radial components to obtain the

so-called splitting vector. When stacked within bins of similar backazimuths, the phase and amplitude of the best fitting curve gives then Φ and *dt*, respectively.

The second type of techniques determines the anisotropy parameters on a per-event basis [Fukao, 1984; Ansel & Nataf, 1989; Silver & Chan, 1991; Menke & Levin, 2003]. A grid search is performed for the splitting parameters which best remove the effect of splitting. Different measures for "best removal" exist. Bowman & Ando [1987] search for the maximum cross-correlation between the two seismogram components, assuming that the wave form of the leading wave (fast-component) is identical to that of the split-wave (slow-component). The eigenvalue method discussed in Silver & Chan [1991] can be visualized by searching for the most linear particle motion.

The arguably most popular method in shear wave splitting is to find "Minimum Energy on Transverse Component" [Silver & Chan, 1991]. For weak anisotropy (delay time small compared with dominant period of signal), the transverse component is identical time derivative of the radial component. If the initial polarisation is known, as with core-reflected and refracted phases (e.g., PcS, SKS, SKKS, PKS, …), one can search for a combination of Φ and *dt*, which minimizes the energy on the transverse component. This corresponds to "removing" the effect of the anisotropic layer from the data.

Wolfe & Silver [1998] present a post-processing stacking method for shear wave splitting. Here, the energy $E_T(\Phi,dt)$ on the transverse component of each measurement is computed for each candidate set of splitting parameter. The stacking of these (then normalized) energy distributions gives a global energy at the station, whose minimum gives then its splitting parameters. This method has the advantage that a formal error can be calculated. However, it assumes a single layer of horizontal anisotropy. Any possible information on the backazimuthal variation of splitting parameters is lost. Complex anisotropic structures cannot be identified.

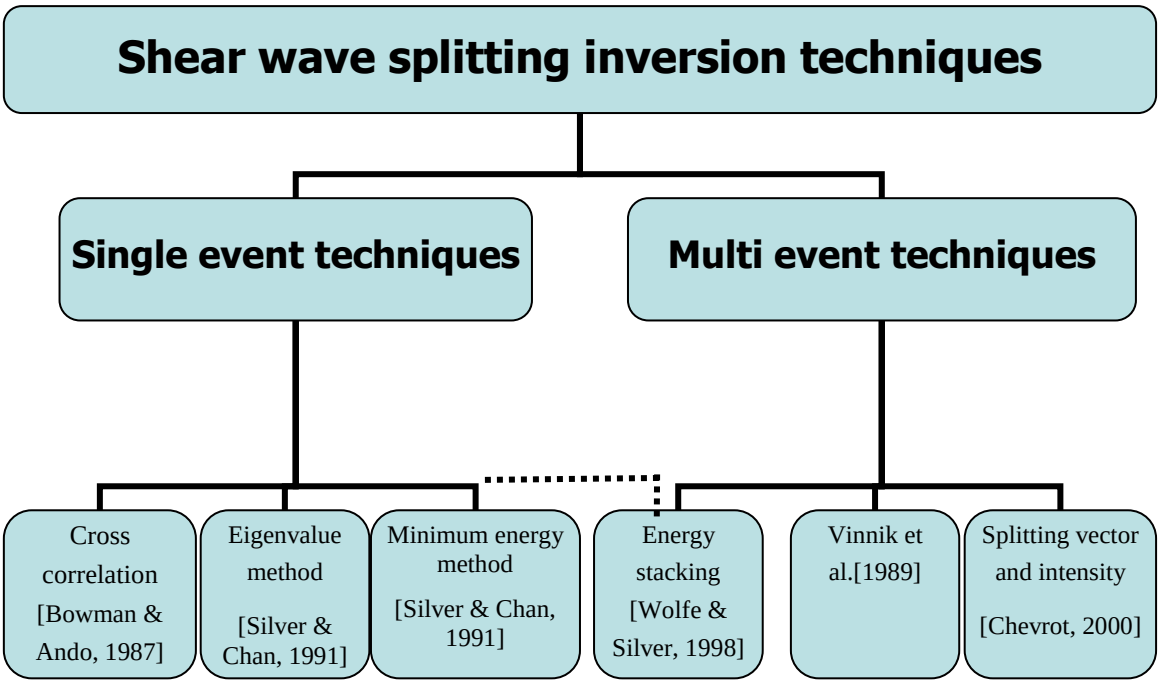

Figure 17: Different techniques have been proposed to measure the splitting parameters

All these methods assume a single layer of anisotropy, with fast- and slow polarisation planes oriented horizontally. This limitation can be overcome by regarding the obtained measurements as an “apparent” [Silver & Savage, 1994]. The backazimuthal variations of these apparent splitting parameters are then characteristic and can be inverted for two layers or even dipping layers [Brechner et al, 1998].

4.3. SplitLab: A shear-wave splitting environment in Matlab

Andreas Wüstefeld[a], Götz Bokelmann[a], Christophe Zaroli[b], Guilhem Barruol[a]

a) Geosciences Montpellier, CNRS, Université de Montpellier II, 34095 Montpellier, France

b) Ecole et Observatoire des Sciences de la Terre, Université Louis Pasteur, Strasbourg, France

splitlab@gmx.net

In Press for Computers & Geosciences, 2007

4.3.1. Abstract

We present a Graphical User Interface to facilitate the processing of teleseismic shear-wave splitting observations. In contrast to a fully automated technique, we present a manual, per-event approach that maintains a user control during the sequence of processing. The SplitLab environment is intended to undertake the repetitive processing steps while enabling the user to focus on quality control and eventually the interpretation of the results. Pre-processing modules of SplitLab create a database of events and link the corresponding seismogram files. The seismogram viewer tool uses this database to perform the measurement interactively. Post-processing of the combined results of such a project includes a viewer and export option. Our emphasis lies in the application to teleseismic shear-wave splitting analysis, but our code can be extended easily for other purposes. SplitLab can be downloaded at http://www.gm.univ-montp2.fr/splitting/

4.3.2. Introduction

Since the early 1990s shear-wave splitting measurements are widely applied to seismological datasets for detecting anisotropy in the Earth (e.g. Vinnik et al., 1989; Silver and Chan, 1991; Silver, 1996; Savage, 1999; Barruol and Hoffmann, 1999; Currie et al., 2004; Walker et al., 2005; Heintz and Kennett; 2006). While seismic anisotropy in the upper crust is primarily controlled by preferred orientations of microcracks (eg, Crampin and Chastin, 2003), it is dominated in the deeper Earth, and particularly in the upper mantle, by the preferred orientation of anisotropic crystals (eg, Tommasi, 1998).

Similar to birefringence in optics, shear wave splitting occurs whenever a seismic shear-wave travels through an anisotropic layer. It is split into two waves propagating at different speeds which are polarized in two perpendicular orientations (Figure 18): one wave is polarized along the seismic fast axis direction and the other perpendicular, along

the seismic slow axis direction. The delay time measured at the Earth's surface between the two split waves depends on the strength of anisotropy and on the thickness of the anisotropic layer.

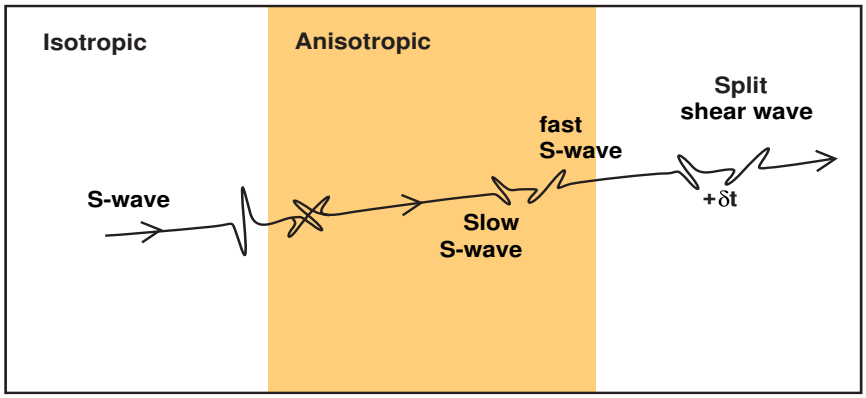

Figure 18: Shear-wave splitting occurs for a shear wave traveling through an anisotropic medium (shaded). When the incident shear wave arrives at an anisotropic medium it splits into two shear waves of perpendicular polarization, along the seismic fast and slow direction, respectively. Traveling through the anisotropic medium the two waves accumulate a delay time δt. The shear-wave splitting techniques invert for δt and the fast polarization direction Φ.

Seismic anisotropy has been observed in many environments and at many depths in the Earth, from the crust down to the core-mantle boundary. In the upper mantle, anisotropy is a common feature and isotropy is rather the exception. Anisotropy is widely accepted to be directly related to mantle deformation aligning rock-forming crystals that are intrinsically anisotropic. Measuring anisotropy remotely from the Earth's surface, is therefore a way to access present or past mantle flow at depth. Anisotropy thus offers the unique possibility to directly observe and measure Earth's properties and geodynamic processes at depth. In order to characterize this upper mantle anisotropy, core shear phase such as SKS and SKKS are generally used. These phases are well detectable at distances between 90° and 130° from the epicenter. They propagate along steeply inclined rays between the core and the surface while the liquid nature of the outer core and the P-to-S conversion at the core-mantle boundary (CMB) ensures that only receiver-side splitting is observed. Reviews of the shear-wave splitting technique and its applications have been given by Silver (1996) and Savage (1999).

A number of codes for performing teleseismic shear-wave splitting measurements exist in the community. Generally these consist of combinations of FORTRAN, C or C++ programs, which are embedded in SAC, SeismicUnix, and SeismicHandler scripts. Such "command line approach" is feasible for small amounts of data. However, more data have become available during the last decade, due to the increasing number of stations from both temporary and permanent networks (like GSN, IRIS, Geoscope, and GEOFON amongst others).

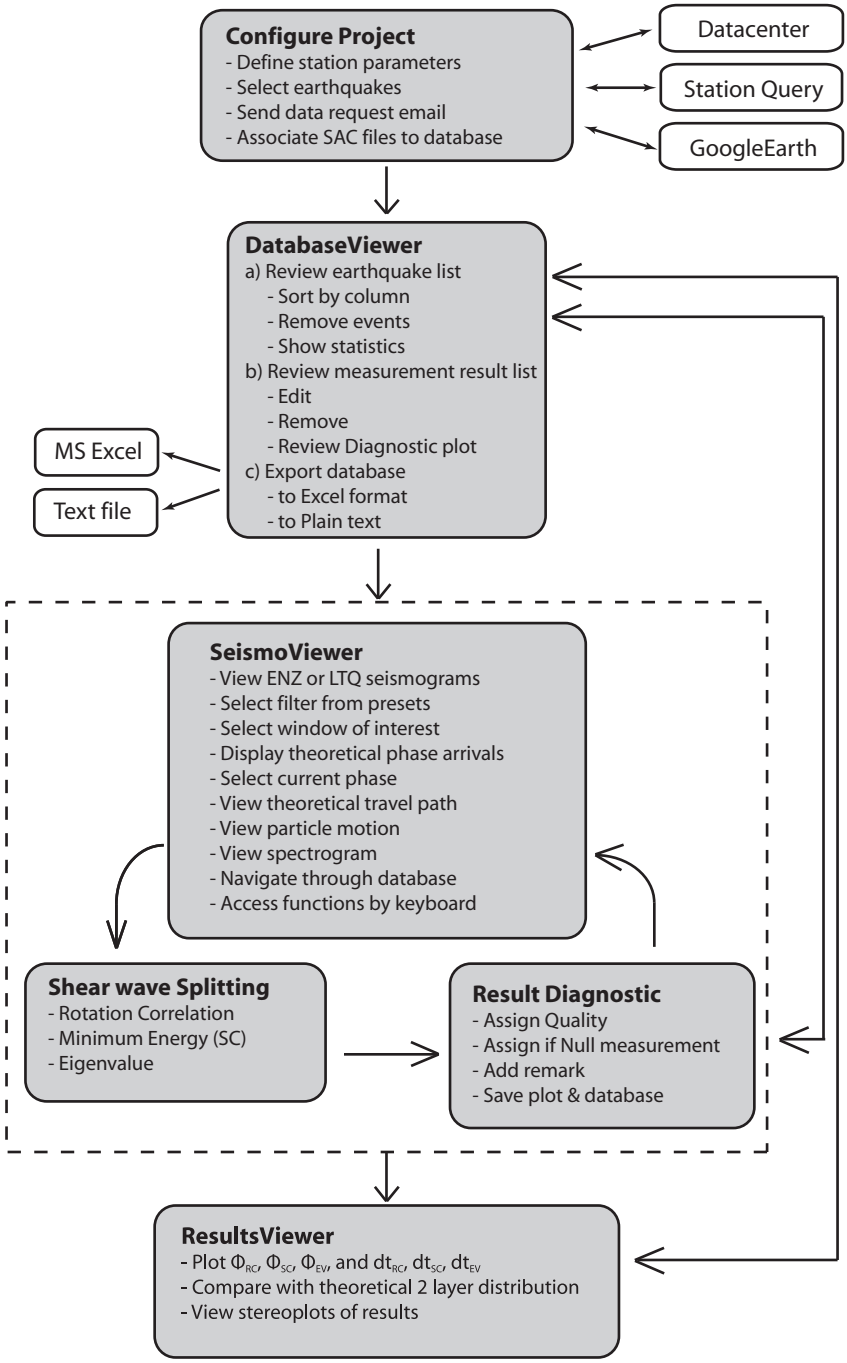

Figure 19: The SplitLab workflow with descriptions of each module.

To efficiently analyze and interpret these growing datasets, we present the new SplitLab processing environment. Splitlab is available for free download at http://www.gm.univ-montp2.fr/splitting. With its intuitive “button approach” we aim to provide a modern, efficient, flexible and user-friendly workflow (Figure 19). Based on Matlab, this environment is platform independent. A set of Graphical User Interfaces (GUIs) embraces the entire splitting workflow, including the selection of appropriate earthquakes and data requests in various formats. Furthermore, a seismogram viewer is provided for the selection of the relevant phase window and the resulting splitting diagnostic plots. The

process for a single station is saved as a ‘Project’, providing for the possibility to conduct multiple analyses on the same data set, resume work at a later time, or the easy exchange of data between researchers.

SplitLab is designed and tested for the use of SKS phases in three-component records in SAC format of permanent stations. However, the shear wave splitting analysis of other phases, such as direct S or ScS, and the analysis of temporary networks are also possible.

4.3.3. Modules Description

The SplitLab workflow (Figure 19) can be divided into several steps: 1) Configuration of the project, data request and database preparation, 2) seismogram validation and shear-wave splitting procedure, and 3) results output and analysis. At each step the database can be accessed with an integrated viewer which also comprises an export option to Microsoft Excel or plain text format.

A SplitLab project consists of the two Matlab-Structure variables “config” and “eq”. Such format eases the extension of SplitLab with any future plug-ins or interaction with user functions. The “config” structure contains fields with general project configuration (file locations, event search and station parameters, etc.) and the “eq” structure contains the earthquake database (e.g. location, magnitude, distance, corresponding SAC files, results, etc). See Appendixes B and C for the actual information stored in the structures. A detailed description of the variable type ‘structure’ is provided in the Matlab manual.

4.3.3.1. The SplitLab Project configuration (splitlab.m)

To create and manage a SplitLab Project, we provide a GUI (Figure 20) where the user can setup the parameters of the project. After entering information concerning the station, the user can choose between the Harvard CMT catalogue and the NEIC catalogue for selecting the earthquake window (time period, distance, magnitude and depth). A statistical plot provides graphical information about the earthquakes matching the given criteria (Figure 21). Both catalogues exist as local files, and an updater helps to download the newest earthquakes from the corresponding web-pages (Figure 20).

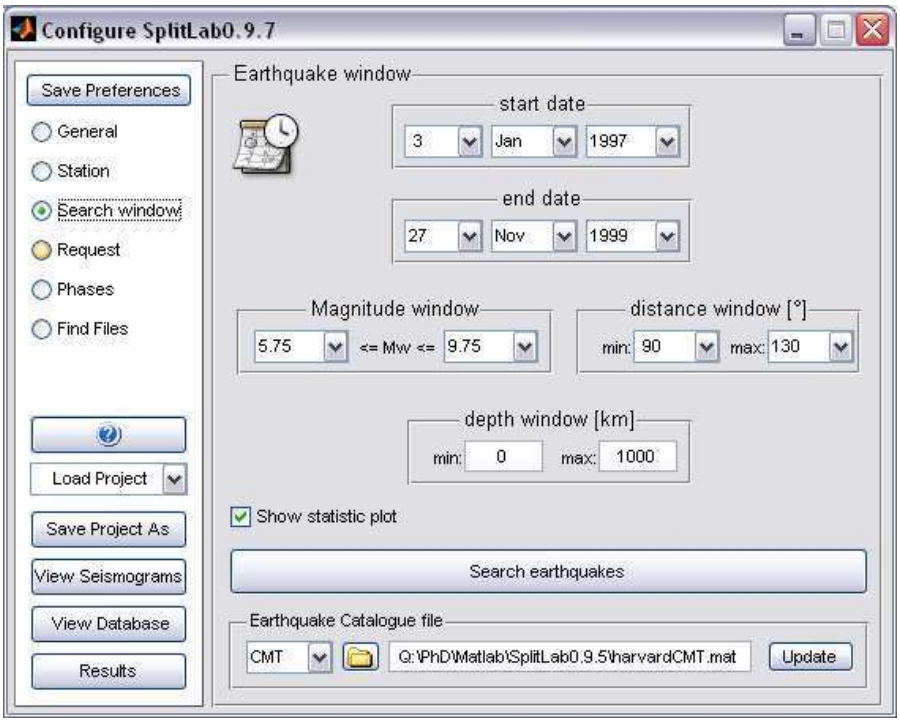

Figure 20: The configuration of SplitLab can be accessed interactively. Here for example the earthquake window selection panel

At this point, SplitLab requires the presence of the waveforms on the local computer. SplitLab allows requesting them from the different datacenters via email in various formats such as AutoDRM, BreqFast, netDC or saved as a plain text table. In case the SAC files are already accessible to the user (old analysis, local/temporary deployments) this request step can be omitted.

Once the datacenters have provided the seismograms and these are converted to SAC format, the “Find Files” panel allows searching for and linking the three files (east, north and vertical components) to the corresponding earthquake entry of the database. This is done by comparing, within a variable search tolerance, the hypocentral time in the catalogue with the start time of the seismogram file as provided by the filename or its header values. A static offset time can also be selected if, for example, the seismograms are provided relative to P-wave arrival. At the same time, phase arrival times of various seismic phases are calculated and added to the database. This processing step is explained in more detail in the SplitLab User Guide.

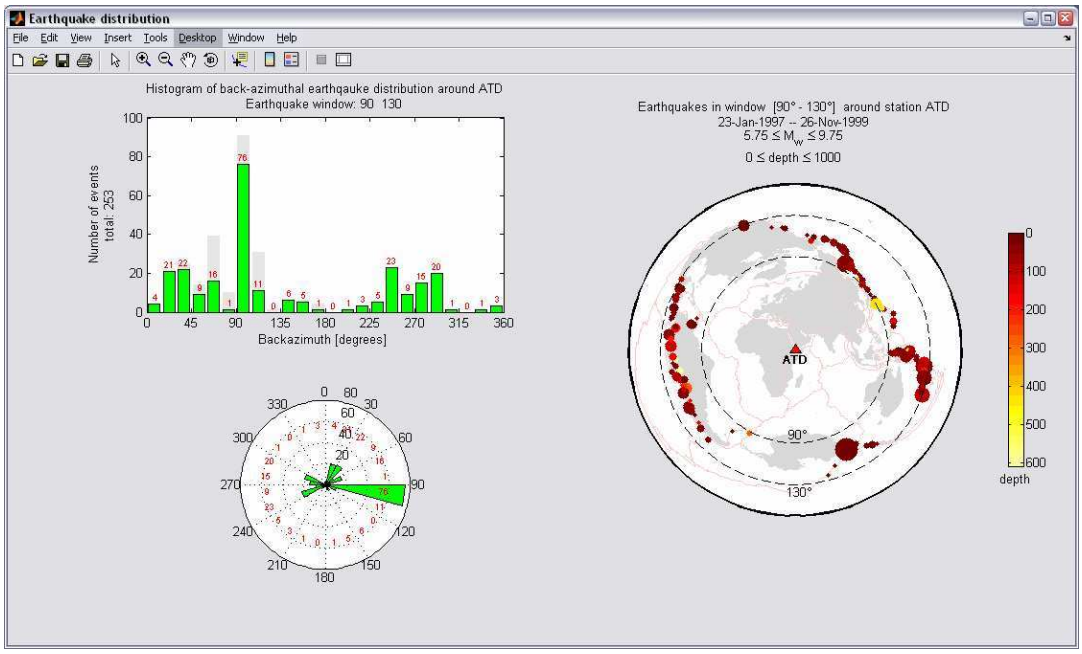

Figure 21: The earthquake distribution statistic plot. Upper left displays the backazimuthal distribution as histogram in 15º bins (in grey displayed are the cumulated earthquakes within these bins for 180º periodicity). Lower left is the same displayed in a rose plot. Right panel gives an equidistant azimuthal map of the earthquake locations.

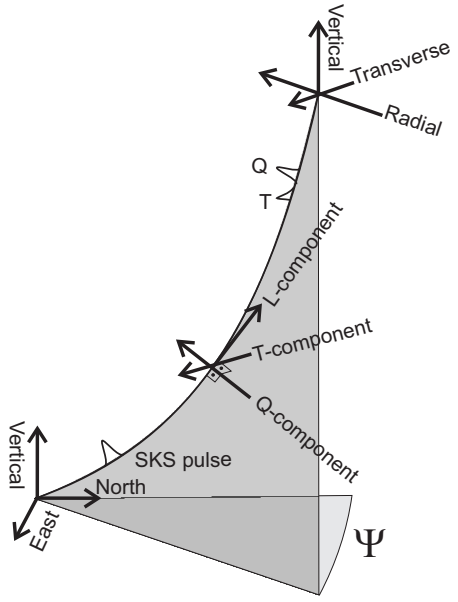

Figure 22: Components of a seismogram in a right-handed L-Q-T system. The ray plane, shown in gray, is given by the L-component (parallel to the ray) and the Q-component (pointing towards the earthquake). The T-component is perpendicular to this ray plane. Ψ is the backazimuth.

4.3.3.2. The Seismogram Viewer

The main environment of the shear-wave splitting procedure is the Seismogram Viewer. Here, the seismograms are read and stored in the temporary structure variable “thiseq” , together with the corresponding earthquake parameters. Furthermore, a rotation into the three dimensional ray system (LQT, Figure 22) is performed:

$$\begin{bmatrix} L \\ Q \\ T \end{bmatrix} = \begin{bmatrix} \cos\delta & -\sin\delta\sin\beta & -\sin\delta\cos\beta \\ \sin\delta & \cos\delta\sin\beta & \cos\delta\cos\beta \\ 0 & -\cos\beta & \sin\beta \end{bmatrix} \cdot \begin{bmatrix} Z \\ E \\ N \end{bmatrix}$$

where β is the backazimuth (positive clockwise from north) and δ is the incidence angle of the wave, measured from vertical (δ = 0º for vertically incident waves; δ = 90º for horizontally incident waves; Plěsinger *et al*., 1986). In this case, the positive (longitudinal) L-component points along the ray path (from the earthquake towards the station), and the Q-component is defined positive when pointing towards the earthquake (Figure 22). The T-component completes the right-handed coordinate system. The incidence angle of each phase is calculated from the ray path function of the matTaup toolbox, which is automatically installed with the Matlab toolboxes during the SplitLab installation.

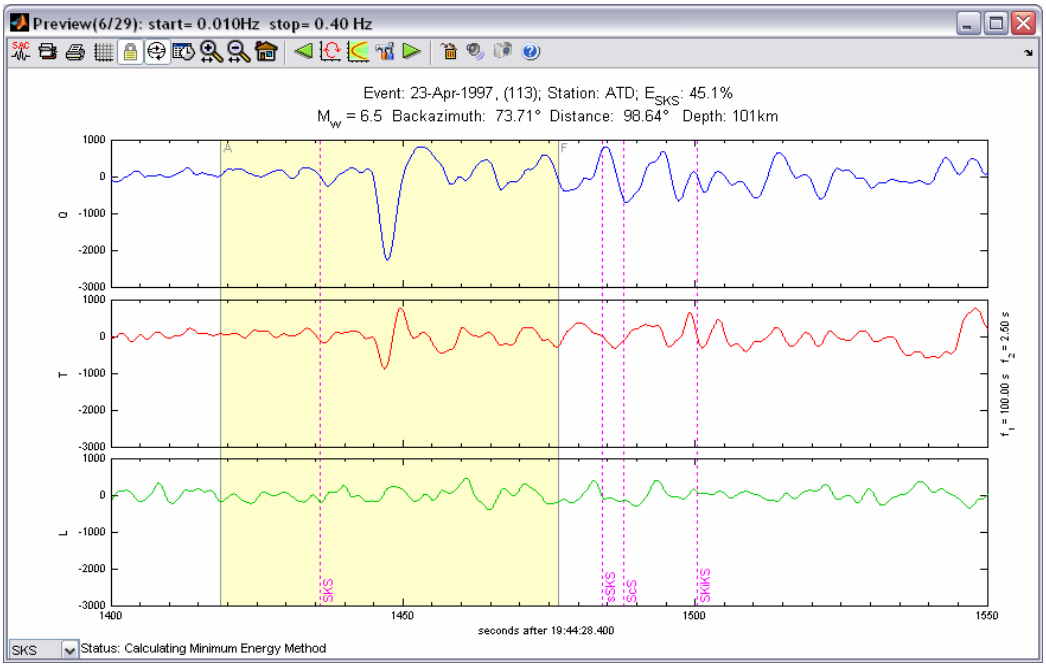

Figure 23 Seismogram viewer with selected window (shaded area). Various menu buttons provide display options and navigation within the SplitLab database. The phase of interest can be selected by a menu in the lower left corner.

By default, SplitLab displays the LQT-seismograms for the incidence angle of the SKS phase, but this can be changed easily in the phase selector menu in the bottom panel of the Seismogram Viewer (Figure 23). This feature can also be used to differentiate between close phase arrivals, e.g. the SKS and the SKKS phases, which should have different energy on the L–component when rotated with the appropriate incidence angle.

Within the Seismogram Viewer environment, the waveforms can be visually inspected and analyzed by the user before shear wave splitting measurements. Functions such as rotations, filters, zooms, particle motion analyses and spectrograms are easily accessible to help the user in the selection of the seismic phase and of the time selection for the further measurement. Several keyboard keys serve as direct access to functions (Table 1). For example, the keys “0” to “9” provide a suite of preset frequency filters, which apply a third-order Butterworth filter twice to produce zero phase distortion. Pressing the “Home” key zooms directly to the selected phase. The users can easily add key-press functions by changing the file seisKeyPress.m. Additional features include a particle motion viewer and an export to SAC format of the current view. The time window on which the user wishes to perform a splitting measurement is selected by mouse clicks.

Key	Function
f	open filter dialog
0	unfiltered data
1	0.01 - 0.1Hz
2	0.02 - 0.2Hz
3	0.02 - 0.3Hz
4	0.01 - 0.3Hz
5	0.01 - 0.4Hz
6	0.02 - 1Hz
7	0.01 - 0.15Hz
8	0.02 – 0.25Hz
9	0.01 - 1Hz
+	Add 0.002Hz to lower filter frequency
-	Substract 0.002Hz from lower filter frequency
*	Add 0.02Hz to upper filter frequency
/	Substract 0.002Hz from upper filter frequency
Space	Switch between ZEN and LQT system
Backspace	Reset zoom state
PageUp	Scroll right
PageDown	Scroll left
Home	Zoom to phase
Enter	Start shear-wave splitting

Table 1: Keyboard presets of SplitLab’s Seismogram viewer. These can be changed or supplementary functions can be added in the script seisKeyPress.m

4.3.3.3. The shear-wave splitting measurement

The effect of shear-wave splitting occurs when an S-wave propagates through an anisotropic layer (Figure 18). The wave is split into two shear waves, polarized in the fast and slow direction and accumulating a delay time along their paths (e.g. Savage, 1999). To remove the effect of splitting (and thus find the fast direction and delay time) SplitLab uses simultaneously three different techniques. The first is the Rotation-Correlation method (in the following RC; e.g. Bowman and Ando, 1987), the second is the minimum energy method (in the following SC; Silver and Chan, 1991) and the third is the eigenvalue method (EV; e.g., Silver and Chan, 1991). The SC technique can be seen as a special case of the EV technique, and may be applied if, as for the SKS phase, the initial polarization of the wave is known. All three techniques perform a grid-search for the splitting parameters Φ (fast axis) and δt (delay time) that best remove the effect of splitting, that is, linearize the particle motion in either the E-N or the Q-T plane. As criterion for best linearization, the RC technique uses the maximization of the cross-correlation coefficient between the waveforms on the radial Q and transverse T components in the selected window. The SC technique searches for the minimum energy of the displacement u_T on the transverse component ($E = \sum u_T^2$). Silver and Chan (1991) point out the similarities between the four eigenvalue-based criteria such as maximizing λ_1 or λ_1/λ_2, and minimizing λ_2 or $\lambda_1 * \lambda_2$. The user of SplitLab can choose between either of these criteria.

The initial polarization of the wave is assumed to be radial in the case of the RC and SC method which are thus only applicable to phases such as SKS, SKKS, PKS etc. For the EV method, SplitLab provides the option to either use the backazimuth as initial polarization or to estimate it from the particle motion after anisotropy correction and linearization of the waveform. The latter should be used for phases where the initial polarization is unknown (direct S, ScS etc.)

The default search grid parameters used in SplitLab are steps of 1º and half the sampling rate for the RC technique and 2º and half the sampling rate for the SC and EV technique, respectively. The determination of the error is discussed in Appendix A (Chapter 4.3.7.1).

For all these calculations the original seismograms are used, which are tapered on both ends. Any existing linear trend is removed from the traces, the mean is subtracted, and finally the whole trace is filtered. Then the seismograms are cut according to the picks. The selection window is extended by 30 seconds before and after the picks and inserted to the splitting calculation routines. The result of these calculation is displayed in a diagnostic plot (Figure 24), containing several graphics allowing the user to quickly visualize and evaluate the measurement. The quality of the measurement can be assigned as proposed by Barruol et al. (1997) via a menu or the measurement can be discarded to

test another time window, another filter, another seismic phase or another seismic event. An optional remark on each measurement can also be added to the database.

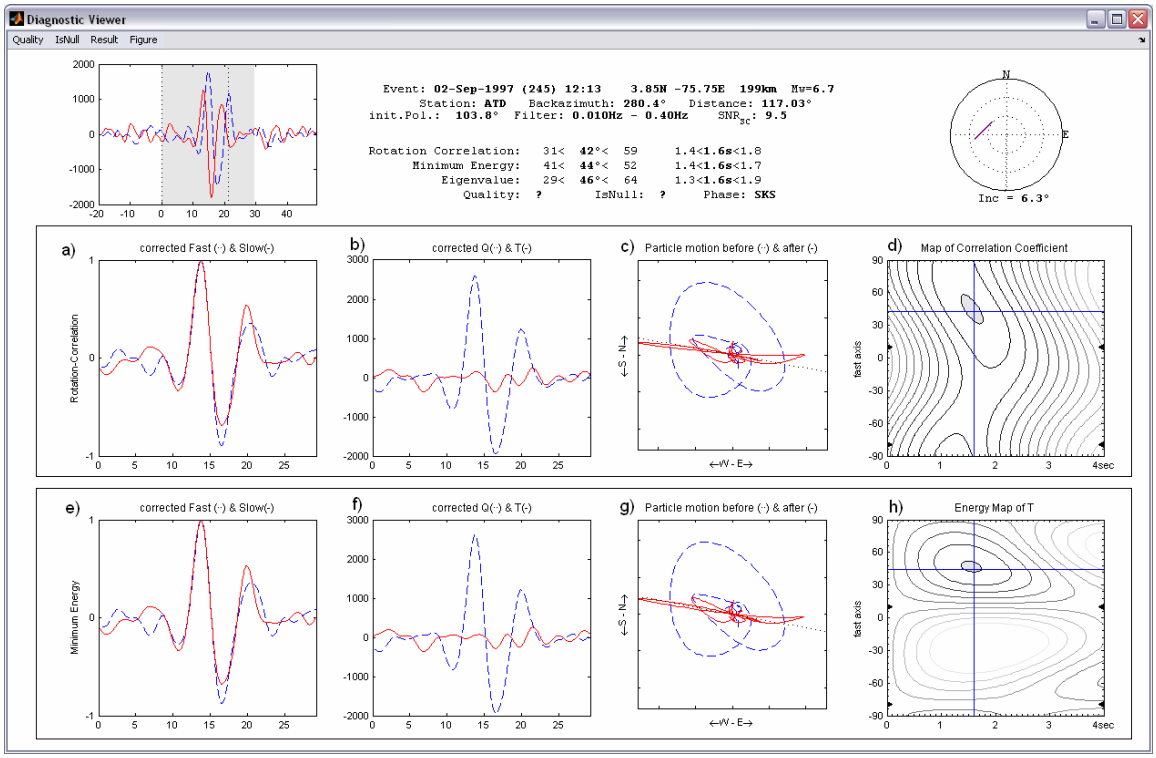

Figure 24: Diagnostic plot of a single measurement. The center panels displays the result for the Rotation-Correlation (RC) technique: a) seismogram components in fast (solid) and slow (dashed) direction for the RC-anisotropy system after RC-delay correction (normalized); b) radial (Q, solid) and transverse (T, dashed) components after RC-correction (not normalized); c) particle motion before (dashed) and after (solid) RC correction; d) map of correlation coefficients. The lower panels display the results for the minimum energy (SC) technique: e) seismograms shown after splitting correction shown on SC-fast and slow components (normalized); f) same on radial and transverse components (not normalized); g) SC particle motion before and after correction; h) map of minimum energy values on transverse component. In the upper left an extended section of the Q (solid) and T (dashed) components before anisotropy correction is displayed. In the upper right a stereoplot of the result is presented. The header gives specifications of the event as well as splitting parameters resulting from the three techniques. Depending of the chosen option, the lower panels e) - h) may display instead of the SC the results of the EV technique

4.3.3.4. The Database Viewer

The database of a SplitLab project can easily be accessed with the database viewer. A table of the events displays some necessary information. Here, the user can sort the event list, for example by backazimuth, depth, distance or magnitude. Selecting one or more events displays the results of previously performed splitting measurements in the lower panel of the database viewer. By selecting one result, a direct access to the corresponding diagnostic plot is possible and allows the user to easily manage previous measurements. Furthermore, the results of the project can be exported in Excel format or as plain text for further analysis.

4.3.3.5. The Result Viewer

The results of a project can finally be presented by the Result Viewer module (Figure 25). The user can interactively choose the desired phases and qualities to be displayed in the plot. The backazimuthal variation of fast axis estimates and delay time estimates of the RC, SC and EV methods are plotted. Such a variation may provide evidence, if any, of the presence of several anisotropic layers beneath the station. In addition, the theoretical backazimuthal distribution of the apparent splitting parameters for two layers of anisotropy can be calculated and plotted (Silver and Savage, 1994). This allows the user to interactively test numerous models and to visualize their fit to the observations.

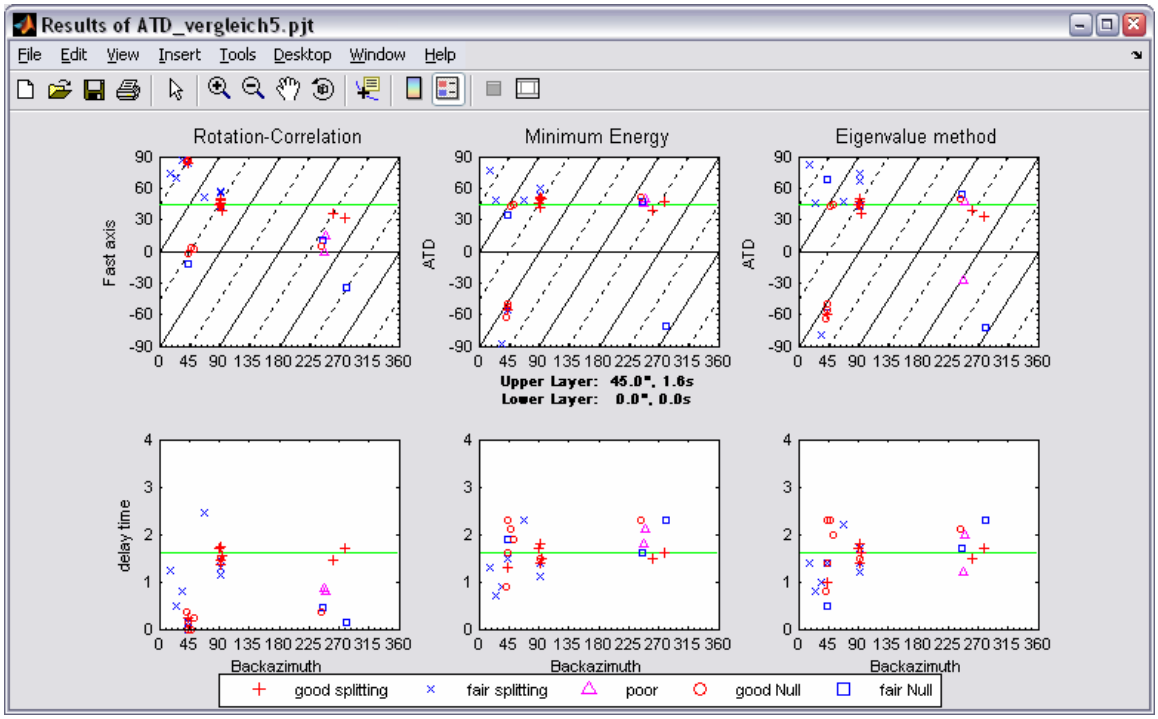

Figure 25: Results of the splitting project for station ATD. The horizontal lines indicate the one-layer solution with parameters $\Phi = 48^{o}$ and $\delta t = 1.6$ sec

4.3.4. Validation

The SplitLab environment has been tested and validated through synthetic tests, but also by analyzing real data that were already processed and published by different authors.

4.3.4.1. Synthetic tests

We performed synthetic tests to compare the accuracy and behavior of the different splitting techniques. Wüstefeld and Bokelmann (2006) explain the results of these tests in detail. In summary, they find that both the RC and SC technique reconstitute input fast axes and delay times very well at different noise levels for backazimuths far from input fast and slow axes, where the energy on the transverse component is large. The higher the Signal-To-Noise ratio (SNR) the wider is the backazimuthal range of reliable splitting parameter estimates.

However, at backazimuths close to fast and slow axes ("Null directions") the RC and SC technique yield characteristic differences. There, the fast axes estimates of the RC technique deviate 45° from the input fast axis while the fast axis estimates from the SC technique, Φ_{SC}, scatter around either the correct fast or the slow axis orientation. The RC delay times estimates, dt_{RC}, tend towards small values, close to zero seconds, while dt_{SC} shows large scattering with values above 0.5 seconds and often close to the maximum allowed by the grid search.

The backazimuth range of good estimates is larger for the SC than for the RC technique. These characteristic differences can be used to identify Nulls in real datasets and to assign a quality to the measurement. Not explicitly discussed in Wüstefeld and Bokelmann (2006) is the behavior of the various eigenvalue methods. These show however similar results to the SC method in the synthetic test.

4.3.4.2. Validation on real data: the Geoscope station ATD

We provide with SplitLab a data example from the Geoscope station ATD (Arta Cave, Djibouti). The choice of this station has been guided by the quality of the data, the clarity of the fast azimuth, the strength of the delay time, and the broad agreement on the splitting parameters obtained from various anisotropy studies previously performed and published at this station (Vinnik et al., 1989; Barruol and Hoffmann, 1999) and also at neighboring stations (e.g., Ayele et al., 2004; Gashaweba et al., 2004). The example SplitLab project file contains the necessary parameters and associations, so that the user can directly test the program. Within the provided SAC files we set the A and F header variable which mark the beginning and end of the time window, respectively. These markers are plotted in the Seismogram Viewer and thus hint an inexperienced user to the best time window selection. The selection itself, however, still has to be done. The splitting parameters obtained from the three methods provided in SplitLab are presented in Table 2 together with the results of Barruol and Hoffmann (1999), performed on the same dataset by using the SC method. Our results are in very good agreement with theirs.

Except for a few events of fair or poor quality, the observed difference falls within ±3° for the azimuth Φ of the fast split shear wave and within ±0.20 s for the delay times. For the measurements qualified as 'good' by Barruol and Hoffmann (1999), the agreement generally falls respectively within ±3° and ±0.05 s. The SplitLab results obtained by using the SC and EV method are similar, indicating for station ATD splitting parameters of Φ = 45º and δt = 1.6 sec. For the non-Null measurements, the difference is generally less than 3° between the azimuth and less than 0.2 s for the delay times. The RC method compares fairly well for the 'good' measurements with the SC method but, for 'fair' and 'poor' quality measurements, displays large differences in some cases up to 45° in azimuth. As

demonstrated by Wüstefeld and Bokelmann (2006), a useful application of the RC method is for distinguishing true Nulls from small delay times in case of noisy records.

		Barruol & Hoffman 1999			Splitlab 2007							
event	phase	Φ	dt	Quality	ΦRC	ΦSC	ΦEV	dtRC	dtSC	dtEV	ΔΦ	Δdt
good												
93.286	SKS	50	1.35	g	49	51	51	1.40	1.40	1.40	1	0.05
93.289	SKS	48	1.50	g	43	49	48	1.50	1.50	1.50	1	0.00
93.298	SKS	48	1.45	g	48	49	48	1.50	1.40	1.40	1	0.05
94.157	SKS	47	1.60	g	31	47	49	1.70	1.60	1.70	0	0.00
94.289	SKS	-61	0.95	g	85	-62	-62	0.40	0.90	0.80	1	0.05
95.079	SKS	47	1.50	g	39	50	41	1.60	1.50	1.60	3	0.00
95.122	SKS	44	1.65	g	44	44	38	1.70	1.70	1.80	0	0.05
95.175	SKS	46	1.70	g	44	46	47	1.70	1.70	1.70	0	0.00
95.175	SKKS	49	1.70	g	49	50	50	1.60	1.50	1.50	1	0.20
95.353	SKS	42	1.80	g	47	42	42	1.80	1.70	1.70	0	0.10
96.162	SKS	48	0.70	g	69	49	45	0.50	0.70	0.90	1	0.00
fair												
93.192	SKS	47	1.95	f	-1	45	3	0.90	1.80	1.20	2	0.15
94.010	SKS	35	1.35	f	37	38	38	1.50	1.50	1.50	3	0.15
94.362	SKS	44	2.35	f	3	42	41	0.10	2.90	2.30	2	0.55
95.226	SKS	58	1.30	f	56	59	63	1.30	1.40	1.70	1	0.10
95.337	SKS	-55	1.40	f	86	-53	-55	0.20	1.60	1.40	2	0.20
96.047	SKS	44	2.05	f	2	44	44	0.30	1.90	1.90	0	0.15
96.053	SKS	-53	1.65	f	84	-55	-56	0.30	1.30	1.00	2	0.35
96.128	SKS	-53	1.45	f	82	-56	-53	0.10	1.50	1.50	3	0.05
poor												
93.323	SKS	82	1.40	p	68	74	76	1.20	1.10	1.20	8	0.30
94.108	SKS	54	1.10	p	49	56	60	1.10	1.20	1.30	2	0.10
94.231	SKS	44	1.20	p	11	47	45	0.50	1.60	1.70	3	0.40
95.211	SKS	51	2.00	p	14	50	51	0.80	2.10	2.00	1	0.10
95.235	SKS	49	2.20	p	52	49	48	2.50	2.30	2.10	0	0.10
95.305	SKS	52	2.30	p	4	51	53	0.40	2.30	2.10	1	0.00
96.120	SKS	49	1.45	p	40	48	49	1.40	1.50	1.40	1	0.05
Nulls												
95.118	SKS	-47	4.00	g	-2	-50	-49	0.00	2.30	2.20	3	1.70
96.038	SKS	40	4.00	g	-12	34	78	0.00	2.10	0.00	6	1.90

Table 2: Anisotropy parameter estimates for station ATD by Barruol and Hoffmann (1999) and SplitLab. Barruol and Hoffman used the SC technique to obtain the splitting parameters, so a direct comparison is only possible to this technique, marked in gray. The last two columns represent the difference in fast axis estimates (ΔΦ) and delay time estimates (Δδt) between Barruol and Hoffmann (1999) and the SplitLab results of the SC technique.

4.3.5. Conclusions

We present a code that performs shear-wave splitting measurements including the entire workflow from pre-processing to data analysis to resulting diagnostics. The SplitLab environment provides an efficient approach to the interactive processing and management of large seismic datasets. Different from other recent approaches (Teanby et al., 2003; Evans et al., 2006), our aim is not to fully automate the whole process. Instead, the chosen interactive approach allows the user to focus on the critical steps such as event selection, quality control, and phase picking while the computer undertakes less important and repetitive aspects of the processing. Based on Matlab, SplitLab is system-independent and directly portable to different operating systems. It has been successfully tested on Windows, MAC and Linux systems. The simultaneous evaluation of three different splitting techniques provides for the maximum information to be obtained from a single measurement.

We encourage users to contact us on modifications they propose to the original code or additional plug-ins. This should enable SplitLab to change and grow dynamically, in the spirit of the GeneralPublicLicense.

4.3.6. Acknowledgements

We thank M. Savage, S. Greve and C. Currie for helpful comments that improved our manuscript. The Rotation Correlation routine is based on a code kindly provided by Georges Herquel. We are grateful to Alexander Gatzemeier, Luisa Buontempo and Sonja Greve for their patience and helpful ideas as test users of earlier versions. Extensive use is made of the SACLAB toolbox by Michael Thorne (http://gcc.asu.edu/mthorne/saclab/) for incorporating the SAC files to Matlab and the matTaup toolbox by Qin Li (http://www.ess.washington.edu/SEIS/FMI/matTaup.htm) to calculate the phase arrivals. Finally we would like to thank Véronique Le Roux for the SplitLab logo.

4.3.7. Appendices

4.3.7.1. Appendix A: Error calculation

We calculate the error of the SC and the EV technique following Silver and Chan (1991). In their approach, the energy $E(\phi, dt) = \sum u_T^2(\phi, dt)$ on the transverse component u_T for a test fast axis Φ and test delay time dt is a χ^2-distributed variable with n degrees of freedom. This assumes a Gaussian noise process, for which the number of degrees of freedom can be estimated from the seismogram. We then estimate the confidence region of Φ and dt that corresponds to 2σ. We use as error bounds the minimum and maximum range of the confidence region, in contrast to the (systematically smaller) marginal error, that is often applied.

To obtain the error information for the Rotation-Correlation technique, one can either relate the correlation coefficient to the sum-of-squares (Bokelmann, 1992), or use the Fisher transformation (Fisher, 1925). The latter transforms the (normalized) correlation coefficient r to an approximately Gaussian-distribution. We illustrate here the Fisher transformation approach:

Let

$$z = arctanh(r) = \tfrac{1}{2}\log\left(\frac{1+r}{1-r}\right)$$

where z is a parameter representing the transformed correlation coefficient. Then, as r changes from 0 to 1, z will pass from 0 to infinity. For small values of r, z is nearly equal to r, but as r approaches unity, z increases without limit. For negative values of r, z is negative. The distribution of z is not strictly normal, but it tends to normality rapidly as the sample number is increased (Fisher, 1925), whatever the value of r. The distribution z has a standard deviation of $\sigma_z = \sqrt{\frac{1}{n-3}}$, from which we can now calculate the 2σ-confidence level μ_z.

This value is then transformed back into r-space, resulting in the 2σ-confidence level of the correlation coefficient:

$$\mu_r = \tanh(\mu_z)$$

4.3.7.2. Appendix B: Fields of variable “config”

```
                version: 'SplitLab0.9.7'
                   host: 'SEALAB'
                project: 'ATD_example.pjt'
                datadir: 'Q:\PhD\_SplitlabExamples\ATD_example'
             projectdir: 'Q:\PhD\_SplitlabExamples\'
                savedir: 'Q:\PhD\_SplitlabExamples\ATD_example\Results'
              calcphase: 1
              calcEnergy: 1
              showstats: 1
                stnname: 'ATD'
                   netw: 'G'
                   slat: 11.5300
                  slong: 42.8470
                   elev: []
                  eqwin: [90 130]
                  z_win: [0 1000]
                   twin: [3 1 1997 27 11 1999]
                     Mw: [5.7500 9.7500]
              catalogue: 'Q:\PhD\Matlab\SplitLab0.9.7\harvardCMT.mat'
              catformat: 'CMT'
              searchstr: '*.SAC'
               searchdt: 420
                 offset: 0
                request:
            label: 'label'
                         format: 'NetDC'
                        reqtime: [-60 2400]
                           comp: 'BH?'
                           user: 'wueste'
                      usermail: 'wueste@dstu.univ-montp2.fr'
                      institut: 'Institut'
                        adress: '99 Example Road, 12345 Mytown, Mycountry'
                         phone: ''
                           fax: ''
                   DataCenters: {5x1 cell}
                        mailto: 'netdc@fdsn.org'
                     timestamp: '24-Jul-2006 16:03:52'

                 phases: {1x20 cell}
             earthmodel: 'iasp91'
           exportformat: '.eps'
                comment: [9x88 char]
               db_index: 1
           maxSplitTime: 4
            splitoption: 'Minimum Energy'
        UseHeaderTimes: 0
              rotation: 0
              SwitchEN: 0
                 signE: 1
                 signN: 1
    FileNameConvention: 'RDSEED'
             PaperType: 'A4'
       tablesortcolumn: 1
```

4.3.7.3. Appendix C: Fields of variable “eq”

```
             date: [1997 1 23 2 15 22.9000 23]
             dstr: '23-Jan-1997'
              lat: -22
             long: -65.7200
            depth: 276
              azi: 85.7850
             bazi: 250.6860
              dis: 111.3551
               Mw: 7.1118
               M0: 5.7900e+026
             meca: [85 4 -175]
           region: 'SOUTHERN BOLIVIA'
        seisfiles: {3x1 cell}
           offset: [3x1 double]
            index: [1 1 1]
            phase: [1x1 struct]
           energy: -0.9336
     polarisation: 71.7136
          results:
                SplitPhase: 'SKS'
                   incline: 6.9695
                   quality: 'good'
                      Null: 'No'
                    filter: [0.0200 1]
                     phiRC: [27.6536 38.6860 47.7654]
                      dtRC: [1.4000 1.8000 2.2000]
                     phiSC: [39.4382 42.6860 49.5506]
                      dtSC: [1.7000 1.9000 2.1000]
                     phiEV: [39.4382 43.7136 49.5506]
                      dtEV: [1.7000 1.9000 2.1000]
                         a: 1.4503e+003
                         f: 1.5012e+003
                       SNR: [4x1 double]
                    remark: ''
                    method: 'Minimum Energy'
                 timestamp: '25-Jul-2006 12:05:55'
                resultplot: '1997.023.02_result_SKS.eps'
                  seisplot: '1997.023.02_LTQseismo_SKS..eps'
```

4.4. Null Detection in Shear-Wave Splitting Measurements

Andreas Wüstefeld & Götz Bokelmann

Geosciences Montpellier, CNRS, Université de Montpellier II, 34095 Montpellier, France

Bulletin of the Seismological Society of America
August 2007; v. 97; no. 4; p. 1204-1211;
DOI: 10.1785/0120060190

4.4.1. Abstract

Shear-wave splitting measurements are widely used to analyze orientations of anisotropy. We compare two different shear-wave splitting techniques, which are generally assumed to give similar results. Using a synthetic test, which covers the whole backazimuthal range, we find however characteristic differences in fast axis and delay time estimates near Null directions between the rotation-correlation and the minimum energy method. We show how this difference can be used to identify Null measurements and to determine the quality of the result. This technique is then applied to teleseismic events recorded at station LVZ in northern Scandinavia, for which our method constrains the fast axis azimuth to be 15° and the delay time 1.1 sec.

4.4.2. Introduction

Understanding seismic anisotropy can help to understand present and past deformation processes within the Earth. If this deformation occurs in the asthenosphere, the accompanying strain tends to align anisotropic minerals, especially olivine (Nicolas and Christensen, 1987). Seismic anisotropy means that a wave travels in one direction faster than in a different direction. Shear waves passing through such a medium are split into two orthogonal polarized components which travel at different velocities. The one polarized parallel to the fast direction leads the orthogonal component. The delay time between those two components is proportional to the thickness of the anisotropic layer and the strength of anisotropy.

Analyzing teleseismic shear-wave splitting has become a widely adopted technique for detecting such anisotropic structures in the Earth's crust and mantle. Two complementary types of techniques exist for estimating the two splitting parameters, anisotropic fast axis Φ and delay time δt. The first type (multi-event techniques) utilizes simultaneously a set of records coming from different azimuths. Vinnik *et al*. (1989) propose to stack the

transverse components with weights depending on azimuths. Chevrot (2000) projects the amplitudes of transverse components onto the amplitudes of the time derivatives of radial components to obtain the so-called splitting vector. Phase and amplitude of the best-fitting curve give then fast axis and delay time, respectively.

The second type of techniques determines the splitting parameters on a per-event basis (Bowman and Ando, 1987; Silver and Chan, 1991; Menke and Levin, 2003). A grid search is performed for the set of parameters which best remove the effect of splitting. Different measures for "best removal" exist.

We will focus here on the second type (per-event methods) and will show that they behave rather differently close to "Null" directions. Such Null measurements occur either if the wave propagates through an isotropic medium or if the initial polarization coincides with either the fast or the slow axis. In these cases the incoming shear wave is not split (Savage, 1999). It is therefore important to identify such so-called Null measurements. Indeed, Null measurements are often treated separately (Silver and Chan, 1991; Barruol *et al*., 1997; Fouch *et al*., 2000; Currie *et al*., 2004) or even neglected in shear-wave splitting studies. In particular, Nulls do not constrain the delay time and the estimated fast axis corresponds either to the (real) fast or slow axis. In the absence of anisotropy the estimated fast axis simply reflects the initial polarization, which for SKS waves usually corresponds to the backazimuth. Therefore, the backazimuthal distribution of Nulls may reflect not only the geometry, but the strength of anisotropy: media with strong anisotropy display Nulls only from four small, distinct ranges of backazimuths while purely isotropic media are characterized by Nulls from all backazimuths. Small splitting delay times may also be observed in weak anisotropic media or in (strongly) anisotropic media with lateral and/or vertical variations over short distances (Saltzer et al. 2000). Such cases may thus resemble a Null. Typically, the identification of Nulls and non-Nulls is done by the seismologist, based on criteria including the ellipticity of the particle motion before correction, linearity of particle motion after correction, the signal-to-noise ratio on transverse component (SNR_T) and the waveform coherence in the fast-slow system (Barruol *et al*., 1997). Such approach has its limits for near-Nulls, where a consistent and reproducible classification is difficult.

Here, we present a Null identification criterion based on differences in splitting parameter estimates of two techniques. We apply this to synthetic and real data. Such an objective numerical criterion is an important step towards a fully automated splitting analysis. Automation gets more important with the rapid increase of seismic data over the past as well as in future years (Teanby et al., 2003).

4.4.3. Single event techniques

When propagating through an anisotropic layer, an incident S-wave is split into two quasi-shear waves, polarized in the fast and the slow direction. The difference in velocity leads to an accumulating delay time while propagating through the medium (see Savage, 1999 for a review). Single-event shear-wave splitting techniques remove the effect of splitting by a grid-search for the splitting parameters Φ (fast axis) and δt (delay time) that best remove the effect of splitting from the seismograms.

Assuming an incident wave $\mathbf{u_0}$ (with radial component u_R and transverse component u_T), the splitting process (Silver and Chan, 1991) can be described as $\tilde{\mathbf{u}}(\omega) = \mathbf{R}^{-1}\mathbf{D}\mathbf{R}\mathbf{u_0}(\omega)$, that is, by a combination of a rotation of $\mathbf{u_0}$ about angle α between backazimuth, ψ, and fast direction Φ_{fast}

$$\mathbf{R} = \begin{bmatrix} \cos\alpha & -\sin\alpha \\ \sin\alpha & \cos\alpha \end{bmatrix} \qquad (1)$$

and simultaneously a time delay δt

$$\mathbf{D} = \begin{bmatrix} e^{i\omega\delta t/2} & 0 \\ 0 & e^{-i\omega\delta t/2} \end{bmatrix}. \qquad (2)$$

The resulting radial and transverse displacements $\tilde{u}_R$ and $\tilde{u}_T$ in the time domain after the splitting of a noise-free initial waveform $w(t)$ are thus given by

$$\begin{aligned} \tilde{u}_R(\alpha,t) &= w(t+\delta t/2)\cos^2\alpha + w(t-\delta t/2)\sin^2\alpha \\ \tilde{u}_T(\alpha,t) &= -\tfrac{1}{2}[w(t-\delta t/2) - w(t+\delta t/2)]\sin 2\alpha \end{aligned} \qquad (3)$$

For the SKS and SKKS phases that are usually studied with this technique, the initial polarization of w(t) is generally in radial direction. α corresponds therefore to the angle between radial direction and fast polarization axis. Silver and Chan (1991) demonstrated that the splitting parameters can be found from the time-domain covariance matrix of the horizontal particle motion

$$C_{ij}(\alpha,\delta t) = \int_{-\infty}^{\infty} \tilde{u}_i(\alpha,t)\tilde{u}_j(\alpha,t-\delta t)dt; \quad i,j = Radial, Transverse. \qquad (4)$$

Two different techniques of this single event approach exist: The first is the rotation-correlation technique (in the following RC), which rotates the seismograms in test coordinate systems and searches for the direction α where the cross-correlation coefficient is maximum and thus returning the splitting parameter estimates Φ_{RC} and δt_{RC} (Fukao, 1984; Bowman and Ando, 1987). This technique can be visualized as searching for the splitting parameter combination (α, δt) that maximizes the similarity in the non-normalized pulse shapes of the two corrected seismogram components.

The second technique considered here searches for the most singular covariance matrix based on its eigenvalues λ_1 and λ_2. Silver and Chan (1991) emphasize the similarity of a variety of such measures such as maximizing λ_1 or λ_1/λ_2 and minimizing λ_2 or $\lambda_1*\lambda_2$. A special case of this technique can be applied if initial wave polarization is known (as with SKS, SKKS) and if the noise level is low. In this case the energy on the transverse component

$$E_{trans} = \int_{-\infty}^{\infty} \tilde{u}_T^2(t)dt \qquad (5)$$

after reversing the splitting can be minimized. In the following we refer to this technique as SC, with the corresponding splitting parameter estimates Φ_{SC} and δt_{SC}.

All of these single event techniques rely on a good signal-to-noise ratio (Restivo and Helffrich, 1999). Another limit is the assumption of transverse isotropy and one layer of horizontal axis of symmetry and thus only provides apparent splitting parameters. This is commonly compensated by analyzing the variation of these apparent parameters with backazimuth (e.g. Özalaybey and Savage, 1994; Brechner *et al*, 1998)

4.4.4. Synthetic test

We first compare the RC with the SC technique in a synthetic test. Figure 26 displays an example result for both techniques for a model that consists of a single anisotropic layer with input fast axes of $\Phi_{in} = 0°$ and splitting delay time $\delta t_{in} = 1.3$sec at a backazimuth of 10°. Our input wavelet w(t) is the first derivative of a Gauss function

$$w(t) = -2\frac{t-t_0}{\sigma} * \exp -\left(\frac{t-t_0}{\sigma}\right)^2 \qquad (6)$$

For σ = 3 the dominant period is ~8sec. This wavelet was then used in the splitting equations (3), given by Silver and Chan (1991), to calculate the radial and transverse components for the given set of splitting parameters (Φ, δt). We added Gaussian-distributed noise, bandpass-filtered between 0.02 and 1Hz, and determined the SNR as

$$SNR_R = \max(|\tilde{u}_R|)/2\sigma_T$$
$$SNR_T = \max(|\tilde{u}_T|)/2\sigma_T \,. \qquad (7)$$

For SNR_R this is similar to Restivo and Helffrich (1999), where the "signal" level is the maximum amplitude of the radial component before correction. The 2σ envelope of the corrected transverse component gives the noise level. For the example in Figure 26 we obtain a SNR_R of 15 and SNR_T of 3, respectively (compare with the seismograms in the first panel on the top).

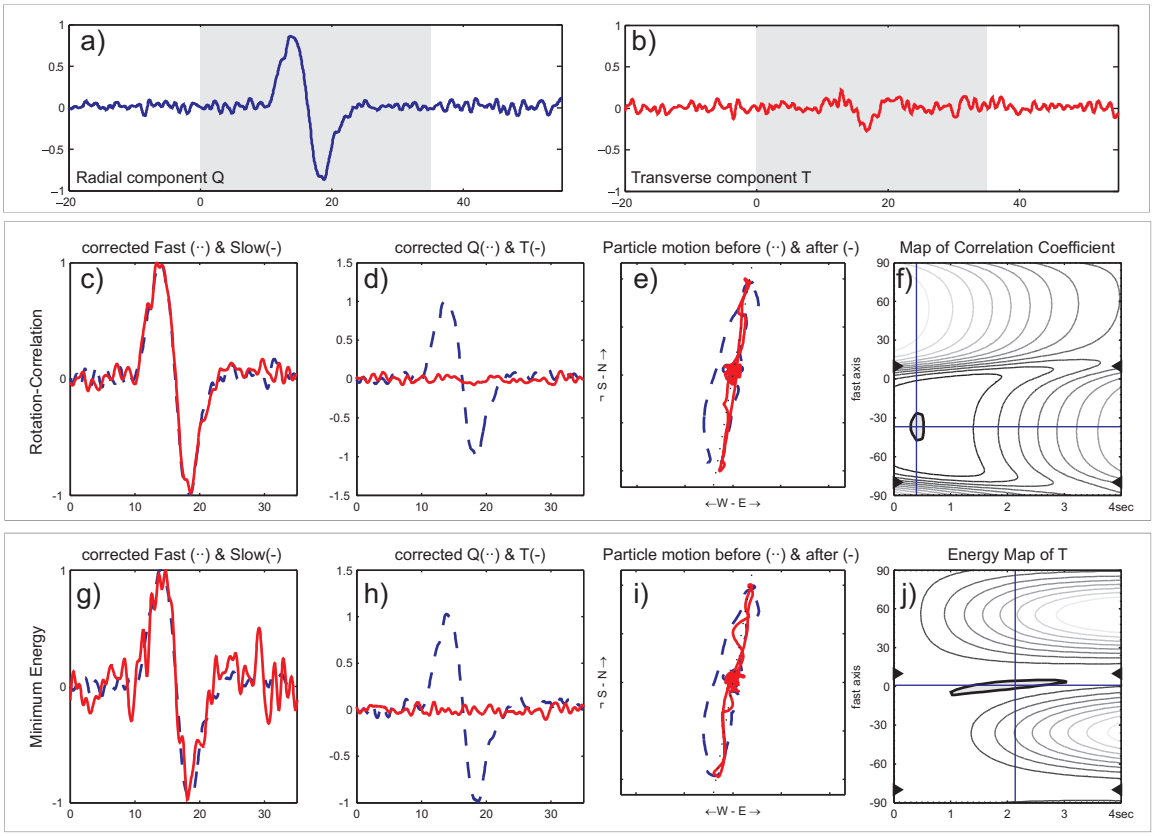

Figure 26: Synthetic splitting example with fast axis at 0º, delay time 1.3sec and backazimuth 10º ("near-Null case") for a Signal-to-Noise Ratio (SNR_R) of 15. Upper panel displays the initial seismograms: a) Radial and b) Transverse component, both bandpass filtered between 0.02 and 1Hz. The shaded area represents the selected time window. The center panel displays the results for the Rotation-Correlation (RC) technique: c) normalized components after rotation in RC-anisotropy system; d) Radial (Q) and transverse (T) seismogram components after RC correction; e) particle motion before and after RC correction and f) map of correlation. Lower panel displays the results for the minimum energy (SC) technique: g) normalized components after rotation in SC anisotropy system; h) corrected (SC) radial and transverse seismogram component; i) SC particle motion before and after correction and j) map of minimum energy on transverse component

The backazimuth for the example in Figure 26 is 10º and it thus constitutes a near-Null measurement. Note that the two techniques produce different sets of optimum splitting parameter estimates. While the optimum for SC recovers approximately the correct

solution, RC deviates significantly. In the following, we will analyze the performance of the two techniques for the whole range of backazimuths.

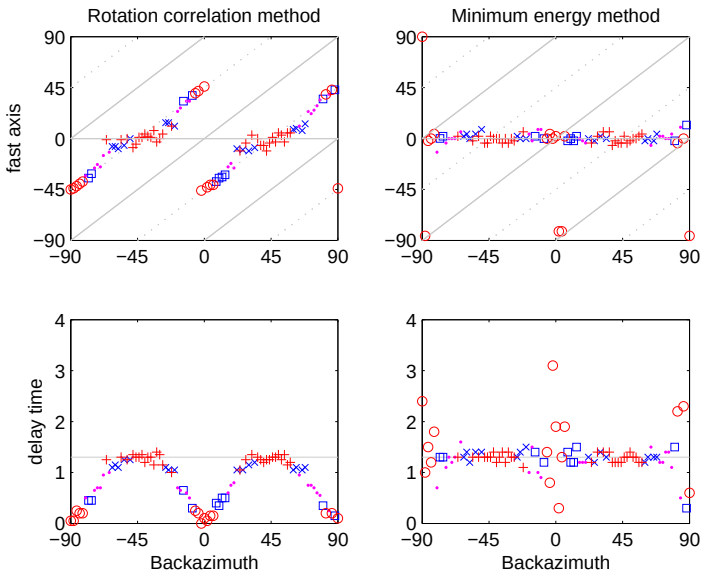

Figure 27: Synthetic test at SNR_R = 15 for the Rotation-Correlation technique (RC, left) and the Minimum Energy technique (SC, right). Upper panels show the resulting fast axes at different backazimuths, lower panels show the resulting delay time estimates. Input values Φ_{in} = 0° and dt_{in} = 1.3sec are indicated by horizontal lines. The SC technique yields stable estimates for a wide range of backazimuths. For lower SNR_R and/or smaller delay times (see electronic supplement) the RC-technique differs even more from the input values. Automatically detected good Nulls are marked as circles, near-Nulls as squares. Good splitting results are marked as plus signs, and fair results as crosses. Poor results are indicated as dots.

Figure 27 displays the splitting parameter estimates (fast axis Φ_{RC} and Φ_{SC} and delay times δt_{RC} and δt_{SC}) for different backazimuths ψ. This synthetic test shows that both techniques give correct values if backazimuths are sufficiently far away from fast- or slow-directions. Near these Null directions there are characteristic deviations, especially for the RC-technique. Values of δt_{RC} diminish systematically, while Φ_{RC} shows deviations of about 45° near Null directions. Perhaps surprisingly, the Φ_{RC} lies along lines that indicate backazimuth ±45°. The explanation of this behaviour is that the RC-technique seeks for maximum correlation between the two horizontal components Q (radial) and T (transverse). However, in a Null case the energy on T is negligible and for any test fast axis F

$$\begin{bmatrix} F \\ S \end{bmatrix} = \begin{bmatrix} \cos\Phi & -\sin\Phi \\ \sin\Phi & \cos\Phi \end{bmatrix} \cdot \begin{bmatrix} Q \\ T \end{bmatrix} = \begin{bmatrix} Q\cos\Phi \\ Q\sin\Phi \end{bmatrix} \qquad (8)$$

the test slow axis S gains its energy only from the Q-component. The waveform on both F and S is identical to the Q-component waveform with no delay time. Consequently, the F-S-cross-correlation yields its maximum for $\Phi = 45°$, where $\sin(\Phi) = \cos(\Phi)$ (anti-correlated for $\Phi = -45°$). For this reason the fast azimuth estimated by the Rotation-

Correlation technique is off by ± 45° near Null directions from the true fast azimuth direction, while δt_{RC} tends towards zero.

In comparison, the SC technique is relatively stable except for large scatter near Nulls. Here, the SC fast axis estimates, Φ_{SC}, deviates around ±n*90º from the input fast axis and the delay time estimates δt_{SC} scatter and often reach the maximum search values (here 4 sec). This results from energy maps with elongated confidence areas along the time axis (Figure 26j), probably in conjunction with signal-generated noise. In agreement with Restivo and Helffrich (1999), it appears that δt_{SC} typically is reliable if the backazimuth differs more than 15º from a Null direction. We tested this result for different input delay times and noise levels (see electronic supplement). The width of the plateau of correct Φ_{RC} and δt_{RC} estimates (Figure 27) is a function of both input delay time and SNR_T. Higher delay times and/or higher SNR_T result in wider plateaus. In contrast, for small input delay times and low SNR_T the backazimuthal range over which Φ_{RC} fall onto the ±45º lines from the backazimuth (dotted in Figure 27) becomes wider, until it eventually encompasses the whole backazimuth range. On the other hand, SC shows scatter for a larger range but no systematic deviation.

Comparing the results of the two techniques can thus help to detect Null measurements. For a Null measurement, the angular difference between the two techniques is

$$\Delta\Phi = \Phi_{SC} - \Phi_{RC} \approx n*45° \qquad (9)$$

where n is a positive or negative integer. For backazimuths deviating from a Null direction, the difference in fast axis estimates decreases rapidly depending on noise level and input delay time. Figure 27 displays that for a SNR_R of 15 a near-Null can be clearly identified as having generally $|\Delta\Phi| \geq 45°/2$. Near Null directions the Rotation-Correlation delay times are biased towards zero. The backazimuth with minimum δt_{RC} is thus a further indicator of a Null direction (Figure 27). Teleseismic non-Null measurements thus require the following criteria: (1) the ratio of delay time estimates from the two techniques (ρ = δtRC/δtSC) is larger than 0.7 and (2) the difference between the fast axis estimates of both techniques, $|\Delta\Phi|$, is smaller than 22.5º. Events with $SNR_T < 3$ are classified as Nulls.

Wolfe and Silver (1998) remark that waveforms containing energy at periods (T) less than ten times the splitting delays are required to obtain a good measurement. However, the arc-shaped pattern of δtRC persists for smaller delay times. Thus, the characteristics of the backazimuthal plots (as discussed above) can provide valuable additional information on the anisotropic parameters.

Detecting Nulls using a data based criterion provides three advantages: first it eliminates subjective measures such as evaluating initial particle motion and resulting energy map. Second, by varying the threshold values of $\Delta\Phi$ and ρ, the user can change the sensitivity

of Null detection. And third, the separation of Nulls is necessary for future automated splitting approaches. Since available data increase rapidly, the automation of the splitting process is a desirable goal in future applications and procedures.

4.4.4.1. Quality determination

We furthermore use the difference between results from the two techniques as a quality measure of the estimation. Again, such a data based measure is more objective than visual quality measures based on seismogram shape and linearization (Barruol *et al.*, 1997). In Figure 28 we compare, similar to Levin *et al.* (2004), both techniques by plotting the difference of fast axis estimates ($|\Delta\Phi|$) versus ratio of delay times ($\rho = \delta t_{RC} / \delta t_{RC}$) of synthetic seismograms.

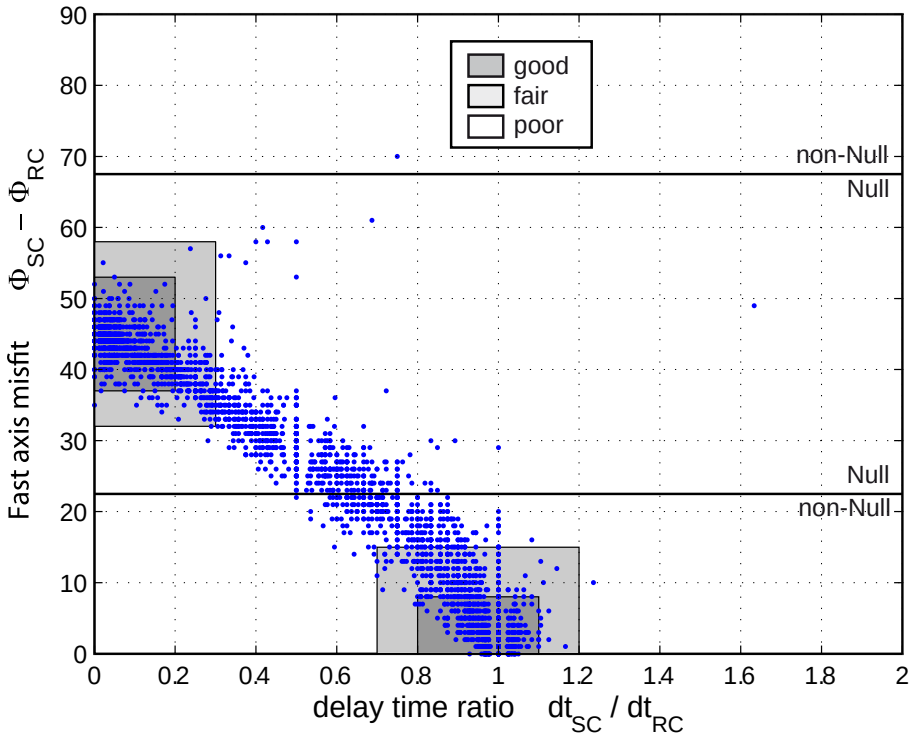

Figure 28: Misfit of delay time and fast axis estimates between Rotation Correlation (RC) and the Minimum Energy (SC) techniques calculated for 3185 synthetic seismograms at five different SNR between 3 and 30 and seven input delay times between 0 and 2 seconds from all backazimuths. The Null criterion helps to identify Null measurements and at the same time gives a quality attribute. Fair Null measurements are equivalent to near-Nulls.

Based on the synthetic measurements (Figure 27), we define as good splitting measurements if $0.8 < \rho < 1.1$ and $\Delta\Phi < 8^o$ and fair splitting if $0.7 < \rho < 1.2$ and $\Delta\Phi < 15^o$. Null measurements are identified as differences in fast axis estimates of around 45° and a small delay time ratio ρ. Near the true Null directions the SC fast axis estimates are more robust than the RC technique (Figure 27). A differentiation between Nulls and near-Nulls is useful in the interpretation of backazimuthal plots (Figure 27). Good Nulls are

characterized by a small time ratio ($0 < \rho < 0.2$) and, following Equations 9, a difference in fast axis estimate close to 45º, that is $37º < \Delta\Phi < 53º$. Near-Null measurements can be classified by $0 < \rho < 0.3$ and $32º < \Delta\Phi < 58º$. Remaining measurements are to be considered as poor quality (See Figure 28 for further illustration).

4.4.5. Real data

We apply our Null-criterion to the shear wave splitting measurements of station LVZ in northern Scandinavia. The analyzed earthquakes ($M_W \geq 6$) occurred between December 1992 and December 2005. The data were processed using the SplitLab environment (Wüstefeld, Bokelmann, Barruol, Zaroli; SplitLab – A shear wave splitting environment in Matlab; submitted to Computers & Geosciences, 2006; See Chapter 4.3). This allows us to analyze events efficiently and to calculate simultaneously both the RC- and SC-technique. We mostly used raw data or, where necessary, applied 3rd-order Butterworth band-pass filters with upper corner frequencies down to 0.2 Hz. Most usable events have backazimuths between 45° and 100°. Such sparse backazimuthal coverage is unfortunately the case for many splitting analysis, and we aim to extract the maximum information about the splitting parameters from these sparse distributions.

In total we analyzed 37 SKS phases from a wide range of backazimuths (Figure 29). Many results resemble Null characteristics by showing low energy on the initial transverse component, elongated to linear initial particle motion and typical energy plot. Such characteristics can be replicated in synthetic seismograms with near-Null parameters, i.e. when the fast axis deviates less then 20º from backazimuth (Figure 26).

The average fast axis of the good events, as detected automatically and manually, is 14.3° and 14.7° for the SC and RC technique, respectively. Such orientation implies Nulls at backazimuths of approximately 15°, 105°, 195° and 285° and favorable backazimuths for splitting measurements in between. Indeed, good and fair splitting measurements are found in backazimuthal ranges between 50° and 70° (Table 1 and Figure 29), where the energy on the transverse component is expected to reach maximum possible values (see Equation 3) and the splitting can be inverted most reliably. Also in good agreement are the detected Nulls at backazimuths between 80° and 110° and around 270°.

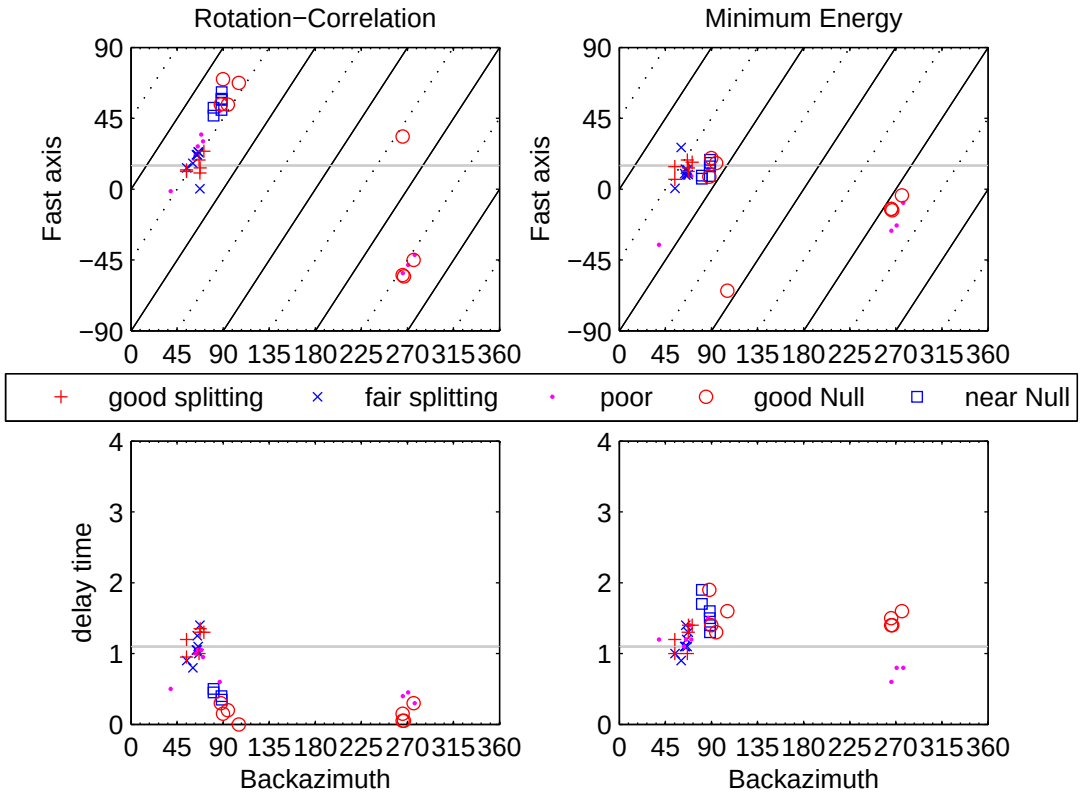

Figure 29: Shear-wave splitting estimates from 33 good and fair measurements from station LVZ. The upper panels display fast axis estimates for Rotation Correlation and Minimum Energy methods. Note that many Rotation-Correlation estimates are situated near the dotted lines that indicate 45º. The lower panels display the delay time estimates. The solid horizontal lines indicates our interpretation of the LVZ with fast axis at 15º and 1.1sec delay time, based on the mean of the good splitting measurements.

Date	Lat	Long	Bazi	Φ_{SC}	Φ_{RC}	dt_{SC}	dt_{RC}	SNR_{SC}	$corr_{RC}$
01-Oct-1994	-17.75	167.63	55.1	19.1	13.1	0.8	0.8	5.85	0.89
17-Mar-1996	-14.7	167.3	54.3	14.3	12.3	1.0	1.0	9.55	0.93
05-Apr-1997	-6.49	147.41	71.1	17.1	24.1	1.4	1.3	6.16	0.88
06-Feb-1999	-12.85	166.7	54.2	6.2	11.2	1.2	1.2	10.43	0.97
10-May-1999	-5.16	150.88	67.3	11.3	10.3	1.3	1.3	5.70	0.87
06-Feb-2000	-5.84	150.88	67.5	13.5	13.5	1.4	1.4	9.33	0.91
18-Nov-2000	-5.23	151.77	66.5	18.5	18.5	1.0	1.0	5.74	0.90

Table 1: Good events of station LVZ as detected automatically. SNR_{SC} is the signal-to-noise ratio of the SC technique and $corr_{RC}$ is the correlation coefficient of the RC technique

Simultaneously, RC delay times systematically tend to smaller values between backazimuths of 80° and 110°, mimicking the trapezoidal shape in the synthetic RC delay times (Figure 27). Mean delay time estimates of good SC and RC are 1.2 and 1.1 seconds, respectively.

4.4.6. Discussion and conclusions

We have presented a novel criterion for identifying Null measurements in shear-wave splitting data based on two independent and commonly used splitting techniques. The two techniques behave very differently near Null directions, where the rotation-correlation technique systematically fails to extract the correct values both for the fast-axis azimuth Φ_{RC} and delay time $\delta t_{RC.}$ That technique should therefore not be used as a "stand-alone" technique. On the other hand, the comparison of the two techniques is valuable for finding Null events. The backazimuths of Nulls ambiguously indicates either fast- or slow-direction. Thus, a Null measurement yields limited, yet important, constraints on anisotropy orientation, especially if the backazimuthal coverage of the station is only sparse. Furthermore, Nulls from a wide range of backazimuths indicate either the lack of (azimuthal) anisotropy or weak anisotropy, at the limit of detection. Restivo and Helffrich (1999) analyzed the splitting procedure for effects of noise. They conclude that for small splitting filtering does not necessarily result in more confident estimates of splitting parameters, since narrow band-pass filters lead to apparent Null measurements. For SNR above 5 our criterion detects Null measurements and classifies near-Nulls. Good events can still be obtained but only for exceptionally good SNR or with backazimuths far away oriented with respect to the anisotropy axes (where the transverse amplitude is larger; see Equation 3).

The comparison of the two shear-wave splitting techniques allows assigning a quality to single measurements (Figure 26). Furthermore, the joint two-technique analysis of all measurements (Figure 27) yields characteristic variations of splitting parameter estimates with backazimuth. This variation can be used to extract the maximum information from the data, and to decide whether a more complex anisotropy than a single-layer needs to be invoked to explain the observations. The practical steps for this should be: First, assume a single-layer case with the most probable fast direction based on the good measurements. Second, verify that Null measurements occur near the corresponding Null directions in the backazimuth plot (Figure 29). In the vicinity of these Null directions, the splitting parameter estimates Φ_{SC} and δt_{SC} should show a larger scatter with a tendency towards large delays. For δt_{RC} we expect to find an arc-shaped variation with backazimuth that should have its minimums near the assumed Null directions. If these conditions are met, a one-layer case can reasonably explain the observations. On the other hand, good events that deviate from these predictions may require more complex anisotropy (multi-layer case or dipping layer). Applied to station LVZ in northern Scandinavia, we were thus able to comfortably characterize the anisotropy by a single layer anisotropy with a fast axis oriented at 15° and a delay time of 1.1 seconds.

4.5. Automatisation of the splitting process

Over the last decades the number of broad band stations has increased rapidly. These seismometers cover a frequency spectrum broad enough for the shear wave splitting process. These permanent stations record each day new split shear waves, which should be processed for a better understanding of anisotropy and thus geodynamic processes. However, not only grew the number of permanent stations, but also the availability of portable stations or even portable networks. Though only recording for a limited time, these data record a reasonable large amount of data.

Growing datasets require new approaches to boost processing efficiency. Furthermore, a uniform processing for all stations limits ambiguity in results, evoked by processing technique [Wüstefeld & Bokelmann, 2007] or by other biases, such as the "human factor". Each seismologist has a priori a personal approach. Personal biases include:

- experience of the seismologist (Null detection, quality assignment, …)
- time window selection (one phase cycle vs. more generous time window, …)
- filter selection (uniform for all stations, or varying filter with "best recovery of signal")

Uniform filtering has the advantage that the same frequency content, and thus wavelength, is analyzed for all events. In this case, each measurement renders always the same sensitivity to a characteristic thickness. On the other hand, variable filtering allows the recovery of the high frequency contents / short wave lengths information. Schmid et al. [2004] analyzed the variation of splitting parameters with filter frequencies of stations around the Mediterranean. Systematic studies of this kind can lead to a better understanding of processes and to new ideas to explain scattering of splitting measurements.

The manual processing furthermore implies shortcomings in the non-uniform distribution of splitting within the dataset. Though being most objective during data analysis, a sequence of poor events followed by an only slightly better measurement, cause inevitably the assignment of a much better quality class. On the other hand, a series of good events degrade a subsequent slightly worse event.

A first step to address these problems has been undertaken by Teanby et al. [2003] and in a slightly altered version by Evans et al. [2006]. These authors propose to automatically vary the phase selection window about the theoretical phase arrival time, resulting in approximately 200 measurements per event. The splitting parameters (fast orientation and delay time) of these measurements are then evaluated in a cluster analysis [Teanby et al., 2003], or a stable plateau of splitting parameters is assumed as correct value [Evans et al.,

2006]. Such approach clearly enhances objectivity in the dataset, though it does not take into account varying filters.

Here, it is proposed to enhance the automatic splitting process by adding a variation of the filter. At the same time, Nulls are detected automatically and a quality class is assigned to each measurement, which allows a weighting to be applied. A first feasibility study is performed for station ATD (Djibouti). This station has very good backazimuthal coverage, and shows clear and strong one layer splitting, with a fast rientation of 45° and delay time of 1.5sec [Barruol & Hofmann, 1999; Wüstefeld & Bokelmann, 2007].

The test parameter set presented here serves only as a basis for possible further enhancements. A parameter study should at a later point clarify the best set, balancing calculation time and accuracy. The parameters are

- Start time (-10 sec to 22 sec after theoretical arrival of SKS, in steps of 4 sec)
- Stop time (-2 sec to 26 sec after theoretical arrival of SKS, in steps of 4 sec)
- Upper band pass filter frequency (1Hz, 0.4Hz, 0.2 Hz)
- Lower band pass filter frequency (fixed to 0.02 Hz)

Because ATD is located on the hot East African Rift system [e.g., Nyblade & Robinson, 1994; Ritsema et al., 1999; Kendall et al., 2005] phase arrivals are highly delayed in respect to their global average of standard earth models. A static shift of 4 sec is therefore added to the theoretic arrivals, before determining the time windows. Time windows of less than 10 seconds, approximately the dominant frequency of SKS, are skipped to ensure that at least one complete phase cycle is analyzed. This selection of parameters leads to a theoretical number of 9 x 6 x 3 x 1 = 162 measurements.

Each individual measurement is then checked for Null event using the Wüstefeld & Bokelmann [2007] technique by comparing the results of Rotation-correlation method and Minimum energy method. In this case, Null simply means, that no significant signal on the transversal component correlates with the signal on the radial component. Surely some windows will lie outside relevant phase information and only try to analyze noise. Non-Nulls of good and fair quality are considered for further analysis.

Both methods proposed by Teanby et al. [2003] (cluster analysis) or by Evans et al. [2006] (plateau) do not address the range of error of each measurement sufficiently. Here it is therefore preferred to modify the approach by Wolfe & Silver [1998]. They proposed to stack the error surface of individual earthquakes and then determine the “global minimum energy” for a station, resulting in a fast orientation and delay time. This approach is only valid for a single layer of anisotropy. Any backazimuthal variations, caused by more complex geometries [Silver & Savage, 1994; Rümpker & Silver, 1998], are smoothed out.

However, stacking of the error surfaces is completely valid for measurements of a single event. Stacking the energy surface of good and fair non-Nulls results in a “total event energy surface”. It is important to filter out Null events from stacking. Nulls are usually characterized by pronounced levels of minimum energy, which can be best described as a lying “U”. Stacking such surface would bias the total event surface towards Nulls. Wolfe & Silver [1998] propose to stack the normalized energy surfaces. In this case it is however more appropriate to stack the energy “as is” and thus maintain the relative topography of each measurement. High topography gradients of specific single measurements are preserved and thus giving it high relative weighting.

Having stacked all good and fair non-Nulls it is now possible to determine the characteristic event minimum energy, yielding an event fast orientation and event delay time. Additionally, the errors can be determined for the total event surface using the same statistics as proposed in Silver & Chan [1991].

Figure 30 and Figure 31 show the result of such a calculation for 330 events with $M_W \geq 6.25$, recorded at station ATD between December 1993 and January 2006. The symbol size and color is proportional to the amount of good and fair measurements stacked. The general splitting parameters found by Barruol & Hofmann [1999] are well recovered by events with a stacking number higher than 40. Some outliers might be the result of contamination by other phases. An intriguing feature of Figure 30 is the decreasing delay time, when the backazimuth is approaching the Null directions. This might be due to the stacking of near-Nulls events. These show for the SC method scattering as well to larger- and smaller-then-real delay times (Figure 27). Too large delay times will be clearly identified as Nulls by the Null-Criterion. The stacking of many near-Nulls results then in a bias towards smaller delay times. Furthermore, the fast orientation appear to turn towards more E-W directions for backazimuths closer to North.

Figure 31 reflects the distribution of results in the result parameter plane. A cluster around the previously manually determined estimates encourages further development of the technique proposed here. Enhancements include a calibration of parameters (window step size, filter frequencies) and the exclusion of time windows containing other phases (especially S, SS), which contaminate the signal considerably. Furthermore, displaying the results in a different manner might reveal further information, not yet considered in the present form. In particular the possible variation of splitting estimates with filter frequency remains yet to be addressed.

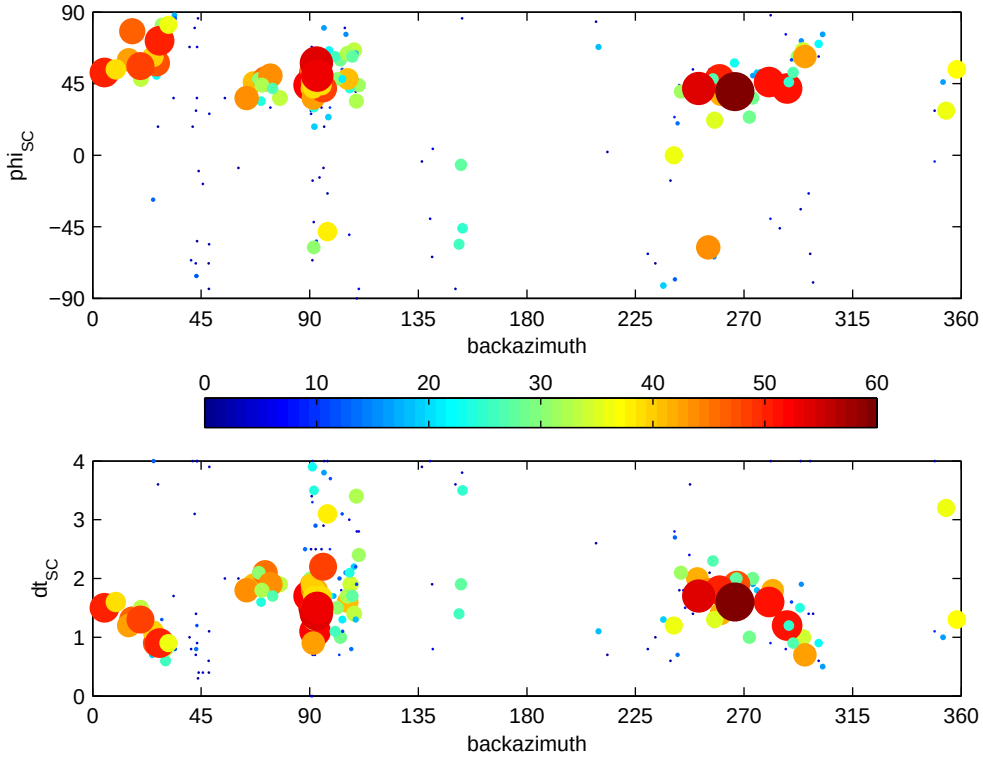

Figure 30: Backazimuthal variation for automated splitting at station ATD. Color and size of symbol corresponds to the stacking number, i.e. the number of good and fair non-Null events used for stacking of the energy surface of the SC method. The splitting parameters Φ and dt represent the minimum of this stacked surface.

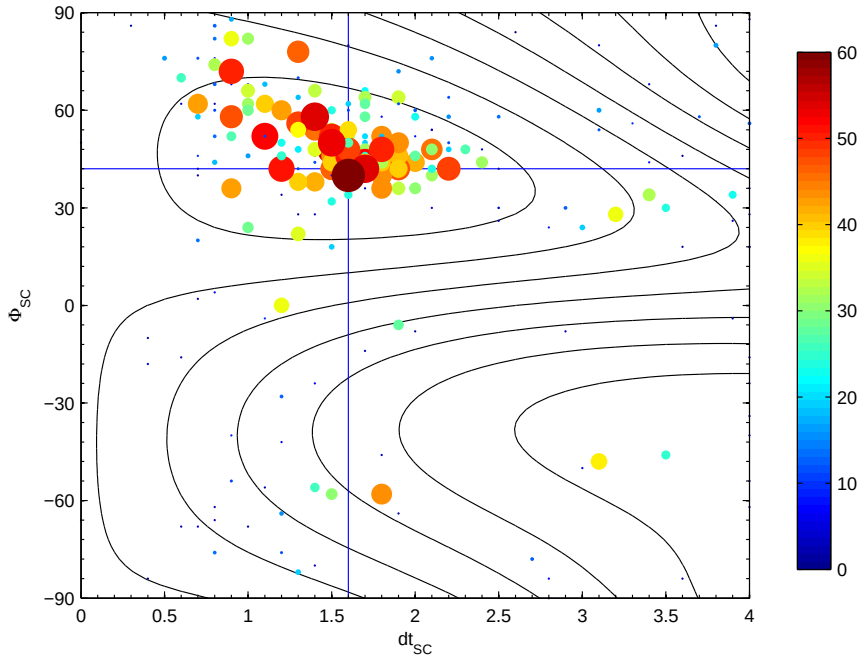

Figure 31: Same as Figure 30, except in (Φ, dt) parameter plane. Size and color of each symbol represents the amount of non-Null measurements recovered for the corresponding seismogram. The contour lines represent the stacked energy map of all non-Null measurements. This energy map has its minimum for Φ=42º and dt = 1.6sec. This is in very good agreement with Barruol & Hoffmann [1999], who manually determined Φ=48º and dt = 1.59sec

4.6. Interactive Shear-wave splitting database

Over the past decades a large number of shear-wave splitting studies have been published in various journals. Some analyse a global station set [e.g. Silver, 1996; Barruol & Hoffmann, 1999], while most focus on regional networks of stations and provide detailed knowledge on a specific area. All these works provide a great knowledge and interpretation of the Earth's anisotropy: beneath all the continents, at island stations [Behn et al., 2004] or even beneath the ocean by using ocean bottom seismometers (OBS).

Future studies, either on anisotropy or on geodynamics and geology, will exploit these interpretations. It is therefore important to facilitate the access and to homogenise the format of these data. A first step has been undertaken by Derek Schutt, who has started a collection of publications and splitting directions and provided this list on his homepage. Matt Fouch continued this list, which can be downloaded at

`http://geophysics.asu.edu/anisotropy/upper/`

In order to build a more complete and accessible database, their work is used as a basis for an interactive database. The features of this presentation are (Figure 32) are:

- Search the database for a specific station
- Search the database within a region
- Download database in plain text format
- Download the database in GoogleEarth format
- Enter new splitting data via a web interface

This database can be accessed with a standard internet browser through the internet homepage of "Geoscience Montpellier". It is available at

`www.gm.univ-montp2.fr/splitting/DB`

The results of the searches are presented in the browser as a list and the corresponding references are given. Most importantly, researchers can add their own data and thus share the results and extend the database. This provides advantages for the provider (who will spread his/her results to a large public) as well as for the user (who will always find the most "up-to-date" information). A web-interface (Figure 33) assures that the input format is consistent for all datasets.

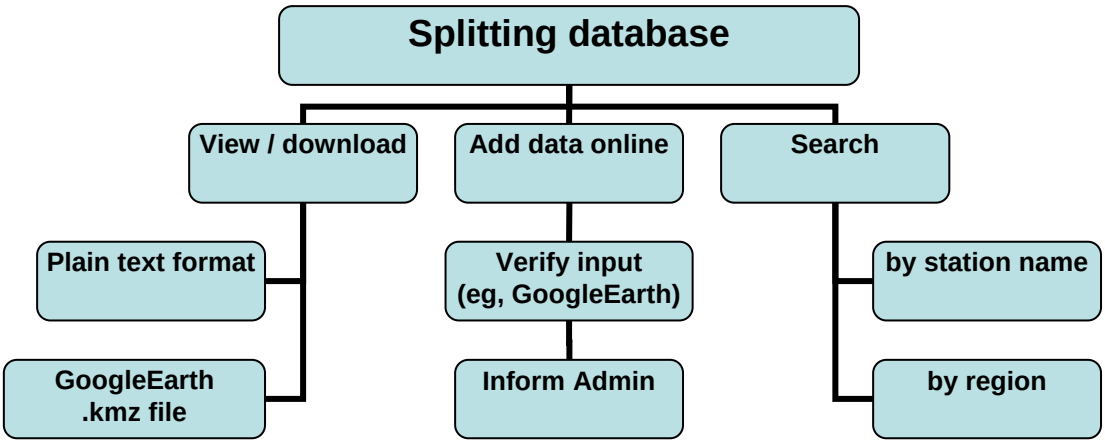

Figure 32: The various options presented by the shear-wave splitting database.

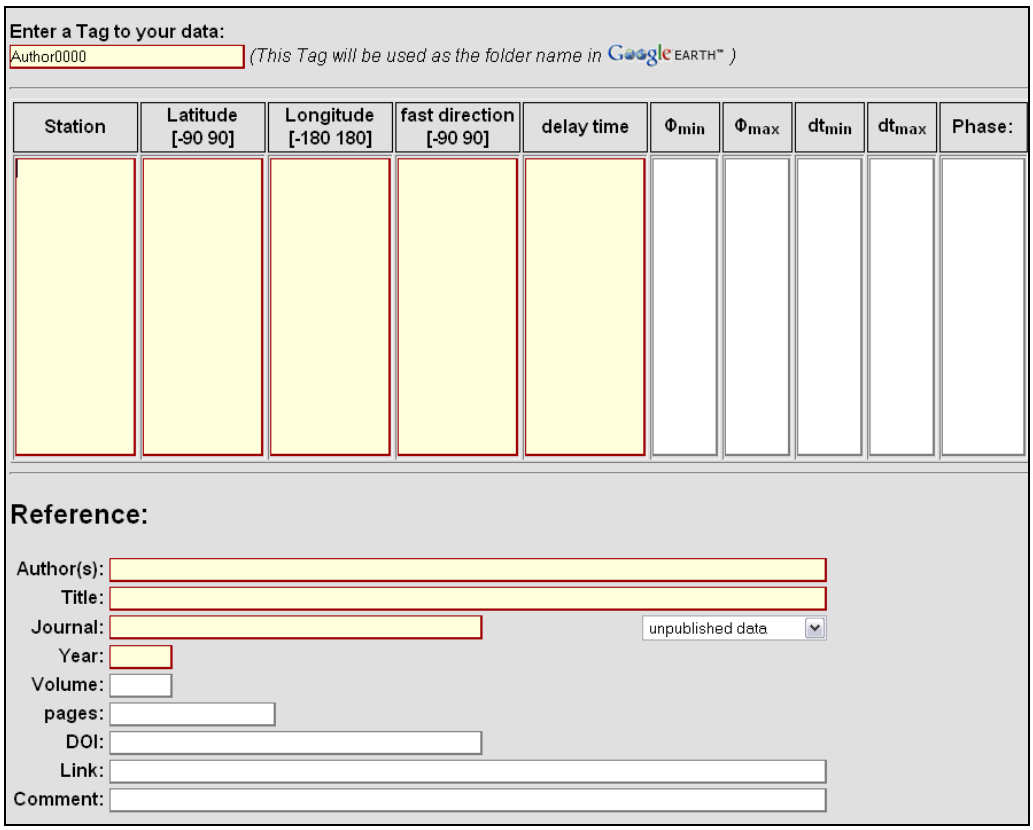

Figure 33: The web interface for adding new data can be accessed from every computer with a common internet browser and internet connection.

The splitting data can be downloaded in two different formats. The first format is plain ASCII text files, one for the data and one for the references. The various fields are separated with a pipe symbol "|". An example script of how to read the data into either Matlab or GMT is provided on the homepage.

The second format is ".kmz", readable by GoogleEarth and a growing number of other geographic mapping applications. This .kmz-file is a zip-compressed file containing a

png-icon for the fast orientation and an ASCII text in “Keyhole Markup Language” style, which is basically a special xml-format (http://earth.google.com/kml/). Once the database is loaded in GoogleEarth, each measurement is displayed as a vector (Figure 34), with its azimuth corresponding to the fast orientation and scaled by the delay time. A small label indicates the station name. By clicking on a station, these anisotropy parameters are displayed in addition to the reference and possible further remarks.

Supplementary geophysical data sets are also provided on the homepage. These include plate boundaries [Bird, 2003], global tomography [Debayle et al., 2005], and global thermal structure [Artemieva, 2006] amongst others. Having these data ready thus provides the possibility to compare different datasets in an easy-to-use environment like GoogleEarth. As such, it may invite researchers from many fields to use the data (Figure 34; Figure 35). This might eventually lead to new combinations of datasets, resulting in new interpretations and finally in a better understanding of the Earth’s processes.

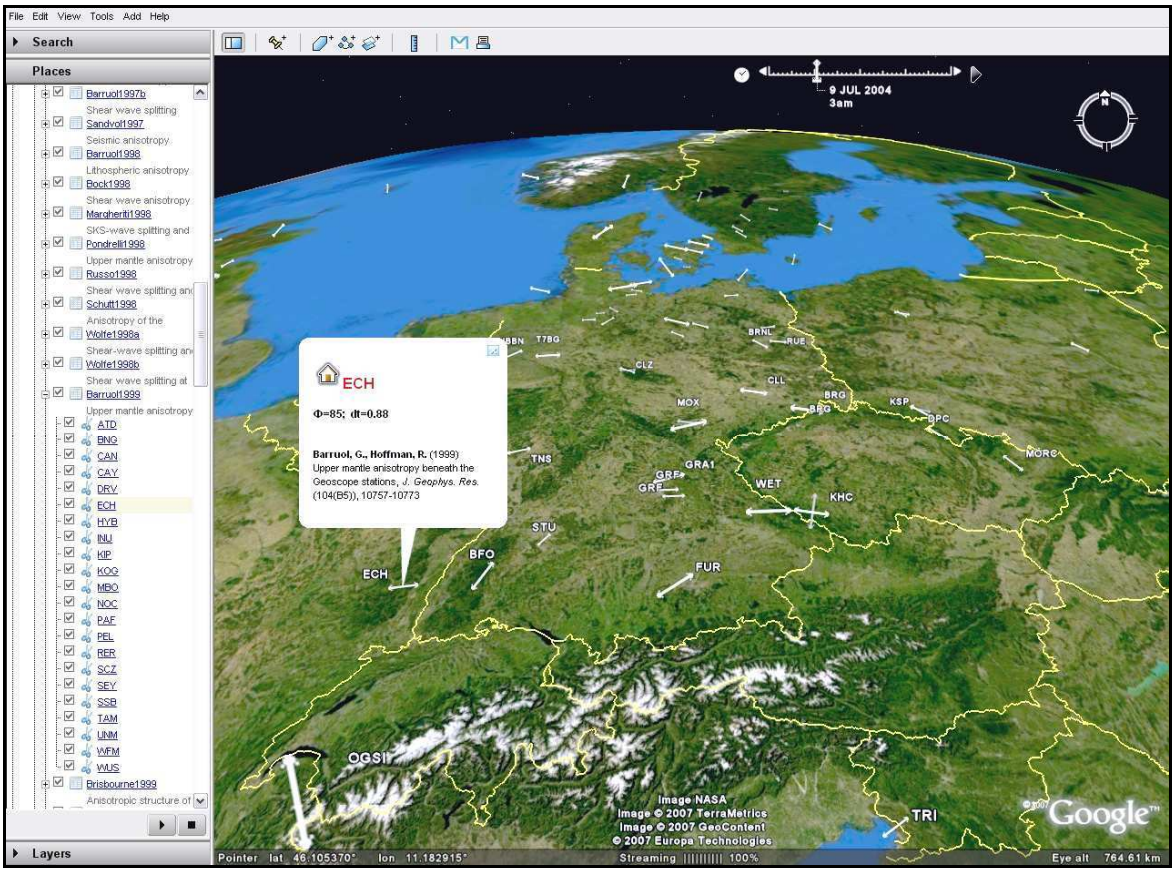

Figure 34: The database as seen in GoogleEarth. Clicking on a symbol reveals the corresponding reference to that measurement and any possible additional information given during entry of the data (e.g., link to the project page, technique used, etc)

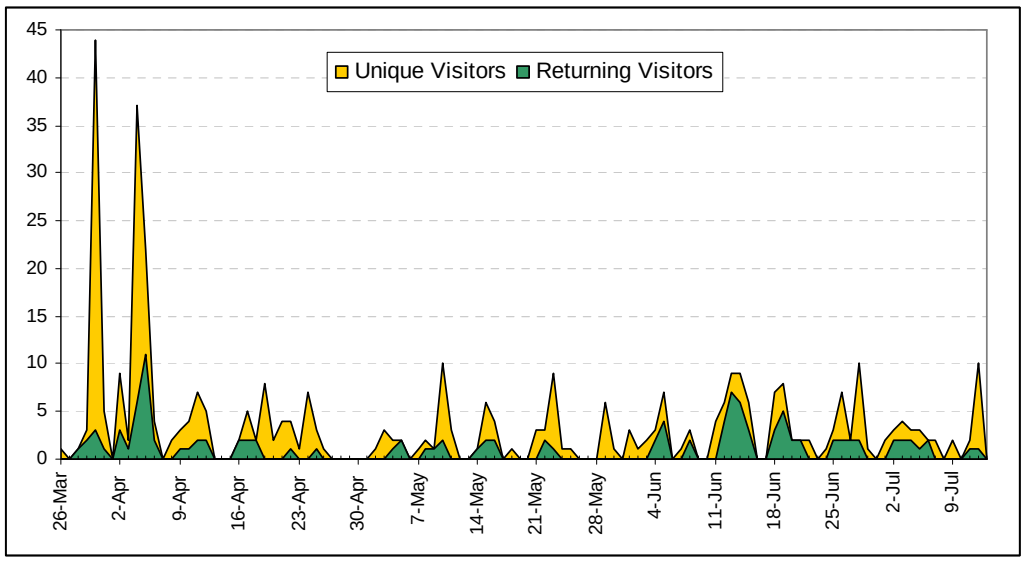

Figure 35: Visitor activity for the splitting database as of July 13th. Continuous visits from around the world underlines the broad interest for such a database.

4.6.1. Global statistics of shear wave splitting

As of July 2007, the database contains 2286 entries. The delay times show a skewed Gaussian distribution with a peak at 1 sec (Figure 36). This is in agreement with Silver [1996]. The fast orientations show a preference for E-W orientations, which might support speculations of uniform a global plate motion relative to the mantle [Steinberger & O'Connel, 1998; Doglioni et al., 1994; 2003]. However, this statistics can only be considered as a first order approach. Most splitting data are on continents, where the azimuth may reflect frozen-in lithospheric anisotropy, not related to the present day geometry of processes. Furthermore, on the continents the stations are not evenly distributed. Temporary experiments are constrained to rather small areas [e.g., Barruol et al., 1998; Fouch et al., 2004; Walker et al., 2005; Flesh et al., 2005], which causes a bias. Finally, not every continent is covered equally, causing a bias of values from North America and Central Europe.

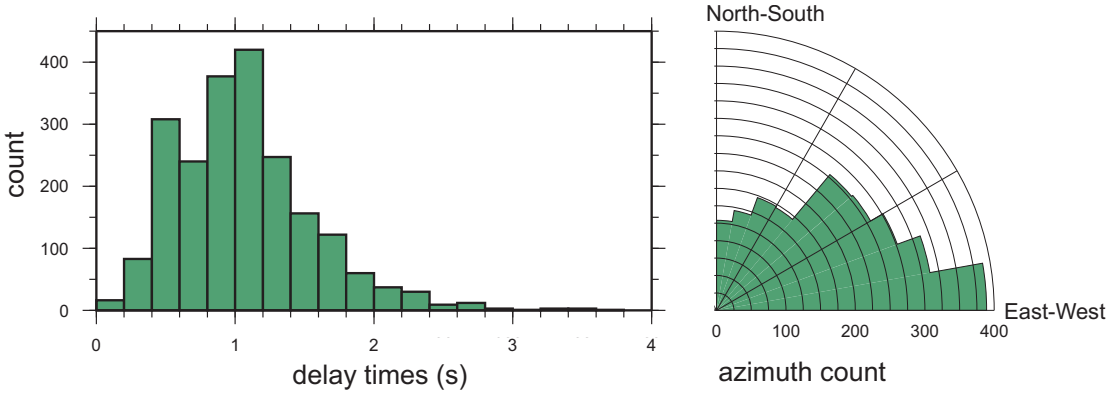

Figure 36: Statistics of 2286 shear wave splitting measurements. Left panel shows delay time distribution. The right panel shows azimuthal variation.

4.6.2. Comparison with surface wave data

The database can be used to study the relation between constraints from shear-wave splitting with those from other datasets, e.g. surface waves. Montagner et al. [2000] devised a method to calculate "predicted" SKS splitting parameters from surface wave results. This approach is similar to several studies which discuss the effect of multiple anisotropic layers on the effective splitting parameters [Silver & Savage, 1994; Wolfe & Silver, 1998; Rümpker & Silver, 1998; Saltzer et al., 2000]. The fast orientation and delay time accumulated in a (weakly) anisotropic layer are related to the elastic parameters $G_s = C_{45}, G_c = \frac{1}{2}(C_{55} - C_{44})$, $L = \frac{1}{2}(C_{44} + C_{55})$, which have been obtained from surface wave studies:

$$dt = \frac{h}{V_{So}} \frac{\sqrt{G_c^2 + G_s^2}}{L}$$

$$\phi_{fast} = \tfrac{1}{2} \arctan\left(\frac{G_s}{G_c}\right)$$

$$\phi_{slow} = \tfrac{1}{2} \arctan\left(\frac{G_s}{G_c}\right) + \frac{\pi}{2}$$

h is the thickness of the anisotropic layer, and V_{So} is the isotropic (average) shear wave velocity. Assuming vertical wave propagation in a horizontally layered anisotropic medium Montagner et al. [2000] showed, that this approach can be generalized for multiple layers at intermediate and long periods (T>10s, i.e. SKS, SKKS,…) and by vertically integrating along the travel path ($a = \Sigma h$):

$$\bar{dt} = \sqrt{\left(\int_0^a \sqrt{\frac{\rho}{L}\frac{G_c}{L}}\,dz\right)^2 + \left(\int_0^a \sqrt{\frac{\rho}{L}\frac{G_s}{L}}\,dz\right)^2}$$

$$\bar{\phi}_{fast} = \tfrac{1}{2} \arctan\left(\frac{\int_0^a \sqrt{\frac{\rho}{L}\frac{G_s}{L}}\,dz}{\int_0^a \sqrt{\frac{\rho}{L}\frac{G_c}{L}}\,dz}\right)$$

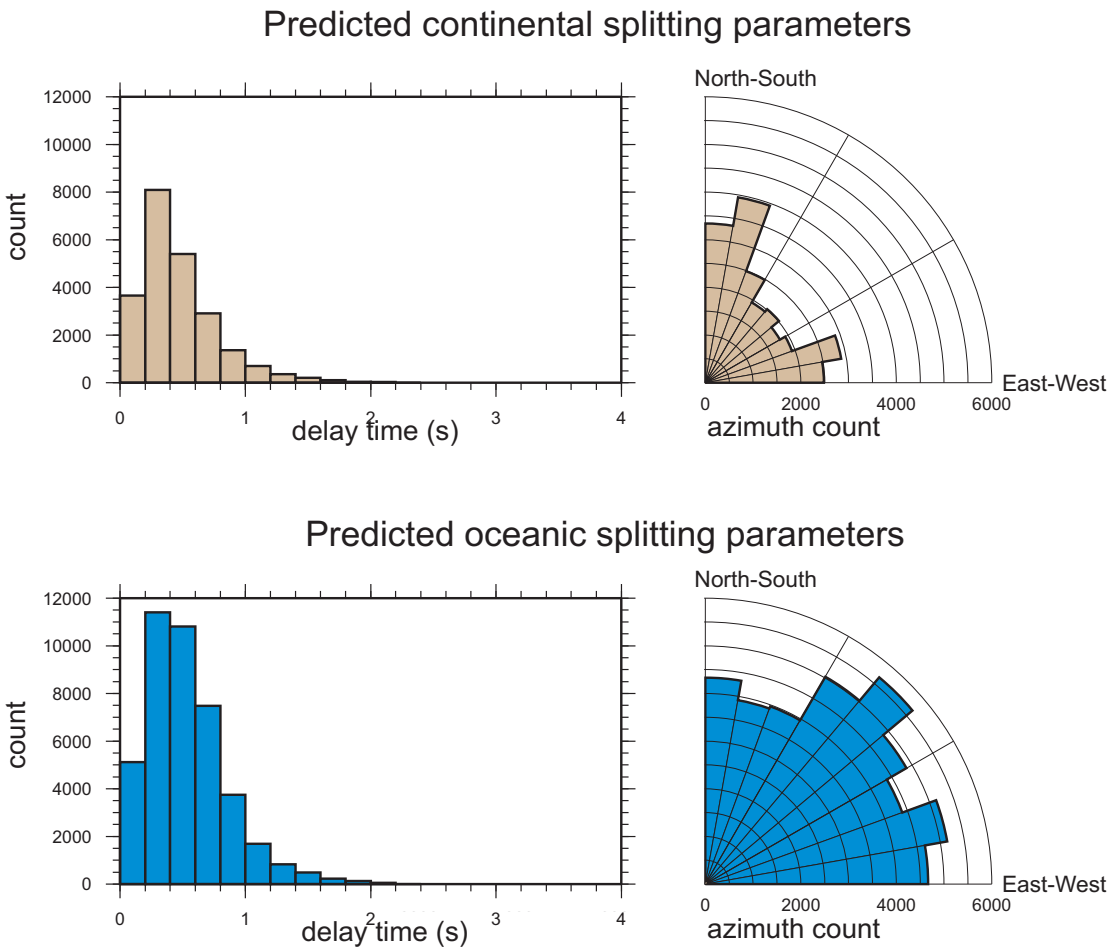

Figure 37: Predicted splitting parameter distribution, calculated from surface wave anisotropy [Debayle et al., 2005] and separated for continents (top) and oceans (bottom). The delay times are systematically smaller than the observed values.

This approach leads to systematically smaller delay times than the observed (Figure 36; Figure 37), which might be due to the damping applied during inversion of surface wave data, low lateral resolution of surface wave and/or to incompatibilities between the assumptions of anisotropy systems inherent to both methods. Many of the predicted continental fast orientations are in contrast to the observed orientations N-S oriented. These appear to be the azimuths from Africa, north-east Asia and Australia (Figure 38), where station coverage is only poor. Predicted oceanic fast orientations are rather uniform.

It is now possible to perform the comparison with a much bigger dataset (2286 measurements from 122 references) of the shear wave splitting dataset presented in the previous Chapter. These data are compared (Figure 38) with the predicted splitting values based on the recent 1°x1° global surface wave model of Debayle et al. [2005] from depths of 50-500km.

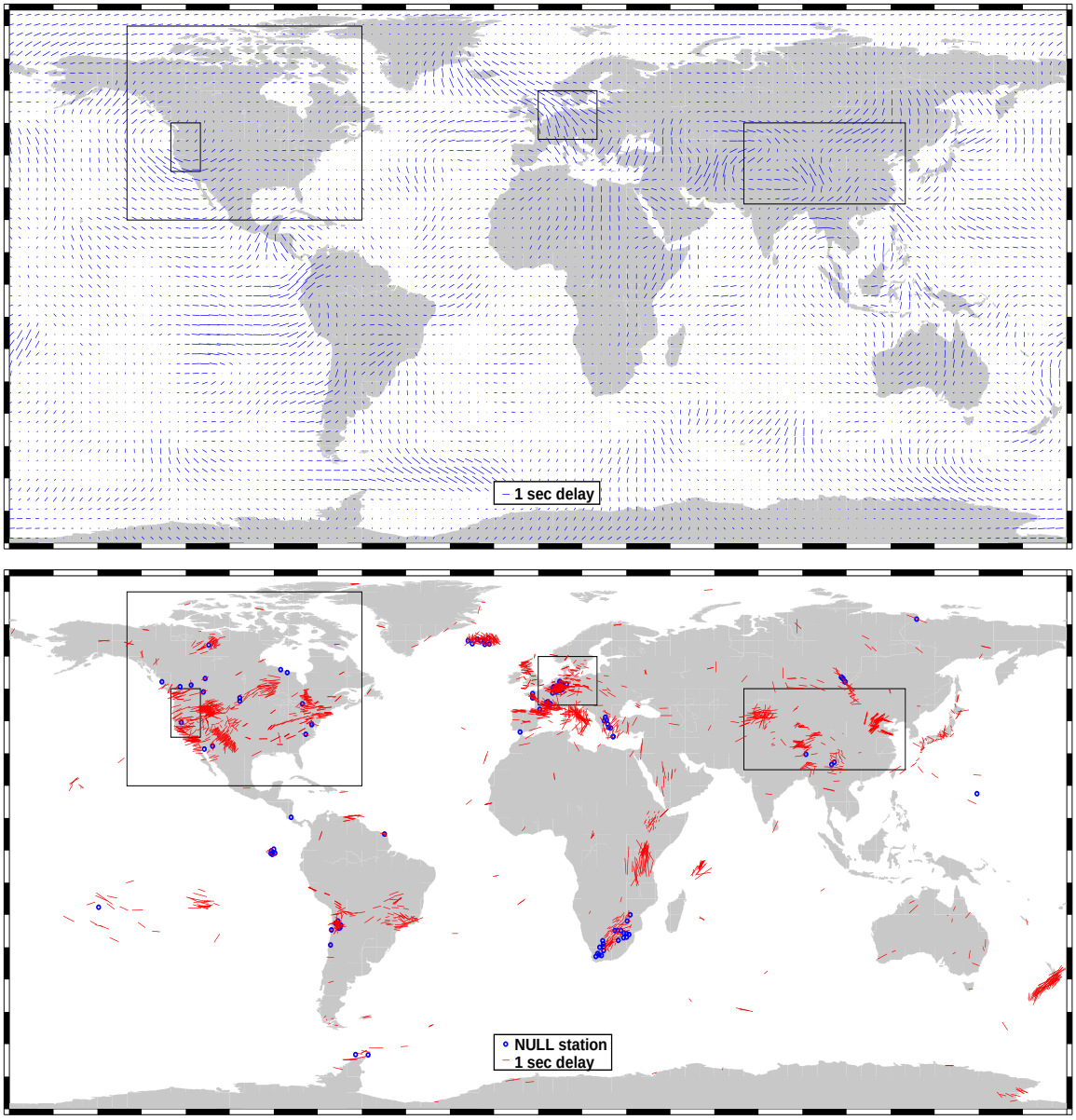

Figure 38: Comparison of predicted (upper panel) with measured (lower panel) shear wave splitting parameters. The predicted values are calculated using the method of Montagner et al. [2000] on the 1°x1° anisotropic tomography model of Debayle et al. [2005] at depths between 50 and 500km. Displayed is the 3°x3° resolution. Note the patches of similar predicted splitting parameters (e.g., Scotia Plate, Himalaya, off-coast California, Central Europe, …). This might reflect large scale structures made visible only through the vertical integration.

A mathematical measure of correlation between those two models can be obtained by using the coherence function similar to Griot et al. [1998a, 1998b]. This function gives a measure of misfit between two models while taking into account two parameters (Φ_1, dt_1; Φ_2, dt_2) on a sphere (co-latitude Θ, longitude Ψ). A correlation factor D_{corr} takes into account the uncertainty of both datasets. Parameter α corresponds to the mean angular misfit of the datasets and varies between -90º and +90º.

$$C(\alpha) = \frac{\int\int_{\Theta\Psi} \left\{ dt_1(\Theta,\Psi) * \sin\Theta * dt_2(\Theta,\Psi) * \sin\Theta * \exp\left(-\frac{(\phi_1(\Theta,\Psi) - \phi_2(\Theta,\Psi) + \alpha)^2}{2D_{corr}^2} \right) \right\} d\Theta d\Psi}{\sqrt{\int\int_{\Theta\Psi} dt_1(\Theta,\Psi)^2 * \sin^2\Theta d\Theta d\Psi} \sqrt{\int\int_{\Theta\Psi} dt_2(\Theta,\Psi)^2 * \sin^2\Theta d\Theta d\Psi}}$$

If the shape of *C(α)* is pseudo-gaussian, there is an overall coherence of the two models. The major peak corresponds to the mean rotation between the models. If *C(α)* is represented by an horizontal line, the two models are uncorrelated.

Unfortunately, the splitting measurements are not homogeneously distributed across the globe (Figure 38). One approach to overcome this can be by interpolating the splitting measurements on a regular grid. However such spherical interpolation of very sparse two-parameter data is not trivial [Bird & Li, 1996]. Therefore, here we follow the approach by Montagner [2000] and interpolate the regular grid of the tomographic anisotropy model to the location of each splitting measurement. By doing this, local studies with dense station coverage are emphasized in the global result.

Montagner et al. [2000] compared splitting parameters as predicted by a global tomographic anisotropy model [Montagner & Tanimoto, 1990] with the shear wave splitting results compiled by Silver [1996]. The result indicated fairly good coherence on a regional scale (Cascadia Mountains and Central Asia), but only weak coherence on a global scale. The authors attribute the latter to: 1) different distribution of sensitivity in the datasets. Surface waves are best resolved in oceanic environment, where coverage of shear wave splitting measurements is only sparse. 2) most splitting data are only inverted for a single layer of anisotropy, which appears to be an oversimplification [Chapter 3.3]. And 3) a difference in (lateral) resolution: SKS waves reflect small-scale structures, while surface waves largely integrate.

Here, the recent tomographic model of Debayle et al. [2005] is used as basis to calculate the predicted splitting parameters. Figure 39 shows the coherence of this model (50-500km depth) with the new splitting database (2286 measurements, 122 references). There is an overall fit, indicating that shear-wave splitting measurements and surface wave anisotropy studies are actually sensitive to similar constraints. a) shows the coherence of a 1° grid with itself, while in b) the coherence of a 1° grid with a 10° grid is displayed. Both agree well, which indicates that resolution is of minor importance in this sort of application. This is probably due to the resolution of 400km of the surface waves used as a basis of the predicted splitting. However, a difference is apparent when comparing the real splitting data with a 1° grid (c) and a 10° grid (d). The former shows a rather good fit for all correlation lengths, which is in contrast to Montagner et al., [2000].

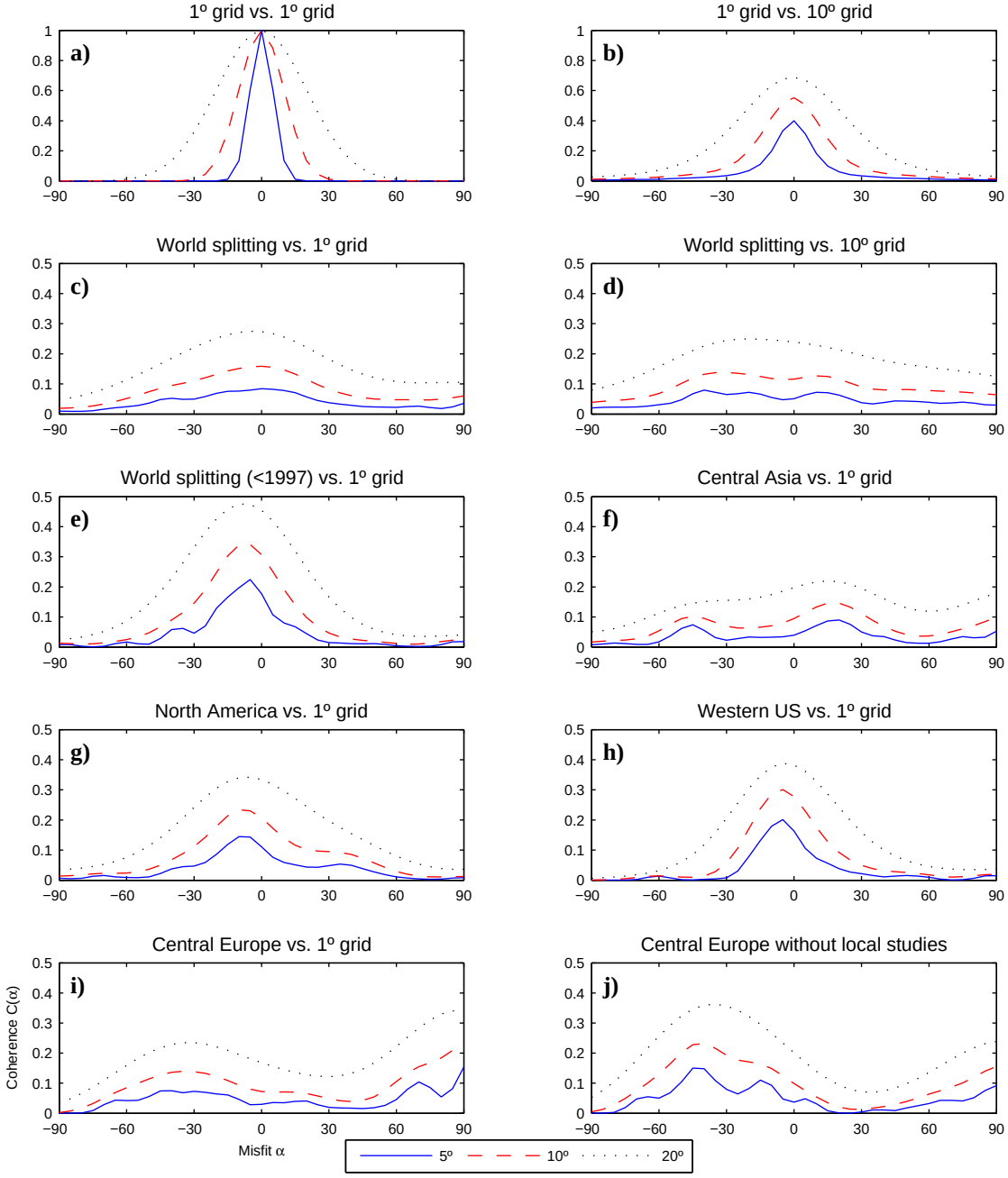

Figure 39: Coherence of splitting database with predicted splitting values for different correlation lengths Dcorr. Several combinations of datasets are tested, such as the effect of a 1° and 10° grid of predicted values (a-e) and a limited set of data (e: studies published before 1997, corresponding to dataset of Silver [1996]). Finally the dataset is limited to certain regions (f-j). See text for discussion

Montagner et al. [2000] used the splitting data collection of Silver [1996]. In Figure 39 e) this dataset is simulated by using only the splitting publications before 1997. The coherence function is still rather broad, but has a clear maximum around 0° misfit. The higher correlation of the sub-dataset of Silver [1996] in comparison to the new global set (e and c, respectively) is probably due to a larger amount of regional studies with a large amount of stations over a relatively small area (e.g., Eifel region; [Walker et al., 2005];

Pyrenees [Barruol et al., 1998]). Any local deviation from the predicted value with a high station coverage biases the global correlation.

The new dataset of this study indicates good correlation between the two models for North America (g; 70°<Long<125°; 20°<Lat<90°). Montagner et al. [2000] observed a rotation of +30º of the two models against each other in the Western US (-125°<Long<-115°; 30°<Lat<50°). In this region, the coherence of the new datasets has improved (h), due to a larger amount of splitting data (109 vs. 47 available in 1996), but perhaps also due to the different model used in this study. The new results indicate a slight rotation (-5º) between the two models in this region. It is somewhat astonishing that surface waves and shear wave splitting "see" the same anisotropic structures when regarding the complex tectonic in this region.

In contrast, for Central Asia (-140°<Long<-60°; 25°<Lat<50°) the new model seems to be less coherent (f). We have 250 measurements in this region, in comparison with 33 available before 1997. Two peaks can be observed: one at +25º and another at -45º. Montagner et al., [2000] used a local high-resolution tomographic model [Griot et al., 1998] was as basis for calculating predicted splitting. The models seem to be rotated by 20°. When Montagner et al., [2000] considered only the depth interval of 80-200km the coherence improved and the rotation reduced to 10º. The discrepancy between the datasets highlights the importance of local high- resolution tomography. Furthermore, more data do not necessarily imply better coherence. Local studies might bias the coherence function. In future approaches the effect of different data density should be considered in greater detail, possibly by normalizing per area.

This can be shown for the dataset of Central Europe (0°<Long<20°; 45°<Lat<60°). The whole dataset for this region contains 179 measurements. The coherence is rather weak (i), although slight maxima can be identified for -35º and 90º. In general, east of approximately 12ºE the fit is good, while west of that line the two datasets are almost perpendicular (Figure 40). Apparently, surface waves are dominated by an anisotropic structure not seen by SKS waves. This can be either vertical anisotropy or shallow features in the upper mantle. When neglecting local studies (the Eifel region [Walker et al., 2005] and the French Massif Central [Barruol & Garnet, 2002; Babuska et al., 2002]), the total of measurements in this region reduce to 92. The coherence is more pronounced (j) and it becomes clear now that the predicted splitting model in this region is rotated against the observed splitting by -40º.

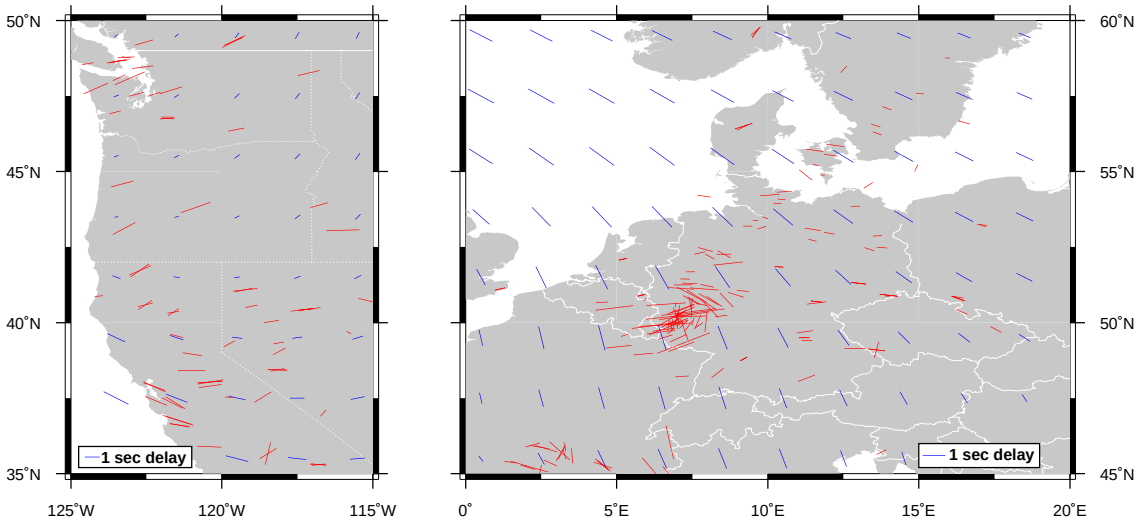

Figure 40: Predicted (blue) and observed (red) shear wave splitting data in the Western US (left) and in Central Europe (right). In the Western United States the coherence is rather good. The fit in Central Europe improves, if local studies in the Eifel Region and the Massif Central are neglected. In general, east of approximately 12ºE the fit is good, while west of that line the two datasets are almost perpendicular.

Figure 41 shows the coherence of predicted with observed splitting parameters at various depth intervals of the tomographic model. On a global scale (left column), the coherence shows only slight variations with depth interval. This reflects the various tectonic regimes and probably also the variety of lithospheric thickness within the continents, where most splitting data are located. The varying continental lithospheric thickness makes it difficult to constrain one (globally valid) depth interval, at which anisotropy originates, be it asthenospheric or lithospheric.

In contrast, by considering only particular regions it is possible to constrain the depth at which splitting probably originates. In the Western US (middle column in Figure 41) the coherence is very good, if only the upper 200km are considered. The depth interval of 200-500km shows two distinct peaks at -30º and 30º, respectively. This indicates no correlation with the surface wave tomography model of the observed shear wave splitting data. Rather, the observed splitting occurs in the upper 200km.

For Central Europe (right column in Figure 41) the coherence is only week for the uppermost 250km. Strongest coherence is found for the depth interval 200-350km, albeit with a relative rotation of both models of -35º. Montagner et al. [2000] attribute a similarly systematic rotation in Central Asia with different lateral averaging of the two methods. It might also indicate that the usual assumptions of relatively weak anisotropy with horizontal axis of symmetry are not fulfilled in certain regions.

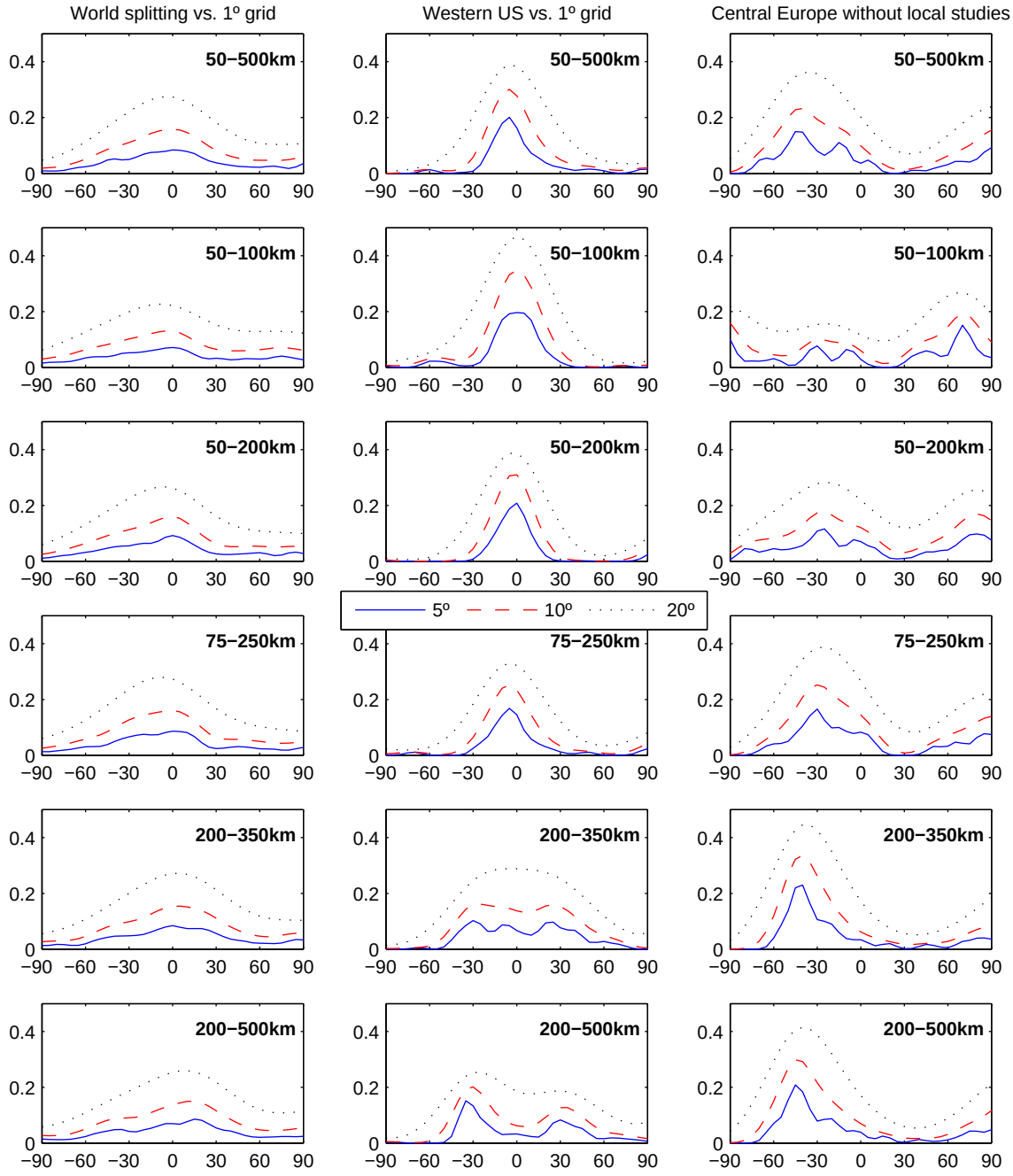

Figure 41: Coherence of predicted with observed splitting parameters at various depth intervals. Left columns show global coherence, middle column coherence for Western US and right column for Central Europe at the six depth interval indicated in the panels.

In conclusion, the results of shear-wave splitting measurements and surface wave anisotropy are globally consistent in fast orientations. The vertical integration of upper mantle anisotropy deduced from surface waves (good vertical resolution) reproduces shear wave splitting measurements (good lateral resolution). This agreement of two different methods with different resolutions highlights the quality of techniques and data used. If both methods “see” the same structures, the upper mantle must be homogeneous over longer (horizontal) distances. Local tectonic processes (e.g., Central Europe) may however

result in substantial systematic deviations. Finally, variations with depth of anisotropy detected by surface waves should be considered when interpreting shear wave splitting data (multi-layer case). The predicted delay times still are smaller than the observed. Perhaps lower mantle anisotropy contributes a not negligible amount of splitting.

There is still only a limited amount of splitting measurements in the oceans. Future (continuously recording) Ocean Bottom Seismometers will eventually enhance coverage with splitting measurements and thus allow for a separate analysis of continents (having a thick lithosphere, with sometimes ancient anisotropy orientations) and oceans (having a much simpler history). It might be also interesting to compare other datasets (World Stress Map, various plate motion reference systems, …) with the predicted shear wave splitting dataset, but this lies beyond the scope of this study.

5. Application: Shear-wave splitting on the East European Craton

The previous chapters highlighted the technical aspects of measuring shear-wave splitting. The Null Criterion provides an objective measure to distinguish Nulls from non-Nulls, which is especially challenging in regions with low anisotropy. SplitLab was developed to handle complex and non-uniform datasets. In this context the East European Craton (EEC) is an ideal area with seismic broadband stations operated by several organizations (IRIS, Geofon, NARS) and data formats. Data are available for various time spans, ranging from 15 years (KIEV) to 18 months (NE53). Previous studies [Silver & Chan, 1988, 1991; Vinnik et al., 1992; Helffrich et al., 1994; Dricker et al., 1999] indicate low anisotropy beneath the EEC with delay time generally smaller than 1 second. Using SplitLab and the Null Criterion it is possible to obtain consistent results for this "virtual experiment".

The choice of the EEC as study area is also motivated by a growing scientific interest in this region [Bogdanova et al., 1996; Thybo et al., 2003, Grad et al.; 2003; Bruneton et al., 2004; Matzel & Grant, 2004; Bogdanova et al., 2006; Vecsey et al., 2007]. Moreover, cratonic areas are currently getting special attention for their shear wave splitting structure [see Fouch & Rondenay, 2006 for a review]. Their thick lithospheric roots are thought to deviate mantle flow [McKenzie, 1979; Bormann et al., 1996, Fouch et al. 2000]. Shear wave splitting Φs in Europe align both with surface geologic features and with the margins of the EEC, which might reflect (asthenospheric) mantle flow around the Craton.

Such pattern can also be identified in anisotropy orientations inferred from P-wave travel times [5.4.2; Figure 50]. Bokelmann [2002] used P-waves anisotropy to infer dipping anisotropy in the North American Craton. This dip is interpreted as being related to shearing at the base of the lithosphere caused by relative motion of lithosphere and asthenosphere. Detecting dipping anisotropy in shear wave splitting is challenging and

requires good backazimuthal coverage, since it results in a complex backazimuthal pattern of splitting parameters [see Brechner et al., 1998].

One of the major question in geodynamics remains at which depth the measured anisotropy occurs [for reviews see Montagner, 1998; Mainprice et al., 2000; Kendall, 2000; see also Chapter 3.3]. In contrast to surface wave studies, shear wave splitting data have excellent lateral resolution, but no (direct) vertical resolution, since the splitting parameters reflect the integrated anisotropy along the travel path. The depth at which splitting occurs can however be inferred indirectly: Qualitatively in the case of multi-layer anisotropy by assessing the typical backazimuthal variation of splitting parameters [Silver & Savage, 1994; Rümpker & Silver, 1998; Saltzer et al., 2000]. An argumentative approach includes correlation with other observables: A large-scale uniform distribution of anisotropy orientations which correlate with plate motion direction strongly support asthenospheric origins. In contrast, regionalized orientations of anisotropy, which correlate with surface-geologic features, indicate lithospheric origins (if vertically coherent deformation throughout the lithosphere and crust is assumed [Silver, 1996]). Conrad et al. [2007] argue, that the former dominates in oceanic environments and thus reflecting present-day processes [e.g., Montagner, 2002, Behn et al., 2004; Hammond et al., 2005; Fontaine et al., 2007], while the latter case appears to be exhibited in (the stable part of) continents, showing frozen-in anisotropy. Gung et al., [2003] interpret the presence of $V_{SH}>V_{SV}$ anisotropy beneath continents at depths between 200km and 400km as an indicator of present day simple shear. This would be consistent with some shear-wave splitting studies, which propose a two-layer anisotropy, one frozen-in in the upper layer, and a deeper layer, related to ongoing processes [e.g. Levin et al., 1999; Fouch et al., 2000; Heintz & Kennett, 2006]. Studying seismic anisotropy in cratonic regions gives an almost unique possibility to analyze deformation processes in the mantle. It is aimed at addressing the following major questions of geodynamics:

- how is mantle flow affected by such a deep and cold obstacle to flow
- how did the lithosphere develop and deform
- how does the topography at the base of the craton affect mantle flow
- is there evidence for multi-layer (asthenospheric plus lithospheric) anisotropy
- how and to what extent do abandoned rifts affect the splitting measurements?
- Is the whole lithosphere affected, or only part of the keel (in the case of lithospheric anisotropy)?

Measuring shear wave splitting can add valuable information to answer some of these questions.

In this part of the thesis I will start with an introduction to the formation of cratons, followed by a review of shear wave splitting interpretations of the major cratons of the Earth. The third part of this Chapter summarizes the geology of the East European Craton, and the fourth part the available geophysical datasets. The results of the shear wave splitting measurements for the 16 analyzed stations is compared with other datasets and then followed by their interpretation in their corresponding regional context. I will conclude with an outlook for future research.

5.1. Structure of cratons

Cratons are the old, Archean and Proterozoic, parts of the continents. Cratons are generally found in the interiors of continents and are characteristically composed of ancient crystalline basement crust of felsic igneous rocks. They have a thick crust and deep roots that extend into the mantle beneath depths of 200 km. The present day distribution of cratonic regions around the globe is shown in Figure 42.

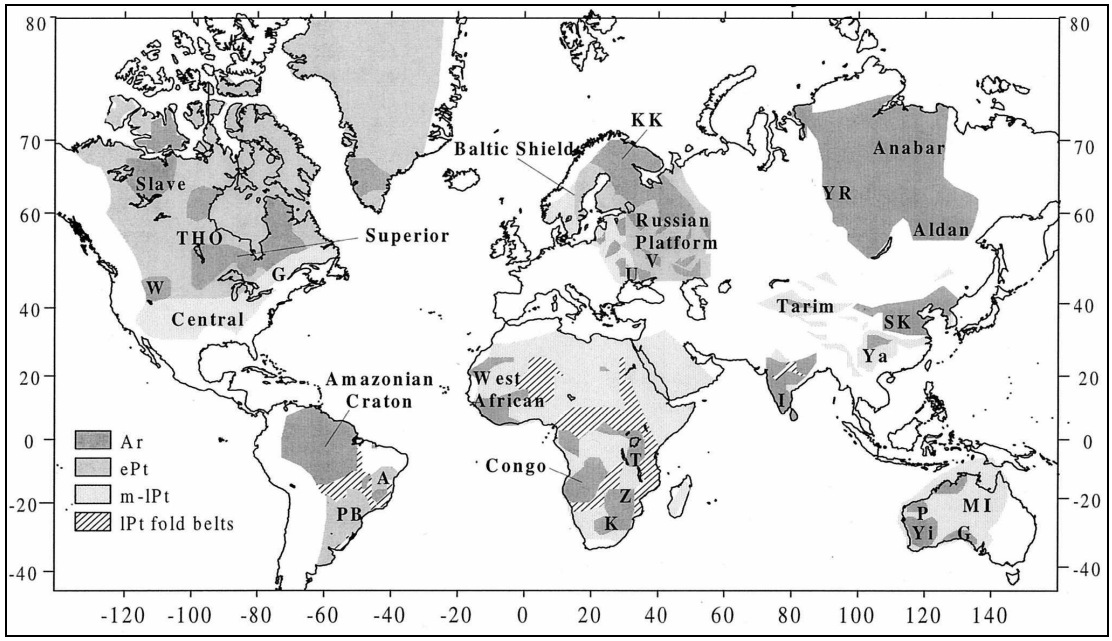

Figure 42: Archean (Ar) and Proterozoic (ePt, early Proterozoic; m-lPt, middle to late Proterozoic) regions of the world (based on data compiled from Goodwin [1996]) and adjacent tectonic structures of different ages considered in the present study. A, Atlantic Shield; G, Gawler Craton; Gr, Grenville Province; I, IndianShield; KK, Kola-Karelian province; K, Kaapvaal Craton; MI, Mount Isa Orogen; P, Pilbara Block; PB, Parana Basin; SK, Sino-Korean Craton; T, Tanzanian Craton; THO, Trans-Hudson [after Artemieva & Mooney, 2001].

Cratons are relatively flat, stable regions that have remained undeformed since Precambrian times, forming the ancient (<1.6Ga) cores of the continents. It is clear that a buoyant root is necessary for the long term survival of a craton [Jordan, 1978; 1981]. Moreover, to resist erosion the root must also be either strong enough to survive

mechanical erosion [Sleep, 2003], or tectonic mobile belts are required to shield the cratons from high mantle stresses [Lenardic et al., 2000].

Several basic models exist to explain the structure of cratons: Snyder et al. [2003] image beneath the Slave Craton (Northern Canada) a deep mantle discontinuity that is interpreted as the continuation of a shallow-dipping ancient subducted slab. The interpretation leads to the hypothesis that cratons form as a result of near-vertical stacking of segments of subducted lithosphere. Such interpretation is supported by Re-Os dating in peridotites [Shirey et al., 2001].

A second hypothesis assumes progressive cooling since the initial formation of first stable platforms. Such a hypothesis however contradicts the present keel structure as such model would implicate a much thicker lithosphere than the observed [King, 2005]. Global seismic tomography studies find fast seismic velocities beneath cratons in the depth range of 200-350km [e.g., Becker & Boschi, 2001; Shapiro & Ritzwoller, 2002; Debayle et al., 2005]. Gung et al. [2003] relate discrepancies between different tomographic models in the depth range of 250-400km to the different sensitivity of anisotropy to different type of data. They also stress that temperatures in this depth range exceed 1000ºC, which is too high to sustain frozen anisotropy and thus implies the detected $V_{SH} > V_{SV}$ anisotropy to be related to ongoing mantle deformation processes. These processes are similar beneath continents and oceans, while for the latter the depth range is located thinner (80-200km depth).

The vertically integrated travel times of vertically polarized shear-waves (S_V) can be seen as a proxy for the lithospheric thickness. Figure 43 shows the S_V travel time residuals over the globe [Poupinet et al., 2003]. In orogenic and rift regions, these residuals are positive, indicating slow (and thus warmer) material. On shields S delays are negative, indicating cooler material. Figure 43 shows increasing delays from the centre of shields outwards.

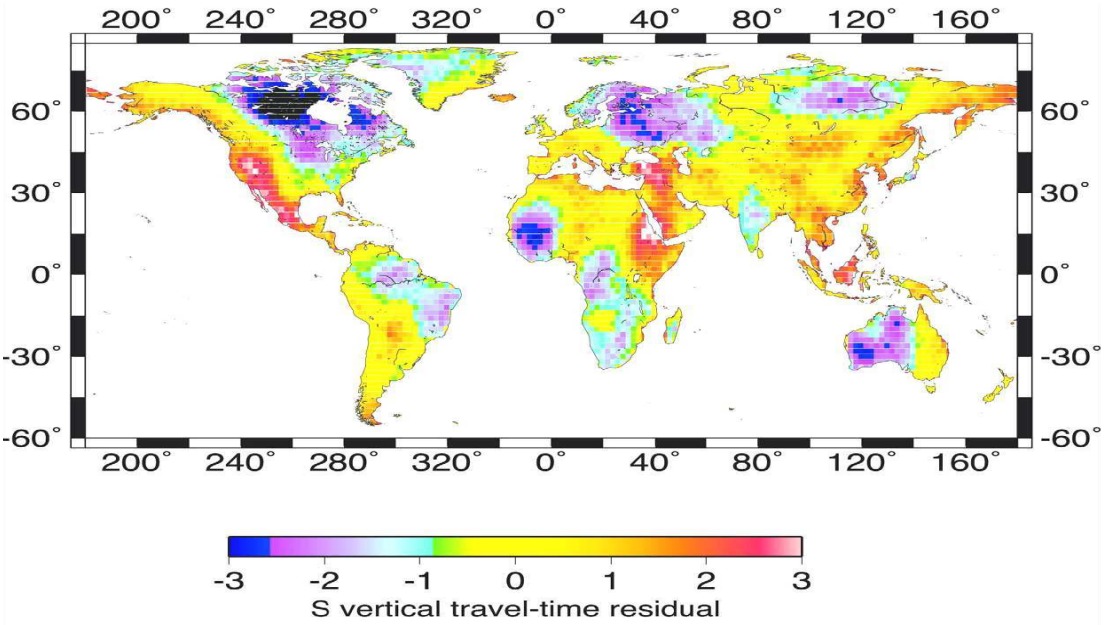

Figure 43: Map of one-way S_V travel time residuals deduced from surface-wave tomography [Shapiro & Ritzwoller, 2002] (after Poupinet et al., [2003]). The blue color represents early arrivals (and thus cooler material) and the late arrivals (warmer). The magnitude of the residual is inverse proportional to the lithospheric thickness. All Precambrian shields are fast and the S-vertical travel time increases regularly outwards from the centers of shields.

Artemieva [2006] presents a global thermal model based on numerous heat flow measurements (Figure 44). The surface heat flow is composed of conductive components (caused by basal heating of the lithosphere due to convection) and internal heating (originating from radioactive decay). Approximately half of the surface heat flow in the continents can be attributed to radioactive decay [Turcotte & Schubert, 2002].

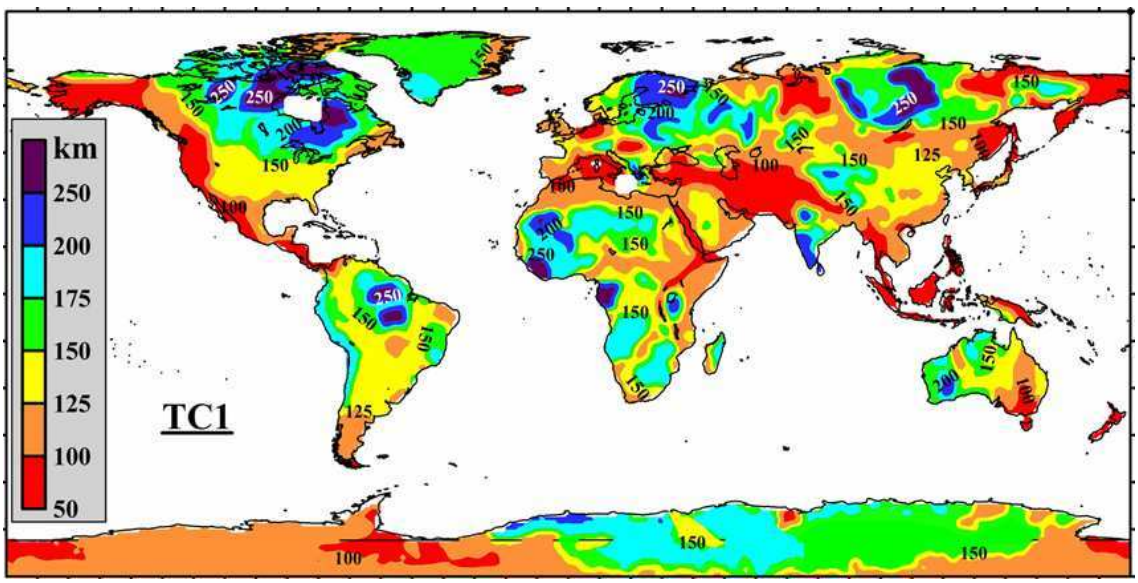

Figure 44: Global lithospheric thermal thickness interpolated with a low-pass filter. The values are based on typical continental geotherms and the age of the basement (after Artemieva [2006]).

Since this heat production decreases with age, the surface heat flow correlates with age. The cratons are the oldest parts of the lithosphere and show low heat flow values (Figure 45), indicating cold and thus denser material. Since these regions show few signs of significant subsidence, the upper mantle beneath them must be naturally buoyant: depletion in Fe compensates the effects of thermal cooling on density [Jordan, 1981]. King [2005] argues however that it seems be highly improbable that a compositional changes would exactly balance thermal cooling trough time at all depths.

Xenolith analyses infer a chemically depleted mantle extending to 175km depth, underlain by a more fertile mantle [Boyd et al., 1985; Kopylova et al., 1999]. Other geochemical observations suggest that cratons are cold, dehydrated and the residue of partial melting [Pearson et al., 2002; Arndt et al., 2002], while metasomatic activity could influence viscosity. The viscosity in turn affects the strain-depth profile and thus the re-orientation of anisotropic minerals [Tommasi, 1998]. From electrical conductivity measurements [Hirth et al., 2000] it is known that mantle in 150-250km is drier over Archean provinces than oceanic mantle.

Geochemical and geothermal data can be balanced by assessing geomagnetic data. The "Curie Temperature" can be considered as the thermal boundary, above which magnetization of the material is lost. For rock magnetism, the most important mineral is Magnetite (Fe_3O_4) with a Curie temperature of 578ºC. Figure 45 shows the depths to the 550ºC isotherm [Artemieva, 2006]. Beneath cratons this transition is relatively deep (40-70km). This indicates that, if crust and upper mantle deform coherently, structures reflected by magnetic intensity anomalies can possibly be extrapolated to these depths.

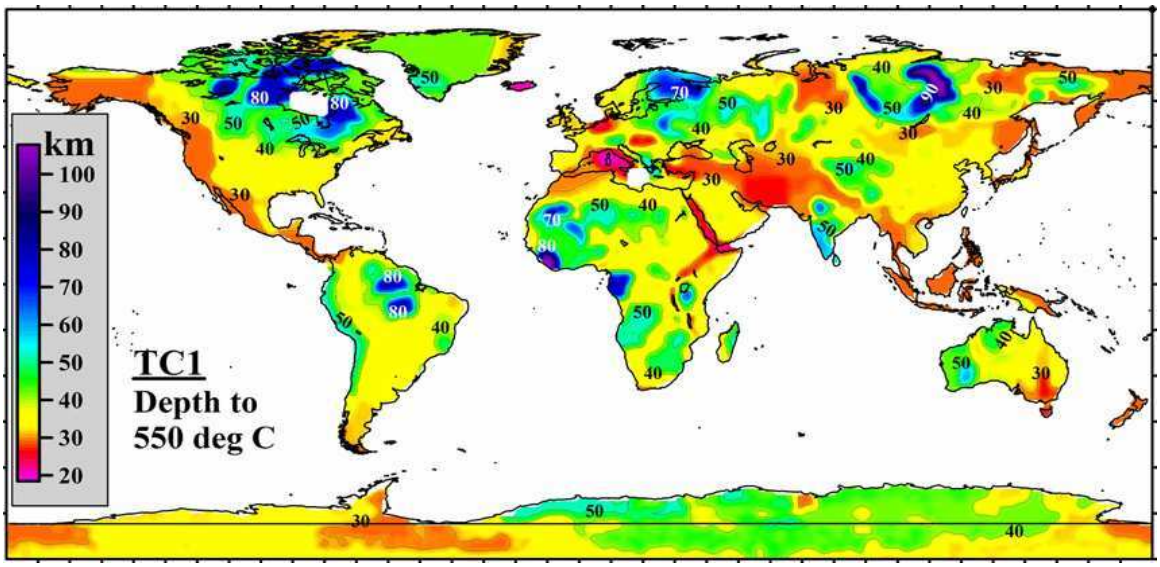

Figure 45: Global thermal model for the continental lithosphere constrained on a 1ºx1º grid: depth to the 550ºC isotherm interpolated with a low-pass filter [Artemieva, 2006].

5.2. A short review of Shear-wave splitting in stable continental environments

The following subchapter will briefly summarize interpretations of shear-wave splitting measurements in cratonic environments around the globe. The terminology used in many publications for a shear-waves splitting result is variable: often “fast axis”, “fast orientation”, “fast direction”, and “fast (S-wave) polarization” refer to the same observable, whose exact description would be “*orientation of the fast S-wave polarization plane*”. In order to improve readability, in the following this orientation is denoted with Φ.

5.2.1. Australia

The shear-wave velocity pattern beneath the Australian continent is marked by a distinct velocity contrast. This NS trending contrast is approximately parallel to the proposed Tasman line, a contact zone dividing the (relatively thick) Precambrian western and the (thinner) Phanerozoic eastern part of Australia [e.g. Debayle & Kennett, 2000a]. This feature can be compared to the Trans-European-Suture-Zone (TESZ) [Chapter 5.3.2]. Simons et al. [2002] found good correlation between surface wave speed heterogeneities and lithospheric ages. However, below 250km this correlation becomes more ambiguous.

Debayle & Kennett [2005] found that Australia is the only continent where azimuthal anisotropy (inferred from surface waves) correlates well with present day absolute plate motion. This correlation is most significant at depths between 150 and 300km.

Heintz & Kennett [2005, 2006] analyzed two years of shear-wave splitting data of a temporary seismic experiment, covering the whole Australian continent. Their preliminary results reproduce the surface geologic features, hinting to fossil deformation as the cause of anisotropy. However, the whole dataset contains many Null measurements from a broad range of backazimuths, suggesting apparent isotropy at these stations. Silver and Savage [1994] point out, that apparent isotropy is consistent with a simple two-layer model, where the two layers exhibit the same intrinsic anisotropy and mutually perpendicular Φs. In such a case, Nulls are measured from all backazimuths.

Simons et al. [2002] applied the method of Montagner et al. [2002] to predict splitting parameters from surface wave data of Australia. The correlation is only weak and predicted splitting times are considerably large. They inferred furthermore, that the depth interval of 140 to 400km, presumably the asthenosphere, contributes the most to the predicted splitting parameters.

At some of the Australian stations clear evidence was found for either EW or NS oriented anisotropic Φs. These findings are consistent with a two-layer model of perpendicular anisotropy orientation in each layer. The anisotropic Φ of the lower layer is roughly

parallel to the (approximately northward) plate motion direction. This model is supported by surface wave tomography studies [Debayle & Kennett, 2000b], with a change in anisotropy pattern at approximately 150 km depth. Moreover, in a study focusing on the GEOSCOPE station CAN, Girardin & Farra [1998] suggested a two-layer model, where the 140km upper layer has a EW oriented Φ and a 40km thick lower layer with a NS Φ, parallel to plate motion.

5.2.2. South America

Several studies discuss splitting parameters of the South American Continent. For these studies show interesting reslts, the following subchapter will present not only cratonic and (and adjacent) stations, but the continent as a whole.

Helffrich et al. [2002] analyzed stations in South America and associated the Φs to absolute plate motion (APM). They suggest that anisotropy originates from basal drag in a ~200km upper mantle flow layer. Mantle flow would originate from a stagnant geoid high, off-coast Peru and this flow is deviated around the South American Continent, passing through the Drake Passage in the south and the Caribbean in the North. These interpretations are consistent with findings of Russo & Silver [1994] and hypotheses of global mantle flow of Alvarez [1982]. However, this study does not take into account the South Atlantic mantle flow, which would counteract such flow pattern.

A detailed analysis of stations in SE Brazil [Heintz et al., 2003] suggests that both lithospheric and asthenospheric fabrics may contribute to anisotropy pattern. Either the frozen fabric in the lithosphere and the APM related asthenospheric fabric are close enough to mimic a single anisotropic layer, or both fabrics originate from the same tectonic event, and no decoupling occurred since then. Neither of these options can clearly be ruled out. The correlation between structural trends and APM favors the first hypothesis, but tomography identifies a low velocity channel, possibly related to the Tristan da Cunha plume, which is regarded as a strong argument supporting the coherent motion of the whole mantle. A lithospheric contribution is supported by both short-range contrasts and very high anisotropy (dt>2sec) associated to transcurrent domains.

In a more recent study, Assumpção et al. [2006] analyzed anisotropy covering the major tectonic provinces in Central and SE Brazil. They confirm the findings of Heintz et al. [2003] while determining that the Φs fan out towards the west. Such fan-shape pattern would be consistent with asthenospheric flow around the São Francisco Craton, supported by APM direction. Short range contrasts favor lithospheric contributions, as well as very high anisotropy (dt > 2 sec) in the transcurrent domains.

In the central Paraná Basin, where a possible cratonic nucleus has been proposed, small delay times (dt < 1.0sec) but consistently EW Φs are found. This might indicate a different

origin of anisotropy, related either to pre-Brasiliano orogens or to the subsidence and/or evolution of the Paraná Basin. Since however EW anisotropy is not restricted to the cratonic domain, pre-Brasiliano orogenic structures appear as an unlikely source.

High delay times indicate that both lithospheric and asthenospheric anisotropy is present. This is in contrast to southern and eastern Africa (Chapter 5.2.4) where only lithospheric contributions are proposed. One explanation for this contrast in the two related regions might be the difference in absolute plate velocity, which is ~15mm/yr for Africa and ~50mm/yr for South America [Gripp & Gordon, 2002]

5.2.3. North America

The oldest portions of the North American Continent remained stable for more than 2.5Ga while regions to the east (Grenville province ~1.3Ga; Appalachians ~300Ma) and west of the Rocky Mountains are much younger [Hoffman, 1989]. Tomographic studies [Grand, 1994; van der Lee & Nolet, 1997; Debayle et al., 2005] revealed seismically fast (presumable cold) material extending to depth of more than 250km. A common feature to these models is that a wedge, or divot, is missing in the eastern part of the keel [Fouch et al., 2000]. This divot approximately coincides with a low velocity corridor found by Rondenay et al. [2000]. Barruol et al. [1997] pointed out that most shear-wave splitting directions in the eastern US (adjacent to the craton) coincide with geologic trends, also indicating lithospheric origins of anisotropy. They could however not exclude asthenospheric contribution for some of their stations.

Analyzing stations in the central US, Silver & Kaneshima [1993] found that for stations S and SE of the keel the Φs appear to wrap around its lateral margins. This would indicate asthenospheric flow around the keel. However, these directions are also parallel to the general trending of orogenic belts, which might support the hypothesis of vertically coherent deformation. Stations within a divot in the keel are roughly oriented E-W, with lateral variations over short distances. Levin et al. [1999] found that a two-layer model could best fit the complexity of shear-wave splitting measurements in this region. Fouch et al. [2000] propose a model for anisotropy beneath the central US, where asthenospheric flow around the cratonic keel dominates. A divot within the keel apparently disturbs the uniform flow, resulting in variations of splitting parameters of a short spatial scale. Moreover, some regions (especially those with the thickest portion of the keel) require lithospheric anisotropy to explain measurement results.

Anisotropy measurements of the patchwork of Archean and Proterozoic terranes that make up the Canadian Shield vary as do their building blocks. The Slave province in the Canadian north-west is a small Archean craton that shows Φs which are sub-parallel to current plate motion [Bank et al., 2000]. Snyder et al. [2003] re-analyzed the shear-wave splitting data beneath the Slave province with more stations and longer record periods.

They found evidence for a two-layer model, one corresponding to plate motion direction and another thinner layer, possibly aligned with regional crustal folding.

5.2.4. South African Craton complex

The Archean Kaapvaal Craton and the Tanzania Craton form the oldest parts of the south-eastern African continent. The plate motion direction of the African plate is not well constrained, since the plate speed is slow (~10mm/yr in southern Africa) [Gripp & Gordon, 1990, 2002].

The Kaapvaal Craton constitutes of several geologic entities, with the oldest parts generally in the east and younger parts in the west [de Wit et al., 1992] all of which were assembled during late Archean Eon (~3.6-2.6Ga). Vinnik et al. [1996] analyzed a set of seven portable broadband stations across the Kaapvaal Craton and found Φs parallel to the HS1-Nuvel1A plate motion direction [Gripp and Gordon, 1990], with delay times systematically larger than 1 sec for the south-western stations and smaller than 1 sec for the north-eastern stations. This pattern correlates with the number of Jurassic kimberlite intrusions. Vinnik et al. [1996] suspect that volatiles could affect both the formation of kimberlites and intensify the recrystalisation of olivine and thus anisotropy. They conclude that seismic anisotropy beneath the Kaapvaal Cratons is primarily related to asthenospheric shear related plate motion.

In contrast, Silver et al. [2001] and Gao et al. [2002] analyzed a total of 80 stations. They point out that the Φs do not correlate with newer plate motion directions of Gripp and Gordon [2002]. The splitting direction correlates however very well with regional geologic trends, suggesting lithospheric origins of anisotropy. This interpretation is supported by surface wave studies [Freybourger et al. 2001; Saltzer, 2002]. Furthermore, a high-density array of 35 station in the Kimberly region found small scale variations in shear wave splitting parameters, which can only be explained by lithospheric origins of anisotropy.

The Tanzania region is significantly more complex because it is juxtaposed to the active East African Rift system and possibly to a plume beneath the Craton [Behn et al., 2004]. Walker et al. [2004] suggest complex origin of anisotropy owing to the superposition of active rifting, asthenospheric flow and fossil anisotropy. Off-craton stations show Φs which mimic the shape of the craton boundaries, while on-craton stations show distinctively different directions, parallel to the ENE-WSW structural trend and delay times vary from 0 to 2.0 sec. Station within the craton tended to be more complex. Their results indicate a lithospheric origin of anisotropy, but the complexity in some regions suggests a component of sublithospheric anisotropy possibly related to plate motion. Lithospheric origins of anisotropy are also indicated by strongly anisotropic mantle xenoliths from the Labait volcano [Vauchez et al., 2005].

5.3. Geology of the East European Craton

Shear wave splitting data of the East European Craton (EEC) are analyzed in this study. In order to present the reader an introduction to the region, the geologic framework of the EEC presented here first.

The ancient core of Europe, the East European Craton (EEC) is composed of three major crustal segments: Fennoscandia, Sarmatia and Volgo-Uralia (Figure 46). The EEC is today mostly covered by Phanerozoic sediments. Only in the north-west (Fennoscandian Shield) and parts in the south (Ukrainian Shield and Voronezh Massif) are Proterozoic and older rocks exposed [Gorbatschev & Bogdanova 1993; Bogdanova, 1996].

U-Pb and Sm-Nd ages suggest Palaeoproterozoic ages (2.0-1.8Ga) for Fennoscandia [Huhma et al., 1991; Bogdanova et al., 1994]. Fennoscandia is formed by an Archean nucleus, the Karelian province, and flanked in the northeast by the Palaeoproterozoic Lapland-Kola mobile belt and in the southwest by the Proterozoic Svecofenninan domain [Gorbatschev & Bogdanova, 1993]. The crustal evolution apparently started by early crustal thickening and accretion of lithospheric blocks during late Archean and Proterozoic times. Nironen et al. [2002] propose a succession of five orogenies, alternating with rifting events. Since at least 1.2Ga the central part of Fennoscandia remained stable. In contrast, the adjacent Sarmatia is a stable Archean Craton, created by late Archean / early Palaeoproterozoic welding of several Archean terranes with different ages ranging from 3.8 to 2.8Ga [Shcherback, 1991]. A ca. 2.1Ga volcanic belt and the East Voronezh Province mark the boundary between Sarmatia and Volgo-Uralia. The Archean crust of Volgo-Uralia underwent apparently reorganization into a system of dome-like structures [Bogdanova , 1996]. Sarmatia is characterized by an average crustal thickness of ca 50km.

Between 2.1Ga and 2.0 the oceanic domain, which was separating Sarmatia from Volgo-Uralia, closed. Simultaneously, subduction started in the (present day) northern edge of Sarmatia and lead to the collision with Fennoscandia at around 1.8Ga. The accretion of the two blocks was completed at around 1.75Ga and accompanied by underplating.

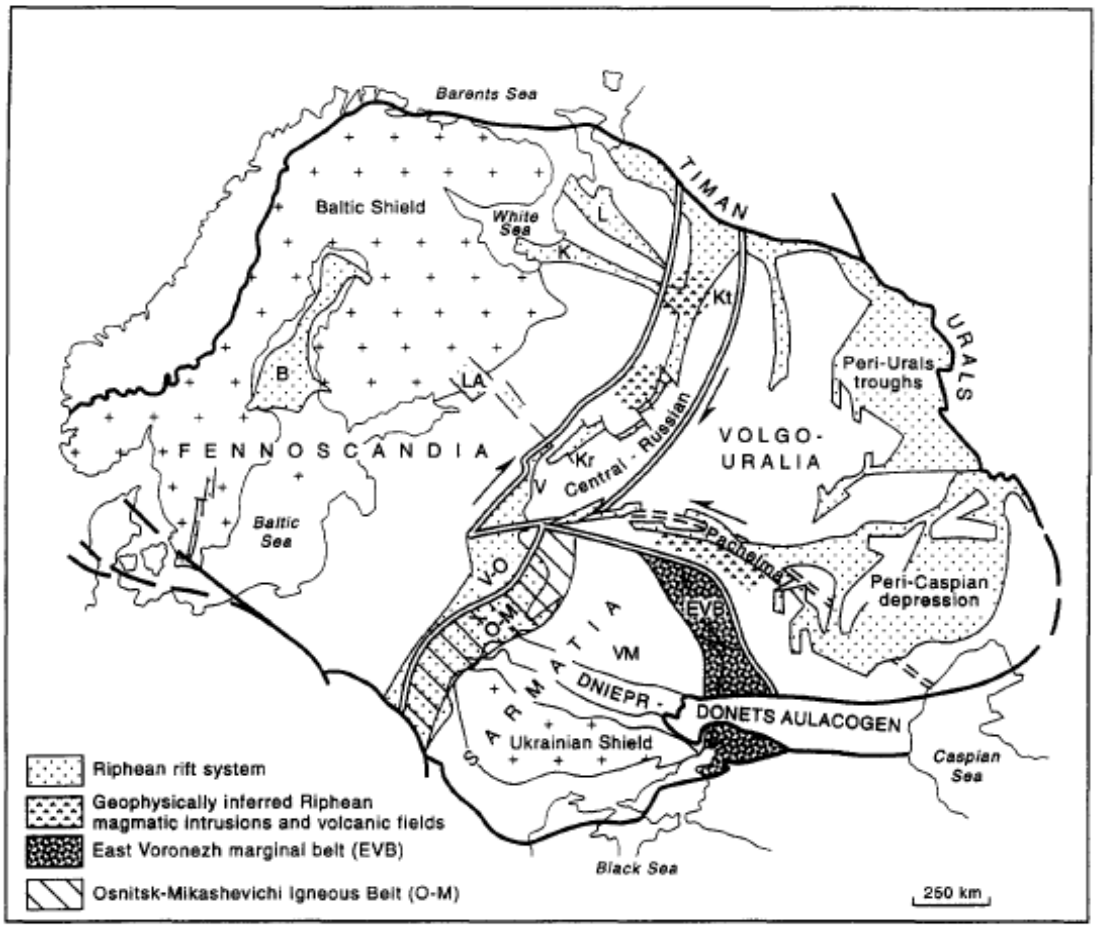

Figure 46: Structural units and rift systems in the East European Craton and their relationships with Palaeoproterozoic intersegment junction zones and boundaries [after Bogdanova, 1996]. Letter symbols are for Riphean troughs: B = Bothnian, K = Kandalaksha, Kr = Krestzy (also Motokovo), L = Leshukonskoye, La = Ladoga-Pasha, V = Valday, V-O = Volhyn-Orsha; for Palaeoproterozoic belts: EVB = East Voronezh Marginal Belt, including the Lipetsk-Losev Volcanic Belt and the East Voronezh Schist Province, and O-M = Osnitsk-Mikashevichi Igneous Belt; Kt = the Kotlas intrusion of presumably Riphean age. Double lines mark the boundaries and transition zones between crustal segments. The Voronezh Massif (VM) is the part of Sarmatia, north of the Dniepr-Donetz Aulacogen. The western margin of the Craton is marked by the TrasEuropean Suture zone (black line in the west)

5.3.1. Central cratonic rift systems

During the Riphean period (1.25-0.8 Ga) assemblage of the three entities Fennoscandia, Sarmatia and Volgo-Uralia was subject of subsequent rifting episodes within the consolidated crust. These riftings occurred mainly along the old suture zones [Bogdanova, 1996]. All large provinces of high crustal magnetization are situated in the periphery of the craton, which is related to mafic igneous activity along the cratonic margin [Bogdanova et al., 1996]. A suite of small failed-arm rifts accompany the major rifts, namely: The late Riphean Volhyn-Orsha trough divides Fennoscandia from Sarmatia and shows purely extensional features. In contrast, the Central Russian rift system is ca. 250km wide and comprised of a series of *en echelon* troughs, showing dextral strike-slip

motion with an extensional component. Finally, the Pachelma rift system is offset by ca 150km to the northwest of the surface trace of the suture. The Pachelma rift system features NW striking, *en echelon* grabens, which can be interpreted as being related to sinistral relative displacement Bogdanova et al. [1996] suggest that during that period Volgo-Uralia acted as a wedge between Fennoscandia and Sarmatia. As such Volgo-Uralia moved to the present west, while Fennoscandia escaped to the present north (Figure 47)

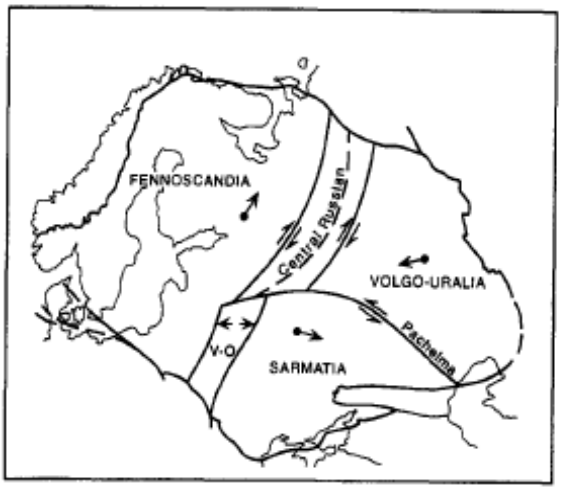

Figure 47: Sketch map of the East European Craton showing hypothetical kinematics of one-time interaction between Fennoscandia, Volgo-Uralia, and Sarmatia during Riphean rifting between 1.4 and 1.1 Ga. [after Bogdanova et al., 1996]

The Dniepr-Donbas aulacogen divided in early Perm the Ukrainian Shield from the Voronezh Massif. It now contains up to 22km of sediments [Zonenshain et al., 1990]. Later profound uplift can be either related to stresses built up by the Hercynian/Uralian orogens or by the activity of an asthenospheric diapir [Chekunov, 1994; Wilson & Lyashkevich, 1996; Grad et al., 2003a; Maystrenko et al. 2003].

5.3.2. The Trans-European Suture Zone (TESZ)

The contact between the Precambrian East European Craton and the Phanerozoic collage of central Europe terranes (Avalonia) is marked by the Trans-European suture zone (TESZ). It is a broad, complex zone resulting from the collision of continental blocks which lasted until the Variscan orogeny [Berthelsen, 1992; Ziegler, 1990; Pharaoh et al., 1997; Grad et al., 2003b]. A deep (up to 10km) basin, parallel to the margin of the EEC, is filled with Permian and Mesozoic sediments as a result of reactivation of the suture in asymmetric rifting. In addition to being a major crustal feature, the TESZ appears to sustain in the upper mantle, as seismic tomography studies separate regions with high S-wave velocities beneath the EEC from low velocity regions beneath the younger terranes [Zielhuis & Nolet, 1994]. The TESZ constitutes of two separate sections: first, the

Teisseyre-Tornquist Zone (TTZ) throughout Poland and passing along the Carpathian Mountains. Second, the Sorgenfrei-Tornquist Zone (STZ) is its northern continuation throughout the Baltic Sea and southern Scandinavia (Figure 46, Figure 48).

A seismic profile crossing the central part of the TTZ (POLONAISE'97, Grad et al., [2003b]) allows two tectonic models for the lower crust and upper mantle. First, a "crocodile-type" collision could have occurred when the EEC indented Avalonia, obducting its upper crust and underplating its lower crust / upper mantle. Such model is supported by the results of other seismic profiles [BABEL working group, 1993; Abramovitz & Thybo, 2000]. The second model assumes that upper mantle material from the EEC underlies the strongly rifted upper crust. The collision would have been relatively "soft". Such model is supported by the lack of deformation within the EEC.

5.3.3. Polish - Lithuanian - Belarus terrane

Bogdanova [2005, and papers therein] points out the strong evidence for a terrane in the area NE of the TTZ and Fennoscandia, comprising NE Poland, parts of Belarus and the Baltic states. According to Bogdanova [2005] geophysical data and drillcore materials in this area identify several tectonic blocks, namely the Osnitsk-Mikashevichi Igneous Belt of NW Sarmatia, the Central Belarus Suture Zone separating Fennoscandia from Sarmatia, the Belarus-Podlasie Granulite Belt with the East Lithuanian Belt, and the West Lithuanian Domain all continue through NE Poland all the way to the TESZ (Figure 48). The evolutionary histories of these belts allow for grouping them into three different subterranes though tectonic reconstruction and age determination remains imprecise.

The Belarussian-Baltic Granulite Belt and the East Lithuanina Belt feature both prominent gravity and (surface) magnetic highs, which trend NNE throughout Belarus, Poland and Lithuania, while swinging EW in Estonia. In contrast, the West Lithuanian Belt is characterized by EW trending gravity and magnetic anomalies.

Bogdanova [2005] suggests that the rocks of the Mazowsze, Ciechanów, Dobrzyn ect. domains should be combined with those of the West Lithuanian Granulite Belt into one single terrane with ages less than 1.85 Ga. Zircon U-Pb ages in the West Lithuanian Belt and in the Mid-Lithuanian Suture Zone [Skridlaite et al., 2003] appear to support such correlation.

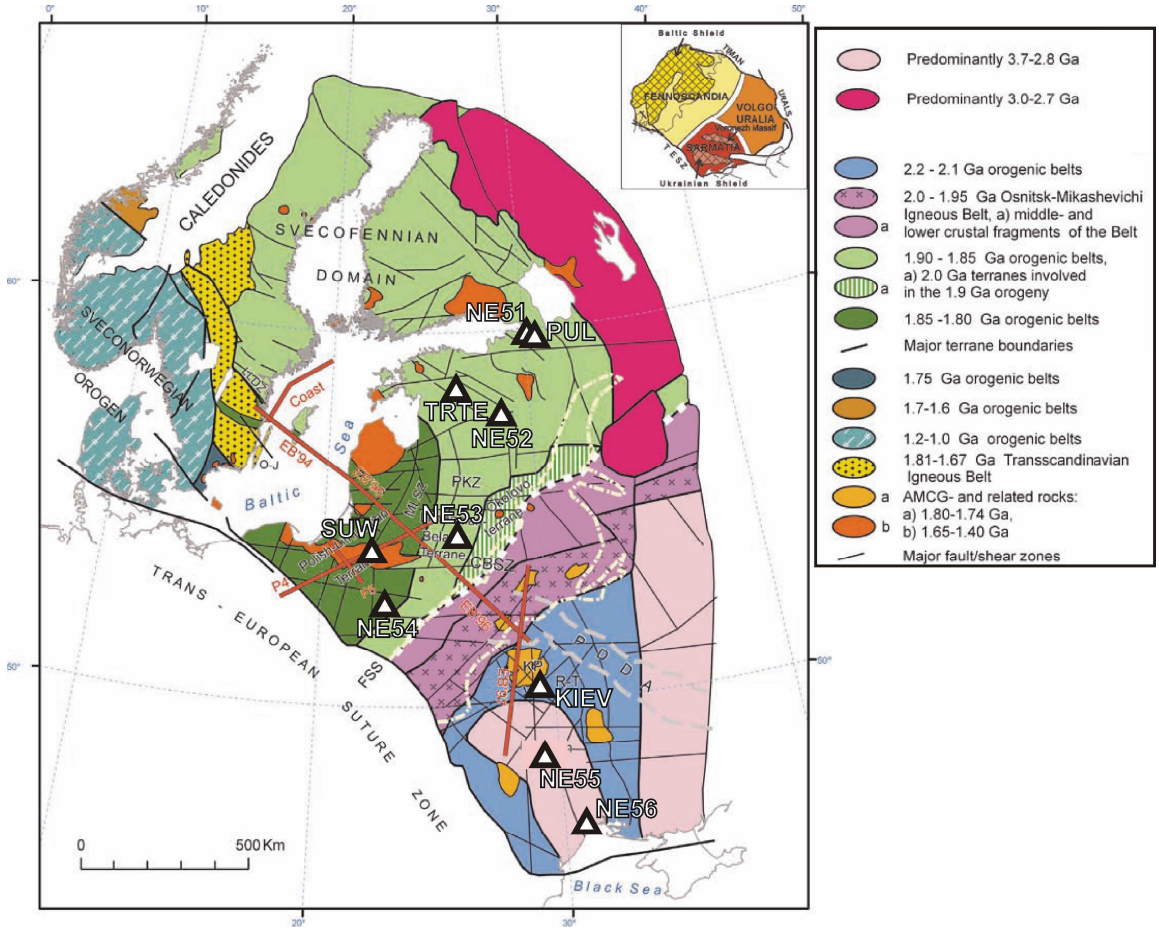

Figure 48: Major tectonic subdivisions of the crust in the western part of the East European Craton with approximate station locations (white triangles) used in this study [modified after Bogdanova et al., 2006]: CBSZ, Central Belarus Suture Zone; KP, Korosten Pluton; LLDZ, Loftahammar–Linköping Deformation Zone; MLSZ, Mid-Lithuanian Suture Zone; O-J, Oskarshamn–Jönköping Belt; PDDA, Pripyat–Dniepr–Donets Aulacogen; PKZ, Polotsk–Kurzeme fault zone. The dashed light yellow line delimits the Volyn–Orsha Aulacogen. Red lines show the positions of the EUROBRIDGE (EB'94, EB'95, EB'96 and EB'97), Coast and POLONAISE (P4 and P5) seismic profiles. The inset shows the three-segment structure of the East European Craton.

5.3.4. The Uralides

The Ural Mountains are the topographic and tectonic feature separating Europe from Asia. The carboniferous (ca. 350Ma) closure of the Ural Paleo-ocean combined the East European Craton and the Siberian Craton, while the convergence continued into early Triassic (~250Ma). The Urals extend North-South more than 2500km, from the Aral Sea to the Arctic Ocean. All its main features strike NS. Along the western flank, a foreland basin overlays the EEC, followed to the east by a thrust and fold belt. Based on the west-vergent nature of many thrust faults, and the geometries and locations of island arc remnants it is generally assumed that the terminal subduction was directed towards the east [Perez-Estaun & Brown, 1996]. The eastern flank is a mosaic of accreted terranes and

obducted slabs [Brown et al., 1996]. The Main Uralian Fault extends for more than 2000km and is the principal suture zone of the Urals. It divides the EEC units from the Siberian units and is dipping towards the East.

5.4. Geophysical properties of the East European Craton

5.4.1. Plate motion

Plate kinematic models describe the velocities of points at the Earth's surface due to plate tectonic motions. These absolute plate motion vectors (APM) are either derived relative plate motion, which can be obtained from (a) geodetic space techniques like VLBI, SLR and GPS [e.g. Drewes, 1998; Sella et al., 2002], or (b) geophysically from sea floor spreading rates, transform fault and earthquake slip azimuths [e.g., Argus & Gordon, 1991; DeMets et al., 1994; Gripp & Gordon, 1990, 2002; Kreemer et al., 2003].

For all these models it is crucial to select the appropriate reference frame [Kubo & Hiramatsu, 1998], which changes with application. Local reference frames are to be considered in regional analysis. The “no-net-rotation” frame (NNR) assumes that vector sum over the globe is zero; i.e. there is no uniform net rotation remaining. This is a mathematical (over-) simplification and these motions only approximate the velocity relative to a fixed mantle. A third category of reference frame assumes that the hotspots are in no significant relative motion [Gripp & Gordon, 1990; 2002]. Hotspots are thought by most to be the surface manifestation of deep mantle plumes [Morgan, 1971]. It remains a matter of debate if the hotspots can be assumed as stationary [Steinberger & O'Connell, 1998; Tarduno et al., 2003; Andrews et al., 2006].

All of these models agree that the APM velocity of Europe is relatively slow. NNR solutions give an average velocity of 25mm/yr and 24.6mm/year for the REVEL2000 [Sella et al., 2002] and APKIM2000 [Drewes, 1998] models, respectively. In the older hotspot reference frame model HS2-Nuvel1A [Gripp & Gordon, 1990], average APM is 10.6mm/yr. This is half the velocity of the latest model, HS3-Nuvel1A, which results in 20mm/yr. However, the directions of the NNR and hotspot reference frames result in opposite directions of plate motion for Europe. In the NNR, Europe moves generally towards NE and E, while in a hotspot frame this motion is SW to west.

For geodynamic interpretation the hotspot frame is the appropriate choice. The HS3 plate motion vectors in Europe bend from W in the Urals to SW in the Iberian Peninsula (Figure 49). With approximately 20mm/yr [Gripp & Gordon, 2002] Eurasia is one of the slowest moving plates. Relative motion between moving plate and underlying mantle aligns the minerals parallel to the direction of this strain [Nicolas & Christensen, 1987]. This effect is independent of plate velocity. Slow moving plates simply require a longer time of

uniform plate motion to align the minerals. Alignment of anisotropic minerals causes a bulk anisotropy, which can be measured (Chapter 2.5). When assuming the simple asthenospheric flow model [Vinnik et al., 1984, Bormann et al., 1993, 1996; Silver, 1996; Chapter 3.3.3], the anisotropic orientations found by numerous shear-wave splitting studies (Figure 49) might be interpreted as a mantle flow that is deviated by the thick lithosphere of the EEC. On the other hand, this pattern also follows the general Hercynian structures, which might indicate lithospheric origins of anisotropy. The continuation of this pattern beneath the EEC will be discussed in Chapter 5.5.

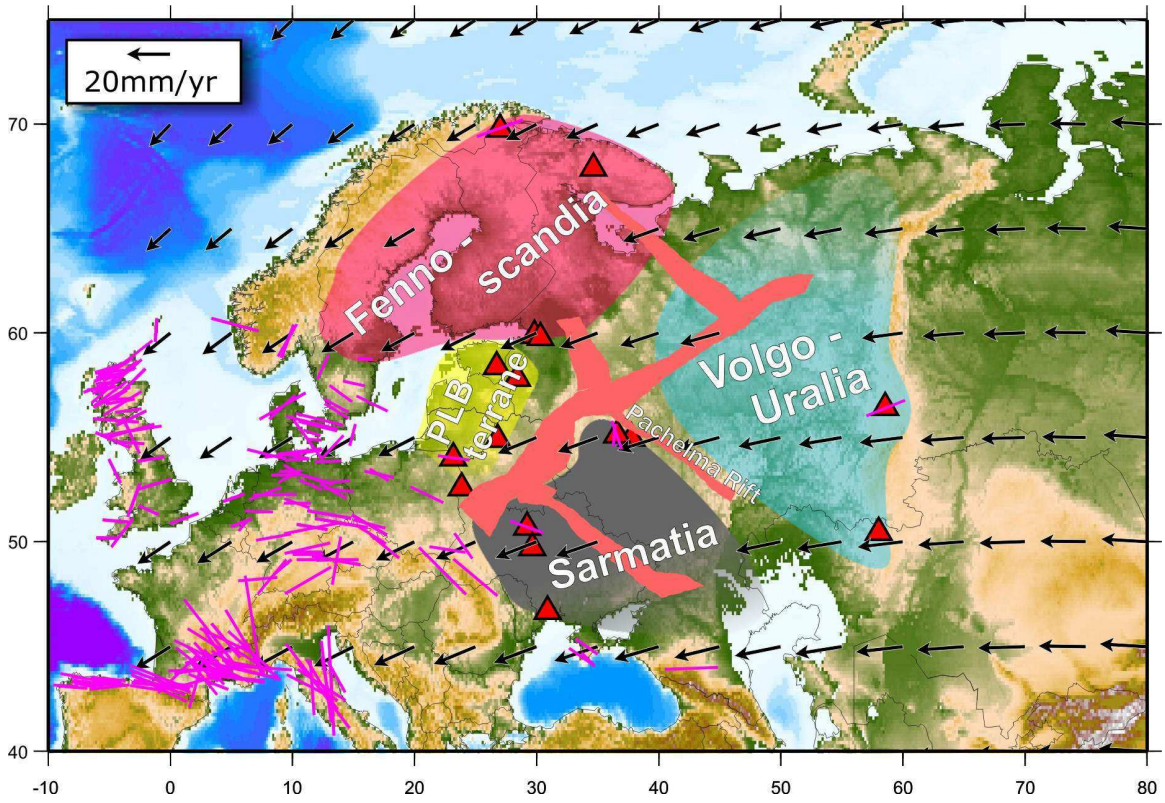

Figure 49: Plate motion vectors in Europe relative a hotspot reference system HS3-Nuvel1A (black arrows, Gripp & Gordon, [2002]). The average velocity is 20mm/yr. Also shown (magenta bars) are the splitting Φs obtained from the splitting database. PLB: Polish-Lithuanian-Belarus terrane, whose south-eastern extend remains unclear.

5.4.2. P-wave anisotropy

The anisotropy inferred from P-wave travel times presented by Bokelmann [2002] reveals a similar anisotropic pattern in Europe (Figure 50; unpublished data, Bokelmann, pers. com. 2007) as the shear wave splitting results presented in Figure 49. In central Europe NW-SE direction dominate. In Scandinavia mostly northerly directions are observed. South of the East-European Craton the anisotropy is E-W oriented. Remarkably, the TTZ can be identified as the transition between NW-SE Φs in the west, and a more complex pattern on the EEC.

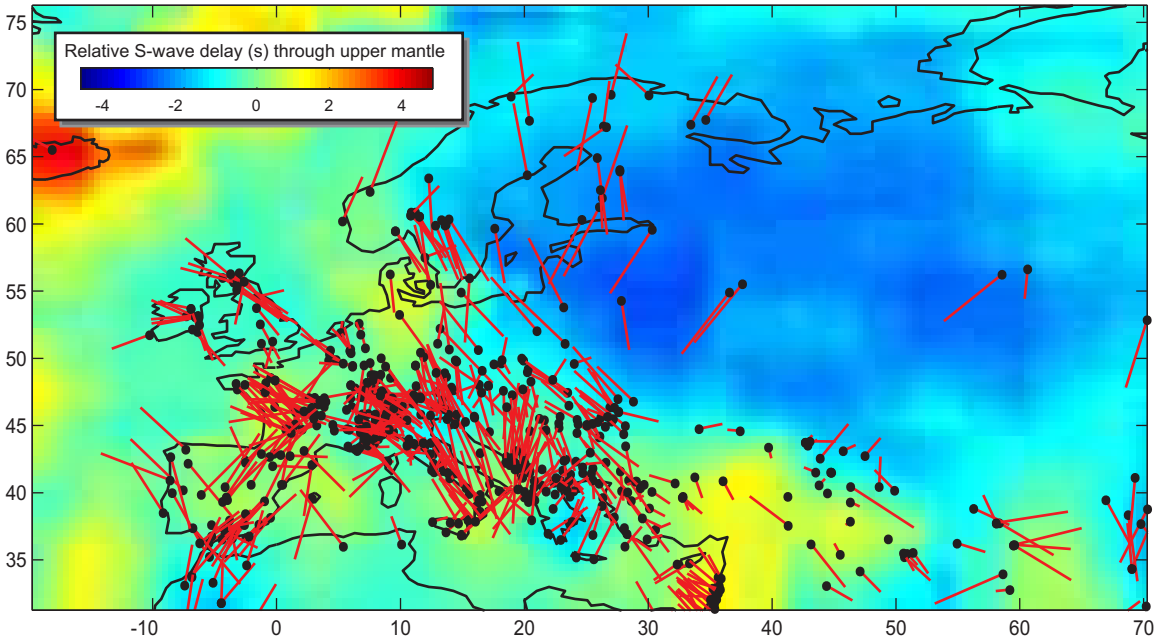

Figure 50: Results of P-wave anisotropy inversion in Europe [after Bokelmann, unpublished data, 2007]. The length of the line represent the dip angle from horizontal, i.e. long lines render horizontal and short lines vertical fast axes. The background model is the integrated travel time residual through the upper mantle from the tomography model by Grand [1994]. See Bokelmann 2002 for further explanations.

5.4.3. Magnetics

Magnetic anomalies represent structural and/or compositional differences at depth up to the Curie Temperature isotherm. At higher temperatures the magnetization of the material is lost. For rock magnetism, the most important mineral is magnetite (Fe_3O_4) with a Curie Temperature of 578ºC. Depending on the geothermal gradient, this temperature is reached in the Earth at depth as shallow as 15km at mid ocean ridges and 30km for continents [e.g., Turcotte & Schubert, 2002]. In cratonic regions the isotherm can be even significantly deeper and reach depths of up to 70 km (e.g., Artemieva, 2006; see Chapter 5.1; Figure 44; Figure 45). Therefore indicates magnetic intensity anomalies reflect largely structures within the crust. Therefore, observed magnetic anomalies reflect only crustal features. The comparison of magnetic lineaments with anisotropic Φs can yield valuable information of crust-mantle interaction. In particular, parallelism of these two independent datasets indicates that the deformation in crust and lithosphere are vertically coherent (VCD, cf. Silver [1996]).

Bogdanova et al. [1996] point out that the long-wavelength magnetic anomalies of T-MAGSAT data correspond to first order to the three major units of the EEC. Two large positive anomalies in the south coincide with Sarmatia and Volgo-Uralia, respectively. In contrast, Fennoscandia features more magnetic inhomogeneity, possibly related to the complex mosaic of crustal provinces. High gradient zones coincide remarkably well with the ancient suture zones combining the three segments of the EEC.

Figure 51 shows the residual magnetic field $(\Delta T)_a$ in the area of the Former Soviet Union (FSU). These data are based a compilation of aeromagnetic surveys during the 1960s. A mosaic series of 18 sheets at 1:2,500,000 scale was published in 1974 by the Ministry of Geology of the U.S.S.R. The digital version of the data can be obtained from NOAA (http://www.ngdc.noaa.gov).

The map can be best described by the division into two main types of features: linear and checkerboard structures. Linear structures render largely the big faults and contact zones in this area. Short-scale variations from strong positive to strong negative values mark these lineaments, for example the Pachelma Rift. Linear features also mark the Polish-Lithuanian-Belarus terrane, curving from NNE-SSW in the south to E-W directions in the northern part of the terrane. The Ural Mountains show patches of positive anomalies largely aligning parallel to the trend of the mountain chain. The boundary between the EEC and Urals is sharply defined as a negative magnetic anomaly. At 58ºN latitude, just north of station ARU, a lineament of alternating positive and negative anomalies aligns E–W.

Interesting features on this map include

- NNW-SSE trending strong magnetization variation in the Ukrainian Shield. These directions are oblique to the general SW-NE geologic trends [Bogdanova, pers. com. 2007], which are possibly related to old sutures of subterranes.
- strong magnetization of the northern Karelian block, close to LVZ
- E-W trending structures north of ARU (perpendicular to the Ural mountain chain)
- Good representation of the Pachelma Rift with NW-SE trending structures
- Good representation of the SW part of the Central-Russian Rift system (CRRS)
- Wedge-like alignment of negative anomalies in the region of the “triple-junction” of Pachelma, Volhyn-Orsha and CRRS rifts
- Bending structures in the Lithuanian-Belarus-Terrane. These structures bend from NE-SW trending in the south to E-W trends in the north, representing well the geologic structure in this region [Bogdanova et al., 2006]

Checkerboard patterns of magnetic intensity are mostly found in the shield regions. A zone of an intense non-segmented positive field of 70-80 mOe can be distinguished in the central part of the Kola Peninsula, close to station LVZ. The central part of the Russian platform can be characterized by a very complex structure of the magnetic field, by a combination of systems of checkerboard field and variously oriented, very extensive linear anomalies. Sections of the magnetic field corresponding to the Ukrainian Shield, and

Voronezh Massif, amongst others, can be distinguished within its limits. However, these limits do not always coincide with their surface expression [Zonenshain et al., 1990]. The magnetic field of the Ukrainian shield can be characterized by great differentiation, by the presence of an anomalous zone with steep horizontal gradients, sometimes as much as 100 mOe/km.

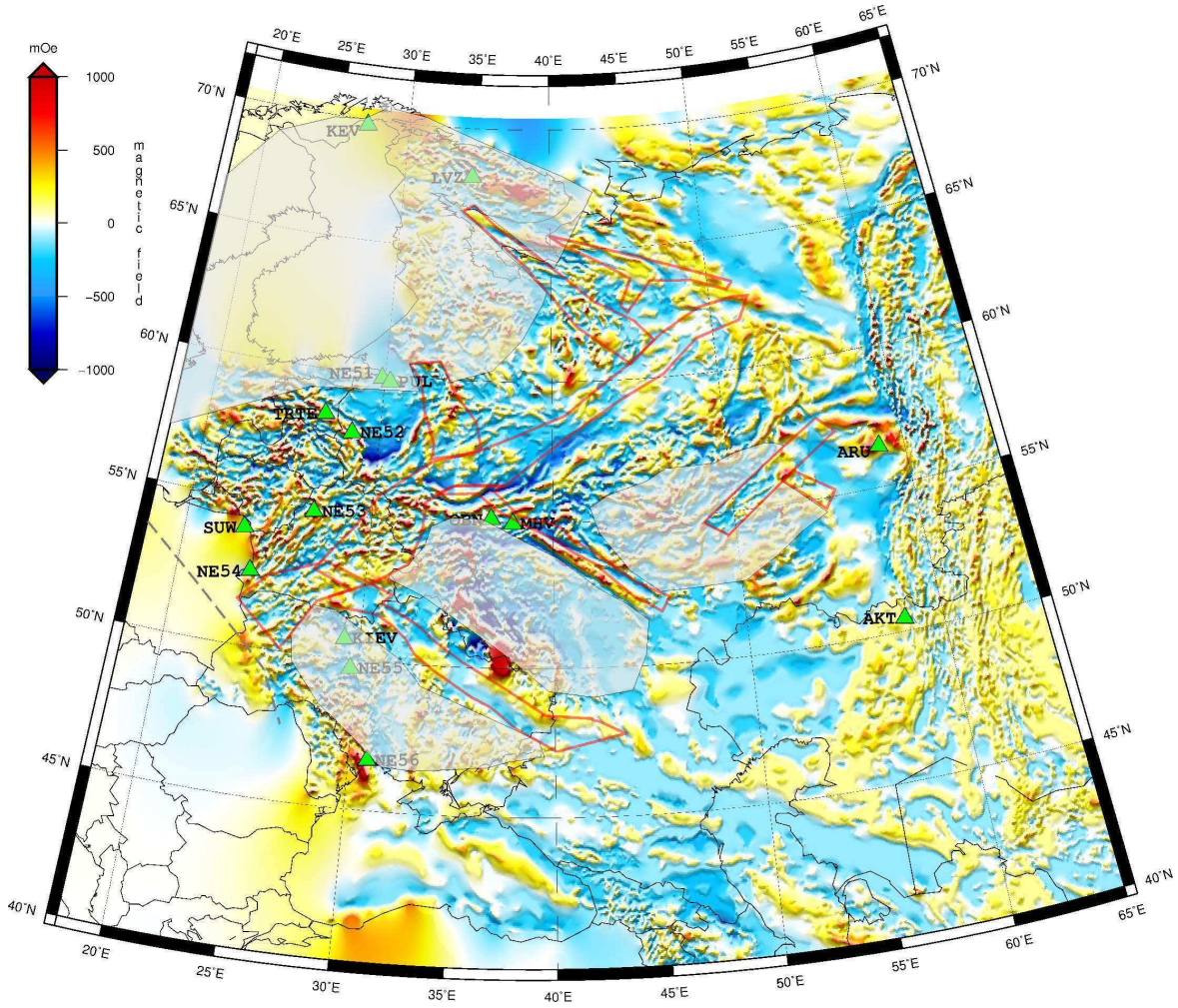

Figure 51: Residual magnetic field in the territory of the Former Soviet Union. Major structural units modified from Zonenshain et al. [1990]. Red lines: Rifts; white shaded areas: Shield regions

5.4.4. Gravity

Figure 52 shows the Free Air gravity anomaly of the EEC. The data are based on the NASA EGM360 Potential model. In the dataset section of the iGMT page [http://www.seismology.harvard.edu/~becker/igmt/], there is a conversion of the EGM360 geoid model into the gravity anomaly, since coefficients of the latter can be obtained by multiplying coefficients of the former by (l+1)/R, where l is the order of the expansion, and R the radius of the Earth. This 0.5degree grid has been resampled to 0.2 degrees in the

region of the EEC. The resolution of theses gravity data is much lower than for the aeromagnetics presented in the previous chapter, since here satellite data are used.

Prominent features on this map are the Urals Mountains the Caucasus, and the Carpathian arc with the Vrancea subduction zone. The boundaries of the three blocks constituting the EEC, are roughly reflected in the region of the Stations OBN/MHV as positive anomalies

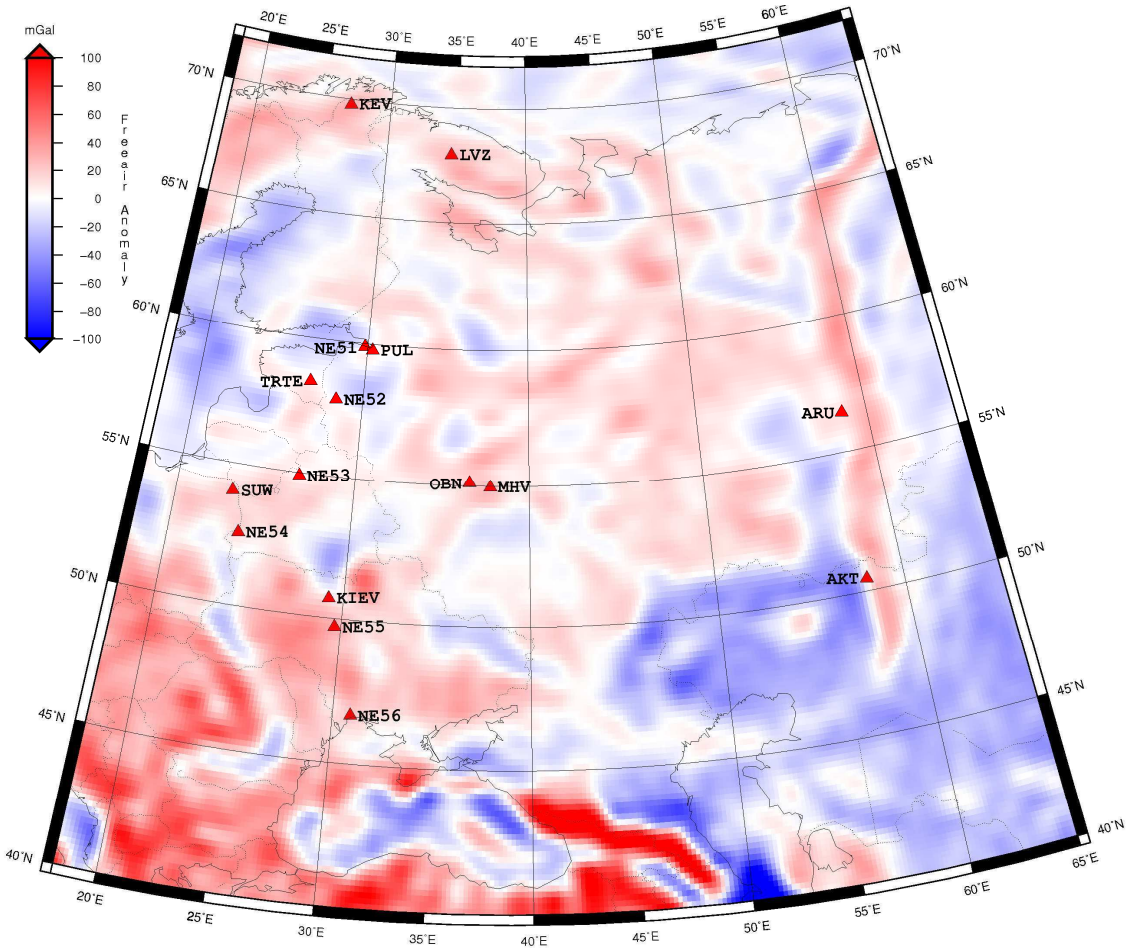

Figure 52: Free air gravity anomaly in the EEC, extracted from global NASA EGM360 model.

5.4.5. Tomography

Surface wave tomography provides the unique possibility to coherently study the lithospheric structure of the vast area covered by the EEC. Here, global model of Debayle et al. [2005] is used. Figure 53 presents this model in the region of the EEC at 150, 175, and 200km depth, respectively. The EEC can be well identified as a region of relatively fast material down to depths well below 200km. Note the thinner-than-average lithosphere beneath Sarmatia.

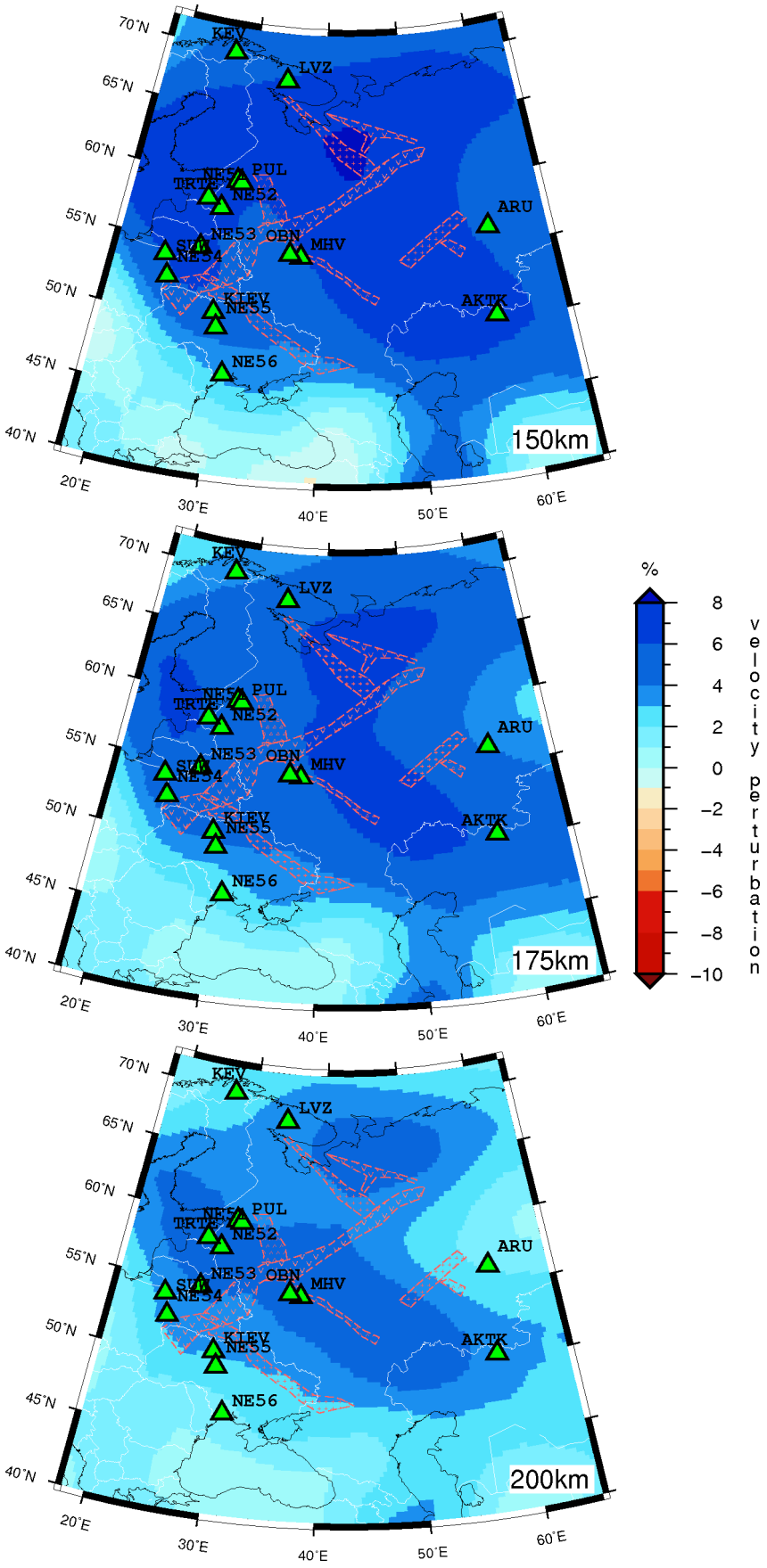

Figure 53: Tomographic velocity residuals beneath the East European Craton at 150, 175, and 200km depth [after Debayle et al., 2005]. Samartia in the SW has systematically higher residuals, indicating a thinner lithosphere. Rifts in red after Zonenshain et al., [1990]

"Perplexity and discontent are the prerequisites for progress"
(Thomas Alva Edison)

5.5. Anisotropic structure of the East European Craton inferred from Shear-wave splitting

Over the past two decades the method of shear-wave splitting has been widely applied in several geologic settings: Subduction zones [e.g., Levin et al., 2004; Margheriti et al., 2003; Nakajima & Hasegawa, 2004], rifts [Kendall, 1994; Gao et al., 1997; Kendall, 2005; Walker et al., 2004], hotspots [Barruol & Granet, 2002; Walker et al., 2001; 2005], oceanic islands [Behn et al., 2004] and orogens [e.g., Barruol et al., 1998; Flesch et al., 2005].

In contrast to these active tectonic zones, cratons constitute the old, stable part of continents. In these environments, a number of valuable observational constraints such as lithospheric flexure are lacking. This renders information on deformation within the upper mantle particularly valuable. Cratonic roots may act as obstacles to mantle flow [Bormann et al., 1993; Fouch et al., 2000]. Analyzing anisotropy in such environments may help to distinguish this present day deformation (if any), associated with plate motion [McKenzie, 1979], from fossil deformation. Several studies analyzed anisotropy beneath the various cratons and their surroundings [Fouch et al., 2000; Heintz & Kennett, 2005; Fouch & Rondenay, 2006; Assumpção et al. 2006].

This study focuses on the anisotropy patterns beneath the East European Craton (EEC). Several studies analyzed a few of the seismic stations in this region [e.g., Silver & Chan, 1991; Vinnik et al., 1992; Helffrich et al., 1994; Dricker et al., 1999], however without discussing the craton as a whole. Growing interest in this region [e.g., Bogdanova 1996; Grad et al., 2003; Bruneton et al., 2004; Bogdanova et al, 2006; Vecsey et al., 2007; Artemieva, 2007] emphasizes the need for addressing the anisotropy patterns of the EEC. Ongoing work in adjacent Central Europe, west of the TTZ [Walther et al., 2007] will eventually add further understanding to the Eurasian plate tectonic system.

Previous splitting studies of numerous researchers identify characteristic pattern of splitting directions (Figure 54), which might indicate mantle flow around the craton [cf., Fouch et al., 2000]. On the other hand, these directions are also close to the trend of the Hercynian fold belt and might suggest that anisotropy is frozen in the subcrustal lithosphere [Bormann et al., 1993]. Bokelmann [2002] identified dipping (P-Wave) anisotropy within the North American Shield and associated this with plate-motion related shearing at the base of the lithosphere. Identifying similar patterns in splitting data of the EEC might put further light on the Eurasian plate system.

5.5.1. Data and processing

The EEC is covered by a number of permanent broad-band seismographs, maintained by several data centers. Table 1 gives an overview of the 16 stations analyzed in this study. The stations are distributed irregularly over the area. However, they cover all important geologic regions of the EEC (Figure 49). The data quality is also variable, where the best signal-to-noise ratios (SNR) were found at stations KEV and ARU. The NARS-network stations [Muyzert et al., 1999] provided only few events for shear-wave splitting measurements.

Handling of data from several datacenters could be easily achieved by using SplitLab (Chapter 4.3). In total we were able to identify 663 SKS shear-wave splitting events. With SplitLab we were able to quickly manage the entire splitting process, and it provides a comprehensive interface to test various filter-time window combinations. This proved helpful since small delay times make careful data and filter selection necessary. Where possible, we used either raw data or a weak band-pass filter (0.01 – 1Hz). The strongest filter we applied to the data was a 0.02 – 0.2Hz band pass.

The dominant frequency of a SKS phase is usually around 0.125Hz. The signal of the split wave on the transverse component is approximately proportional to the derivative of the radial signal [Silver & Chan, 1991]. Filtering in this range not only suppresses the noise, but also removes important information contents from the signal. In effect, stronger filtering usually results in a Null event and thus has a strong influence on the resulting splitting parameter estimates. Levin et al. [1999] tested the influence of filtering on synthetic seismograms modeled for a multilayer case. They found that the apparent splitting parameters are most variable for the lowest band pass filter applied, in their case 0.05 - 0.15Hz. We remark that low, narrow filters (e.g., 0.01-0.15Hz) may in general be applied for shear-wave splitting measurements. These require however SNR of above 10. Here the SNR is defined as the ratio of the maximum amplitude on the radial component to the standard deviation of the transverse components, both after the removal of splitting [Restivo & Helffrich, 1999].

The quality of our measurements has been determined using the automatic method of Wüstefeld & Bokelmann [2007]. This method reliably detects Null-measurements and assigns a quality indicator [Chapter 4.4]. Such automatic detection is important to produce a homogeneous dataset for all stations by eliminating possible bias for specific stations. Such bias can be caused by a low Signal-to-Noise ratio, in which case the seismologist tends to assign a too high quality. Furthermore, bias can be caused by a sequence of Null events followed by a rather poor event (or a sequence of good events followed by a fair one). A dataset with automatic Null- and quality detection is therefore reproducible with fixed criteria for each assignment, and thus objective.

Most of the usable events have backazimuth between 45º and 100º (Tonga subduction zone). Another set of events originate from the Andean subduction zone, having backazimuths of 240º to 310º. It is intriguing, that the latter origin region shows small, but systematic differences in splitting parameters (see later discussion).

5.5.2. Results

We analyzed the shear-wave splitting of 16 broad band seismograph stations on the East European Craton. The observed splitting is generally low, with delay times varying between 0.4 and 1.1 seconds. As will be discussed in the following subchapters, the Φs vary for each tectonic unit, indicating frozen-in, lithospheric anisotropy. Such interpretation is supported by a variable correlation of Φs with plate motion direction, which seems to be parallel only by chance and does not reflect large-scale asthenospheric processes(see discussion below, Chapter 5.5.3).

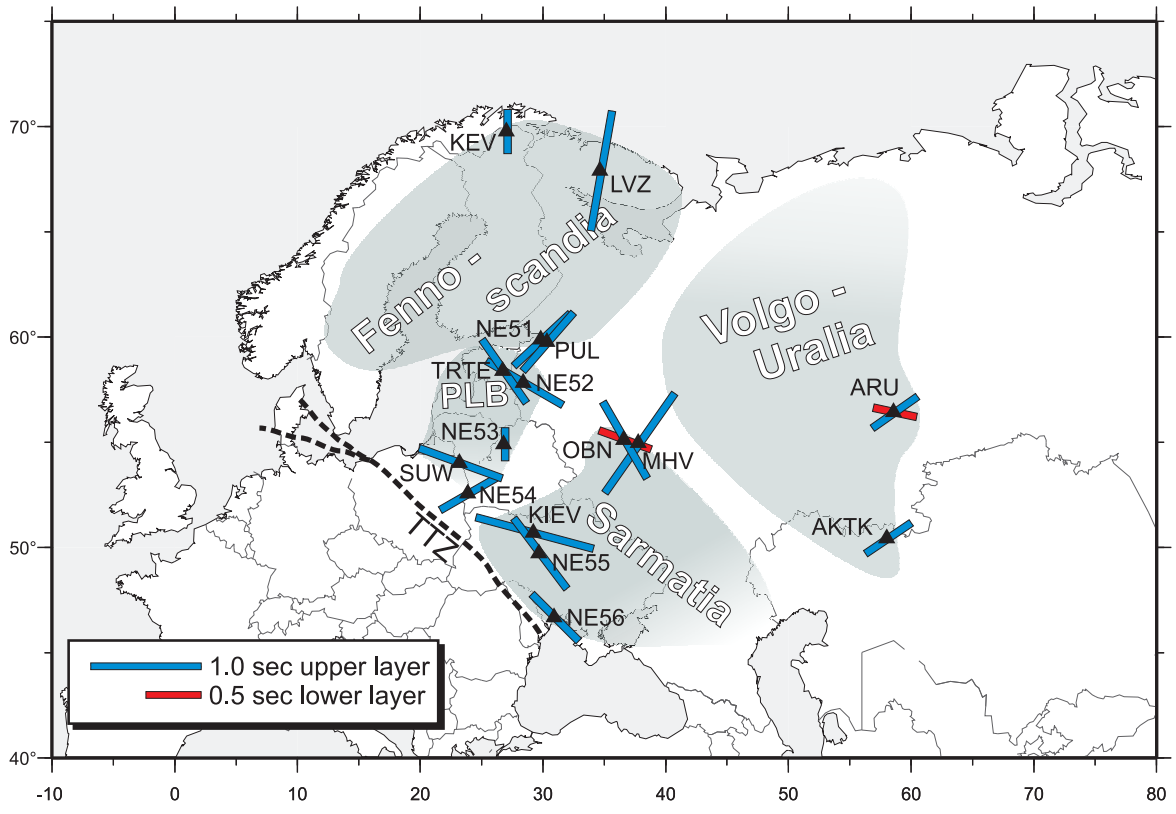

Figure 54: Shear-wave splitting results of this study. Blue and red markers indicate upper and lower layer respectively. Blue markers, if only single anisotropic layer has been identified. PLB = Polish-Lithuanian-Belarus terrane; TTZ = Tesseyre-Tornquist Zone

Station	Lat	Long	Network	total	automatic / manual	Φ		dt	
						Upper	Lower	Upper	Lower
AKTK	50.435	58.02	Kazachstan	35	6g + 1f + 10p + 2fN + 16gN 3g + 6f + 6p + 11fN + 9gN	56°		0.5	
ARU	56.43	58.56	GSN	139	34g + 19f + 35p + 20fN + 31gN 49g + 32f + 11p + 26fN + 21gN	55°	-78°	0.5	0.4
KEV	69.76	27.01	GSN	44	4g + 3f + 12p + 9fN + 16gN 3g + 4f + 0p + 19fN + 18gN	0°		0.4	
KIEV*	50.69	29.21	GSN	61	3g + 4f + 24p + 3fN + 27gN 19g + 14f + 5p + 13fN + 10gN	-75°		1.1	
LVZ	67.9	34.65	GSN	41	10g + 8f + 6p + 7fN + 10gN 16g + 7f + 1p + 9fN + 8gN	10°		1.1	
MHV	54.96	37.77	GEOFON	61	4g + 2f + 10p + 2fN + 13gN 5g + 6f + 3p + 8fN + 9gN	35°		1.1	
NE51	59.881	29.826	NARS	12	4g + 0f + 3p + 2fN + 3gN 5g + 4f + 0p + 0fN + 3gN	47°		0.7	
NE52*	57.819	28.39	NARS	8	1g + 0f + 4p + 0fN + 3gN 1g + 0f + 0p + 5fN + 2gN	-60°*		0.8	
NE53	54.904	26.793	NARS	18	0g + 1f + 5p + 3fN + 9gN 2g + 1f + 3p + 6fN + 6gN	NS		<0.5	
NE54	52.568	23.861	NARS	3	1g + 0f + 1p + 0fN + 1gN 1g + 1f + 0p + 1fN + 0gN	60°		0.6	
NE55	49.716	29.656	NARS	6	0g + 1f + 2p + 0fN + 3gN 1g + 0f + 0p + 1fN + 4gN	-37°		0.8	
NE56	46.676	30.899	NARS	6	4g + 0f + 1p + 0fN + 1gN 3g + 1f + 0p + 0fN + 2gN	-45°		0.6	
OBN**	55.11	36.57	GSN	115	12g + 16f + 42p + 8fN + 37gN 26g + 22f + 13p + 24fN + 30gN	-30°	-70°	0.8	0.5
PUL	59.77	30.32	GEOFON	20	2g + 1f + 5p + 0fN + 12gN 4g + 4f + 0p + 1fN + 11gN	41°		0.7	
SUW	54.012	23.18	GEOFON	72	13g + 11f + 20p + 8fN + 20gN 19g + 21f + 2p + 15fN + 15gN	-70°		0.8	
TRTE	58.38	26.72	GEOFON	22	1g + 5f + 7p + 3fN + 6gN 6g + 7f + 0p + 5fN + 4gN	-35°		0.7	

* More complex geometry possible/beyond resolvability

** for 2 sec dominant frequency

Table 5: Splitting results of the stations on the East European Craton. Manual and Automatic quality and Null assignment are given: g=good; f=fair; p=poor; fN=fair Null; gN = good Null

5.5.2.1. AKTK

The station AKTK close to the Kazakh town of Aktyubinsk is located at the southern tip of the Ural Mountains (Figure 76). We analyzed 35 SKS events for our study of which we

classified 6 good, 1 fair, 10 poor, 16 good Nulls, and 2 fair Nulls (Figure A- 4). Westerly events resulted solely in Null measurements. Events from the east give ambiguous results since Nulls and non-Nulls are observed from similar backazimuths. This kind of effect can be observed if either two layers of anisotropy with mutually perpendicular Φs are present [e.g., Silver & Savage, 1994; Heintz & Kennett, 2006] or if the anisotropy is only weak. Short delay times of non-Null measurements indicate only weak anisotropy, which causes Null measurements in case of only weak signal on the initial radial component.

We propose for AKTK a one layer model with splitting parameters of Φ = 60º, dt = 0.6 sec. This is parallel to the upper layer found for station ARU. The lack of usable Andean events with westerly backazimuths hinders a clear interpretation at this moment, but might become clearer with a growing dataset over the next years.

5.5.2.2. ARU

Upper mantle anisotropy beneath ARU has been previously studied by Helffrich et al. [1994], who report a mean Φ of 68º and a delay time of 1 sec. Levin et al. [1999] present a detailed study of the anisotropy beneath ARU. However, their location (Figure 16 in Levin et al. [1999]) close to the city of Perm, in the Uralian foredeep, is wrong (latitude and longitude seem to have been confused). The correct location as given by IRIS Station Query is 56.4302ºN, 58.5625ºE. This location is close to the front of the Ural Mountains. They propose a 3-layer model to explain the complex pattern of shear-wave splitting results. This model is based on anisotropic receiver function studies by Levin and Park [1997], who find anisotropic uppermost and lower crust with hexagonal symmetry and strong tilt in symmetry axes.

The parameters of their model are: a 42km crust with a slow axis oriented at 230º and plunging 65º (from vertical), followed by a 58km upper mantle layer with a Φ of 50º and plunging 80º (almost horizontal). The lower mantle layer is 140km thick with a Φ of 90º, plunging 130º. This is equivalent to a tilting towards the west, i.e. orientation 270º, plunge 50º and not a plunge of 40º as stated in Levin et al. [1999].

During our analysis we processed 139 SKS waveforms (34 good, 19 fair, 35 poor, 31 good Nulls, and 20 fair Nulls). The stereoplot of SC results (Figure 55) shows consistently ENE directions, with characteristic variations of Φs and delay times systematically smaller for steep incident waves. A best fit one layer model has splitting parameters of Φ = 75º and dt = 1.1sec (Figure A- 2). This model does however not render well the results from westerly backazimuths, whose apparent Φs are systematically closer to E-W directions than events from easterly backazimuths. A two layer model (Figure A- 3) with splitting parameters Φ = 55º, dt = 0.5sec for the upper layer and Φ = -78º, dt = 0.4sec for the lower layer is only weakly constrained due to gaps in backazimuthal coverage. However, comparison with the theoretical stereo plot (Figure 55) increases confidence in that model. The values are

calculated following the method suggested by Silver & Savage [1994] for backazimuthal variation. Here, the results of such calculation are plotted each 7.5º at an incidence of 10º, which is representative for SKS waves.

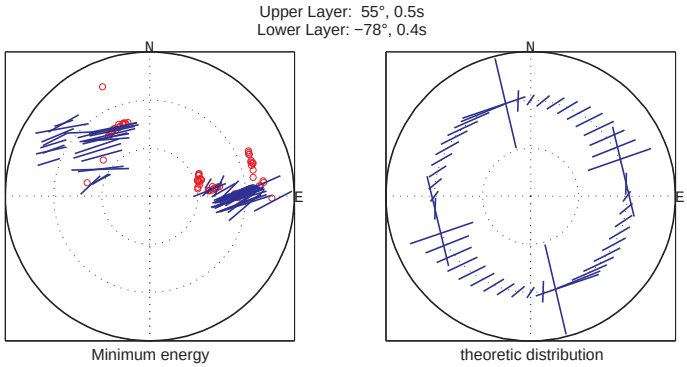

Figure 55: Stereoplot for station ARU. Left: SKS and SKKS results are shown according to their incident angle and backazimuth, with length of the symbol correspond to SC delay times. Only 15º sector from vertical is shown, with gridlines every 5º. Null measurements are shown as circles at their corresponding incident and backazimuth pierce-point. Right image shows theoretical stereoplot at 10º incidence.

A Φ for the lower layer of Φ = -78º is approximately perpendicular to the trending of Ural Mountains, but parallel to an anomaly in the total magnetic field north of ARU (Figure 51).

5.5.2.3. KEV

The station KEV near the town of Kevo in northern Finland operates broadband instruments since 1987. Digital seismograms are available for download from the IRIS/GSN network since June 1993. By investigating P-wave first polarisations, we found that the station is mis-oriented by +10°. We informed the IRIS consortium and they will fix the orientation during the next scheduled service of the station. Of 901 earthquakes occurring between June 1993 and July 2006 with magnitude $M_W \geq 6$ the seismograms of 750 earthquakes could be retrieved from the data center. These resulted in 44 usable SKS splitting events: 4 good, 3 fair, 12 poor, 16 good Nulls, and 9 fair Null measurements. The large amount of Nulls can be attributed to the generally weak anisotropy beneath KEV deduced from delay times of dt=0.4sec of the good events. This is in good agreement with the study of Silver and Chan [1991], who identified KEV as an isotropic station. We are confident that our weak splitting is real, due to our improved splitting methodology by comparing the results of two techniques [Wüstefeld & Bokelmann, 2007]. After correction for misorientation we find a Φ of Φ=5º. An interesting feature of the measurements is that delay time correlates with incidence angle: the more vertical the incident, the shorter the delay time (Figure 56). This might be attributed to thicker lithosphere in the East.

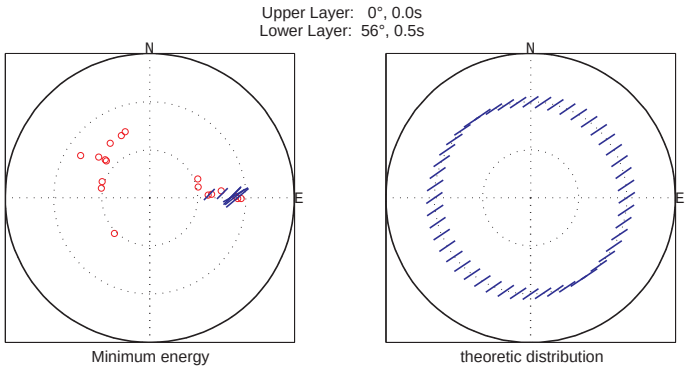

Figure 56: Stereoplot for KEV with automatically assigned quality (displayed only good and fair measurements) and Nulls (circles). Only 15º sector from vertical is shown, with gridlines every 5º. The algorithm of Silver & Savage [1994] has been used to calculate the theoretic distribution. Theoretical splitting parameters are displayed at an incident angle of 10º from vertical. For a single layer model the splitting parameters do not vary with backazimuth. For a two-layer case, more complex pattern is expected.

5.5.2.4. KIEV

The GSN/IRIS station KIEV is located on the Ukrainian Shield in proximity to the Pripyat Trough / Dnepr-Donets Palaeorift (Figure 49). The EUROBRIDGE project provides detailed geological and geophysical dataset along the profile (Figure 57).

The Volhyn Block is a Palaeoproterozic gneiss complex with ages ranging between 2.4 and 2.1Ga. The Korosten Pluton appears to extend to depths of ~12 km based on seismic refraction interpretation [Thybo et al., 2003] and gravity modeling [Yergorova et al., 2004]. It was formed between 1.8 and 1.74Ga ago. Whether this Pluton is a result of mantle underplating or caused by post-collisional tectonic events in the NW remains a matter of debate [see Bogdanova et al., 2006].

Digital data are provided for events dating back from January 1995. This rich earthquake database and for Central Europe relatively good backazimuthal coverage makes KIEV an ideal station location for analyzing shear-wave splitting. A first such study was presented by Dricker et al. [1999] who report a Φ of Φ = -70º and a delay time of dt = 1.3 sec.

KIEV is a good example of the advantages of the automated quality and Null detection by Wüstefeld & Bokelmann [2007]. Manual quality assignment, as described by Barruol et al. [1997], leads to an assignment of a number of non-Null. These events showed clear evidence for signal on transverse and an elongated, but clearly elliptical particle motion. In total we assigned 61 events manually (19 good, 14 fair, 5 poor, 10 good Nulls, and 13 fair Nulls). Figure 58 displays the stereoplot of this approach, showing in a complex pattern, which can be fitted with a model of two almost perpendicular layers, with similar delay times. Such a configuration has been found for the Australian Craton [Heintz & Kennett, 2005].

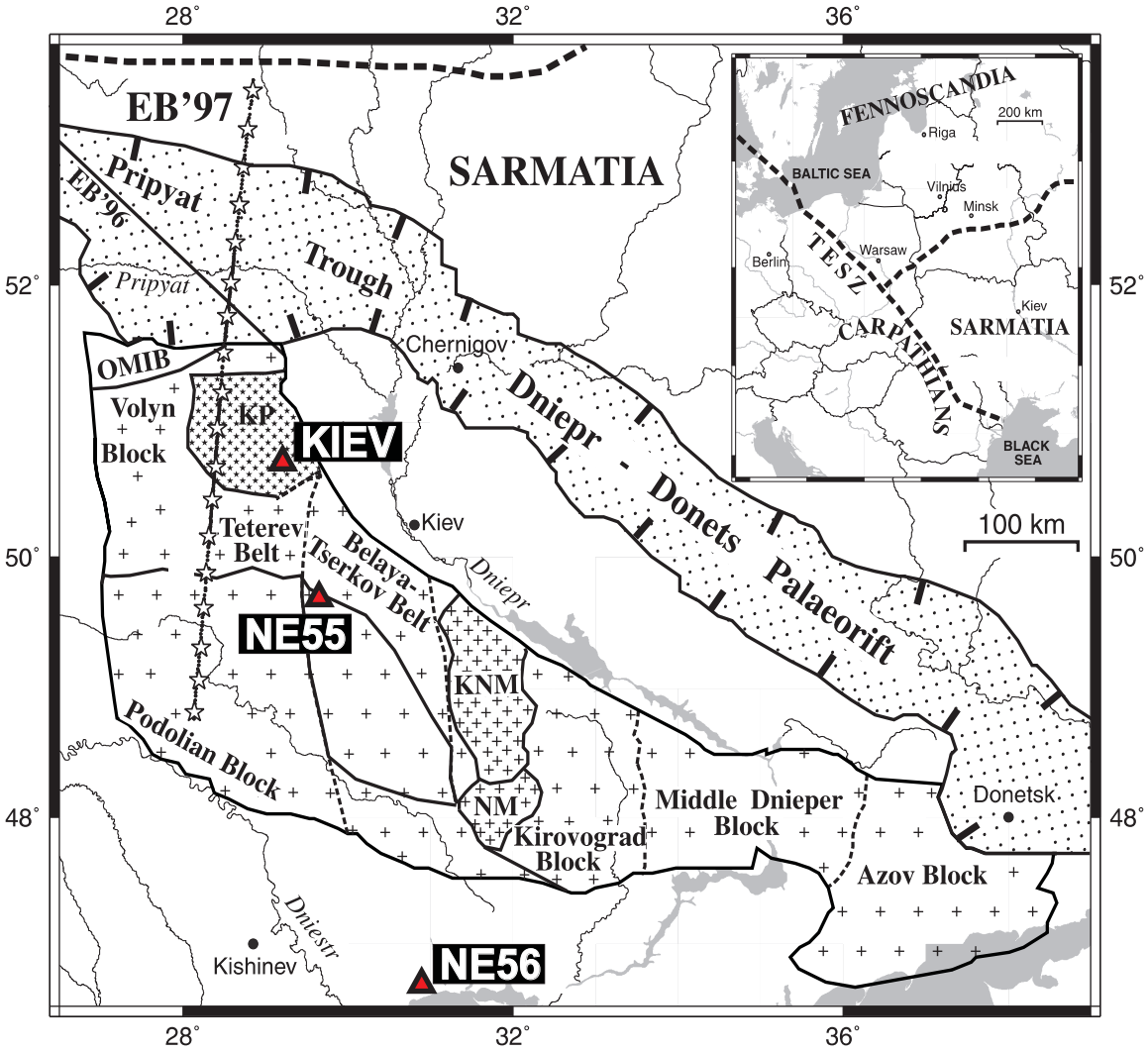

Figure 57: Map of western Sarmatia showing the different segments of the Ukrainan Shield ('+' hatching) and the Dniepr-Donets-Palaeorift. Station KIEV is located on the Koroston Pluton (KP). Asterisks mark the shot points of the EUROBRIDGE'97 refraction profile.

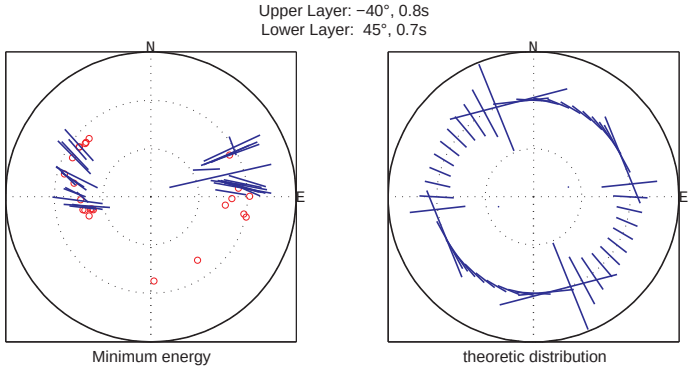

Figure 58: KIEV stereoplots with manual quality determination. A complex pattern of Φs can be identified. This pattern can only be fit with a model of two almost perpendicular layers, with similar delay times.

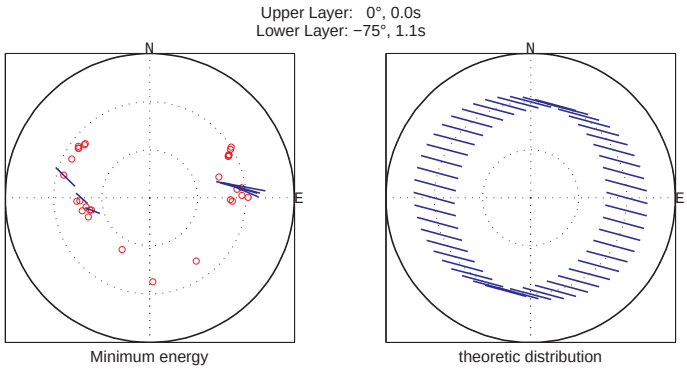

Figure 59: KIEV stereoplots for automated quality and Null detection.

It is however obvious, that for KIEV most the Φs of events from the West are parallel to their according backazimuths, which is a strong indicator of Nulls. The assignment of Nulls for the whole range of westerly backazimuths supports this hypothesis. The automatic Null detection gives a somewhat different result: here, the events are classified as 3 good, 4 fair, 24 poor, 27 good Nulls, and 3 fair Nulls (Figure 59).

A further comparison of the results with the automatic splitting code by Teanby et al. [2003] is presented in Figure 60. This approach also yields 7 events (which are divided in our approach in 3 good + 4 fair) with a similar backazimuthal distribution and similar distribution.

The combined interpretation of these approaches is a clear anisotropy with a Φ of Φ = -75º and a delay time of dt = 1.1 sec from the East. These waves pass through the Ros-Tikich Domain, between the Ukrainian Shield the Pripyat Trough. This unit is composed of sediments and metamorphosed volcanic rocks of Archean ages. If the Ros-Tikich Domain is considered as heterogeneity to the east of KIEV, it might explain the fact that there are non-Nulls from easterly backazimuths and Nulls from the westerly backazimuths. However, Nulls from the west are common throughout the entire EEC, which indicates a much more large-scale cause than such heterogeneity.

As for most stations on the EEC, the splitting from westerly directions remains unconstrained. Such one layer model still does not account for all the Nulls and variations of Φ perhaps indicate a more complex anisotropic environment, which may include any combination of heterogeneity, multilayer and dipping anisotropy.

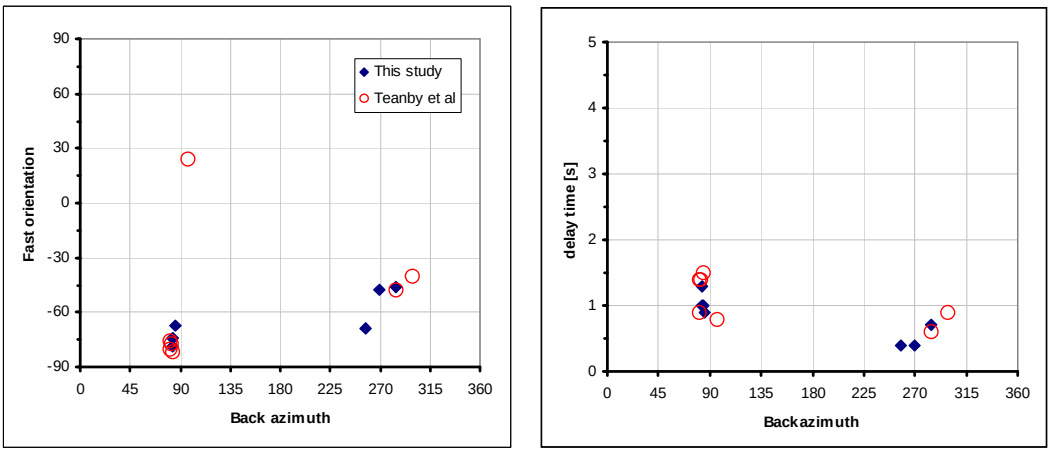

Figure 60: Results for KIEV using this study (blue diamonds) and the automated splitting approach by Teanby et al. [2003] (red circles)), available at http://www.isc.ac.uk/SKS/ with the suggested standard parameters. Seven splitting events could be retrieved, yielding a scatter in Φs and in delay time estimates.

5.5.2.5. LVZ

The anisotropy beneath station LVZ close to the town of Lovozero, Russia has been analyzed in detail by Wüstefeld & Bokelmann [2007, Chapter 4.4]. A total of 40 usable events yield 10 good, 8 fair, 6 poor, 10 good Nulls, and 7 fair Nulls. Splitting parameters indicate a Φ of Φ=10° and a delay time of dt=1.1 seconds. As for station KEV (see above), all Andean events resulted in Null measurements, despite large initial backazimuthal coverage from this direction (Figure 61). Most Andean events arrive from backazimuths perpendicular to the resulting Φ from the Tonga region events and thus are expeted to be Nulls, not showing any splitting. The results at this station can be explained by a single layer and do not require a more complex situation such as two anisotropic layers.

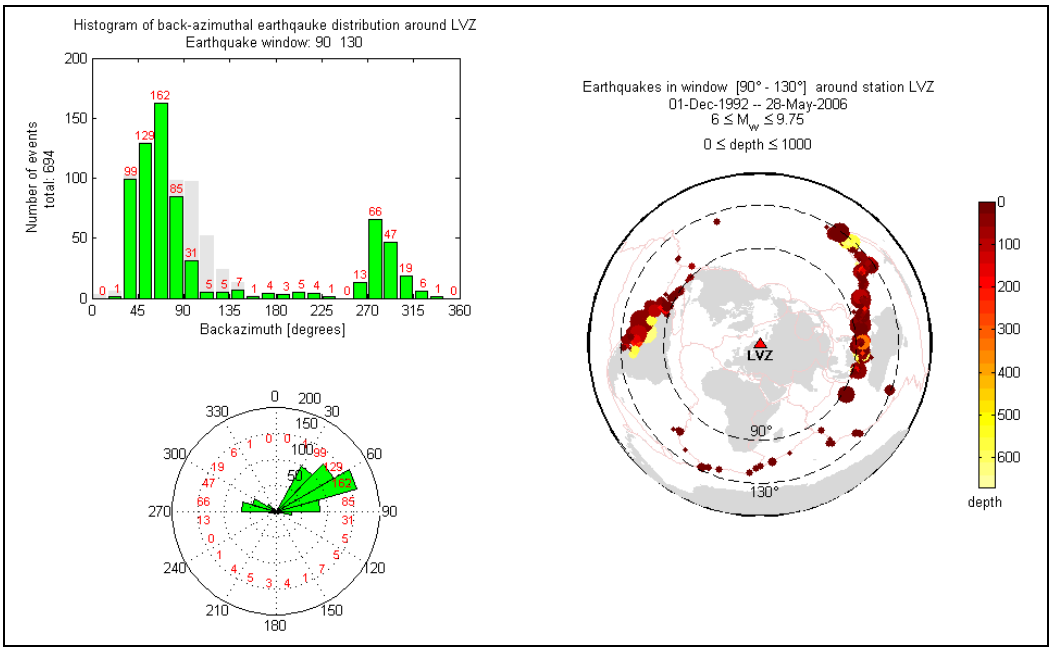

Figure 61: Earthquake distribution statistics for LVZ in a distance window between 90º and 130º. Only a fraction of these earthquakes yield measurable splitting.

5.5.2.6. MHV

At 78 km to the east of OBN the GEOFON station MHV operates since May 1995. It is located close to the NW-SE trending Pachelma rift [Zonenshain et al., 1990], which divides Sarmatia from Volgo-Uralia (Figure 47; Figure 49). In total we measured 31 events: 4 good, 2 fair, 10 poor, 2 fair Null, and 13 good Null. As for the Baltic Shield stations, MHV yields mostly Null measurements from Andean earthquakes. The results indicate a Φ of Φ = +35º with a delay time of dt = 1.1sec. This direction is sub-perpendicular to the adjacent Pachelma rift system.

5.5.2.7. NE51/PUL

The GEOFON station PUL close to St. Petersburg and the NARS station NE51 are located only 30km apart and will be thus presented here together. NE51 resulted in 12 usable measurements (4 good, 3 poor, 3 good Null, 2 fair Null) while PUL yielded a total of 20 results (2 good, 1 fair, 5 poor, 12 good Null). As expected both stations yield similar splitting parameters (Φ = 41º; dt = 0.7sec for NE51 and Φ = 47º; dt = 0.7sec for PUL)

5.5.2.8. NE52

At distance of 135km from TRTE the NARS station NE52 gives similar results. A total of 8 usable events resulted in 1 good, 0 fair, 5 poor, 2 good Null, and 0 fair Null measurements. The good event gives a single layer with splitting estimates of Φ = -60º; 0.8sec; Figure 62). This direction aligns well with the magnetic anomaly in this region (Figure 51). However, the Null measurements scatter too much and backazimuthal

coverage is too sparse to fix this result (Figure A- 10). But the similarity with neighboring TRTE encourages to assume a 1-layer case with those parameters.

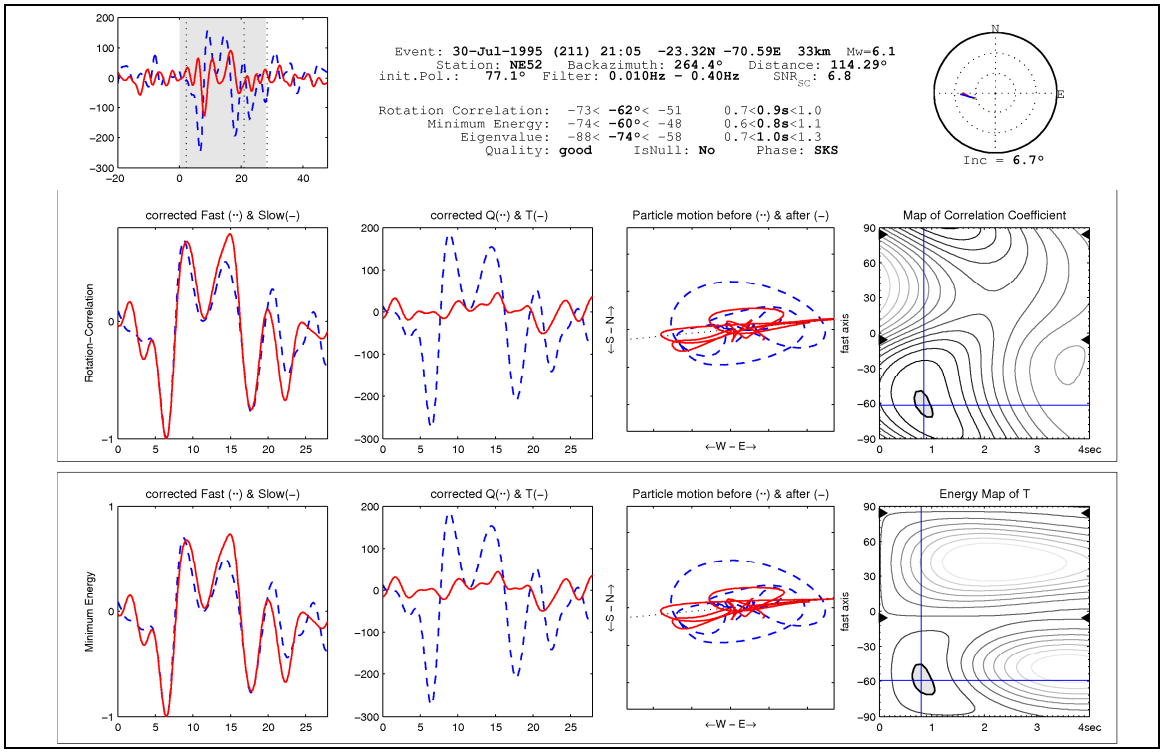

Figure 62: The only good event for station NE52 shows clear results for a Φ of -60º and dt of 0.8sec.

5.5.2.9. NE53

NARS station NE53 is located at the Belarusian-Lithuanian border. Operating since July 1995 until the end of 2000, we retrieved data from the ORFEUS data center for 166 earthquakes. Many noisy events reduced the number of usable data to 22. Examining the P-wave polarizations we found a misorientation of this station of -15º. However, a number of events indicate a misorientation of +15º. These are not in a continuous time span, which could indicate an effect of maintenance. We removed these events from our database which consists thus of 0 good, 1 fair, 5 poor, 3 fair Null, and 9 good Nulls. The non-Nulls are characterized by small delay times in the order of dt = 0.3 sec. The Φ estimates for such small delay times of teleseismic phases are ambiguous, due to a large error (cf. Figure 63).

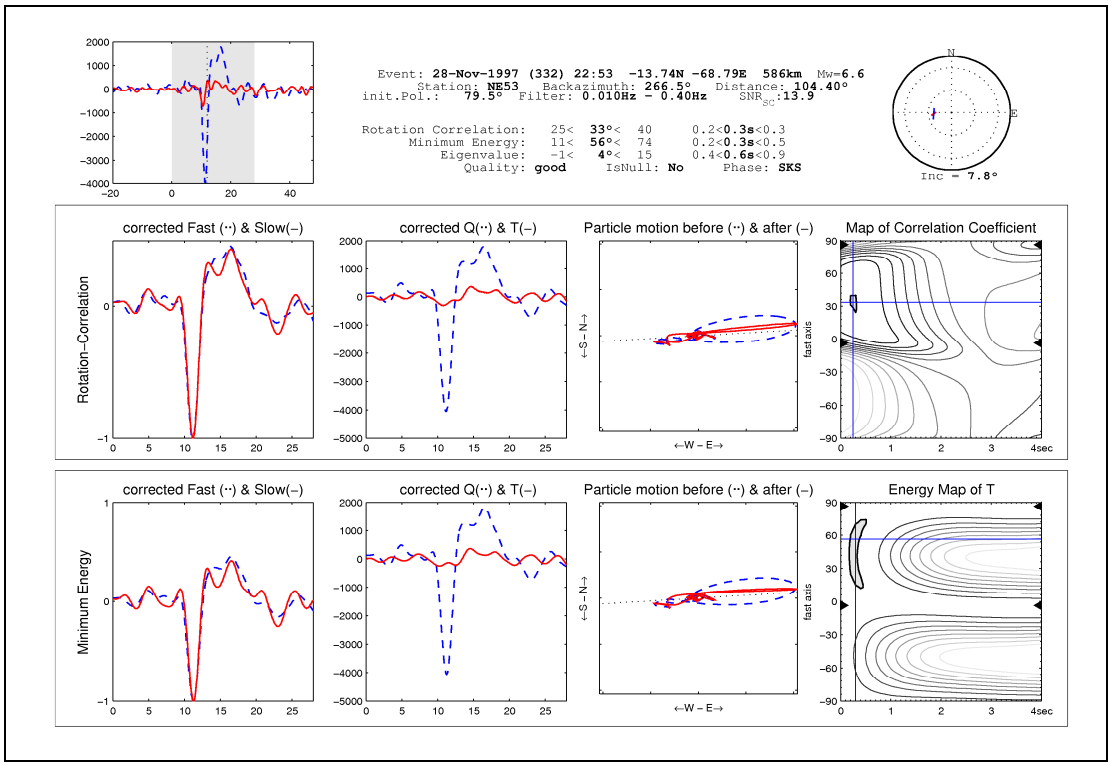

Figure 63: Typical event at NE53 with very small delay times (<0.5 sec) and larger errorbar for SC Φ

The backazimuthal coverage is very poor, with events coming only from a narrow window of easterly and westerly directions, respectively (Figure A- 11).

5.5.2.10. NE54

The NARS station NE54 close to the city of Brest in west Belarus is operational since July 1995. Data availability and noise level resulted however only in a total of three measurements, 1 good, 1 fair, and 1 fair Null. These data suggest a Φ of Φ = -60º and delay time of dt = 0.6sec. The backazimuth of the Null measurement (309.3º) coincides with the expected Null direction, and thus confirming the result.

5.5.2.11. NE55

The NARS station NE55 is located near Skvira, Ukraine. As for NE54, the limited data availability and quality resulted in only 6 splitting measurements: 1 good, 1 fair Null, and 4 good Nulls. Our “best-fit model” is largely based on the single good non-null measurement, but the backazimuths of the Null measurements are in good agreement with a Φ of Φ = -37º and delay time of dt = 0.8sec. Such finding is also consistent with the general NW-SE anisotropic orientation found close to the TTZ.

5.5.2.12. NE56

The NARS station NE56 is located close to the city of Odessa, Ukraine at the Black Sea and is the southern most station in this study. We identified 3 good, 1 fair and 2 good Null measurements, indicating splitting parameters of (Φ = -45º; dt = 0.6sec).

5.5.2.13. NE57 / NE58

NE57 was located near Gomel, Belarus, at 52.603°N, 31.081°E and NE58 further south close to Poltava, Ukraine, at 49.603°N, 34.543°E. The two temporary NARS stations provided only few useable three-component data. The quality of those seismograms was poor. Unfortunately no shear wave splitting measurement could be performed for these two stations.

5.5.2.14. OBN

The IRIS station OBN is located between the NW-SE trending Pachelma rift in the east, the SW-NE trending Volhyn-Orsha rift in the north and the Voronez massif in the south-west. [Zonenshain et al., 1990; Figure 49]. OBN operates since September 1988 and thus theoretically provides fairly good backazimuthal coverage. We were able to analyze 114 events, of which the automatic detection classified 12 good, 16 fair, 42 poor, 23 fair Null, and 37 good Nulls. The SC-stereoplot (Figure 64) indicates a complex pattern of Φ estimates, showing approximately Φ = -25º for events from WNW, +15º from ENE and -65º from ESE.

This stereoplot distribution is not easily explained. A possible model with such pattern is presented in Figure 64. It contains a two-layer case (Φ_{upper} = -30°; Φ_{lower} = -70°; dt_{upper} = 0.8 sec; dt_{lower} = 0.5 sec) with however a low dominant frequency of 2 sec, i.e. a relatively short wave length (see also Figure A- 16). The dominant frequency of SKS phases usually approximately 8 sec. Our best-fit two-layer model with 8sec dominant period is shown in Figure 65 and Figure A- 15. The splitting parameters of the upper layer are (Φ = -15º; dt = 0.6 sec) and of the lower layer are (Φ = 35º; dt = 0.4 sec). This model does not appropriately explain the Φ of Φ = 50º for earthquakes from ENE. Note, that both models do not explain the Nulls arriving from the NW. The influence of the dominant frequency on splitting is not yet well studied.

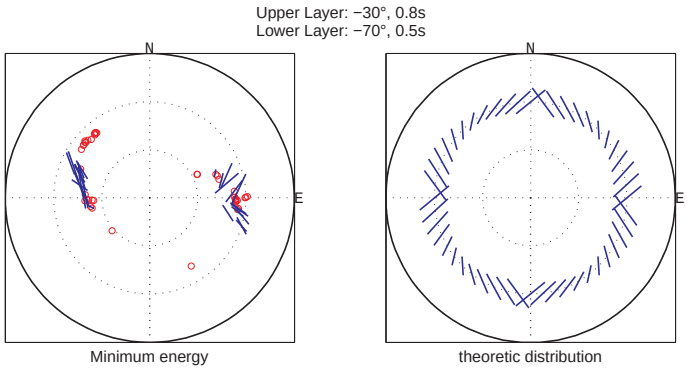

Figure 64: OBN stereoplot. Theoretical stereoplot is calculated for a dominant period of 2 sec.

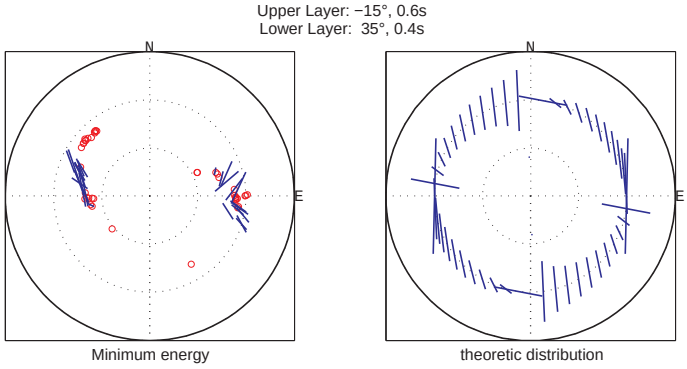

Figure 65: OBN stereoplot. Theoretical stereoplot is calculated for dominant period of 8 sec.

5.5.2.15. SUW

Station SUW in north-east Poland of the GEOFON network showed many high-quality SKS phases ready for splitting with generally high SNR. We recovered a total of 72 measurements. The manual classification resulted in 19 good, 21 fair, 2 poor, 15 good Null and 15 fair Null. However, our automatic classification criterion [Wüstefeld & Bokelmann, 2007] classified 13 good, 11 fair, 20 poor, 20 good Null, and 8 fair Null. The automatisation classifies most events from the west as Nulls, which is a result of the low RC delay times. A closer look at the SC Φs for the events manually classified fair or good, reveals their proximity to backazimuth (Figure 66a). The automatic classification thus improved the measurement, by preventing unjustified efforts to fit the data to a complex model.

Our best fit one-layer model with (Φ = -70º; dt = 0.8sec) does thus only account for the eastern hemisphere events (Figure A- 18). Nulls from a large range of westerly backazimuths might indicate the influence of heterogeneity. Wiejacz [2001] proposes the Tesseyre-Tornquist zone, where either the material of the contact zone is crushed into small clusters of possibly different orientations, or East- and West-European structure lay atop each other. The observed Φ of Φ = -70º aligns well with the finding for central Europe [cf., Brechner et al, 1998; Figure 49]. This might indicate a similar mechanisms on both sides of the Tesseyre-Tornquist, of and on the Craton.

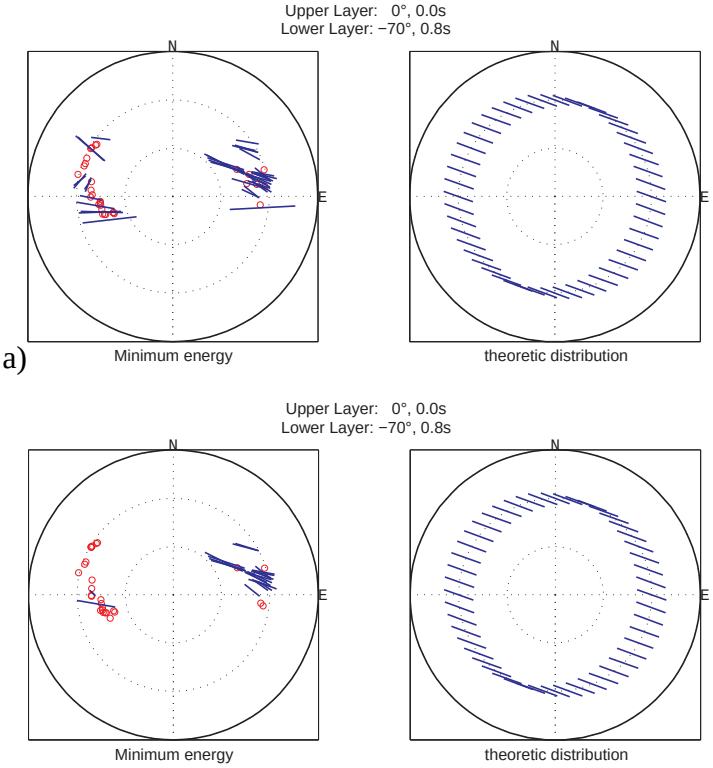

Figure 66: Comparison of stereoplots at SUW for a) manual and b) automatic quality determination.

5.5.2.16. TRTE

The GEOFON station TRTE close to the Estonian town of Tartu operates since June 1996 and resulted in 22 splitting measurements: 1 good, 5 fair, 7 poor, 6 good Nulls, and 3 fair Nulls (Figure A- 19). We interpret the results as a single layer with splitting parameters of Φ = -35º; dt = 0.7sec. This NW-SE orientation is almost perpendicular to those found in close proximity in the Baltic Shield (cf. station PUL and NE51).

5.5.2.17. Nulls from the Andean

Events from the west (Andean) result staggeringly often in Null measurements. This holds true for most stations over the whole EEC. This finding could indicate a (supposedly additional) deeper-than-lithosphere layer, common for the whole EEC. Interestingly, the stations of the German GRSN network in central Europe show opposite behavior [M. Walther & T. Plenefisch, pres.com. 2007]: here events from the Pacific subduction in the East result preferably in Nulls, while Andean events yield good measurements.

Wiejacz [2001] attributes the effect of Nulls from the west to a heterogeneity caused by the Tesseyre-Tornquist zone. He suggests that either the material of the contact zone is crushed into small clusters of possibly different orientations, or East- and West-European structure lay atop each other. That seems a plausible explanation for small scale effects at

a single station, but does not explain the consistency of that finding throughout the EEC. A continent-scale mechanism seems to be more likely.

These findings might be related to opposite inclining of the Φs: If the Φs in Central Europe inclined eastward, this would result in Nulls for waves coming from these directions. Within the EEC the inclination should differ from that to explain non-nulls from the East. First results of Φs derived from P-wave travel times cannot constrain such hypothesis (Figure 50; Chapter 5.4.2)

This is also beyond the resolution of the currently available data for shear wave splitting. Even with many more years of recordings it seems improbable to achieve sufficiently good backazimuthal coverage to resolve the dipping of fast axes beneath the EEC using shear wave splitting, as the long-running stations ARU and KIEV show.

5.5.3. Discussion

The major challenge when interpreting shear wave splitting is to constrain the depth of anisotropy. Asthenospheric anisotropy is generally interpreted for if the plate motion is parallel to the observed seismic fast direction. Olivine develops a preferred crystal orientation (CPO) in association with present deformation and flow of the asthenospheric mantle that accommodates or causes plate motion, which is the main cause of upper mantle anisotropy beneath oceanic basins [e.g., Hess, 1964; Tommasi, 1998; Montagner, 1998, 2002; Fontaine et al., 2005, 2007].

On the other hand, lithospheric anisotropy is due to past tectonic processes. If these are assumed to be vertically coherent [Silver, 1996], one possible supportive argument is parallelism of seismic fast S-wave orientation and surface geological features. For the EEC thick sediments cover many structures [Laske & Masters, 1997]. Here, the crustal structure is reveal by regarding magnetic anomalies. A different approach can be the correlation between Bouguer gravity anomaly and topography in order to identify “mechanical anisotropy” [Simons & van der Hilst., 2003]. This technique however requires topography which is often eroded in the stable continental interiors, as is the case for the EEC. But first, let us compare the shear wave splitting results with predicted parameters.

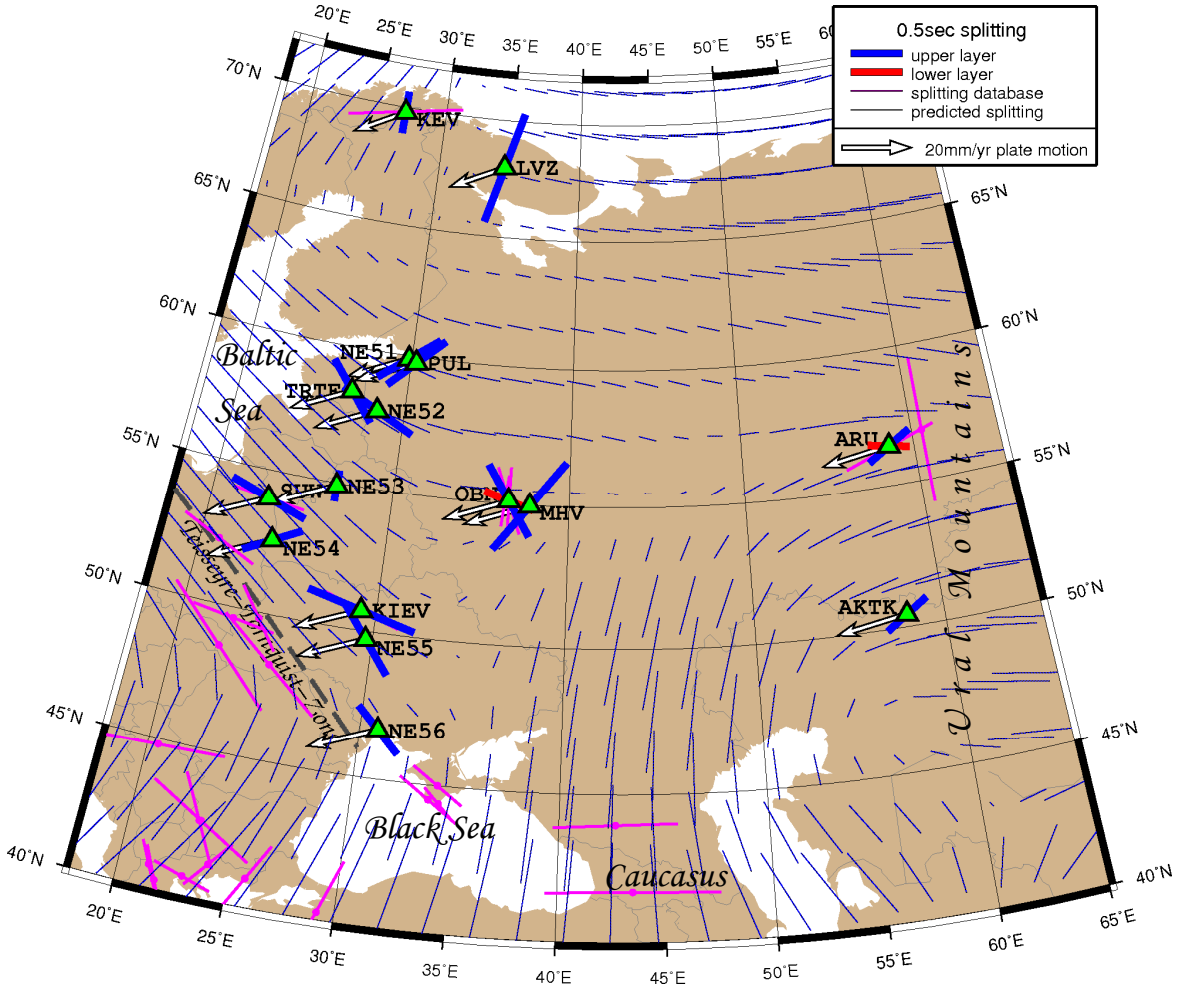

Figure 67: Overview of splitting parameters in the region of the East European Craton. The results of this study are presented in bold bars, blue for upper layer (or single layer) and red for lower layer (ARU, OBN). Magenta bars represent the values from the splitting database. Thin, blue lines represent predicted splitting parameters using the surface wave model of Debayle et al. [2005]. Plate motion vectors are plotted as white arrows.

5.5.3.1. Surface-wave derived splitting parametersg

The almost vertically incident SKS waves used in splitting analyses integrate the anisotropy along their travel path. Using the anisotropic layers determined from surface waves studies, Montagner et al. [2000] devised a method to calculate predicted splitting parameters (Figure 67; see also Chapter 4.6.2.). In continental regions, the geologic domains are generally smaller than the lateral resolution of surface waves (~400km), which may thus only reflect lateral integration of various anisotropic domains. A comparison of global splitting database of mostly continental stations with the predicted splitting (Chapter 4.6.2) showed however general coherence.

The predicted splitting parameters for the EEC show three prevailing domains: First in the west below the Baltic Sea, the predicted fast directions are oriented ENE-WSE, which is

parallel to the TTZ. This behavior has already been discussed in Chapter 4.6.2. The Φs turn gently southward beneath Romania and the Black Sea. This coincides with observed splitting directions, except for NE51 and PUL. Second, further to the East large splitting times with N-S azimuths are observed in the Caucasus, perpendicular to the observations by Dricker et al. [1999]. These directions turn to approximately E-W orientations in the Urals. This fits rather well with the observations for AKTK and ARU. At the latitude of ARU the orientation changes smoothly from ESE-WNW in the south to ENE-WSW orientations in the North. Interestingly, both of these directions are recovered in the two layer model.

The third dominant pattern is North of 57ºN, where the predicted splitting directions rotate from E-W in the Urals to N beneath eastern Scandinavia. These northerly directions are consistent with splitting results at KEV and LVZ. The large deviation for LVZ (one of the best stations in this study) from predicted parameters may be attributed to the resolution capacity of the surface wave model in this northern region. These three domains encompass a region of low predicted splitting beneath Sarmatia. Most notably close to OBN/MHV the predicted splitting remains ambiguous, with virtually no predicted splitting delay times and orientations which are varying on a short-scale. This is an agreement with the observations for these two stations with many Null measurements from nearly all available backazimuths.

The coherence observed between predicted and observed splitting parameters in large parts of the EEC indicates that both methods at least “see” the same anisotropies. This is in agreement with the global comparison presented in Chapter 4.6.2. Local discrepancies should be attributed to the relatively low lateral resolution of surface waves and thus to small geologic domains.

Although shear wave splitting represents the depth-integrated anisotropy along the travel path, we compare the Φs with those recovered at each depth layer of the surface wave model. Figure 68 shows for each station variation with depth of the angular difference between the Φs determined by splitting and surface wave tomography. Also shown is the relative magnitude of anisotropy in each layer. If the main contribution of splitting originates in the strongest anisotropic layer, the orientations of both methods should be parallel there. This is the case for KIEV, MHV, N52, OBN and SUW. For OBN and MHV, the absolute anisotropy is small, and the good correlation is only in the lower layers which are only weakly constrained in surface wave inversions. For SUW and NE52 the results strongly indicate that the observed splitting occurs in the upper 150 km and 100 km of the mantle, respectively. At KIEV the difference between the two methods is low (<12°) at the depth interval of 100 – 175km which constrains the observed splitting to this depth interval.

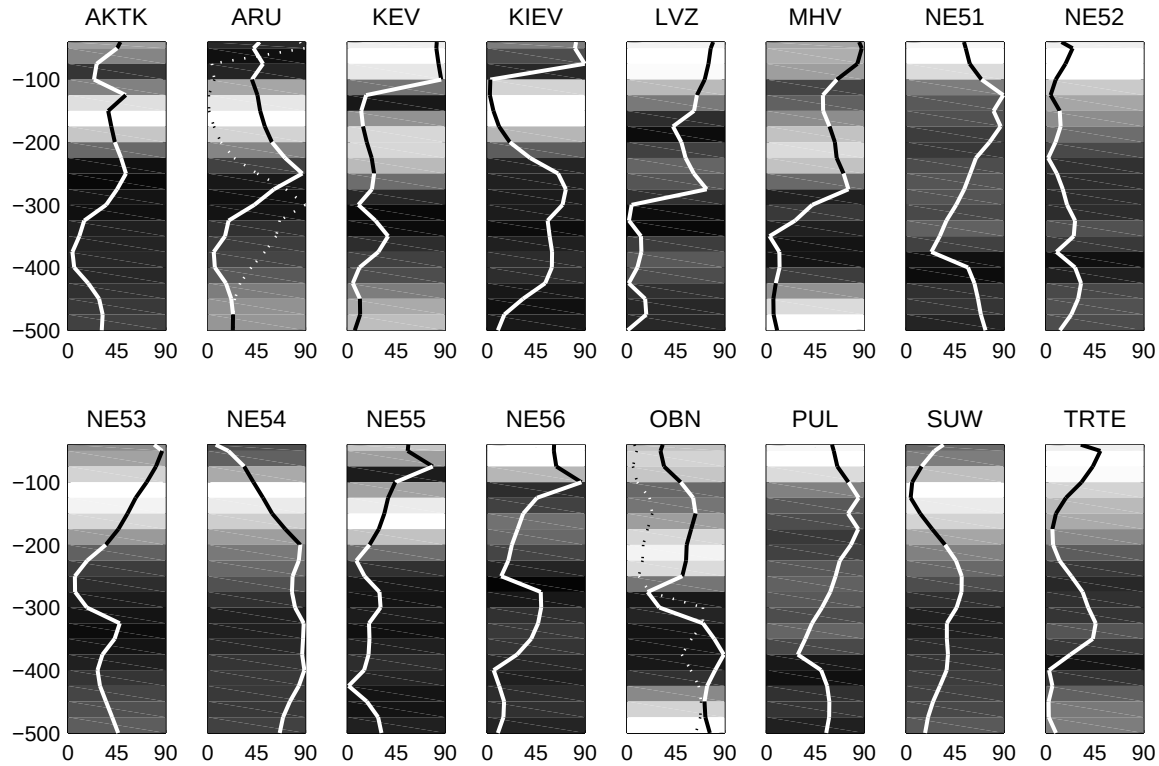

Figure 68: Variation with depth of anisotropy orientation between surface wave and splitting model at each station of the EEC. The difference varies between 0° (orientations are parallel) and 90° (perpendicular). Dashed line corresponds to lower layer if two a layer model is identified from splitting. The variation of the line color is only for display purposes. Background shading is the relative magnitude of anisotropy. For each station, white represents the maximum of anisotropy beneath that station, black is the minimum. This limits the comparability of each plot, but allows for easily identifying the relative magnitude variation with depth.

An interesting example is also station NE54. Predicted and observed splitting is almost perpendicular (Figure 67). The depth variation indicates that in the upper 75km correlation is rather good (<25°). Only below 200km, the difference is constantly larger than 75°. This may suggest the large contribution of the 200-500km depth layers to the predicted splitting, and that the observed splitting at NE54 results from the upper 75km of the mantle.

5.5.3.2. Plate motion

The plate motion of the EEC in a hotspot reference frame is small (20mm/year, Gripp & Gordon [2002]), however significantly different from zero (stagnancy) and might thus in principle be able to produce a CPO. Only longer timescales (with constant plate motion directions) are required than for fast moving plates. Other hotspot reference frame models show also clear evidence for plate motion, but with smaller magnitude [10mm/yr; Gripp & Gordon, 1990]. NoNetRotation frames have plate motion magnitude of 25mm/yr but pointing in opposite directions [Drewes, 1998; Sella et al., 2002]. This is however expected to produce similar final-stage CPO due to the 180°-symmetry of anisotropy.

Figure 69 shows the angular difference of the plate motion direction s at each station and the observed Φ. The difference is limited between 0° and 90°, which reflects parallel and perpendicular orientations, respectively. Independent of model, the correlation between plate motion direction and Φ is poor.

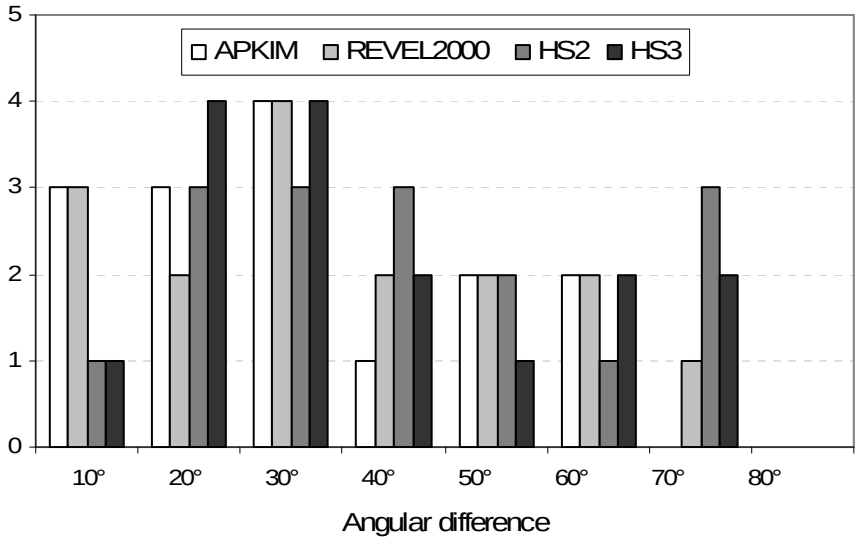

Figure 69: The splitting directions of the 16 analyzed stations on the EEC show no correlation with any of the 4 plate motion models. Neither a preference for parallelism (0°) nor perpendicular adjustment (90°) of plate-motion-vector and Φ can be observed.

Coherence between observed fast axis and plate motion vector can only be observed for ARU, NE51/PUL and NE54. Since plate motion is uniform and splitting orientations change over short spatial distances, particularly in the west, this coherence seems to be only coincidental. At the other stations, plate motion vector and Φs are almost perpendicular. The absence of coherence between splitting and plate motion indicates thus at most only small, if any, asthenospheric contributions to shear wave splitting. Topography at the base of the lithosphere might also cause small scale variations.

5.5.3.3. Comparison with magnetic anomalies

Subsurface imprints of tectonic activities are visible in magnetic maps. As discussed in Chapter 5.4.3, magnetic anomalies reflect only crustal features. This exclusive constraint can not be achieved by similar methods, e.g. using topography and gravity anomalies to detect subsurface features for comparison with anisotropy orientations [Simons & van der Hilst, 2003]. The gravity field always contains long-wavelength information of the mantle which can not be filtered out completely.

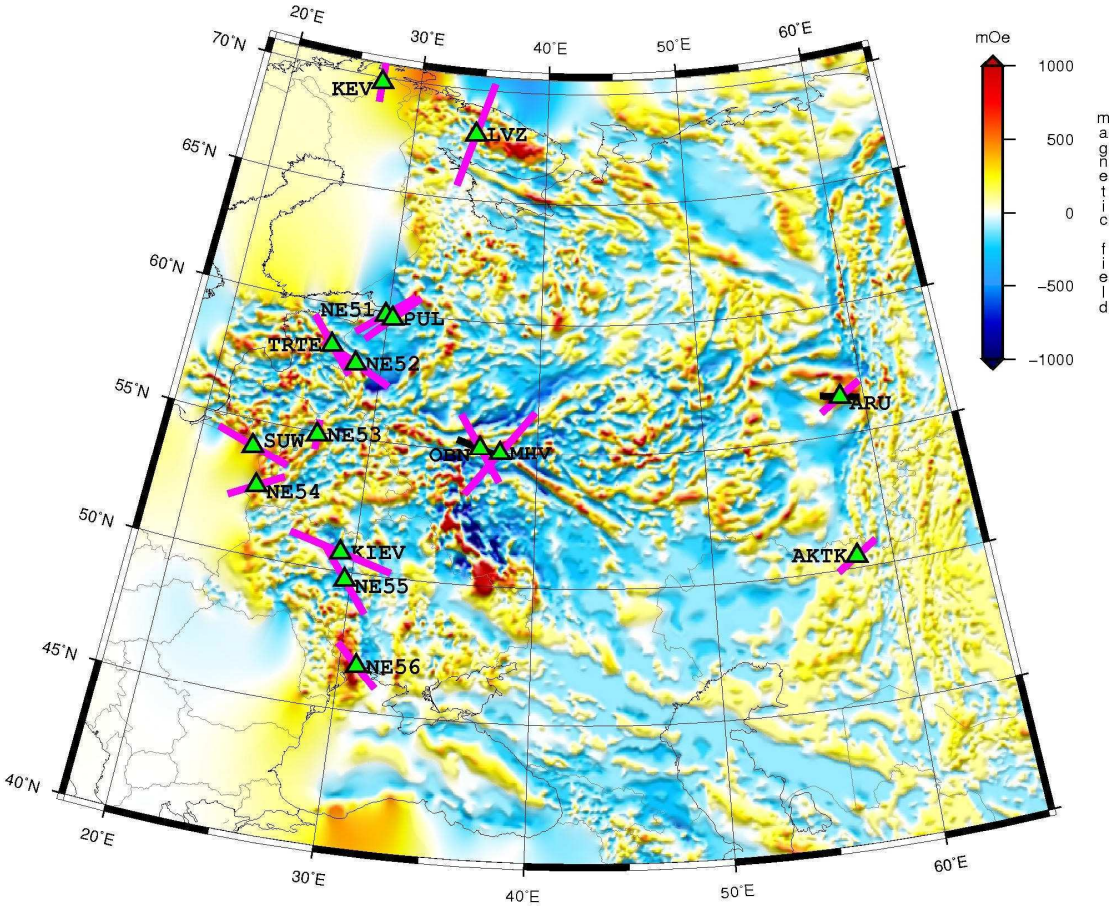

Figure 70: Map of magnetic intensity anomaly. Clearly to identify are the Ural Mountains and the Pachelma Rift, south-east of station MHV. Φs are plotted in magenta and black for the upper and lower layer respectively.

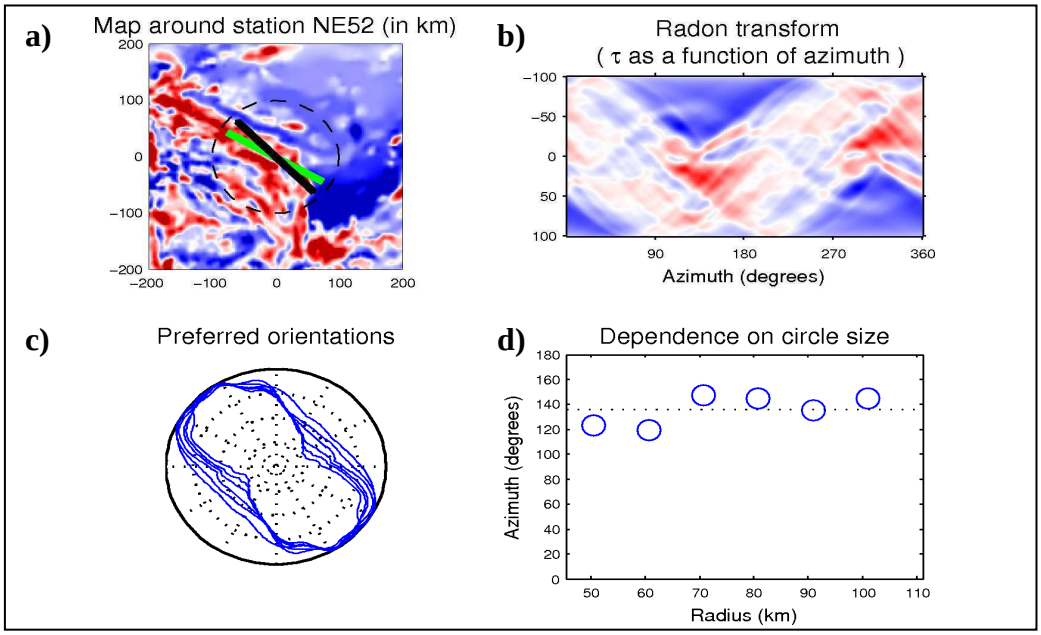

Figure 71: a) Magnetic intensity map around station NE52. Dashed circle indicates area of largest test region. A radon transform (b) reveals a mean orientation of magnetic alignments of 135° (black line in a). This is in good agreement with the Φ of -60° observed by shear wave splitting (green line in a). c) shows the orientation distribution for six different test regions. d) The preferred orientation of a smoothed version of c) is stable for various radii around the station

How can we relate magnetic structures to tectonic regimes and, more specifically, to seismic anisotropy? In collisional regimes folding and faulting yields magnetic structures parallel to the collision front [Chapter 3.4.3]. Seismic fast S-wave orientations in orogens are also oriented along the main trend of the mountain chain.

Magmatic dikes represent extension. In high-resolution aeromagnetic maps dikes and dike-swarms can be clearly identified as linear structures of alternating positive and negative anomalies. The associated cracks are filled with volcanic material of different magnetic properties than the surrounding rock. Generally these basalts have a higher iron contents and thus a higher susceptibility. In the centre of rift zones, seismic anisotropy is related to magma (fluid) filled cracks, which results in seismic fast axes oriented parallel to the rift [Gao et al., 1997; Kendall et al., 2006, Chapter Rifting].

Bokelmann et al. [in prep, 2007] compare seismic fast S-wave orientations with dominant alignments in a high-resolution (1km) magnetic map of the North American Craton. A Radon Transform of the magnetic intensity reveals dominant orientations of linear features. The orientations are calculated for several circular test regions around each station with radii between 50 and 100km. The smallest circle thus represents approximately the Fresnel zone in the uppermost mantle for shear waves with 10sec dominant period. This ensures that similar regions of crust and mantle are examined. Similar azimuths recovered from several test regions indicate the robustness of the result.

The authors find a very good correlation of shear-wave splitting Φs and crustal magnetic fabric for the North American Shield. Especially in the Western superior province, magnetic anomalies and Φs are parallel to directions of ancient Suture zones in that region [e.g., Hoffman, 1989]. Also, the gradual rotation within that region is visible in both datasets. There is little correlation for the more complex (active) tectonics in western North America

Magnetic anomalies reflect compositional and/or structural contrasts in the crust. A parallelism between Φs (associated with mantle processes) and crustal magnetic lineaments thus suggests vertically coherent deformation (VCD). Applied to the stations on the EEC, a heterogeneous picture evolves: fast axes on the Polish-Lithuanian-Belarus terrane (TRTE, NE52, NE53) are sub-parallel to the curved trend of the magnetic anomaly (Figure 70; Figure 71; Table 6).

More generally, for the whole EEC the difference in fast axis orientation and magnetic trend has a maximum at around 25°. This remains if only trends with standard deviations smaller than 25° are considered. The standard deviation has been determined from the different trends of the six test areas around the corresponding station. Assuming an error of 15° in both Φs and magnetic alignment, the deviation is still relatively large. It might be attributed to (a) the varying tectonic setting across the EEC; (b) small amount of available

seismic stations; (c) the resolution of the available magnetic data (5km in contrast to 1km in North America) which does not resolve small-scale features; (d) contributions of sub-crustal anisotropy with systematically different orientation.

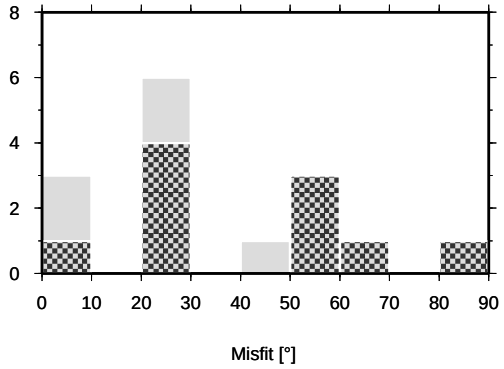

Figure 72: Histogram of Table 6. Hatched columns corresponds to misfits with magnetic trend standard deviation smaller than 25°

Station	Magnetic trend Ψ	standart deviation σ	|Φ - Ψ|
AKTK	172.5°	13.1°	63.5°
ARU	83.0°	4.3°	28.0°
KEV	-	-	-
KIEV	155.0°	4.4°	50.0°
LVZ	135.5°	11.1°	54.5°
MHV	93.0°	8.2°	58.0°
NE51	5.0°	30.3°	42.0°
NE52	140.0°	12.2°	20.0°
NE53	1.5°	9.7°	1.5°
NE54	59.5°	36.5°	0.5°
NE55	135.5°	62.5°	7.5°
NE56	163.0°	0.5°	28.0°
OBN	67.5°	10.3°	82.5°
PUL	16.0°	26.3°	25.0°
SUW	136.5°	30.0°	26.5°
TRTE	118.0°	0.5°	27.0°

Table 6: Difference in (upper layer) seismic anisotropy fast axis orientation Φ and dominant magnetic alignments Ψ for stations of the EEC. Station KEV is outside the available aeromagnetic data of the Former Soviet Union.

Major differences (>45°) are found for AKTK, LVZ, KIEV, MHV and OBN. The latter two stations are located close to the mutually perpendicular Central Russian Rift and the Pachelma Rift (Figure 47; Figure 54), both of which showing clear magnetic signatures. However, anisotropy in such a rift triple-junction is not yet understood, but is likely to produce complex overprinting of lithospheric anisotropy. Gao et al. [1997] analyzed the effects of rifts using a profile which crosses the Baikal rift. They determined a characteristic rotation from rift-parallel to rift perpendicular with growing distance from the rift (see also Chapter 3.4.1). The effect on the anisotropy in a stable shield caused by two superimposing rifting episodes should be complex and cannot be determined from a single station.

The observed splitting directions are less well constrained, showing a complex backazimuthal pattern and many Nulls, which is also observed for KIEV. The theoretical splitting (Chapter 5.5.3.1) predicts in this region virtually no splitting, in agreement with the observations. It is therefore plausible to assume, that low anisotropy in Central and North-Eastern Sarmatia exist, and poorly constrained fast directions thus causing the poor correlation with magnetic trends.

On the other hand, the 28° difference for the Ural station ARU might be explained by (a) the distance from the deformation front and (b) the strong magnetic anomaly north of ARU, which trends ENE-WSE. The correlation for stations in the Polish-Lithuanian-Belarus Craton indicates vertically coherent deformation of crust and lithosphere in this region.

5.5.4. Interpretation

The comparison of shear wave splitting Φs with several other datasets give hints for lithospheric origin of anisotropy, albeit of relatively low strength with delay times between 0.4 and 1.1 sec. Lithospheric anisotropy in continental regions is in agreement with a recent global model of strain orientations by Conrad et al. [2007]. They use a viscous model driven by mantle density heterogeneities and (No-Net-Rotation) plate motion to determine the “infinite strain axis (ISA)”. This ISA should approximate LPO if olivine crystals rotate faster towards ISA than the ISA changes along flow lines [Kaminski & Ribe, 2002].

Good fit between this model and observed splitting Φ lead Conrad et al. [2007] to locate oceanic anisotropy in the asthenosphere (in agreement with Montagner, [2002] and Becker et al. [2003]). In continental regions the fit is less well, indicating lithospheric origins of anisotropy. Conrad et al. [2007] point out, that the fit for their model improves for many continental regions (particularly eastern and western US, Africa, South America) when allowing lateral viscosity variations. This effort however degrades the fit for Eurasia, which the authors associated either with the slow plate motion velocity or with a bias of station coverage in orogenic and cratonic areas.

Fouch & Rondenay [2006] suggest that the oceanic asthenospheric flow model might not be appropriate beneath continents. Becker et al. [2007] present a stochastic model of anisotropy, which shows a relatively short correlation length of splitting parameters of L ~ 600km for orogens and volcanic zones. A smoother pattern (L ~ 1600km) is observed in stable continental regions, which the authors relate to large-scale tectonic processes such as past continent-continent collision and thus lithospheric anisotropy. In oceanic regions the correlation length determined from surface waves is much longer (L ~ 4500km). This strongly supports the idea that ongoing large-scale mantle convection processes cause the observed oceanic anisotropy within the asthenosphere.

Supporting this finding, many indicators of anisotropy in the lithosphere of the EEC have been presented in the previous chapter. Additionally, the weak observed anisotropy may explain the difficulties reported by Conrad et al. [2007] to constrain that particular region within the global model. The shear-wave splitting results of stations on the East European Craton indicate regional conformity on length scales smaller than the global average determined by Becker et al. [2007]. Each tectonic block seems to have its own characteristic anisotropy pattern.

5.5.4.1. The Baltic Shield

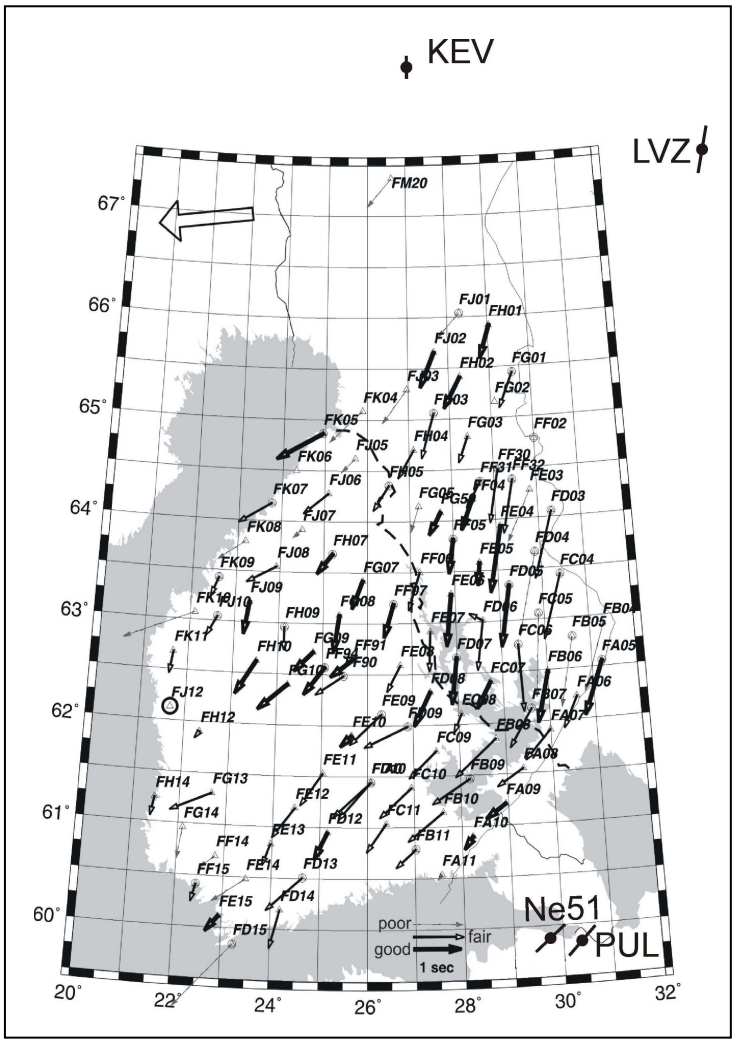

Figure 73: Anisotropic fast azimuth of a single shear wave splitting event in the SVEKALAPKO experiment region [modified after Vecsey et al., 2007]. The backazimuth of that event is indicated by the large arrow in the upper left corner. The inversion method of Plomerova et al. [1996] has been applied, which simultaneously inverts for P-wave and SKS splitting in three dimensions. Therefore only the results of single events can be analyzed at a time. The results of the station analyzed in this study (solid circles; KEV, LVZ, NE51, PUL) have been added to the plot.

The observed shear-wave splitting Φs for the Baltic Shield show NS-directions in the North (KEV/LVZ) and NE-SW directions in the south-eastern part of the Baltic Shield (PUL/NE51). This discrepancy between the north and south might perhaps be interpreted as different origins of anisotropy. However, observations by Vecsey et al. [2007, Figure 73] of the dense array of the SVEKALAPKO-98/99 experiment in central Finland indicate a smooth, progressive transition in fast directions in this region from northerly directions in the North and Central Finland to NE-SW directions of anisotropy in southern Finland. Our result indicates that this trend continues also east of the SVEKALAPKO experiments region towards the margin of the Baltic Shield.

Seismic tomography shows thinning lithosphere towards the west, the rim of the craton (Figure 53). Shorter delay times there (dt_{KEV} = 0.4 sec) than further east (dt_{LVZ} = 1.1 sec) thus show positive correlation with lithospheric thickness in this region.

For the two northern stations, a positive correlation between delay time and lithosphere thickness (as determined from surface wave tomography; Figure 53) suggests lithospheric origins of anisotropy. A missing correlation of the Φ with the absolute plate motion [Gripp & Gordon, 2002; Figure 49] supports this hypothesis. The anisotropy beneath the Baltic shield seems to be caused by fossil deformation recorded in the lithosphere.

5.5.4.2. Sarmatia

Stations can be divided into two classes: the poorly constrained three NARS stations and three stations reflecting complex anisotropy due to the tectonic setting. MHV, OBN and KIEV are located on (or close to) shields and in the vicinity of two perpendicular rifts. For KIEV these rifts are the Volshyn rift in the north (separating Fennoscandia from Sarmatia) and the younger Pripyat-Dniepr-Donets Aulacogen (separating the Ukrainian Shield from the Voronezh Massif). OBN and MHV are located at the triple-junction of the three units making up the EEC.

Gao et al. [1997] analyzed the effects of rifts using a profile which crosses the Baikal rift. They determined a characteristic rotation from rift-parallel to rift perpendicular with growing distance from the rift. The effect on the anisotropy in a stable shield caused by two superimposing rifting episodes should be complex and cannot be determined from a single station.

The complex tectonic setting appears to be reflected in the shear-wave splitting data. Yergorova et al. [2004] report several NE-SW and NW-SE trending major crustal faults, reflecting a multi-stage tectonic history. The Pripyat Trough and Korosten Pluton might have played a major role. Shear-wave splitting in such domains is not yet understood [Özlalaybey & Chen, 1999; Pulford et al., 2003; Crampin & Gao, 2006; Heintz & Kennett, 2006].

The observed Φ at KIEV aligns well with the general pattern of shear wave splitting measurements in central Europe. Comparison with the other stations along the TTZ indicates a certain spatial coherence of such Φs at a large-scale (see SUW, NE54, NE55).

One hypothesis to explain the spatial coherence across the TTZ might perhaps be current mantle flow around the EEC causing splitting directions beneath this part of Eastern Europe. This would however require that the same mechanism continues east of the TTZ, indicating mechanical erosion at the lateral edge of the EEC lithosphere. Such lateral erosion would be consistent with thinner lithosphere beneath Sarmatia (Figure 53). This interpretation is at the limit of resolution of tomography available at this moment.

Zielhuis & Nolet [1994] suppose the TTZ as an ancient (south-westward dipping) subduction zone. In such subduction environment, the observed Φs parallel to the TTZ in the western part of the ECC would reflect anisotropy in the hinterland of the lower plate. The influence of the subduction process in the hinterland is only poorly discussed in literature. Numerical models suggest strong variations in the forearc region of subduction [Lassak et al. 2006; Kneller, 2007]. Nakajima & Hasegawa [2004] observed a complex pattern of anisotropy for stations in Japan across the subduction arc, with forearc stations oriented arc-parallel and backarc stations arc-perpendicular Φs. Further studies are needed to clarify the influence of subduction to the anisotropy in the hinterland.

To judge whether the spatial coherence within the tectonic units of the EEC may be explained by fossil deformations, we may resort to geological observations of fabrics at the surface or to spatial trends in geophysical data such as anomalies in the magnetic field (Figure 51). Unfortunately, the number of studies published in international literature is only starting to grow now.

5.5.4.3. Polish - Lithuanian - Belarus terrane

The three stations TRTE, NE52, and NE53 are located in the Polotsk-Kurzem fault zone [Figure 48; Bogdanova et al., 2006]. Faults within this zone are parallel to the observed Φ. Also the magnetic anomalies follow that trend. Finally, these directions differ sharply at a short distance from those observed in adjacent Fennoscandia. All these arguments support lithospheric anisotropy, which is coherent throughout the crust.

This region has only recently been proposed as a separate tectonic unit [Bogdanova, 2005]. The anisotropy studies presented here support this interpretation. In future studies the tectonic history of this block might be revealed, eventually allowing to further identify the processes causing the anisotropy orientations in much more detail.

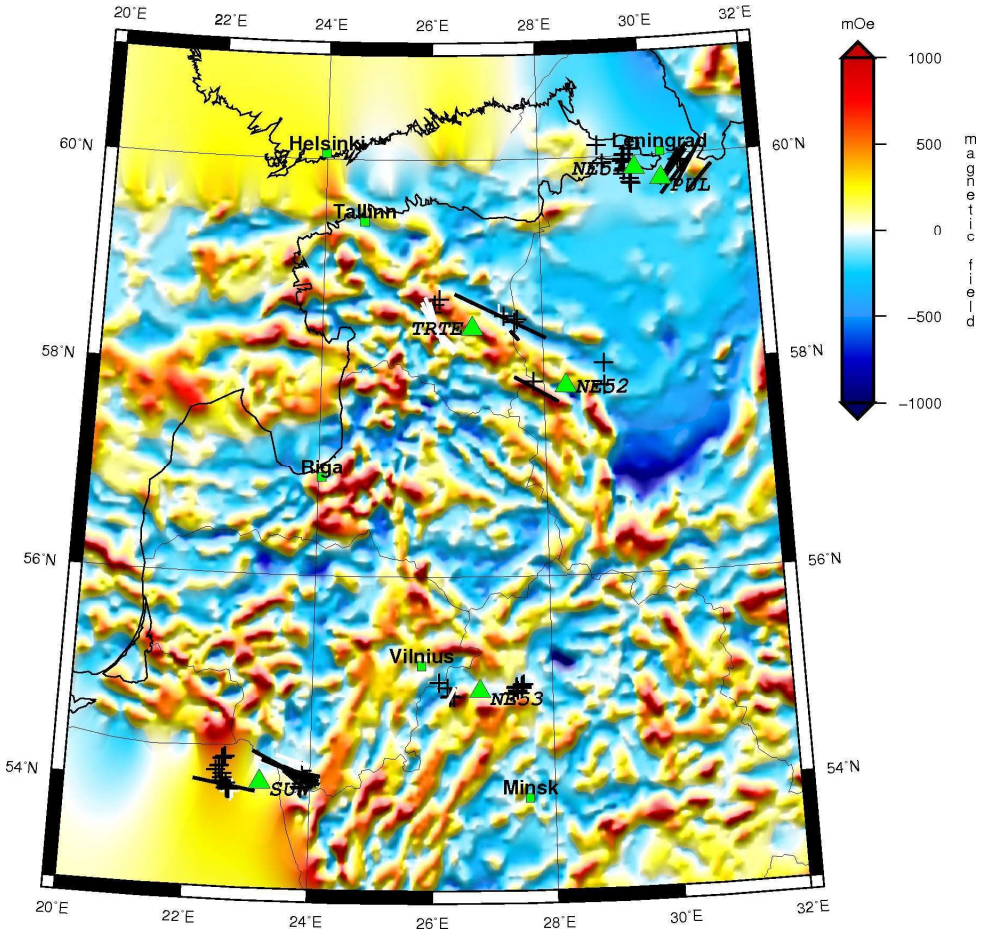

Figure 74: Magnetic anomaly map in the region of the Polish-Lithuanian-Belarus terrane. Also shown are the individual good (black) and fair (white) splitting results (Nulls as crosses, non-Nulls as vectors with lengths according to delay time) at their projected position at 200km along the ray path.

5.5.4.4. Volgo-Uralia

Both stations close to the Ural Mountains show splitting directions perpendicular to the geologic trend of the mountain chain (Figure 75). Furthermore, the two layer model for ARU shows directions sub-perpendicular to the mountain chain. The Φ of the single layer determined for AKTK is parallel to the upper layer found for station ARU.

Despite a distance of 770km, AKTK and ARU show similar splitting patterns. This might suggest a common tectonic framework; a similar mechanism causing anisotropy at depth seems reasonable. Interestingly, the observed Φs for ARU and AKTK are also parallel to current plate motion (Figure 49). Nevertheless, ancient processes seem preferable when considering the results of SVE (56.8ºN, 60.6ºE)within the mountain chain of the central Urals. The model of vertically coherent deformation [e.g., Silver, 1996; Chapter 3.3; Chapter 3.4.3] associated with the Ural orogeny, predicts Φs parallel to the mountain chain. Vinnik et al. [1992] studied analogue seismograms of station SVE. They report a Φ of Φ = 0° and a delay time of dt = 1.4sec. This direction is parallel to the trend of the mountain chain.

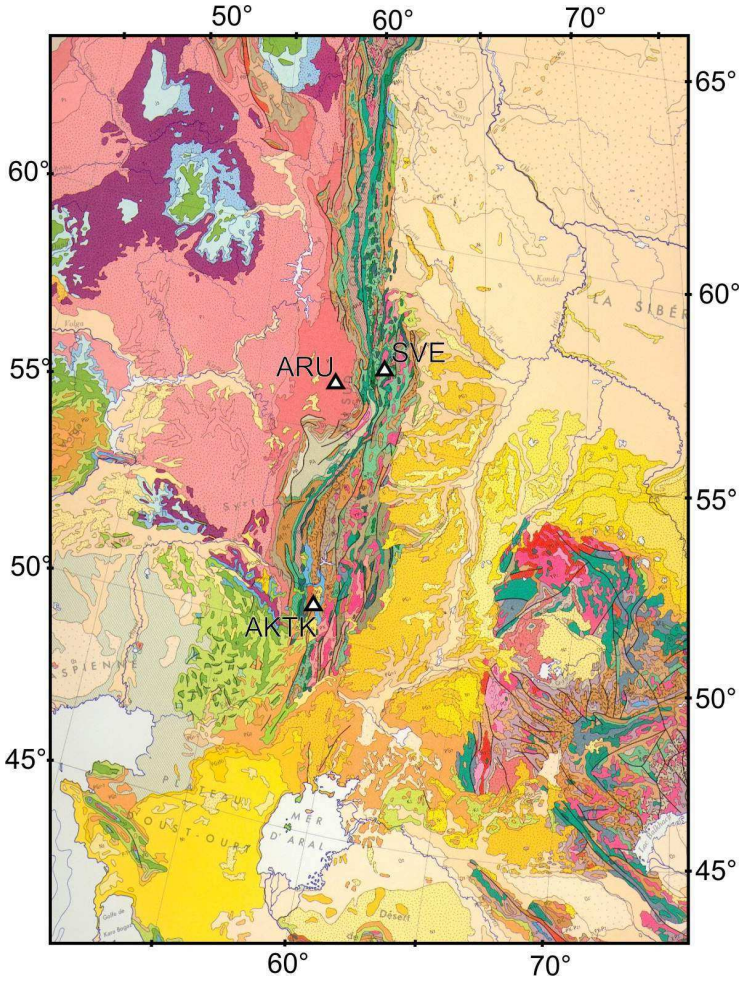

Figure 75: Geologic map of the Uralides [modified from the UNESCO Geological world atlas, 1976]. ARU is located in the early Permian foredeep, which coincides with a eastward bend in the general NS-trending Urals. AKTK is located on the western front of the mountains

The distance from ARU to the deformation front could indicate that the region beneath ARU is beyond the reach of influence of the deformation mechanisms of the Ural orogeny, i.e. in the foredeep, other mechanisms may dominate: a) large-scale thrusting associated with subduction process or b) that the observed Φs reflect ancient plate motions direction, either during the assemblage of the Cratonic blocks [Bogdanova, 1996] or during collision of the EEC with north-western Asia and thus the Uralian Orogeny [Brown et al., 1996].

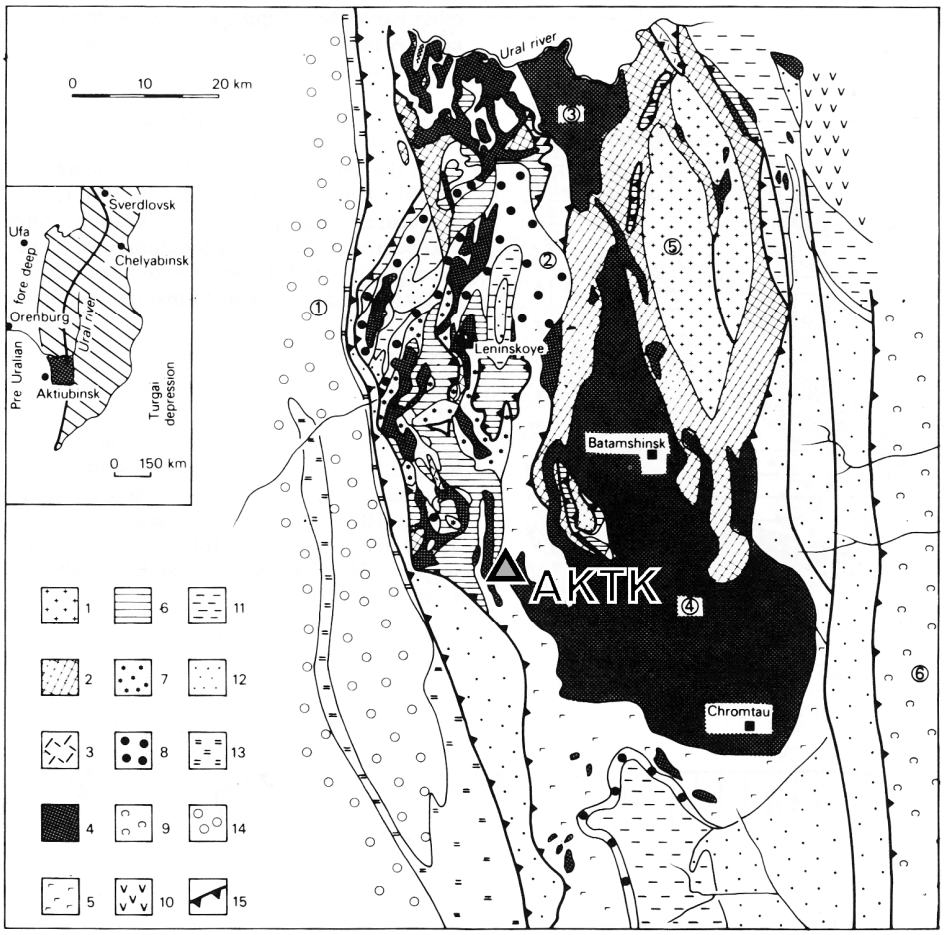

Figure 76: Geological map of the South Sakmaran zone [after Zonenshain et al. 1990]. Autochthon: 1. Precambrian; 2. lower Ordovician; 3. middle-upper Ordovician. Allochthon: 4. ultramafics, gabbro, serpentennite mélange; 5. Silurian oceanic basalts; 6. Silurian cherts; 7. island arc assemblages; 8. neo-autochthon; 9; Middle Devonian oceanic basalts; 10. Middle Devonian island arcs; 11. Middle-Upper Devonian rocks; 12. upper Devonian-Lower Carboniferous; 13. Carboniferous; 14. Permian; 15. main thrusts. Basement is hatched. Encircled numbers are: 1. Uralian foredeep; 2. Sakmara Zone; 3. Khabarny ultramafic massif; 4. Kempirsai ultramafic massif; 5. Ebetin antiform ; 6. West Mugodjar zone. Thick line corresponds to the Main Uralian thrust

5.5.5. Concluding remarks

We analyzed the shear-wave splitting of 16 broad band seismograph stations on the East European Craton. The observed splitting is generally low, with delay times varying between 0.4 and 1.1 seconds. This is in agreement with general findings in several other shield regions (see Chapter 5.2), although some of the highest splitting delay times (>2sec) on the globe are observed on the Canadian Shield.

In order to constrain the depth of anisotropy we compared the observed Φs with several datasets: (1) The Φs vary for each tectonic unit, indicating “frozen-in”, lithospheric anisotropy. Such interpretation is supported by (2) a variable correlation of Φs with plate motion direction, which seems to be parallel only by chance at some stations and thus does not reflect large-scale asthenospheric processes. (3) the trend of (crustal) magnetic

structures aligns relatively well with the observed splitting orientations at half of the analysed stations (Figure 72). This indicates vertically coherent deformation throughout crust and upper-most mantle and supports the idea that continental splitting reflects the last tectonic event. It becomes thus clear that aeromagnetic data can be used as a proxy for crustal fabric orientation. The aeromagnetic data are especially valuable in inaccessible regions or regions with thick sediments, which are covering the underlying tectonics. (4) future geological observations of mineral fabrics might further constrain these conclusions.

There appears to be no indicator of present day mantle flow causing the anisotropy. The spatial coherence of Φs across the TTZ is however an intriguing observation. If caused by current mantle flow, this would however require that the same mechanism applies across the TTZ. Such mechanism might be lateral mechanical erosion at the edge of the EEC lithosphere. Such lateral erosion would be consistent with thinner lithosphere beneath Sarmatia (Figure 53). Such interpretation is however at the limit of resolution of tomography and anisotropy studies available at this moment.

For the remaining stations of the EEC, no indicator of mantle flow deviated by the keel of the EEC can be observed in splitting measurements. Also, the observed delay times are too small to resolve for any dipping anisotropies. We discuss in Appendix (Chapter 7.1) the implications, if the origin of anisotropy would be located in the D”-layer at the core-mantle boundary.

The availability of information about the geology of the EEC in international literature is only growing by now. Furthermore, the station coverage of the vast area of the East European Craton is only sparse at this moment. The findings of this study should however build a central framework for the planning of further studies, focusing of specific parts of the EEC. Suitable regions for such seismic experiment would be an array over the Polish-Belarus-Lithuanian Terrane, the Pachelma Rift /Certral Russian Rift system junction close to OBN and MHV and across the Ural Mountains.

Integrating the hitherto largely unidentified anisotropy beneath the EEC in the global geodynamic models might eventually lead to a better understanding of processes in the deep Earth. Later comparison with ongoing work in adjacent Central Europe, west of the TTZ [Walther et al., 2007] and the Mediterranean [Schmid et al., 2004] will eventually improve the understanding of anisotropy producing processes of the large Eurasia-Mediterranean tectonic plate system.

6. References

Alvarez, W. (1982), 'Geological evidence for the geographical pattern of mantle return flow and the driving mechanism of plate tectonics', *J. Geophys. Res.* **87**, 6697-6710.

Anderson, M. L.; Zandt, G.; Triep, E.; Fouch, M. & Beck, S. (2004), 'Anisotropy and mantle flow in the Chile-Argentina subduction zone from shear wave splitting analysis', *Geophys. Res. Let.* **31**, 23608-+. DOI:10.1029/2004GL020906

Ando, M. & Ishikawa, Y. (1982), 'Observations of shear-wave velocity polarization anisotropy beneath Honshu, Japan: two masses with different polarizations in the upper mantle', *J. Phys. Earth* **141**, 191-199.

Andrews, D. L.; Gordon, R. G. & Horner-Johnson, B. C. (2006), 'Uncertainties in plate reconstructions relative to the hotspots; Pacific-hotspot rotations and uncertainties for the past 68 million years', *Geophys. J. Int.* **166**(2), 939-951.

Ansel, V. & Nataf, H. (1989), 'Anisotropy beneath 9 stations of the geoscope broadband network as deduced from shear-wave splitting', *Geophys. Res. Let.* **16**(5), 409-412.

Argus, D. F. & Gordon, R. G. (1991), 'No-net-rotation model of current plate velocities incorporating plate motion model NUVEL-1', *Geophys. Res. Let.* **18**, 2039-2042.

Arndt, N. T.; Lewin, E. & Albarede, F.Fowler, C. M. R., ed. (2002), *Strange partners: formation and survival of continental crust and lithospheric mantle*, Vol. 199, Spec. Publ.-Geol. Soc. Lond..

Artemieva, I. M. (2006), 'Global 1º x 1ºthermal model TC1 for the continental lithosphere: Implications for lithosphere secular evolution', *Tectonophysics* **416**(1-4), 245-277.

Artemieva, I. M. & Mooney, W. D. (2001), 'Thermal thickness and evolution of Precambrian lithosphere: A global study', *J. Geophys. Res.* **106**(B8), 16387-16414.

Artemieva, I. M. (2007), 'Dynamic topography of the East European craton: Shedding light upon lithospheric structure, composition and mantle dynamics', *Global and Planetary Change* **58**, 411-434.

Assumpcao, M.; Heintz, M.; Vauchez, A. & Silva, M. E. (2006), 'Upper mantle anisotropy in SE and Central Brazil from SKS splitting: Evidence of asthenospheric flow around a cratonic keel', *Earth Planet. Sci. Let.* **250**(1-2), 224-240.

Audoine, E.; Savage, M. K. & Gledhill, K. (2004), 'Anisotropic structure under a back arc spreading region, the Taupo Volcanic Zone, New Zealand', *J. Geophys. Res.* **109**(B18), B11305. DOI:10.1029/2003JB002932

BABEL Working Group (1993), 'Deep seismic reflection/refraction interpretation of crustal structure along BABEL profiles A and B in the southern Baltic Sea', *Geophys. J. Int.* **112**, 325-343.

Babuska, V. & Plomerova, J. (2006), 'European mantle lithosphere assembled from rigid microplates with inherited seismic anisotropy', *Phys. Earth Planet. Int.* **158**(2-4), 264-280. DOI:10.1016/j.pepi.2006.01.010

Babuska, V.; Plomerová, J.; Vecsey, L.; Granet, M. & Achauer, U. (2002), 'Seismic anisotropy of the French Massif Central and predisposition of Cenozoic rifting and volcanism by Variscan suture hidden in the mantle lithosphere', *Tectonics* **21**, X-1. DOI:10.1029/2001TC901035

Baccheschi, P.; Margheriti, L. & Steckler, M. S. (2007), 'Seismic anisotropy reveals focused mantle flow around the Calabrian slab (Southern Italy)', *J. Geophys. Res.* **34**, 5302-+. DOI:10.1029/2006GL028899

Backus, G. E. (1962), 'Long-Wave Elastic Anisotropy Produced by Horizontal Layering', *J. Geophys. Res.* **67**, 4427-+.

Backus, G. E. (1965), 'Possible Forms of Seismic Anisotropy of the Uppermost Mantle under Oceans', *J. Geophys. Res.* **70**, 3429-+.

Bank, C. G.; Bostock, M. G.; Ellis, R. M. & Cassidy, J. F. (2000), 'A reconnaissance teleseismic study of the upper mantle and transition zone beneath the Archean Slave craton in NW Canada', *Tectonophysics* **319**(3), 151-166.

Barruol, G. & Granet, M. (2002), 'A Tertiary asthenospheric flow beneath the southern French Massif Central indicated by upper mantle seismic anisotropy and related to the west Mediterranean extension', *Earth Planet. Sci. Let.* **202**, 31-47.

Barruol, G. & Hoffmann, R. (1999), 'Upper mantle anistropy beneath the Geoscope stations', *J. Geophys. Res.* **104**(B5), 10757-10773.

Barruol, G.; Silver, P. G. & Vauchez, A. (1997), 'Seismic anisotropy in the eastern US: Deep structure of a complex continental plate', *J. Geophys. Res.* **102**(B4), 8329-8348.

Barruol, G.; Souriau, A.; Vauchez, A.; Diaz, J.; Gallart, J.; Tubia, J. & Cuevas, J. (1998), 'Lithospheric anisotropy beneath the Pyrenees from shear wave splitting', *J. Geophys. Res.* **103**(B12), 30039-30053.

Barruol, G. & Kern, H. (1996), 'Seismic anisotropy and shear-wave splitting in lower-crustal and upper-mantle rocks from the Ivrea Zone--experimental and calculated data', *Phys. Earth Planet. Int.* **95**, 175-194.

Becker, T. W. & Boschi, L. (2001), 'A comparison of tomographic and geodynamic mantle models', *Geochem. Geophys. Geosys.* **3**(1), 1003. DOI:10.129/2001GC000168

Becker, T. W.; Kellogg, J. B.; Ekstrom, G. & O'Connell, R. J. (2003), 'Comparison of azimuthal seismic anisotropy from surface waves and finite strain from global mantle-circulation models', *Geophys. J. Int.* **155**(2), 696-714. DOI:10.1046/j.1365-246X.2003.02085.x

Becker, T. W.; Browaeys, J. T. & Jordan, T. H. (2007), 'Stochastic analysis of shear-wave splitting length scales', *Earth Planet. Sci. Let.* **259**, 526-540. DOI:10.1016/j.epsl.2007.05.010

Behn, M. D.; Conrad, C. P. & Silver, P. (2004), 'Detection of upper mantle flow associated with the African Superplume', *Earth Planet. Sci. Let.* **224**, 259-274. DOI:10.1016/j.epsl.2004.05.026

Berthelsen, A. (1990), *A Continent Revealed - The European Geotraverse*, Cambridge Univ. Press, chapter Mobile Europe, pp. 11-32.

Bird, P. (2003), 'An updated digital model of plate boundaries', *Geochem. Geophys. Geosys.* **4**(3), 1027. DOI:10.1029/2001GC000252

Bird, P. & Li, Y. (1996), 'Interpolation of principal stress directions by nonparametric statistics: Global maps with confidence limits', *J. Geophys. Res.* **101**, 5435-5444. DOI:10.1029/95JB03731

Bogdanova, S. (1996), *Europrobe 1996 - Lithosphere dynamics*, The EUROPROBE Secretariat Uppsala, chapter Eurobrigde, pp. 80-89.

Bogdanova, S.; Gorbatschev, R.; Grad, M.; Janik, T.; Guterch, A.; Kozlovskaya, E.; Motuza, G.; Skridlaite, G.; Starostenko, V. & Taran, L. (2006),EUROBRIDGE: new insight into the geodynamic evolution of the East European Craton, *in* D. G. Gee & R. A. Stephenson, ed.,'European Lithosphere Dynamics', GEOLOGICAL SOCIETY OF LONDON - Memoirs, , pp. 599-626.

Bogdanova, S. V. (2005), 'The East-European craton: some aspects of the Proterozoic evolution in its south-west', *Mineral. Soc. Poland - Special Papers* **26**, 18-24.

Bogdanova, S. V.; Bibikova, E. V. & Gorbatschev, R. (1994), 'Palaeoproterozoic U---Pb zircon ages from Belorussia: new geodynamic implications for the East European Craton', *Precambrian Research* **68**(3-4), 231-240.

Bokelmann, G.; Wüstefeld, A. & et al. (2007), 'Crust and mantle geological fabric under North America', *in prep.* **-**, -.

Bokelmann, G. H. R. (1995), 'P-wave array polarization analysis and effective anisotropy of the brittle crust', *Geophysical Journal International* **120**(1), 145-162. DOI:10.1111/j.1365-246X.1995.tb05917.x

Bokelmann, G. H. R. (2002a), 'Convection-driven motion of the North American craton: Evidence from P-wave anisotropy', Geophys. J. Int. 248(2), 278-287.

Bokelmann, G. H. R. (2002b), 'Which forces drive North America?', *Geology* **30**(11), 1027-1030.

Bormann, P.; Burghardt, P.; Makeyeva, L. I. & Vinnik, L. P. (1993), 'Teleseismic shear-wave splitting and deformations in Central Europe', *Phys. Earth Planet. Int.* **78**, 157-166. DOI:10.1016/0031-9201(93)90153-Z

Bormann, P.; Grünthal, G.; Kind, R. & Montag, H. (1996) ,Upper mantle anisotropy beneath Central Europe from SKS wave splitting: Effects of absolute plate motion and lithosphere-asthenosphere boundary topography?', *Journal of Geodynamics* **22**(1-2), 11-32, DOI:

Bowman, J. R. & Ando, M. (1987), 'Shear-wave splitting in the upper-mantle wedge above the Tonga subduction zone', *Geophys. J. R. Astron. Soc.* **88**, 25-41.

Boyd, F. R.; Gurney, J. J. & Richardson, S. H. (1985), 'Evidence for a 150–200 km thick Archean lithosphere from diamond includes thermobarometry', *Nature* **315**, 851-860.

Brechner, S.; Klinge, K.; Krüger, F. & Plenefisch, T. (1998), 'Backazimuthal Variations of Splitting Parameters of Teleseismic SKS Phases Observed at the Broadband Stations in Germany', *Pure Appl. Geophys.* **151**, 305-331.

Brown, D.; Puchov, V.; Alvarez-Marron, J. & Perez-Estaun, A. (1996), 'The structural architecture of the footwall to the main Uralian Fault', *Earth Sci. Rev.* **40**, 125-140.

Bruneton, M.; Pedersen, H. A.; Farra, V.; Arndt, N. T.; Vacher, P.; Achauer, U.; Alinaghi, A.; Ansorge, J.; Bock, G.; Friederich, W.; Grad, M.; Guterch, A.; Heikkinen, P.; Hjelt, S.; Hyvцnen, T. L.; Ikonen, J.; Kissling, E.; Komminaho, K.; Korja, A.; Kozlovskaya, E.; Nevsky, M. V.; Paulssen, H.; Pavlenkova, N. I.; Plomerová, J.; Raita, T.; Riznichenko, O. Y.; Roberts, R. G.; Sandoval, S.; Sanina, I. A.; Sharov, N. V.; Shomali, Z. H.; Tiikkainen, J.; Wielandt, E.; Wilegalla, K.; Yliniemi, J. & Yurov, Y. G. (2004), 'Complex lithospheric structure under the central Baltic Shield from surface wave tomography', *J. Geophys. Res.* **109**(#B18#), 10303-+. DOI:10.1029/2003JB002947

Chastel, Y. B.; Dawson, P. R.; Wenk, H. & Bennett, K. (1993), 'Anisotropic convection with implications for the upper mantle', *J. Geophys. Res.* **98**, 17757-+.

Chekunov, A. V. (1994), 'The geodynamics of the Dniepr-Donets rift syneclise', *Geophys. Journal* **16**(3), 3-13 (in Russian).

Chevrot, S. (2000), 'Multichannel analysis of shear wave splitting', *J. Geophys. Res.* **105**(B9), 21579-21590. DOI:10.1029/2000JB900199

Christensen, N. I. & Crosson, R. S. (1968), 'Seismic anisotropy in the upper mantle', *Tectonophysics* **6**, 93-102.

Conrad, C. P.; Behn, M. D. & Silver, P. G. (2007), 'Global mantle flow and the development of seismic anisotropy: Differences between the oceanic and continental upper mantle', *J. Geophys. Res.* **112**, B07317.

Crampin, S. (1984), 'Effective anisotropic elastic constants for wave propagation through cracked solids', *Geophys. J. R. Astron. Soc.* **76**, 135-145.

Crampin, S. (1991), 'An alternative scenario for earthquake prediction experiments', *Geophys. J. Int.* **107**, 185-189.

Crampin, S. & Chastin, S. (2003), 'A review of shear wave splitting in the crack critical crust', *Geophys. J. Int.* **155**, 221-240.

Crampin, S. & Gao, Y. (2006), 'A review of techniques for measuring shear-wave splitting above small earthquakes', *Phys. Earth Planet. Int.* **159**(1-2), 1-14. DOI:10.1016/j.pepi.2006.06.002

Curie, P. (1895), 'Magnetic Properties of Materials at Various Temperatures', *Ann. Chim. Phys.*.

Debayle, E.; Kennett, B. & Priestley, K. (2005), 'Global azimuthal seismic anisotropy and the unique plate motion deformation of Australia', *Nature* **433**, 509-512. DOI:10.1038/nature03247

Debayle, E. & Kennett, B. L. N. (2000a), 'The Australian continental upper mantle: Structure and deformation inferred from surface waves', *J. Geophys. Res.* **105**, 25423-25450. DOI:10.1029/2000JB900212

Debayle, E. & Kennett, B. L. N. (2000b), 'Anisotropy in the Australasian upper mantle from Love and Rayleigh waveform inversion', *Earth Planet. Sci. Let.* **184**, 339-351.

DeMets, C.; Gordon, R. G.; Argus, D. F. & Stein, S. (1994), 'Effect of recent revisions to the geomagnetic reversal time scale on estimates of current plate motions', *Geophys. Res. Let.* **21**, 2191-2194.

Doglioni, C. (1994), 'Foredeeps versus subduction zones', *Geology* **22**(3), 271-274.

Doglioni, C.; Carminati, E. & Bonatti, E. (2003), 'Rift asymmetry and continental uplift', *Tectonics* **22**, 8-1. DOI:10.1029/2002TC001459

Drewes, H. (1998),Combination of VLBI, SLR and GPS determined station velocities for actual plate kinematic and crustal deformation models, *in* M. Feissel, ed.,'Geodynamics, IAG Symposia', Springer, .

Dricker, I. G.; Roecker, S. W.; Kosarev, G. L. & Vinnik, L. P. (1996), 'Shear-wave velocity structure of the crust and upper mantle beneath the Kola peninsula', *Geophys. Res. Let.* **23**(23), 3389-3392. DOI:10.1029/96GL03262

Duclos, M.; Savage, M. K.; Tommasi, A. & Gledhill, K. R. (2005), 'Mantle tectonics beneath New Zealand inferred from SKS splitting and petrophysics', *Geophys. J. Int.* **163**(2), 760-774.

Evans, M. S.; Kendall, J. & Willemann, R. J. (2006), 'Automated SKS splitting and upper-mantle anisotropy beneath Canadian seismic stations', *Geophys. J. Int.* **165**(3), 931-942.

Flesch, L. M.; Holt, W. E.; Silver, P. G.; Stephenson, M.; Wang, C. & Chan, W. W. (2005), 'Constraining the extent of crust-mantle coupling in central Asia using GPS, geologic, and shear wave splitting data [rapid communication]', *Earth Planet. Sci. Let.* **238**, 248-268. DOI:10.1016/j.epsl.2005.06.023

Fontaine, F. R.; Barruol, G.; Tommasi, A. & Bokelmann, G. H. R. (2007), 'Upper-mantle flow beneath French Polynesia from shear wave splitting', *Geophys. J. Int.*, 223-. DOI:10.1111/j.1365-246X.2007.03475.x

Fontaine, F. R.; Hooft, E. E. E.; Burkett, P. G.; Toomey, D. R.; Solomon, S. C. & Silver, P. G. (2005), 'Shear-wave splitting beneath the Galápagos archipelago', *Geophys. Res. Let.* **32**, 21308-+. DOI:10.1029/2005GL024014

Forsyth, D. W. (1975), 'The early structural evolution and anisotropy of the oceanic upper mantle', *Geophys. J. R. Astron. Soc*. **43**, 103-162.

Forsyth, D. W. & Uyeda, S. (1975), 'On the relative importance of the driving forces of plate motions', *Geophys. Journal* **43**, 163-200.

Fouch, M. J.; Fischer, K. M.; Parmentier, E. M.; Wysession, M. E. & Clarke, T. J. (2000), 'Shear wave splitting, continental keels, and patterns of mantle flow', *J. Geophys. Res.* **105**(B3), 6255-6275.

Fouch, M. J. & Rondenay, S. (2006), 'Seismic anisotropy beneath stable continental interiors', *Phys. Earth Planet. Int.* **158**(2-4), 292-320. DOI:10.1016/j.pepi.2006.03.024

Fouch, M. J.; Silver, P. G.; Bell, D. R. & Lee, J. N. (2004), 'Small-scale variations in seismic anisotropy near Kimberley, South Africa', *Geophys. J. Int.* **157**(2), 764-774. DOI:10.1111/j.1365-246X.2004.02234.x

Fouch, M. J. & Fischer, K. M. (1998), 'Shear wave anisotropy in the Mariana subduction zone', *Geophys. Res. Let.* **25**, 1221-1224. DOI:10.1029/98GL00650

Freybourger, M.; Gaherty, J. B. & Jordan, T. H. (2001), 'Structure of the Kaapvaal craton from surface waves', *Geophys. Res. Let.* **28**, 2489-2492. DOI:10.1029/2000GL012436

Fukao, Y. (1984), 'Evidence from Core-Reflected Shear Waves for Anisotropy in the Earth's Mantle', *Nature* **309**(5970), 695-698.

Gamar, F. & Bernard, P (1997) 'Shear wave anisotropy in the Erzinian basin and its relationship with crustal strain', *J. Geophys. Res.* **102**, 20373-20394

Gao, S.; Davis, P. M.; Liu, H.; Slack, P. D.; Rigor, A. W.; Zorin, Y. A.; Mordvinova, V. V.; Kozhevnikov, V. M. & Logatchev, N. A. (1997), 'SKS splitting beneath continental rift zones', *J. Geophys. Res.* **102**(B10), 2281-22798.

Gao, S. S.; Silver, P. G. & Liu, K. H. (2002), 'Mantle discontinuities beneath Southern Africa', *Geophys. Res. Let.* **29**, 129-1.

Garnero, E. J. (2000), 'Heterogeneity in the lowermost mantle', *Annu. Rev. Earth Planetary Sci.* **28**, 509-537. DOI:10.1146/annurev.earth.28.1.50

Gerst, A. & Savage, M. K. (2004), 'Seismic Anisotropy Beneath Ruapehu Volcano: A Possible Eruption Forecasting Tool', *Science* **306**(5701), 1543-1547. DOI:10.1126/science.1103445

Girardin, N. & Farra, V. (1998), 'Azimuthal anisotropy in the upper mantle from observations ofP-to-S converted phases: application to southeast Australia', *Geophys. J. Int.* **133**(3), 615-629. DOI:10.1046/j.1365-246X.1998.00525.x

Gorbatschev, R. & Bogdanova, S. (1993), 'Frontiers in the Baltic Shield', *Precambrian Research* **64**(1-4), 3-21.

Grad, M.; Gryn', D.; Guterch, A.; Janik, T.; Keller, R.; Lang, R.; Lyngsie, S. B.; Omelchenko, V.; Starostenko, V. I.; Stephenson, R. A.; Stovba, S. M.; Thybo, H. & Tolkunov, A. (2003b), '"DOBREfraction'99"--velocity model of the crust and upper mantle beneath the Donbas Foldbelt (East Ukraine)', *Tectonophysics* **371**(1-4), 81-110.

Grad, M.; Jensen, S. L.; Keller, G. R.; Guterch, A.; Thybo, H.; Janik, T.; Tiira, T.; Yliniemi, J.; Luosto, U.; Motuza, G.; Nasedkin, V.; Czuba, W.; Gaczyński, E.; Środa, P.; Miller, K. C.; Wilde-Piórko, M.; Komminaho, K.; Jacyna, J. & Korabliova, L. (2003), 'Crustal structure of the Trans-European suture zone region along POLONAISE'97 seismic profile P4', *J. Geophys. Res.* **108**, 2541. DOI:10.1029/2003JB002426

Grand, S. P. (1994), 'Mantle shear structure beneath the Americas and surrounding oceans', *J. Geophys. Res.* **99**(B6), 11591–11622.

Griot, D.; Montagner, J. & Tapponnier, P. (1998), 'Phase velocity structure from Rayleigh and Love waves in Tibet and its neighboring regions', *J. Geophys. Res.* **103**, 21215-21232. DOI:10.1029/98JB00953

Griot, D.; Montagner, J. & Tapponnier, P. (1998), 'Confrontation of mantle seismic anisotropy with two extreme models of strain, in Central Asia', *Geophys. Res. Let.* **25**, 1447-1450. DOI:10.1029/98GL00991

Gripp, A. E. & Gordon, R. G. (1990), 'Current plate velocities relative to the hotspots incorporating the NUVEL-1 global plate motion model', *Geophys. Res. Let.* **17**(8), 1109-1112.

Gripp, A. E. & Gordon, R. G. (2002), 'Young tracks of hotspots and current plate velocities', *Geophys. J. Int.* **150**, 321-361.

Gung, Y.; Panning, M. & Romanowicz, B. (2003), 'Global anisotropy and the thickness of continents', *Nature* **422**, 707-711. DOI:10.1038/nature01559

Gu, Y. J.; Dziewonski, A. M. & Ekstrцm, G. (2001), 'Preferential detection of the Lehmann discontinuity beneath continents', *Geophys. Res. Let.* **28**, 4655-4658. DOI:10.1029/2001GL013679

Hall, C. E.; Fischer, K. M.; Parmentier, E. M. & Blackman, D. K. (2000), 'The influence of plate motions on three-dimensional back arc mantle flow and shear wave splitting', *J. Geophys. Res.* **105**, 28009-28034. DOI:10.1029/2000JB900297

Hammond, J. O. S.; Kendall, J.; Rümpker, G.; Wookey, J.; Teanby, N.; Joseph, P.; Ryberg, T. & Stuart, G. (2005), 'Upper mantle anisotropy beneath the Seychelles microcontinent', *J. Geophys. Res.* **110**(#B9#), 11401-+. DOI:10.1029/2005JB003757

Heintz, M. & Kennett, B. L. N. (2005), 'Continental scale shear wave splitting analysis: Investigation of seismic anisotropy underneath the Australian continent', *Earth Planet. Sci. Let.* **236**(1-2), 106-119.

Heintz, M. & Kennett, B. L. N. (2006), 'The apparently isotropic Australian upper mantle', *Geophys. Res. Let.* **33**, L15319. DOI:10.1029/2006GL026401

Heintz, M.; Vauchez, A.; Assumpcao, M.; Barruol, G. & Egydio-Silva, M. (2003), 'Shear wave splitting in SE Brazil: an effect of active or fossil upper mantle flow, or both?', *Earth Planet. Sci. Let.* **211**(1-2), 79-95.

Helffrich, G.; Silver, P. & Given, H. (1994), 'Shear-wave splitting variation over short spatial scales on continents', *Geophys. J. Int.* **119**(2), 561-573. DOI:10.1111/j.1365-246X.1994.tb00142.x

Helffrich, G.; Wiens, D. A.; Vera, E.; Barrientos, S.; Shore, P.; Robertson, S. & Adaros, R. (2002), 'A teleseismic shear-wave splitting study to investigate mantle flow around South America and implications for plate driving forces', *Geophys. J. Int.* **149**, F1-F7.

Hess, H. H. (1964), 'Seismic Anisotropy of the Uppermost Mantle under Oceans', *Nature* **203**, 629-631. DOI:10.1038/203629a0

Hirth, G.; Evans, R. L. & Chave, A. D. (2000), 'Comparison of continental and oceanic mantle electrical conductivity: is the Archean lithosphere dry?', *Geochem. Geophys. Geosys.* **1**(12), .. DOI:10.1029/2000GC000048.

Hoffman, P.Bally, A. W. & Palmer, A., ed. (1989), *Precambrian geology and tectonic history of North America*, Vol. A, Geol. Soc. Am., Boulder, CO.

Huhma, H.; Puura, V.; Klein, V. & Мдпттдri, I. (1991), 'Nd-isotopic evidence for Paleoproterozoic crust in Estonia', *Geol. Survey Finnland* **Special Paper 12**, 67-68.

ben Ismail, W. & Mainprice, D. (1998), 'An olivine fabric database: an overview of upper mantle fabrics and seismic anisotropy', *Tectonophysics* **296**(1-2), 145-157.

James, D. E. & Assumpcao, M. (1996), 'Tectonic implications of S-wave Anisotropy beneath SE Brazil', *Geophys. J. Int.* **126**(1), 1-10.

Jordan, T. H. (1981), 'The Origin and Evolution of the Earth's Continental Crust', *Philosophical Transactions of the Royal Society of London. Series A, Mathematical and Physical Sciences* **301**(1461), 359-373.

Jordan, T. H. (1978), 'Composition and development of the continental tectosphere', *Nature* **274**, 544-548. DOI:10.1038/274544a0

Jung, H. & Karato, S. (2001), 'Water-Induced Fabric Transitions in Olivine', *Science* **293**, 1460-1463. DOI:10.1126/science.1062235

Kaminski, E. & Ribe, N. M. (2002), 'Timescales for the evolution of seismic anisotropy in mantle flow', *Geochem. Geophys. Geosys.* **3**(8), 1051. DOI:10.1029/2001GC000222.

Kendall, J.; Pilidou, S.; Keir, D.; Bastow, I.; Stuart, G. & Ayele, A. (2006),Mantle upwellings, melt migration and magma assisted rifting in Africa: Insights from seismic anisotropy, *in* G. Yirgu; C. J. Ebinger & P. K. H. Maguire, ed.,'Structure and evolution of the rift systems within the Afar volcanic province, Northeast Africa', pp. 57-74.

Kendall, J.; Stuart, G.; Ebinger, C.; Bastow, I. & Keir, D. (2005), 'Magma-assisted rifting in Ethiopia', *Nature* **433**, 146-148.

Kendall, J. M. (1994), 'Teleseismic arrivals at a mid-ocean ridge: Effect of mantle melt and anisotropy', *Geophys. Res. Let.* **21**, 301-304.

Kendall, J. M. (2000), 'Seismic anisotropy in the boundary layers of the mantle', *Geophysical monograph* **117**(4), 133-159.

Kendall, J. & Silver, P. G. (1996), 'Constraints from seismic anisotropy on the nature of the lowermost mantle', *Nature* **381**, 409-412. DOI:10.1038/381409a0

King, S. D. (2005), 'Archean cratons and mantle dynamics', *Earth Planet. Sci. Let.* **234**, 1-14. DOI:10.1016/j.epsl.2005.03.007

Kneller, E. A.; van Keken, P. E.; Katayama, I. & Karato, S. (2007), 'tress, strain, and B-type olivine fabric in the fore-arc mantle: Sensitivity tests using high-resolution steady-state subduction zone models', *J. Geophys. Res.* **112**(B4), B04406. DOI:10.1029/2006JB004544

Kopylova, M. G.; Russell, J. K. & Cookenboo, H. (1999), 'Petrology of peridotite and pyroxenite xenoliths from Jericho Kimberlite: implications for the thermal state of the mantle beneath the Slave Craton, northern Canada', *J. Petrol.* **40**, 79-104.

Kosarev, G. L.; Makeyeva, L. I. & Vinnik, L. P. (1984), 'Anisotropy of the mantle inferred from observations of P to S converted waves', *Geophys. J. Int.* **76**(1), 209-220. DOI:10.1111/j.1365-246X.1984.tb05037.x

Kreemer, C.; Holt, W. E. & Haines, A. J. (2003), 'An integrated global model of present-day plate motions and plate boundary deformation', *Geophys. J. Int.* **154**, 8-34.

Kubo, A. & Hiramatsu, Y. (1998), 'On Presence of Seismic Anisotropy in the Asthenosphere beneath Continents and its Dependence on Plate Velocity: Significance of Reference Frame Selection', *Pure Appl. Geophys.* **151**(2 - 4), 281-303. DOI:doi:10.1007/s000240050115

Kumazawa, M. & Anderson, O. L. (1969), 'Elastic moduli, pressure derivatives, and temperature derivatives of single-crystal olivine and single-crystal forsterite', *J. Geophys. Res.* **74**, 5961-5972.

Laske, G. & Masters, G. (1997), 'A Global Digital Map of sediments Thickness', *EOS Trans. AGU* **78**, F483.

Lassak, T. M.; Fouch, M. J.; Hall, C. E. & Kaminski, E. (2006), 'Seismic characterization of mantle flow in subduction systems: Can we resolve a hydrated mantle wedge?', *Earth Planet. Sci. Let.* **243**(3-4), 632-649. DOI:10.1016/j.epsl.2006.01.022

Lay, T. & Wallace, T. C. (1995), *Modern Global Seismology*, Academic Press, London.

Lay, T.; Williams, Q. & Garnero, E. J. (1998), 'The core-mantle boundary layer and deep Earth dynamics', *Nature* **392**, 461-468. DOI:10.1038/33083

van der Lee, S. & Nolet, G. (1997), 'The upper mantle S velocity structure of North America', *J. Geophys. Res.* **102**(B10), 22815.

Lenardic, A.; Moresi, L. & Mühlhaus, H. (2000), 'The role of mobile belts for the longevity of deep cratonic lithosphere: The crumple zone model', *J. Geophys. Res.* **27**(8), 1235–1238.

Lev, E.; Long, M. D. & van der Hilst, R. D. (2006), 'Seismic anisotropy in Eastern Tibet from shear wave splitting reveals changes in lithospheric deformation', *Earth Planet. Sci. Let.* **251**, 293-304. DOI:10.1016/j.epsl.2006.09.018

Leven, J. H.; Jackson, I. & Ringwood, A. E. (1981), 'Upper mantle seismic anisotropy and lithospheric decoupling', *Nature* **289**, 234-239. DOI:10.1038/289234a0

Levin, V.; Droznin, D.; Park, J. & Gordeev, E. (2004), 'Detailed mapping of seismic anisotropy with local shear waves in southeastern Kamchatka', *Geophys. J. Int.* **158**(3), 1009-1023.

Levin, V.; Menke, W. & Park, J. (1999), 'Shear wave splitting in the Appalachians and the Urals: A case for multilayered anisotropy', *J. Geophys. Res.* **104**(B8), 17,975–17,994.

Levin, V. & Park, J. (1997), 'Crustal anisotropy in the Ural Mountains foredeep from teleseismic receiver functions', *Geophys. Res. Let.* **24**, 1283-1286. DOI:10.1029/97GL51321

Lévкque, J. J.; Debayle, E. & Maupin, V. (1998), 'Anisotropy in the Indian Ocean upper mantle from Rayleigh- and Love-waveform inversion', *Geophys. J. Int.* **133**, 529-540. DOI:10.1046/j.1365-246X.1998.00504.x

Mainprice, D.; Barruol, G. & ben Ismail, W.Union, A. G., ed. (2000), *The seismic anisotropy of the earth's mantle : From single crystal to polycrystal*, Vol. 117, AGU.

Mainprice, D. & Silver, P. G. (1993), 'Interpretation of SKS-waves using samples from the subcontinental lithosphere', *Phys. Earth Planet. Int.* **78**, 257-280. DOI:10.1016/0031-9201(93)90160-B

Mainprice D. (1997) 'Modelling the anisotropic seismic properties of partially molten rocks found at mid-ocean ridges' *Tectonophysics* **279**(1-4), 161-179

Makeyeva, L.; Vinnik, L. & Roecker, S. (1992), 'Shear wave splitting and small-scale convection in the continental upper mantle', *Nature* **358**, 144-147.

Margheriti, L.; Lucente, F. P. & Pondrelli, S. (2003), 'SKS splitting measurements in the Apenninic-Tyrrhenian domain (Italy) and their relation with lithospheric subduction and mantle convection', *J. Geophys. Res.* **108**, 2218. DOI:10.1029/2002JB001793

Matzel, E. & Grand, S. P. (2004), 'The anisotropic seismic structure of the East European platform', *J. Geophys. Res.* **109**, B01302. DOI:10.1029/2001JB000623

Maystrenko, Y.; Stovba, S.; Stephenson, R.; Bayer, U.; Menyoli, E.; Gajewski, D.; Huebscher, C.; Rabbel, W.; Saintot, A.; Starostenko, V.; Thybo, H. & Tolkunov, A. (2003), 'Crustal-scale pop-up structure in cratonic lithosphere: DOBRE deep seismic reflection study of the Donbas fold belt, Ukraine', *Geology* **31**(8), 733-736. DOI:10.1130/G19329.1

McKenzie, D. (1979), 'Finite deformation during fluid flow', *Geophys. J. Int.* **58**(3), 689-715. DOI:10.1111/j.1365-246X.1979.tb04803.x

Menke, W. & Levin, V. (2003), 'The cross-convolution method for interpreting SKS splitting observations, with application to one and two-layer anisotropic earth models', *Geophys. J. Int.* **154**(2), 379-392.

Molnar, P. & Lyon-Caen, H. (1988), 'Some simple physical aspects of the support, structure, and evolution of mountain belts', *GSA - Special Paper* **218**, 197-207.

Montagner, J. (1998), 'Where Can Seismic Anisotropy Be Detected in the Earth's Mantle? In Boundary Layers...', *Pure Appl. Geophys.* **151**(2 - 4), 223-256. DOI:doi:10.1007/s000240050113

Montagner, J. & Kennett, B. L. N. (1996), 'How to reconcile body-wave and normal-mode reference earth models', *Geophys. J. Int.* **125**(1), 229-248. DOI:10.1111/j.1365-246X.1996.tb06548.x

Montagner, J. (1986), 'Dimensional structure of the Indian Ocean inferred from long period surface waves', *Geophys. Res. Let.* **13**, 315-318.

Montagner, J. (2002), 'Upper mantle low anisotropy channels below the Pacific Plate', *Earth Planet. Sci. Let.* **202**, 263-274.

Montagner, J.; Griot-Pommera, D. & Lavé, J. (2000), 'How to relate body wave and surface wave anisotropy?', *J. Geophys. Res.* **105**, 19015-19028. DOI:10.1029/2000JB900015

Montagner, J. & Tanimoto, T. (1990), 'Global anisotropy in the upper mantle inferred from the regionalization of phase velocities', *J. Geophys. Res.* **95**, 4797-4819.

Moore, M. M.; Garnero, E. J.; Lay, T. & Williams, Q. (2004), 'Shear wave splitting and waveform complexity for lowermost mantle structures with low-velocity lamellae and transverse isotropy', *J. Geophys. Res.* **109**(#B18#), 2319-+. DOI:10.1029/2003JB002546

Morgan, W. (1971), 'Convection plumes in the lower mantle', *Nature* **132**, 42-43.

Morris, G. B.; Raitt, R. W. & G., S. G. (1969), 'Velocity anisotropy and delay-time maps of the mantle near Hawaii', *J. Geophys. Res.* **74**, 4300-4316.

Muyzert, E.; Paulsen, H. & Snieder, R. (1999), 'A Seismic Cross-Section through the east European Continent', *Geophys. J. Int.* **136**, 695-704.

Nakajima, J. & Hasegawa, A. (2004), 'Shear-wave polarization anisotropy and subduction-induced flow in the mantle wedge of northeastern Japan', *Earth Planet. Sci. Let.* **225**, 365-377. DOI:10.1016/j.epsl.2004.06.011

Nicolas, A.; Boudier, F. & Boullier, A. M. (1973), 'Mechanisms of flow in naturally and experimentally deformed Peridotites', *Am. J. Sci.* **273**, 853-876.

Nicolas, A. & Christensen, N. I. (1987),Formation of anisotropy in upper mantle peridotites - A review, *in* K. Fuchs & C. Froideveaux, ed.,'Composition structure and dynamics of the lithosphere asthenosphere system', AGU, Washington D.C., pp. 111-123.

Nironen, M.; Lahtinen, R. & Korja, A. (2002),Paleoproterozoic tectonic evolution of the Fennoscandian shield - Comparison to modern analogues, *in* Lahtinen et al., ed.,'Lithospere 2002 - Second Symposium on the Structure, Composition and Evolution of the Lithosphere in Finnland; Progamme and extended Abstracts', pp. 95-97.

Nye, J. F. (1972), *Physical Properties of crystals. Their representation by tensors and matrixes*, Oxford Univ. Press.

Ozalaybey, S. & Chen, W. (1999), 'Frequency-dependent analysis of SKS/SKKS waveforms observed in Australia: evidence for null birefringence', *Phys. Earth Planet. Int.* **114**(3-4), 197-210.

Pearson, D. J.; Irvine, G. J.; Carlson, R. W.; Kopylova, M. G. & Ionov, D. A.Fowler, C. M. R., ed. (2002), *The development of lithospheric keels beneath the earliest continents: time constraints using PGE and Re–Os isotope systematics*, Vol. 199, Spec. Publ.-Geol. Soc. Lond..

Perez-Estaun, A. & Brown, D. (1996), *Europrobe 1996 - Lithosphere dynamics*, The EUROPROBE Secretariat Uppsala, chapter Uralide, pp. 80-89.

Pharaoh, T.; England, R. W.; Verniers, J. & Zelazniewicz, A. (1997), 'Geological and geophysical studies in the Trans-European Suture zone', *Geol. Mag.* **134**(5), 585-590.

Plomerova, J.; Babuska, V.; Vecsey, L.; Kozlovskaya, E. & Raita, T. (2006), 'Proterozoic-Archean boundary in the mantle lithosphere of eastern Fennoscandia as seen by seismic anisotropy', *Journal of Geodynamics* **41**(4), 400-410. DOI:10.1016/j.jog.2005.10.008

Polet, J.; Silver, P. G.; Beck, S.; Wallace, T.; Zandt, G.; Ruppert, S.; Kind, R. & Rudloff, A. (2000), 'Shear wave anisotropy beneath the Andes from the BANJO, SEDA, and PISCO experiments', *J. Geophys. Res.* **105**, 6287-6304. DOI:10.1029/1999JB900326

Poupinet, G.; Arndt, N. & Vacher, P. (2003), 'Seismic tomography beneath stable tectonic regions and the origin and composition of the continental lithospheric mantle', *Earth Planet. Sci. Let.* **212**(1-2), 89-101. DOI:10.1016/S0012-821X(03)00258-9

Pulford, A.; Savage, M. & Stern, T. (2003), 'Absent anisotropy: the paradox of the Southern Alps orogen', *Geophys. Res. Let.* **30**, 2051. DOI:10.1029/2003GLO17758

Ranalli, G. (1995), *Rheology of the Earth*, Springer-Verlag GmbH.

Restivo, A. & Helffrich, G. (1999), 'Teleseismic shear wave splitting measurements in noisy environments', *Geophys. J. Int.* **137**(3), 821-830.

Restivo, A. & Helffrich, G. (2006), 'Core-mantle boundary structure investigated using SKS and SKKS polarization anomalies', *Geophys. J. Int.* **165**(1), 288-302. DOI:doi: 10.1111/j.1365-246X.2006.02901.x

Rondenay, S.; Bostock, M. G.; Hearn, T. M.; White, D. J. & Ellis, R. M. (2000), 'Lithospheric assembly and modification of the SE Canadian Shield: Abitibi-Grenville teleseismic experiment', *J. Geophys. Res.* **105**, 13735-13754. DOI:10.1029/2000JB900022

Russo, R. M. & Silver, P. G. (1994), 'Trench-Parallel Flow Beneath the Nazca Plate from Seismic Anisotropy', *Science* **263**, 1105-1111. DOI:10.1126/science.263.5150.1105

Rümpker, G. & Silver, P. G. (1998), 'Apparent shear-wave splitting parameters in the presence of vertically varying anisotropy', *Geophys. J. Int.* **135**(3), 790-800.

Saltzer, R. L.; Gaherty, J. B. & Jordan, T. H. (2000), 'How are vertical shear wave splitting measurements affected by variations in the orientation of azimuthal anisotropy with depth?', *Geophys. J. Int.* **141**, 374-390.

Saltzer, R. L. (2002), 'Upper mantle structure of the Kaapvaal craton from surface wave analysis-a second look', *Geophys. Res. Let.* **29**, 17-1.

Savage, M. K. & Silver, P. G. (1993), 'Mantle deformation and tectonics: constraints from seismic anisotropy in the western United States', *Phys. Earth Planet. Int.* **78**(3-4), 207-227.

Schmid, C.; van der Lee, S. & Giardini, D. (2004), 'Delay times and shear wave splitting in the Mediterranean region', *Geophys. J. Int.* **159**(1), 275-290.

Schulte-Pelkum, V. & Blackman, D. K. (2003), 'A synthesis of seismic P and S anisotropy', *Geophys. J. Int.* **154**, 166-178. DOI:10.1046/j.1365-246X.2003.01951.x

Schulte-Pelkum, V.; Masters, G. & Shearer, P. M. (2001), 'Upper mantle anisotropy from long-period P polarization', *J. Geophys. Res.* **106**, 21917-21934. DOI:10.1029/2001JB000346

Sella, G. F.; Dixon, T. H. & Mao, A. (2002), 'REVEL: A model for recent plate velocities from space geodesy', *J. Geophys. Res.* **107**, B4. DOI:10.1029/2000JB000033

Shapiro, N. M. & Ritzwoller, M. H. (2002), 'Monte-Carlo inversion of broad-band surface wave dispersion for a global shear wave velocity model of the crust and upper mantle', *Geophys. J. Int.* **151**, 88-105.

Shcherbak, N. P. (1991), 'The Precambrian subdivision of the Ukrainian Shield and their comparision with USSR and international scales', *Geologicheskiy Zhurnal* **4**, 3-9 (in Russian).

Shearer, M. (1999), *Introduction to seismology*, Cambridge Univ. Press.

Shearer, P. M. (1990), 'Seismic imaging of upper-mantle structure with new evidence for a 520-km discontinuity', *Nature* **344**, 121-126.

Shirey, S. B.; Carlson, R. W.; Richardson, S. H.; Menzies, A.; Gurney, J. J.; Pearson, D. G.; Harris, J. W. & Wiechert, U. (2001), 'Archean emplacement of eclogitic components into the lithospheric mantle during formation of the Kaapvaal Craton', *Geophys. Res. Let.* **28**, 2509-2512. DOI:10.1029/2000GL012589

Silver, P. G. (1996), 'Seismic Anisotropy Beneath the Continents: Probing the Depths of Geology', *Annu. Rev. Earth Planet. Sci.* **24**, 385-432.

Silver, P. G. & Chan, W. W. (1991), 'Shear Wave Splitting and Subcontinental Mantle Deformation', *J. Geophys. Res.* **96**(B10), 16429-16454.

Silver, P. G. & Savage, M. (1994), 'The interpretation of shear-wave splitting parameters in the presence of two anisotropic layers', *Geophys. J. Int.* **119**, 949-963.

Silver, P. G. & Chan, W. W. (1988), 'Implications for continental structure and evolution from seismic anisotropy', *Nature* **335**, 34-39.

Silver, P. G.; Gao, S. S. & Liu, K. H. (2001), 'Mantle deformation beneath southern Africa', *Geophys. Res. Let.* **28**(13), 2493-2496. DOI:2000GL012696

Silver, P. G. & Holt, W. E. (2002), 'The Mantle Flow Field Beneath Western North America', *Science* **295**, 1054-1058. DOI:10.1126/science.1066878

Silver, P. G. & Kaneshima, S. (1993), 'Constraints on mantle anisotropy beneath Precambrian North America from a transportable teleseismic experiment', *Geophys. Res. Let.* **20**, 1127-1130.

Simons, F. J.; van der Hilst, R. D.; Montagner, J. & Zielhuis, A. (2002), 'Multimode Rayleigh wave inversion for heterogeneity and azimuthal anisotropy of the Australian upper mantle', *Geophys. J. Int.* **151**(3), 738-754. DOI:10.1046/j.1365-246X.2002.01787.x

Simons, F. J. & van der Hilst, R. D. (2003), 'Seismic and mechanical anisotropy and the past and present deformation of the Australian lithosphere', *Earth Planet. Sci. Let.* **211**, 271-286.

Skridlaite, G.; Wiszniewska, J. & Duchesne, J. (2003), 'Ferro-potassic A-type granites and related rocks in NE Poland and S Lithuania: west of the East European Craton', *Precambrian Research* **124**(2-4), 305-326. DOI:10.1016/S0301-9268(03)00090-1

Sleep, N. H. (2003), 'Survival of Archean cratonal lithosphere', *J. Geophys. Res.* **108**, 8-1. DOI:10.1029/2001JB000169

Smith, M. L. & Dahlen, F. A. (1973), 'The azimuthal dependence of Love and Rayleigh wave propagation in a slightly anisotropic medium', *J. Geophys. Res.* **78**, 3321-3333.

Snyder, D. B.; Bostock, M. G. & Lockhart, G. D. (2003), 'Two anisotropic layers in the Slave craton', *Lithos* **71**(2-4), 529-539.

Stein, S. & Wysession, M. (2003), *An Introduction to Seismology, Earthquakes, and Earth Structure*, Blackwell Publishing.

Steinberger, B. & O'Connel, R. J. (1998), 'Advection of plumes in mantle flow: implications for hotspot motion, mantle viscosity and plume distribution', *Geophys. J. Int.* **132**(2), 412-434.

Tarduno, J. A.; Duncan, R. A.; Scholl, D. W.; Cottrell, R. D.; Steinberger, B.; Thordarson, T.; Kerr, B. C.; Neal, C. R.; Frey, F. A.; Torii, M. & Carvallo, C. (2003), 'The Emperor Seamounts: Southward Motion of the Hawaiian Hotspot Plume in Earth's Mantle', *Science* **301**, 1064-1069. DOI:10.1126/science.1086442

Teanby, N.; Kendall, J. M. & van der Baan, M. (2003), 'Automation of shear-wave splitting measurements using cluster analysis', *Bull. Seism. Soc. Am.* **94**, 453-463.

Thybo, H.; Janik, T.; Omelchenko, V. D.; Grad, M.; Garetsky, R. G.; Belinsky, A. A.; Karatayev, G. I.; Zlotski, G.; Knudsen, M. E.; Sand, R.; Yliniemi, J.; Tiira, T.; Luosto, U.; Komminaho, K.; Giese, R.; Guterch, A.; Lund, C. E.; Kharitonov, O. M.; Ilchenko, T.; Lysynchuk, D. V.; Skobelev, V. M. & Doody, J. J. (2003), 'Upper lithospheric seismic velocity structure across the Pripyat Trough and the Ukrainian Shield along the EUROBRIDGE'97 profile', *Tectonophysics* **371**(1-4), 41-79. DOI:10.1016/S0040-1951(03)00200-2

Tommasi, A. (1998), 'Forward modeling of the development of seismic anisotropy in the upper mantle', *Earth Planet. Sci. Let.* **160**(1-2), 1-13.

Tommasi, A.; Mainprice, D.; Cordier, P.; Thoraval, C. & Couvy, H. (2004), 'Strain-induced seismic anisotropy of wadsleyite polycrystals and flow patterns in the mantle transition zone', *J. Geophys. Res.* **109**(#B18#), 12405. DOI:10.1029/2004JB003158

Tsvankin, I. (2001), *Seismic signatures and analysis of reflection data in anisotropic media*, Elsevier Science Pub. Co., Inc..

Turcotte, D. L. & Schubert, G. (2002), *Geodynamics*, Cambridge University Press, Cambridge.

Vauchez, A.; Dineur, F. & Rudnick, R. (2005), 'Microstructure, texture and seismic anisotropy of the lithospheric mantle above a mantle plume: Insights from the Labait volcano xenoliths (Tanzania)', *Earth Planet. Sci. Let.* **232**(3-4), 295-314.

Vauchez, A.; Tommasi, A.; Barruol, G. & Mauma, J. (2000) 'Upper mantle deformation and seismic anisotropy in continentla rifts' *Physics and Chemistry of the Earth* **A25**, 111-117

Vauchez, A. & Nicolas, A. (1991), 'Mountain building: strike parallel motion and mantle anisotropy', *Tectonophysics* **185**, 183-201.

Vecsey, L.; Plomerová, J.; Kozlovskaya, E. & Babu ska, V. (2007), 'Shear wave splitting as a diagnostic of variable anisotropic structure of the upper mantle beneath central Fennoscandia', *Tectonophysics* **438**, 57-77.

Vinnik, L. P.; Farra, V. & Romanniwicz, B. (1989), 'Azimuthal anisotropy in the earth from observations of SKS at GEOSCOPE and NARS broadband stations', *Bull. Seism. Soc. Am.* **79**(5), 1542-1558.

Vinnik, L. P.; Green, R. W. E. & Nicolaysen, L. O. (1996), 'Seismic constraints on dynamics of the mantle of the Kaapvaal craton', *Phys. Earth Planet. Int.* **95**, 139-151.

Vinnik, L. P.; Kosarev, G. L. & Makeyeva, L. I. (1984), 'Anisotropiya litosfery po nablyudeniyam voln SKS and SKKS', *Dokl. Akad. Nauk USSR* **278**, 1335-1339.

Wüstefeld, A. & Bokelmann, G. (2007), 'Null Detection in Shear-Wave Splitting Measurements', *Bull. Seism. Soc. Am.* **97**(4), 1204-1211. DOI:10.1785/0120060190

Walker, K. T.; Bokelmann, G. H. R. & Klemperer, S. L. (2001), 'Shear-wave splitting to test mantle deformation models around Hawaii', *Geophys. Res. Let.* **28**, 4319-4322.

Walker, K. T.; Bokelmann, G. H. R.; Klemperer, S. L. & Bock, G. (2005), 'Shear-wave splitting around the Eifel hotspot: evidence for a mantle upwelling', *Geophys. J. Int.* **163**(3), 962-980.

Walker, K. T.; Nyblade, A. A.; Klemperer, S. L.; Bokelmann, G. H. R. & Owens, T. J. (2004), 'On the relationship between extension and anisotropy: Constraints from shear wave splitting across the East African Plateau', *J. Geophys. Res.* **109**(#B18#), 8302-+. DOI:10.1029/2003JB002866

Walther, M.; Plenefisch, T. & Ruempker, G. (2007), 'Automated analysis of SKS shear-wave splitting for regional seismic networks', *EGU Geoph. Res. Abstracts* **9**(SRef-ID: 1607-7962/gra/EGU2007-A-07475), 07475.

Wiejacz, P. (2001), 'Shear wave splitting across Tornquist-Teisseyre zone in Poland', *J. Balkan Geophys. Soc.* **4**(4), 91-100.

Wilson, M. & Lyashkevich, Z. M. (1996), 'Magmatism and the geodynamics of rifting of the Pripyat-Dnieper-Donets rift, East European Platform', *Tectonophysics* **268**(1-4), 65-81.

de Wit, M. J.; de Ronde, C. E. J.; Tredoux, M.; Roering, C.; Hart, R. J.; Armstrong, R. A.; Green, R. W. E.; Peberdy, E. & Hart, R. A. (1992), 'Formation of an Archaean continent', *Nature* **357**(6379), 553-562.

Wolfe, C. J. & Silver, P. G. (1998), 'Seismic anisotropy of oceanic upper mantle: Shear wave splitting methodologies and observations', *J. Geophys. Res.* **B1**, 749-771.

Wolfe, C. J. & Solomon, S. C. (1998), 'Shear-Wave Splitting and Implications for Mantle Flow Beneath the MELT Region of the East Pacific Rise', *Science* **280**(5367), 1230-1232. DOI:10.1126/science.280.5367.1230

Yang, X.; Fisher, K. M. & Abers, G. A. (1995), 'Seismic anisotropy beneath the Shumagin Islands segment of the Aleutean-Alaska subduction zone', *J. Geophys. Res.* **100**, 18165-18177.

Yegorova, T. P.; Starostenko, V. I.; Kozlenko, V. G. & Yliniemi, J. (2004), 'Lithosphere structure of the Ukrainian Shield and Pripyat Trough in the region of EUROBRIDGE-97 (Ukraine and Belarus) from gravity modelling', *Tectonophysics* **381**(1-4), 29-59. DOI:10.1016/j.tecto.2002.06.003

Ziegler, P. A. (1990), *Geological Atlas of Western and Central Europe*, Shell Internationale Petroleum Maatschappij B.V./Geological Society of London/Elsevier.

Zielhuis, A. & Nolet, G. (1994), 'Shear-wave velocity in the upper mantle beneath central Europe', *Geophys. J. Int.* **117**, 695-715.

Zonenshain, L. P.; Kuzmin, M. I. & Natapov, L. M.Page, B. M., ed. (1990), *Geology of the USSR: A Plate-Tectonic Synthesis*, Vol. 21, AGU.

7. Appendix

7.1. Deep anisotropy as an alternative explanation?

Tonga earthquakes show good splitting measurements, with often strong energy on the transverse component. In contrast, the Andean earthquakes, although coming from almost opposite directions, often result in Null measurements. In general, the anisotropy beneath the EEC can be separated into two regions: In the south-western part, adjacent Central Europe, the fast axis orientations are approximately NE-SW oriented and thus align with general pattern observed in Europe (Figure 49). In the Northern and central part of the EEC the fast axis orientations show N to NNE orientations. Delay times for all stations vary between 0.4 and 1.1 seconds.

Teleseismic shear-wave splitting measurements have the advantage of excellent lateral resolution. The almost vertical incident of SKS and SKKS phase guarantee that the Fresnel zone sensitive to anisotropy is directly beneath the station. However, this technique has no vertical resolution as the splitting could have been caused by an anisotropic layer anywhere between the CMB and the surface. Candidate anisotropic layers causing shear-wave splitting are

- The D”-layer just above the CMB [e.g., Kendall & Silver, 1996; Moore et al., 2004, Restivo & Helffrich, 2006]: In this case, the expected fast axis pattern projected to that depth would be coherent over larger areas and ignore any surface geologic structures. It is however not possible to distinguish between splitting at the CMB or large-scale trends between stations. This may perhaps be achieved by simultaneous comparison of SKS and SKKS phases [Restivo & Helffrich, 2006].
- The asthenosphere: Strain between the convecting mantle and the overlying tectonic plate aligns anisotropic minerals, mostly olivine, in the upper mantle [Nicolas & Christensen, 1987; Tommasi, 1998]. Such mechanism causes the seismic fast axis to be parallel to the absolute plate motion vector (APM), with

the exemption of flow deflected by the topography of the lithosphere-asthenosphere boundary (subduction zones, rifts, cratons, …). Bokelmann [2002] inferred such a mechanism from studying P- and S-wave anisotropy beneath the Canadian Shield, in addition to a lithospheric anisotropy.

- The lithosphere: anisotropic directions are "frozen-in" the rock after past tectonics events aligned them. Shear-wave splitting patterns should in such case show a relation with geologic structures at the surface, if the deformation between crust and mantle portion of the lithosphere is coherent.

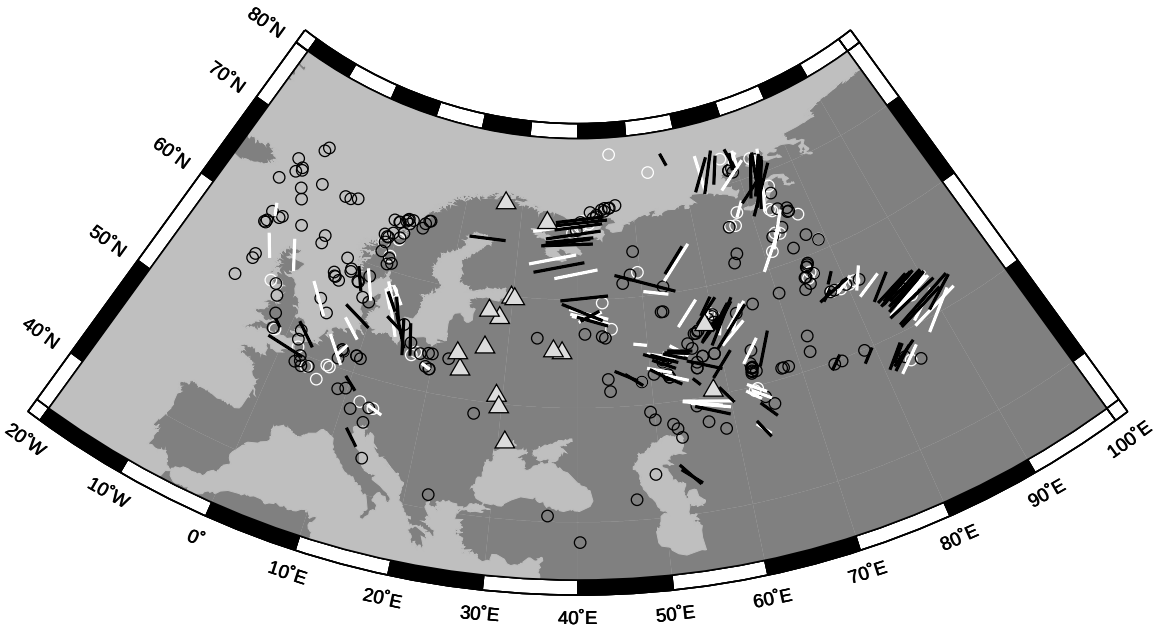

Figure A- 1: Splitting projected along the ray path to the depth of the core-mantle boundary. Good measurements are in black, fair in white. Circles represent Null measurements. Triangles mark the location of seismic stations.

Figure A- 1 shows splitting parameters projected to the receiver-side pierce point of the ray along at the CMB. A smoothly varying trend is apparent. Beneath the North Sea, the trend is NNW to NW with many Nulls. Beneath the EEC fast axis orientations are roughly E oriented. Further to the east, beneath the Ural Mountains and Siberia the direction fan out, showing NE-SW directions in the North and ESE-WNW directions further south.

It is possible to distinguish such D"-layer anisotropy from upper mantle anisotropy by inspecting on le lower hemisphere under each station. Angular coherence within such stereoplot would indicate an origin closer to the surface. Variations indicate either complex anisotropy (two-layers or dipping), or deep mantle origins.

7.2. Backazimuthal variation plots

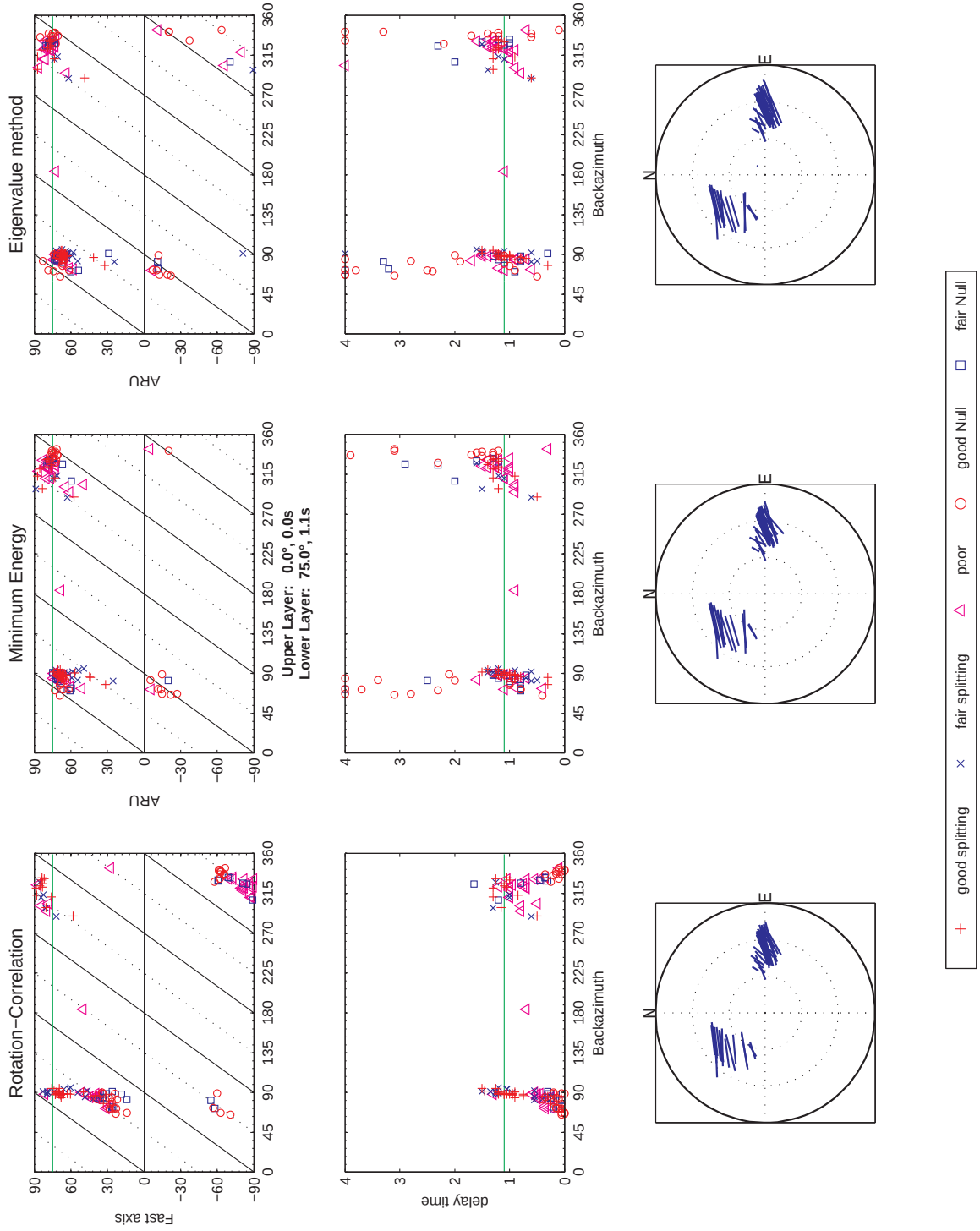

Figure A- 2: ARU single-layer model fit. Three different splitting techniques are compared (Rotation-correlation, Minimum Energy and Eigenvalue). For each technique the backazimuthal variation of fast orientation estimate (top row) and delay time estimates (center row) are shown. The bottom row displays a stereoplot of good and fair quality non-Nulls. Markers are plotted at their according backazimuth and incident angle (grid lines each 5°). Marker lengths are according to delay time. Comparing these plots constrains final splitting parameter estimates [see Wüstfeld & Bokelmann, 2007]

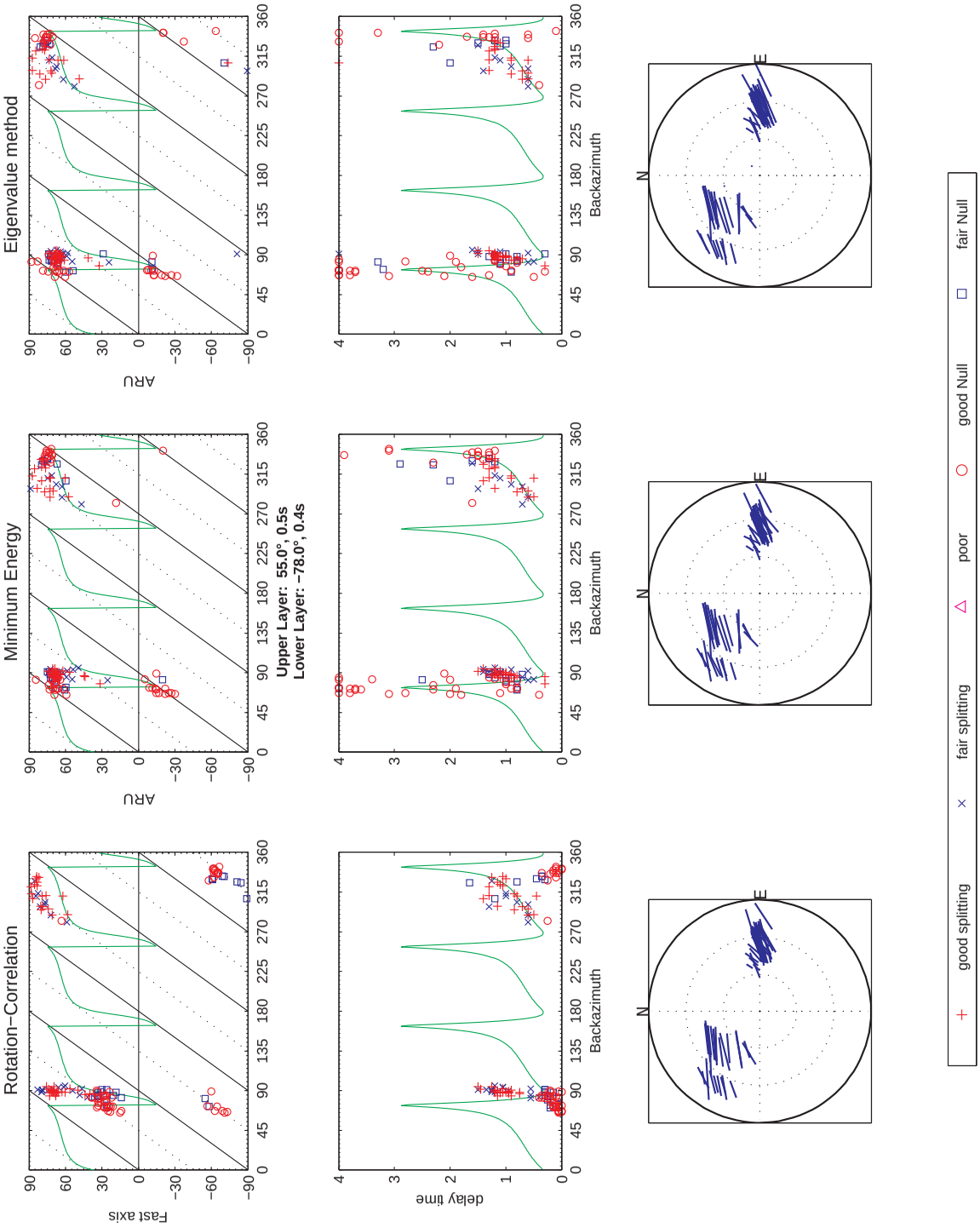

Figure A- 3: ARU two-layer model fit

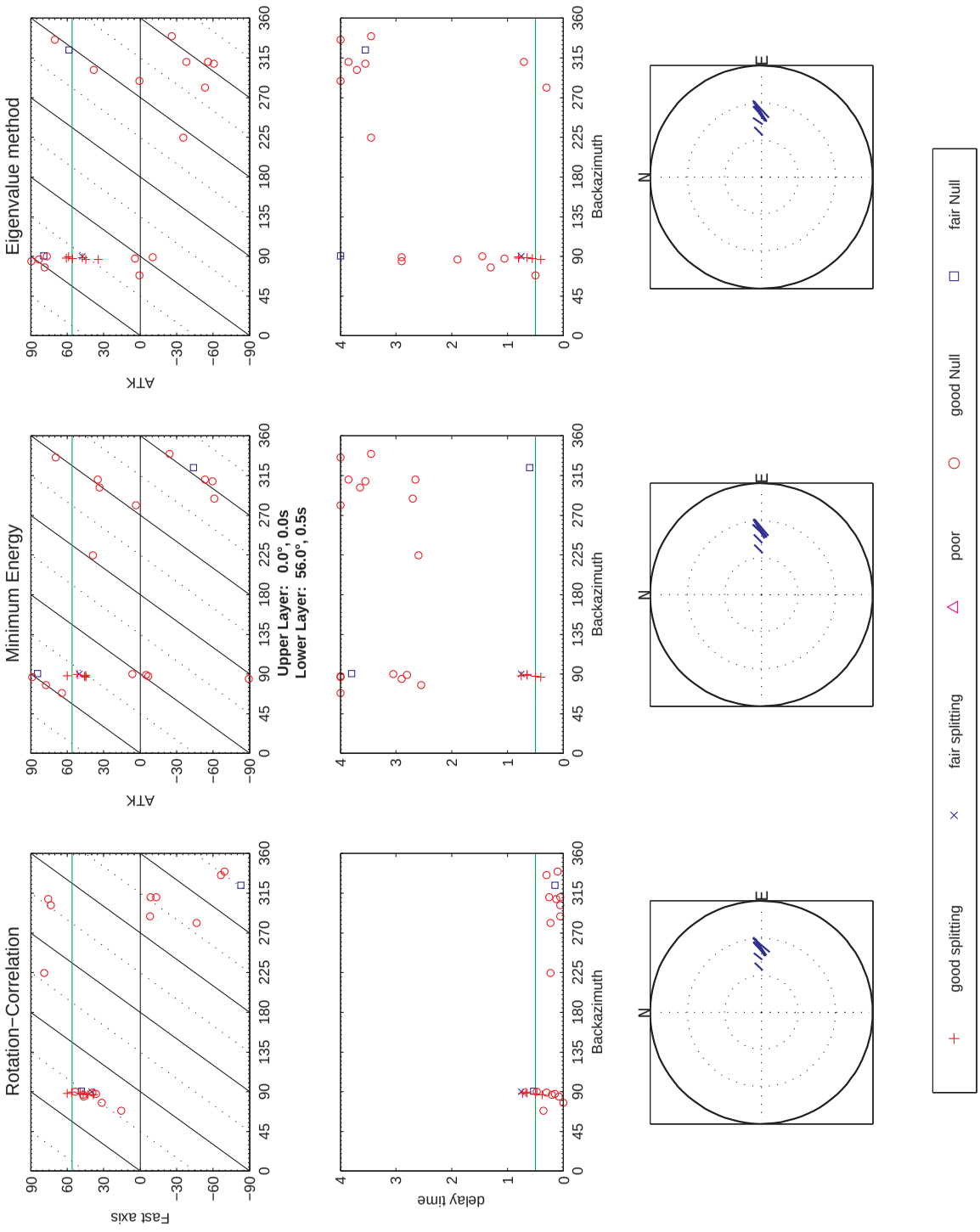

Figure A- 4: AKTK results and a single layer fit

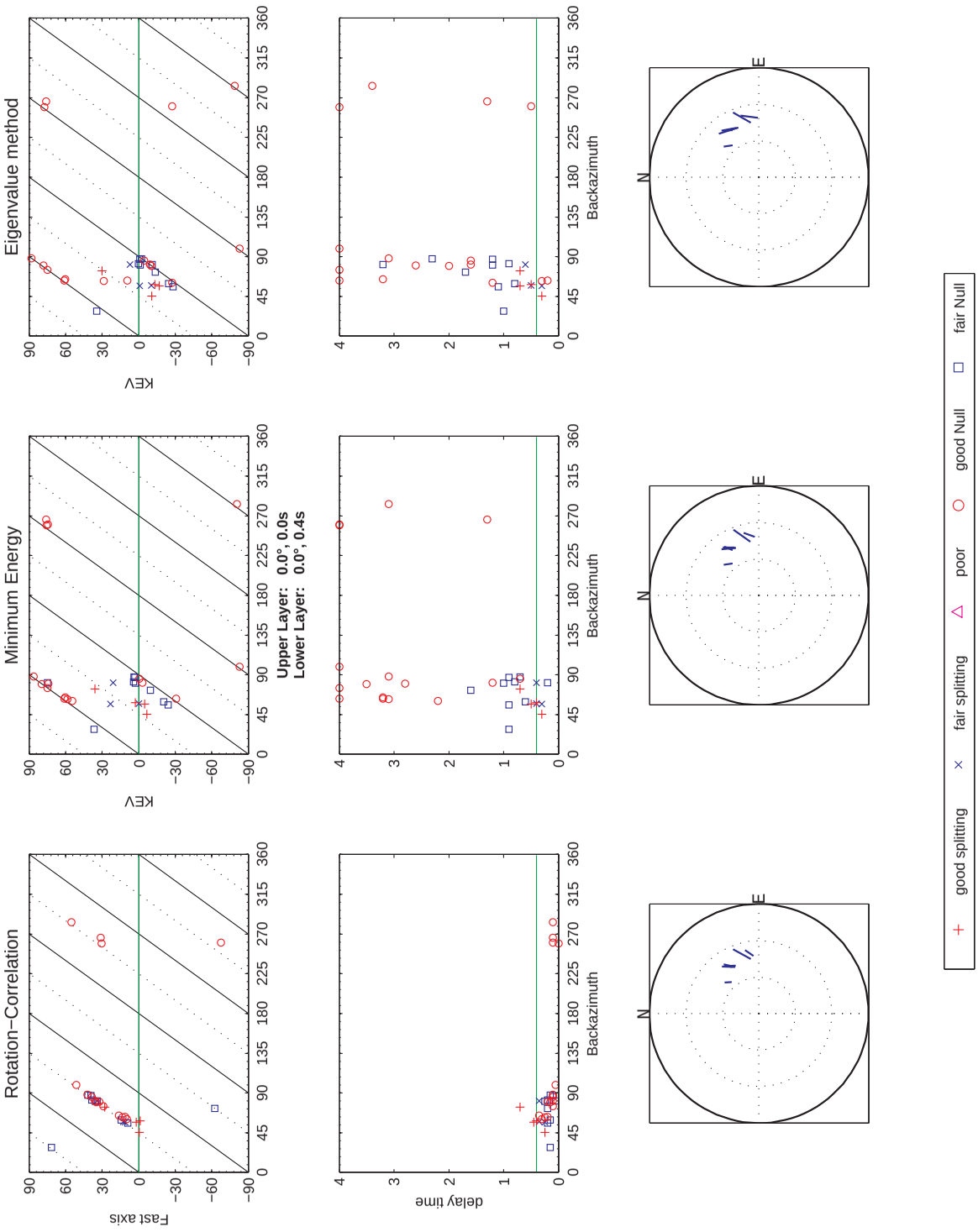

Figure A- 5: Backazimuthal distribution and stereoplots for station KEV.

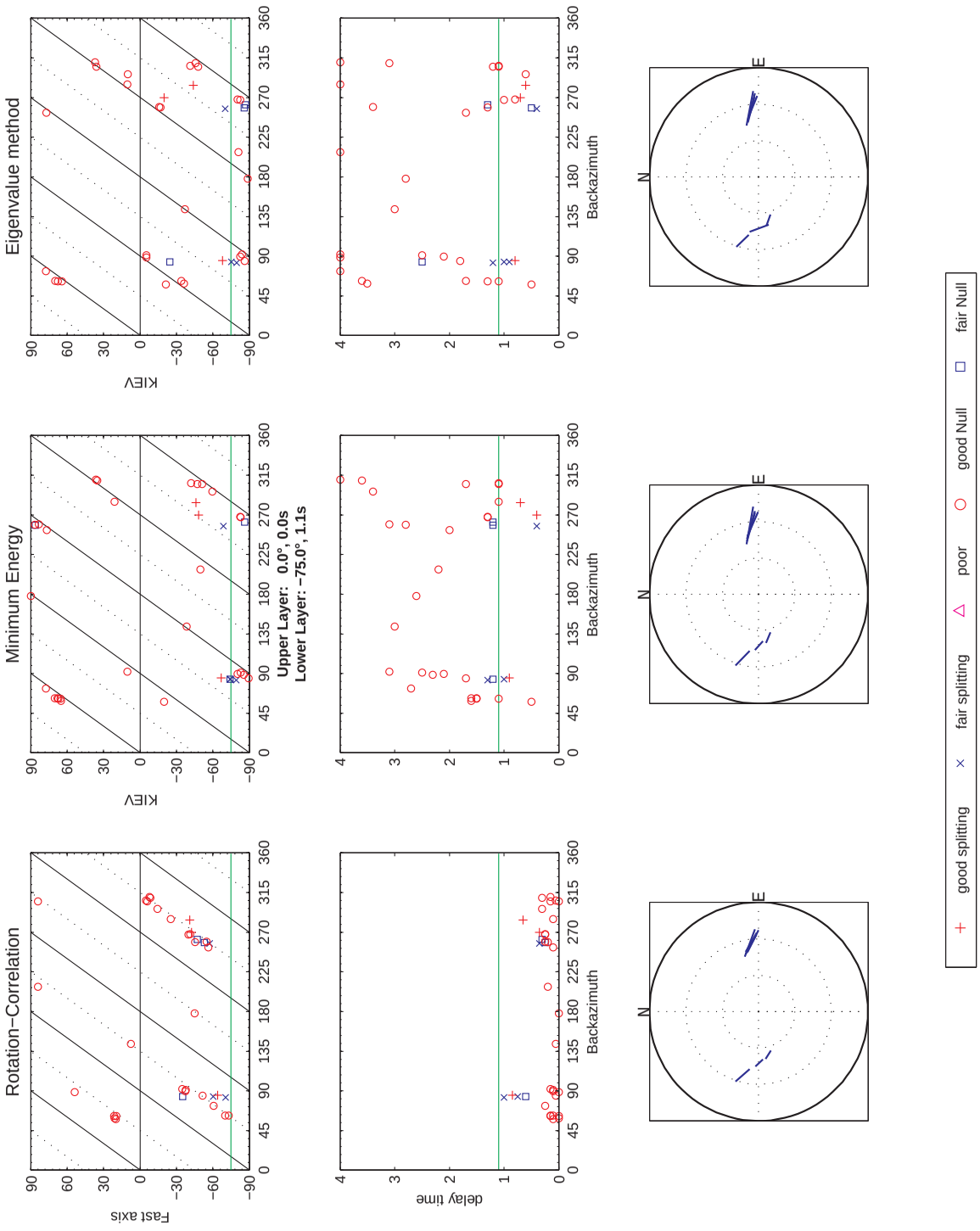

Figure A- 6: KIEV backazimuthal plots

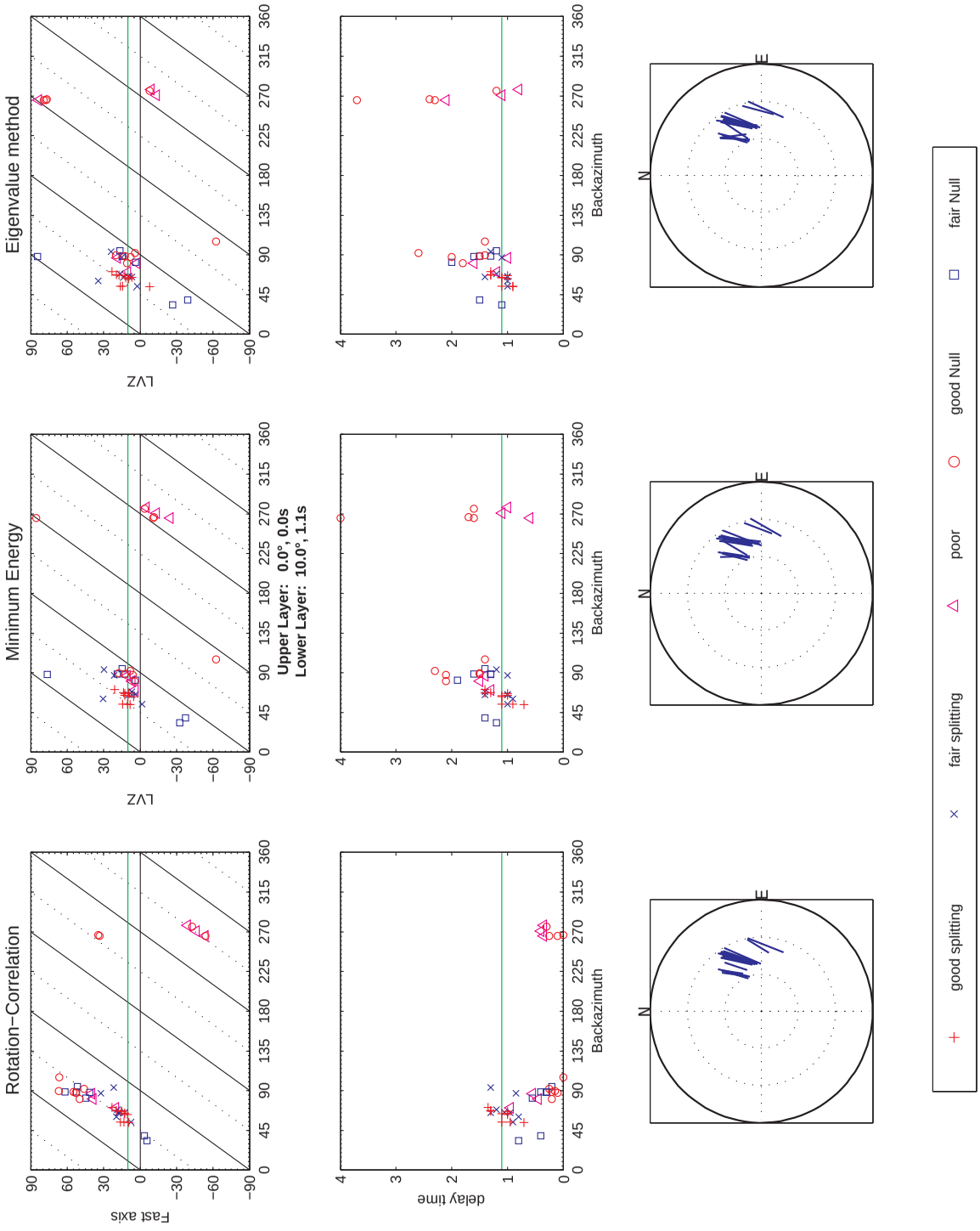

Figure A- 7: Backazimuthal plot for LVZ

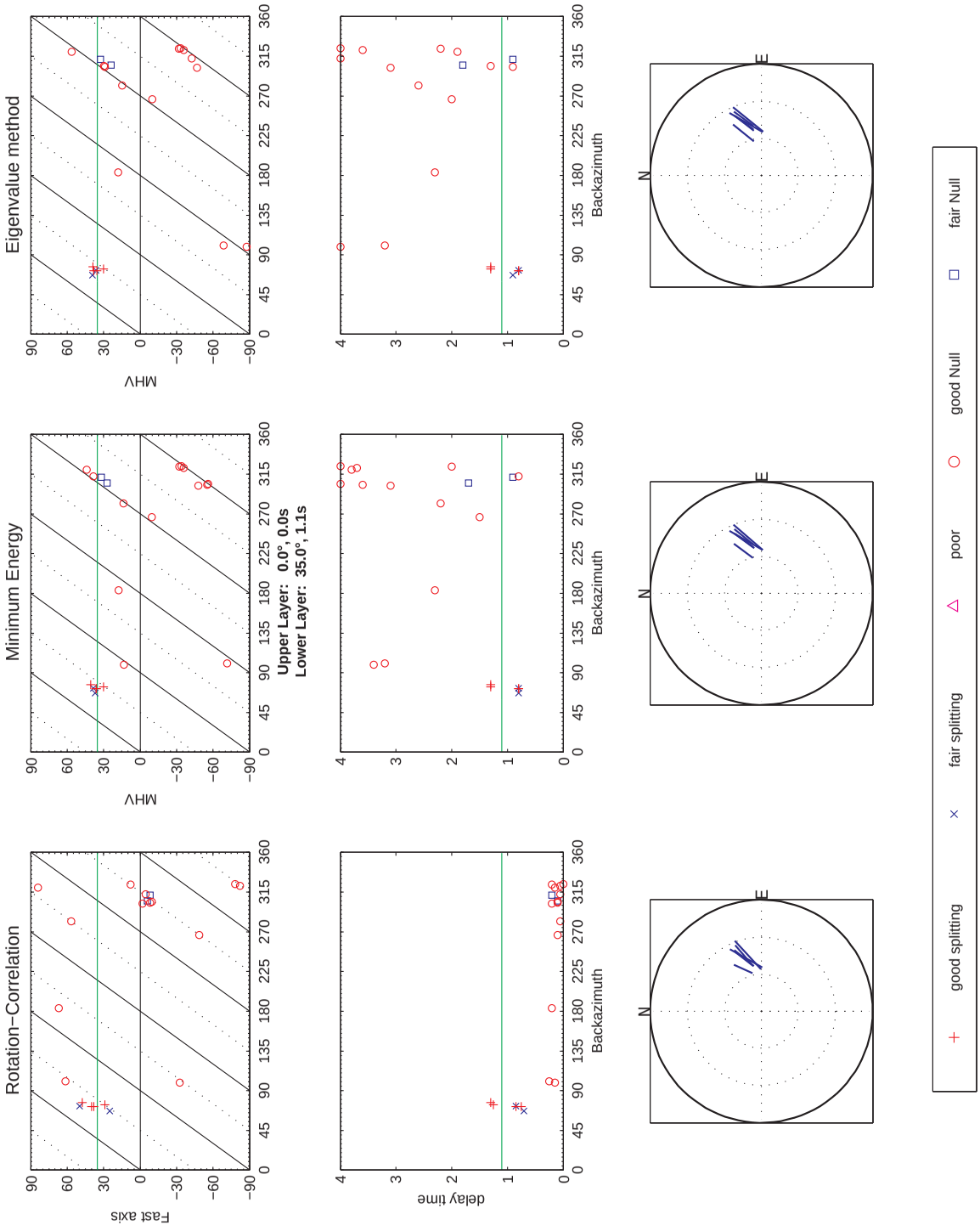

Figure A- 8: Backazimuthal plots for station MHV with best single layer model fit

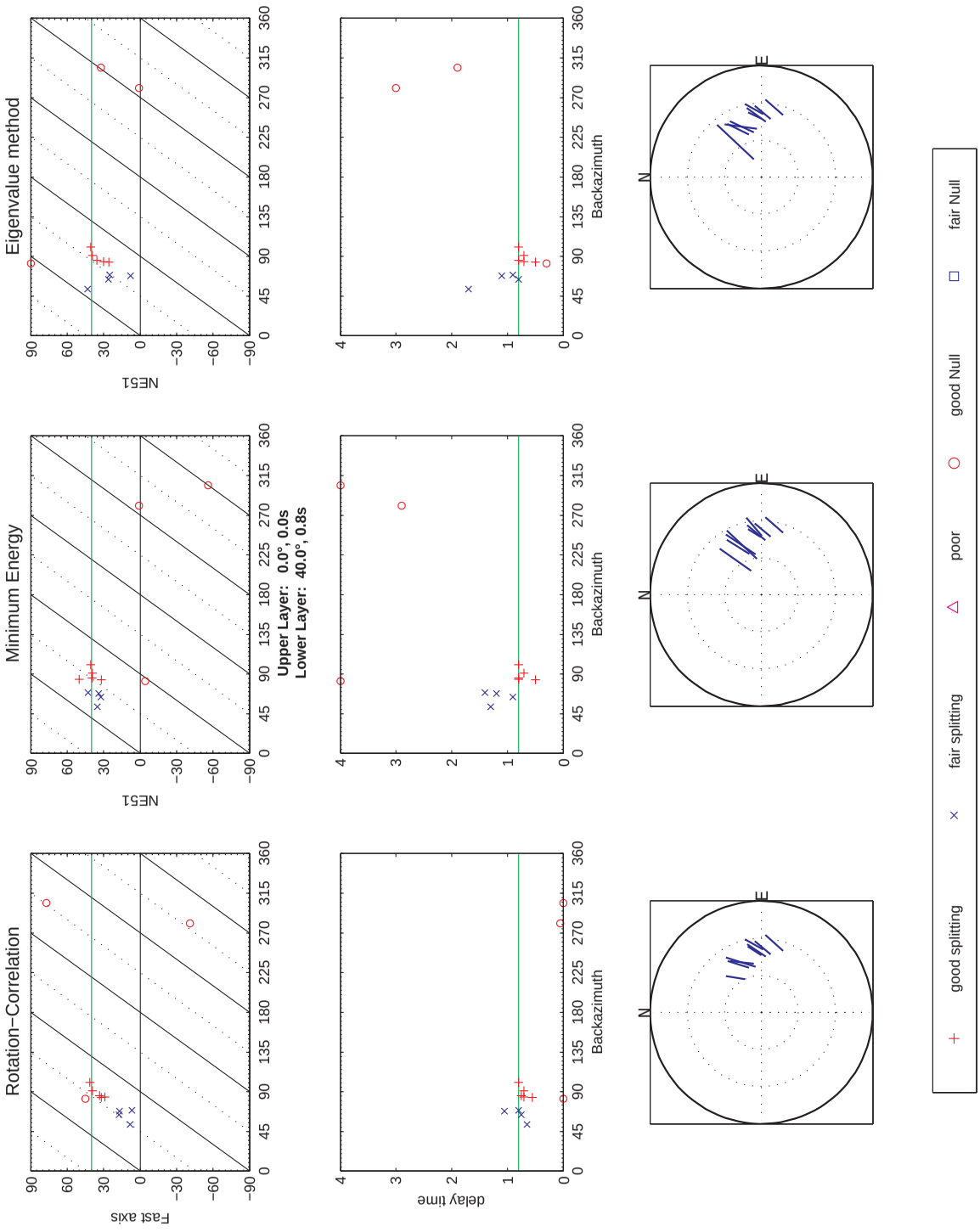

Figure A- 9: NE51 backazimuthal plot

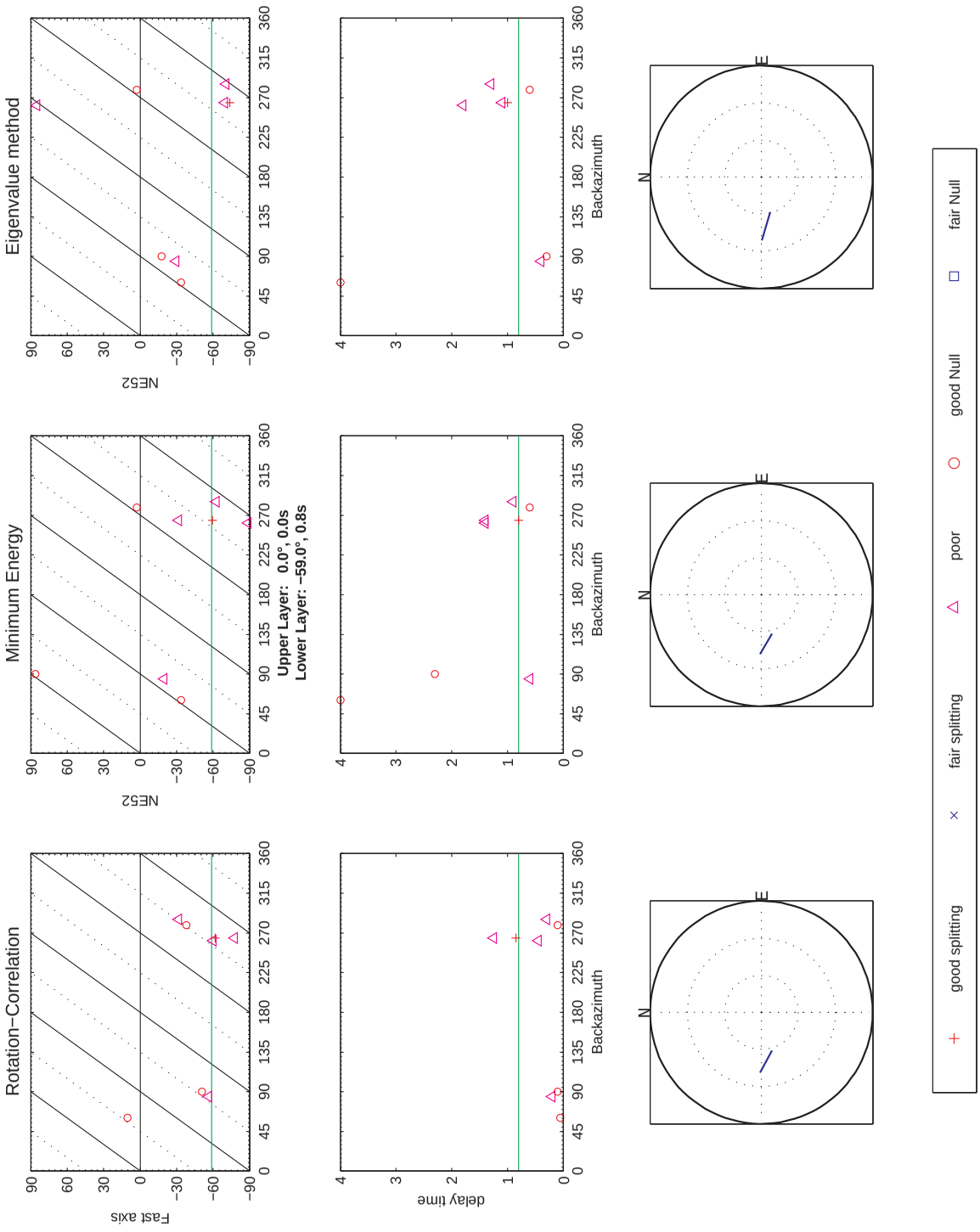

Figure A- 10: Splitting results for station NE52 and one-layer fit

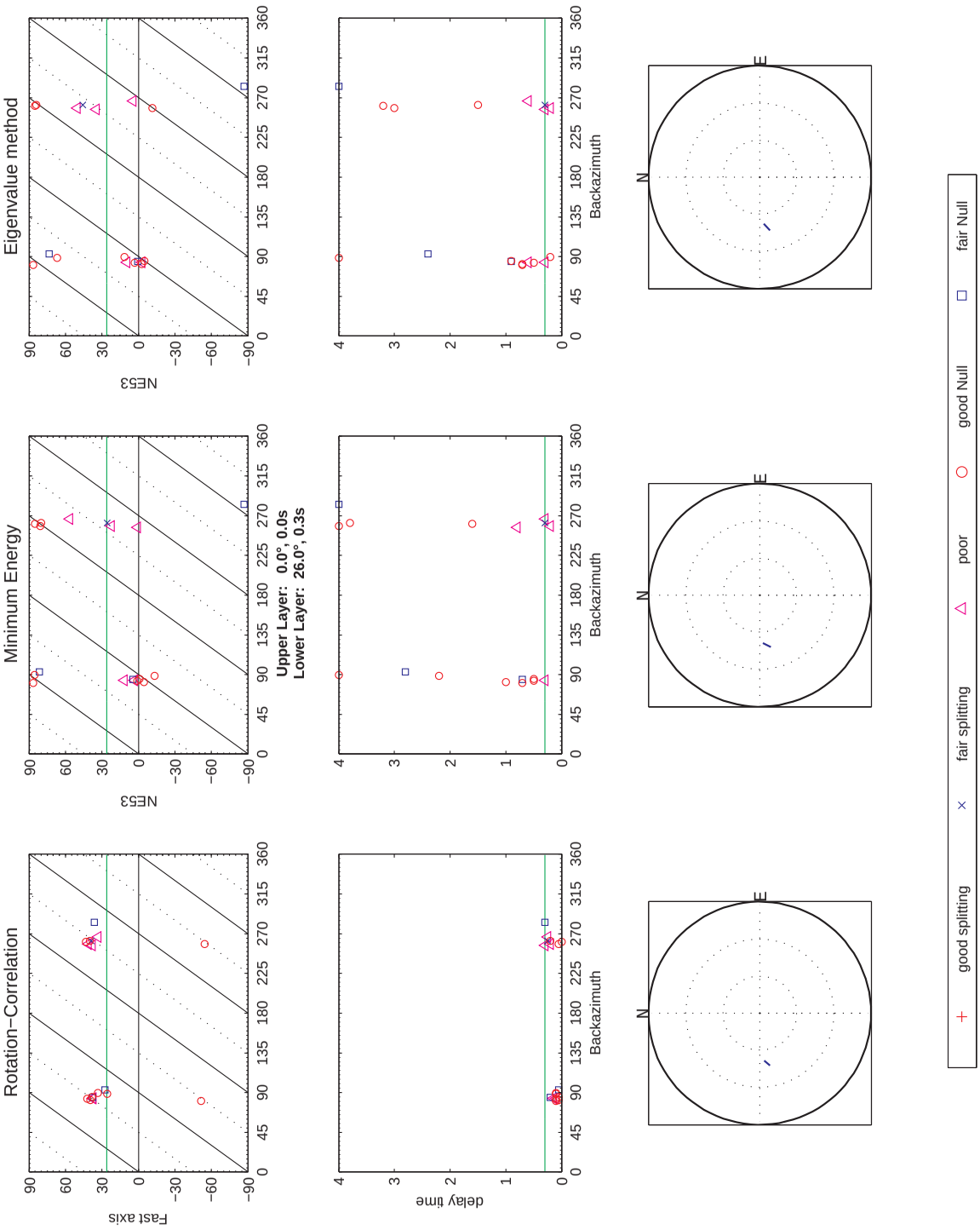

Figure A- 11: Splitting results for station NE53

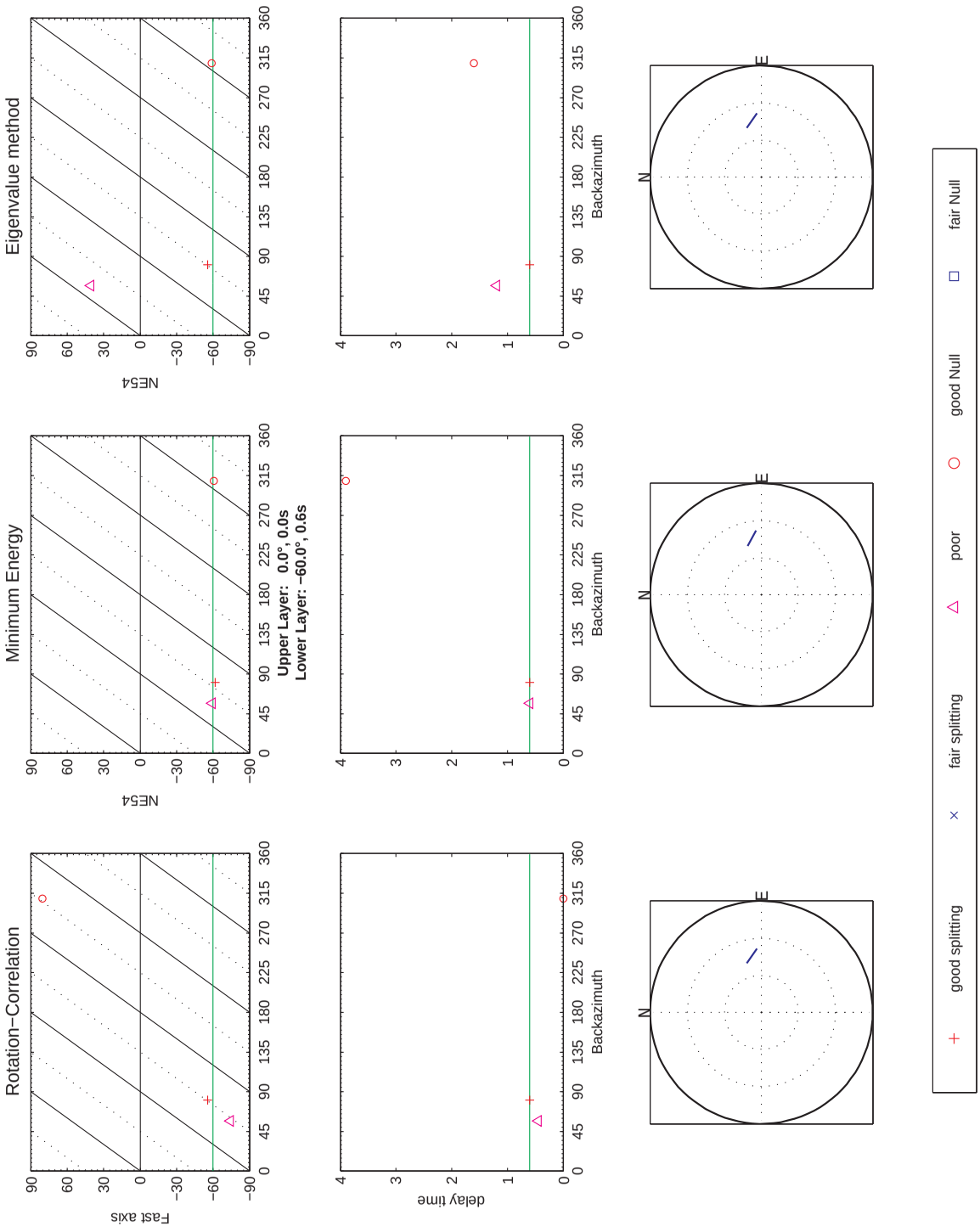

Figure A- 12: Backazimuthal plot for NE54

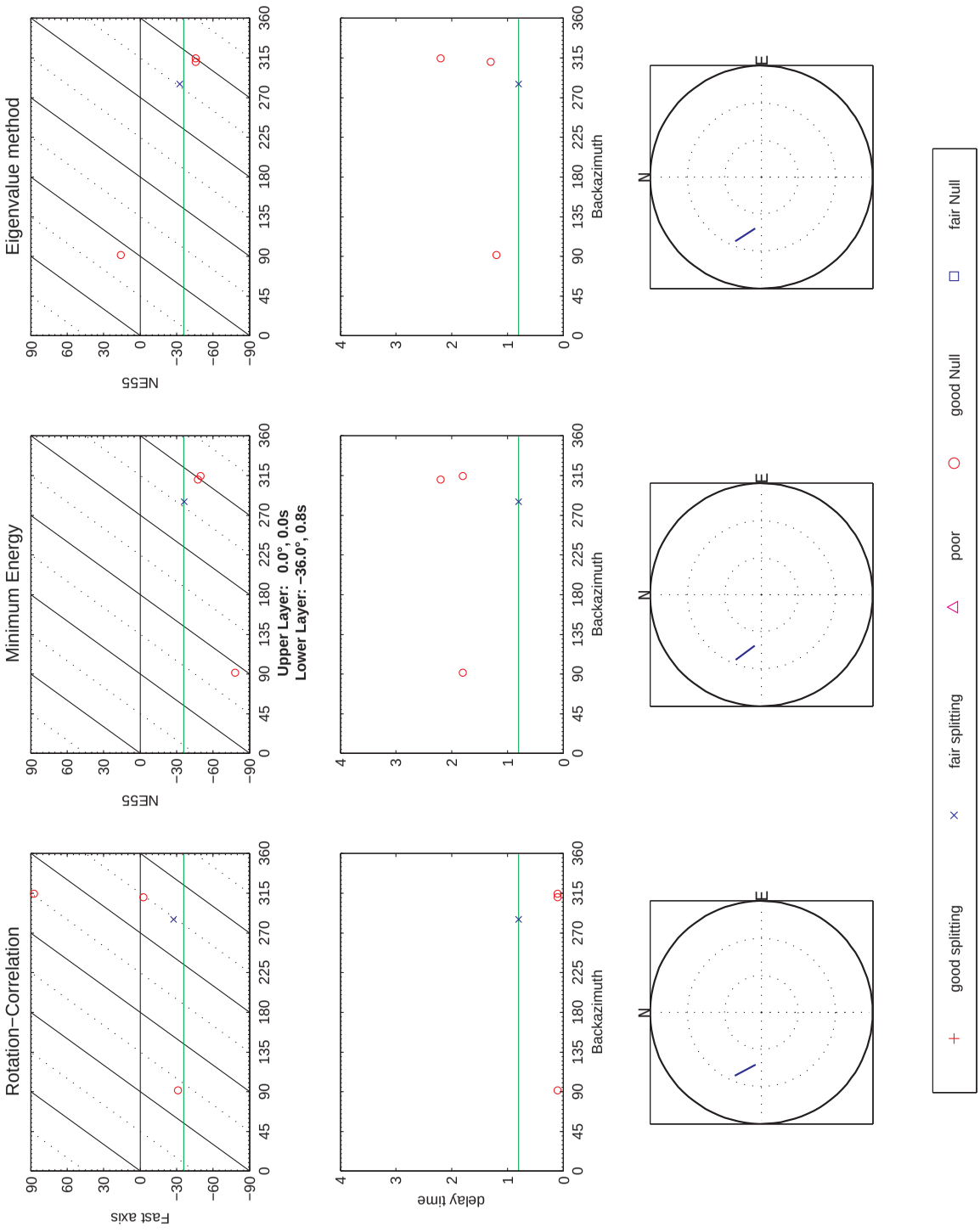

Figure A- 13: Backazimuthal plot for NE55

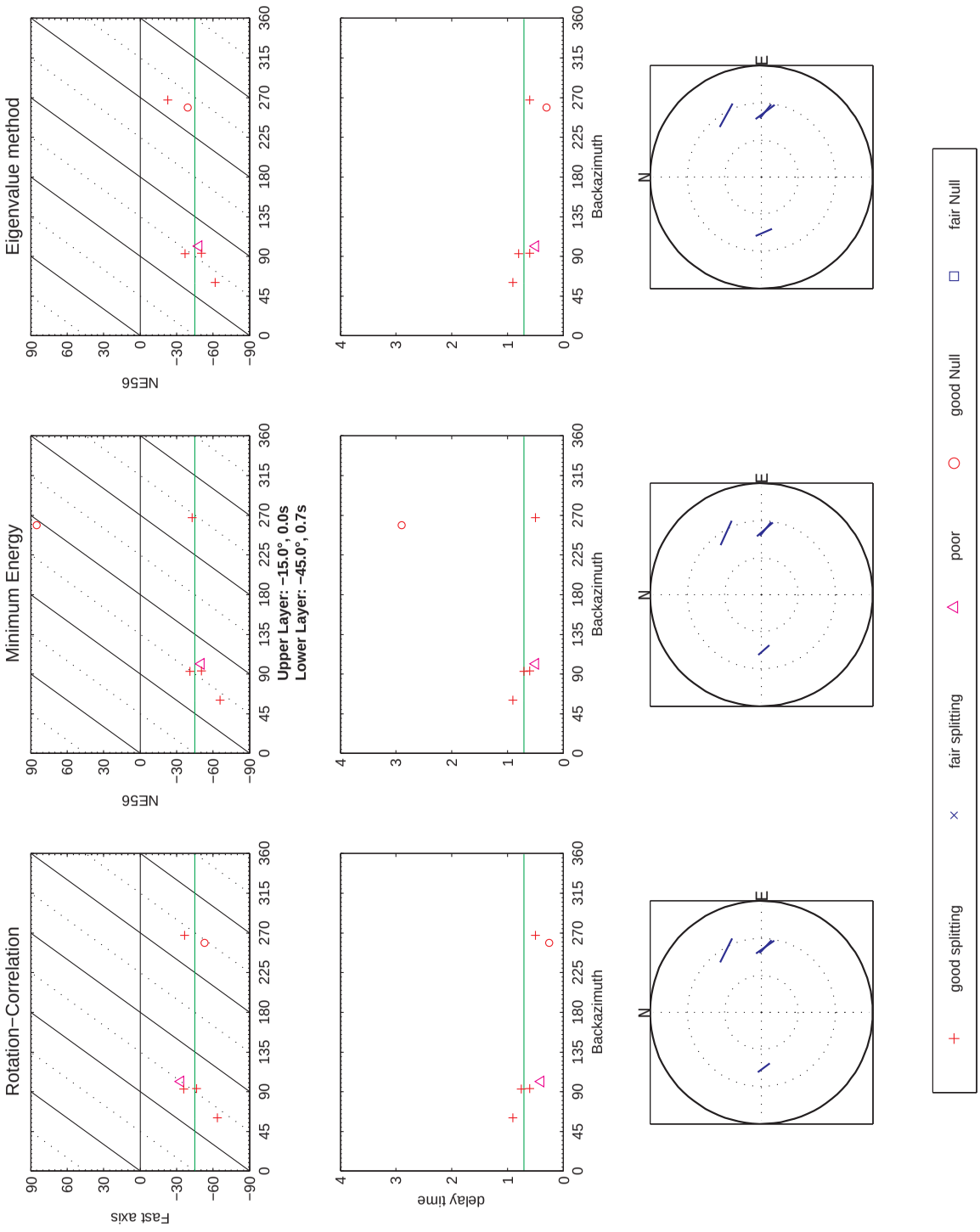

Figure A- 14: Backazimuthal plot for NE56

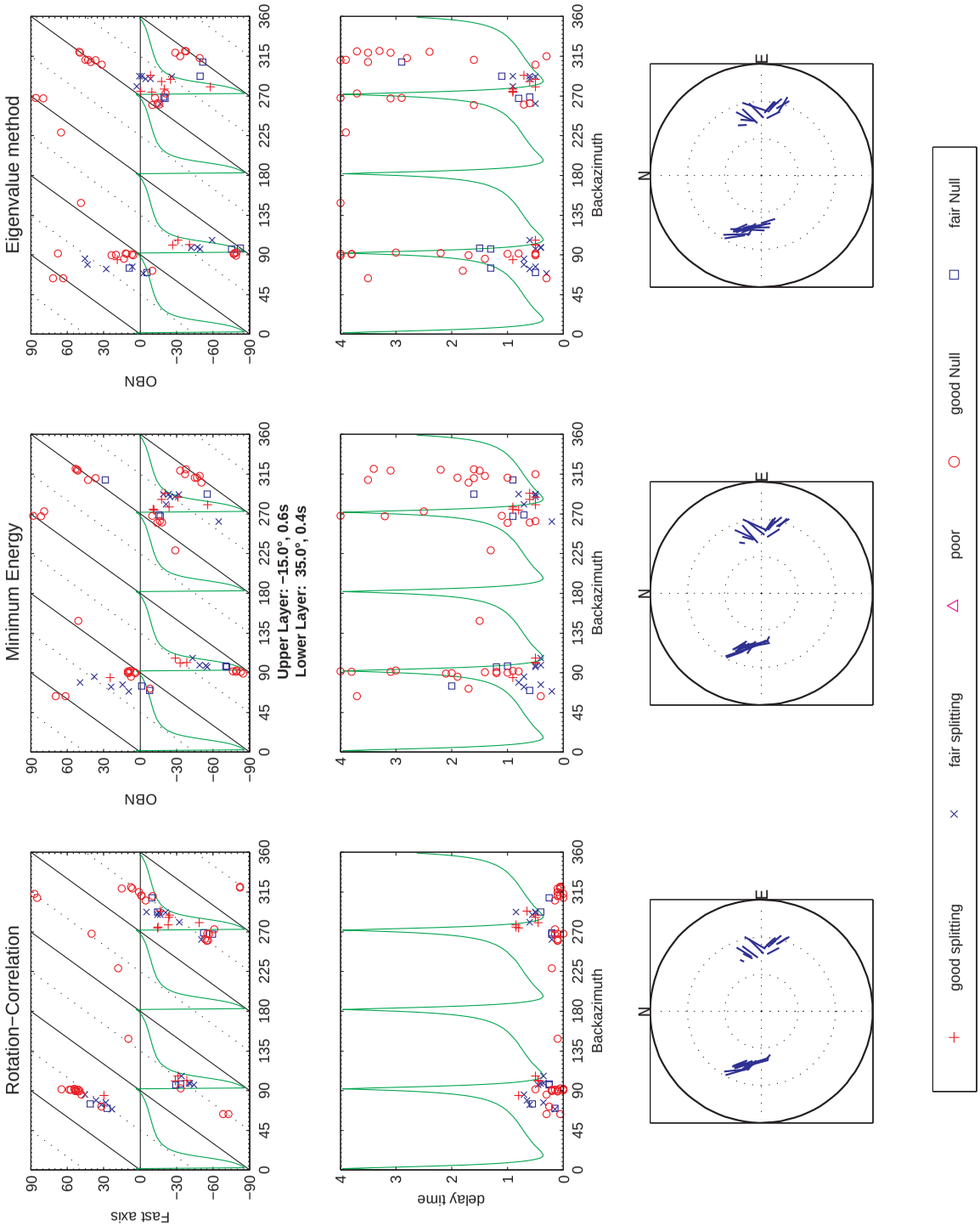

Figure A- 15: Backazimuthal plots for station OBN with best two layer model fit at 8sec dominant frequency

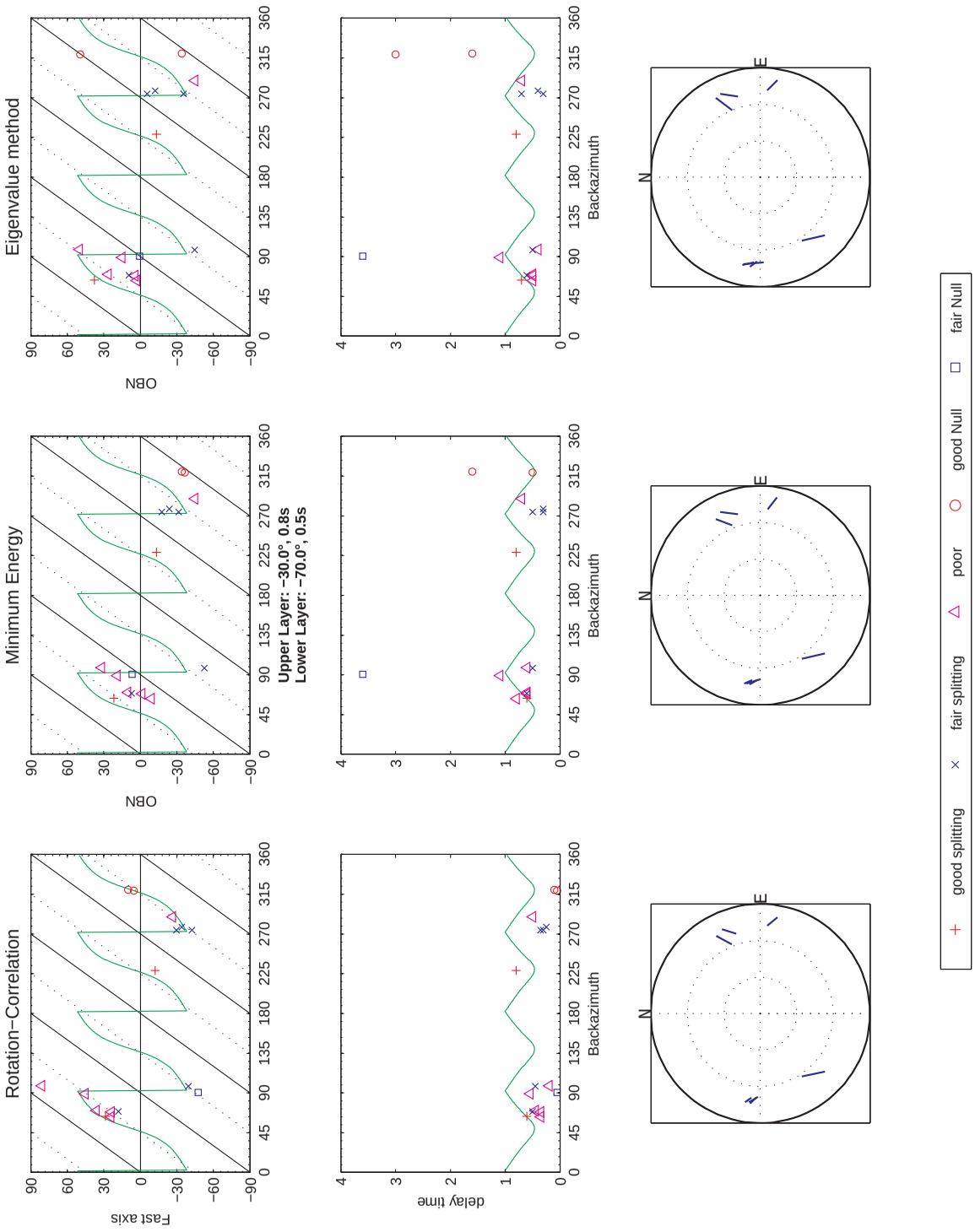

Figure A- 16: Backazimuthal plots for station OBN with best two layer model fit at 2sec dominant frequency. Nulls are not displayed.

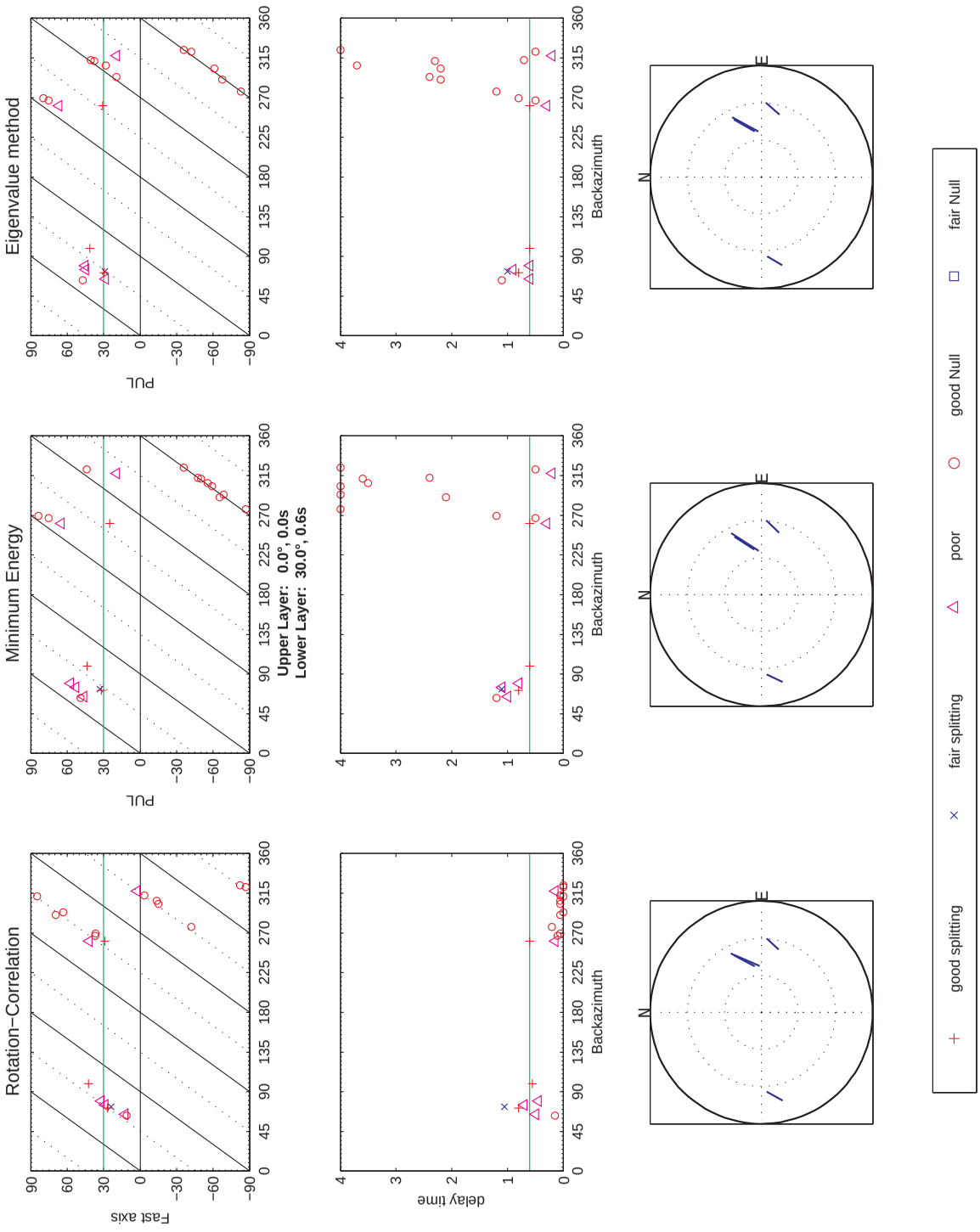

Figure A- 17: Backazimuthal plot for PUL

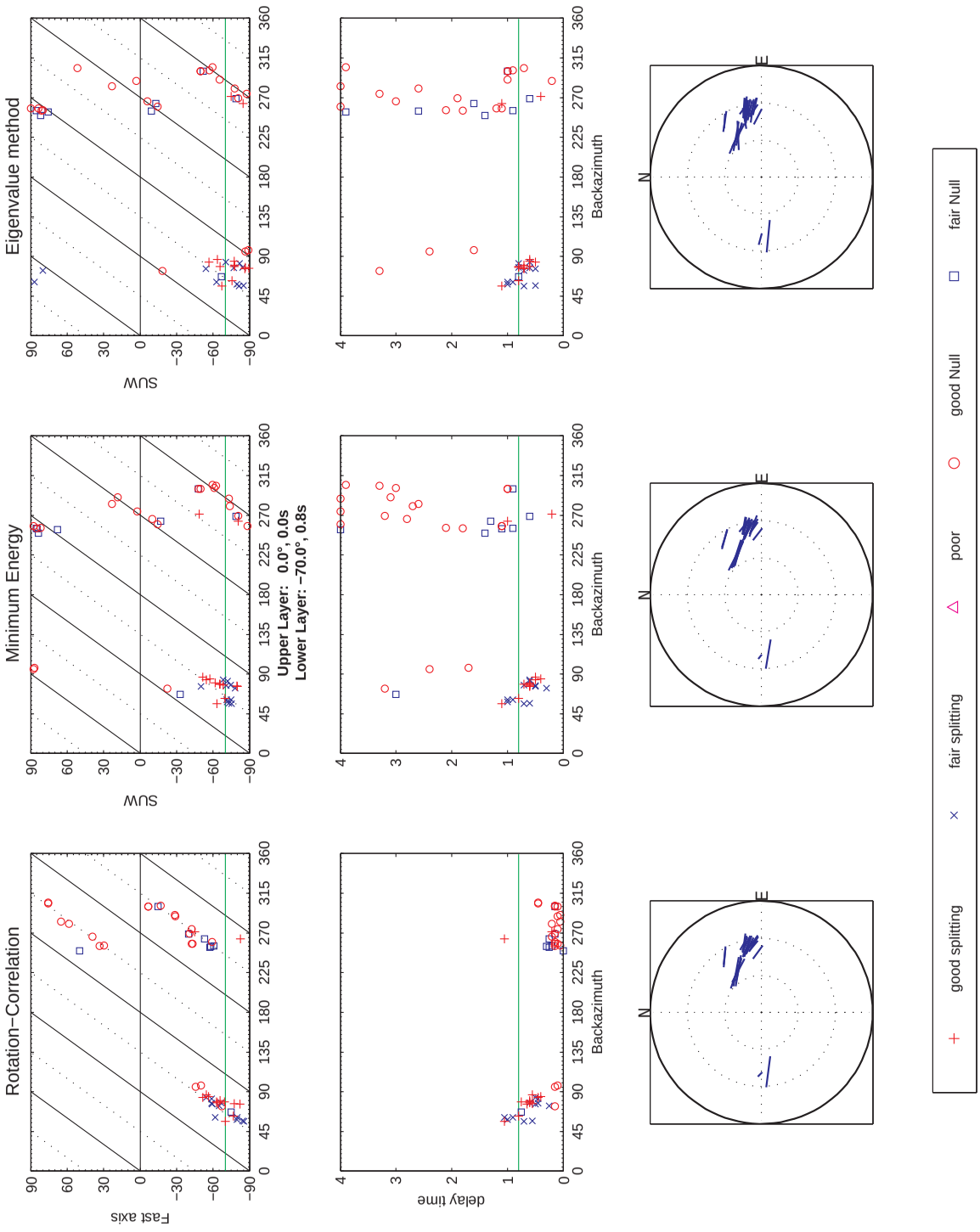

Figure A- 18: Splitting results for station SUW

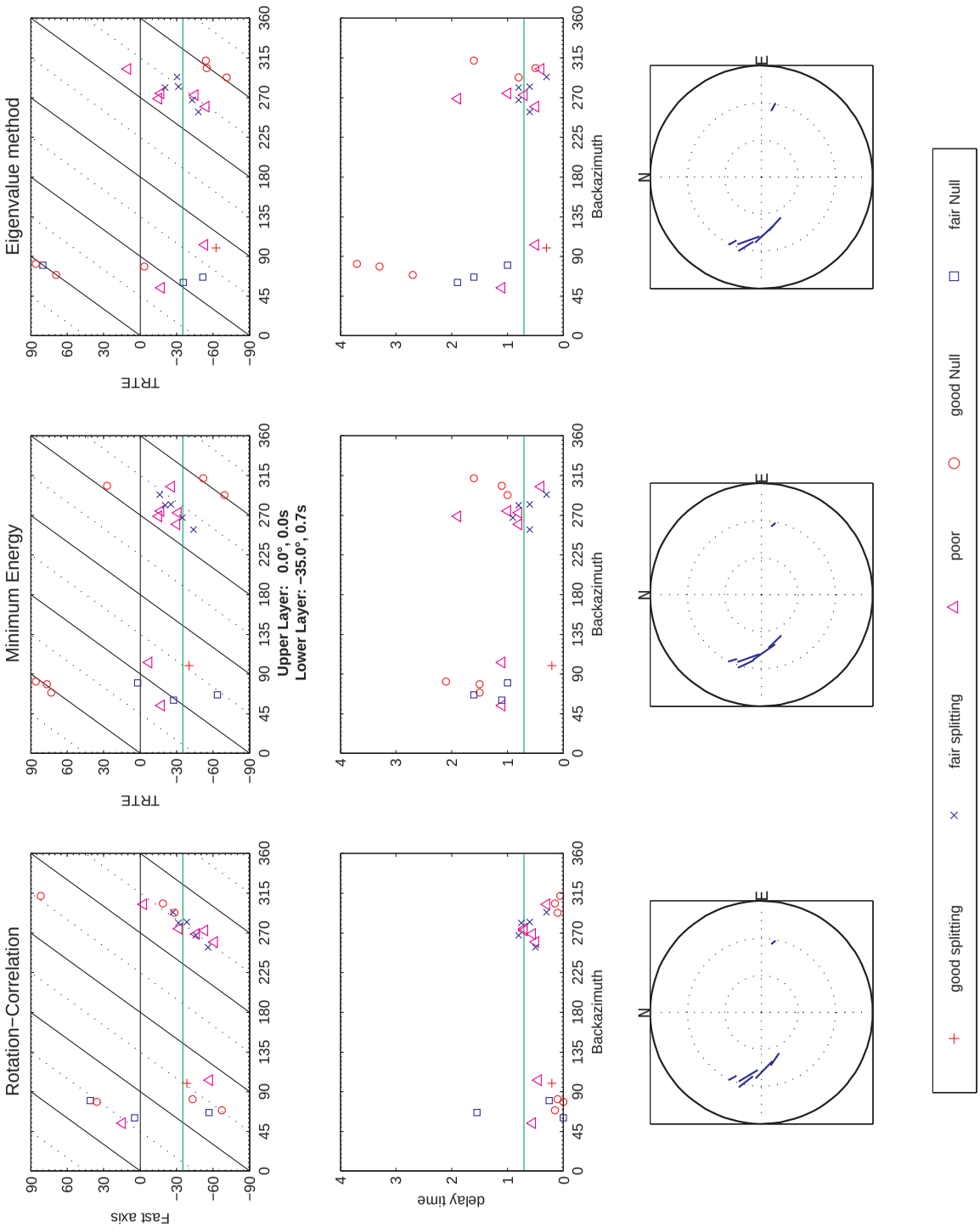

Figure A- 19: Splitting results for station TRTE with one layer fit

7.3. SplitLab - The User Guide

7.3.1. Preface

7.3.1.1. Requirements

SplitLab should run on every computer system (MS Windows, MAC, Linux, SUN) with *Matlab7.0* or higher and the *Mapping toolbox* and for full functionality the *Signal Processing toolbox.*

For information on MatLab please visit the homepage:

http://www.mathworks.com/store/default.do

7.3.1.2. License:

SplitLab is PostCard ware! If you like it, please send a Postcard of the place you live to:

Andreas Wüstefeld
Laboratoire Tectonophysique
Place Eugene Bataillon
34095 Montpellier, France

A selection of the best Postcards will be places on the SplitLab homepage SplitLab is free software; you can redistribute it and/or modify it under the terms of the GNU General Public License as published by the Free Software Foundation; either version 2 of the License, or (at your option) any later version.

SplitLab is distributed in the hope that it will be useful, but WITHOUT ANY WARRANTY; without even the implied warranty of MERCHANTABILITY or FITNESS FOR A PARTICULAR PURPOSE. See the GNU General Public License for more details.

7.3.1.3. Bug report:

If you think you found a bug, don't hesitate and write an email to splitlab@gmx.net. Please include the project file and the 3 SAC files in your email. This simplifies the search for the bug. Please also copy and paste the complete error message in the email, i.e. everything, that Matlab outputs in red...

In general, any comments are welcome, especially positive ones:-)

7.3.1.4. Suggestions:

Please report wishes for additional features or any changes in the source codes to splitlab@gmx.net. This helps every user and allows for the maximum functionality for every user.

7.3.2. Installation

After unzipping the SplitLab package, put the SplitLab directory at your favorite place

1. Start Matlab
2. In Matlab, go in the SplitLab directory
3. The installation of SplitLab is made by running the macro named "*install_SplitLab.m*". Type "**`install_SplitLab`**" inside Matlab. This macro makes several things
    - it installs the matTaup package as a Matlab toolbox in the Matlab directories. matTaup is a Java program that allows the calculation of the travel times, of the hodochrons, and of the ray path through the Earth.
    - it also installs in the SplitLab directory the event catalog files, such as the NEIC epicenter locations and the Harvard Centroid Moment Tensor (CMT). Either file is used in the following processes for the event selection and to create the virtual link between the seismograms and the events.
4. Restart Matlab

Perhaps Troubleshooting (Chapter 7.3.8) helps case of problems

7.3.3. Running SplitLab

In the Matlab environment, type the command "**`SplitLab`**". It opens the "*Configure SplitLab*" window that will allow you to prepare your project, i.e. your data selection, your data request, and to build your seismic database that will allow you to manage easily data and results in the processes of shear wave splitting measurements.

What is a *SplitLab project*? A project can be defined as a set of seismic data associated to a set of events derived from a given selection. Any given project concerns a single station

since the selection of data is performed from station-events epicentral distances. A project is generally related to a directory where data are stored. A given project may concern only part of seismic data in the directory and alternatively, several projects may coexist in a given directory where data are stored: a first project may be focused on SKS splitting measurements, a second on P-wave analyses, etc.

In order to have the project OK and operational, one has to follow the six steps presented on the left end side of the "configure" window: general -> station -> Event -> request -> phases -> find files.

7.3.4. The Project Configuration Window

7.3.4.1. The "General" panel

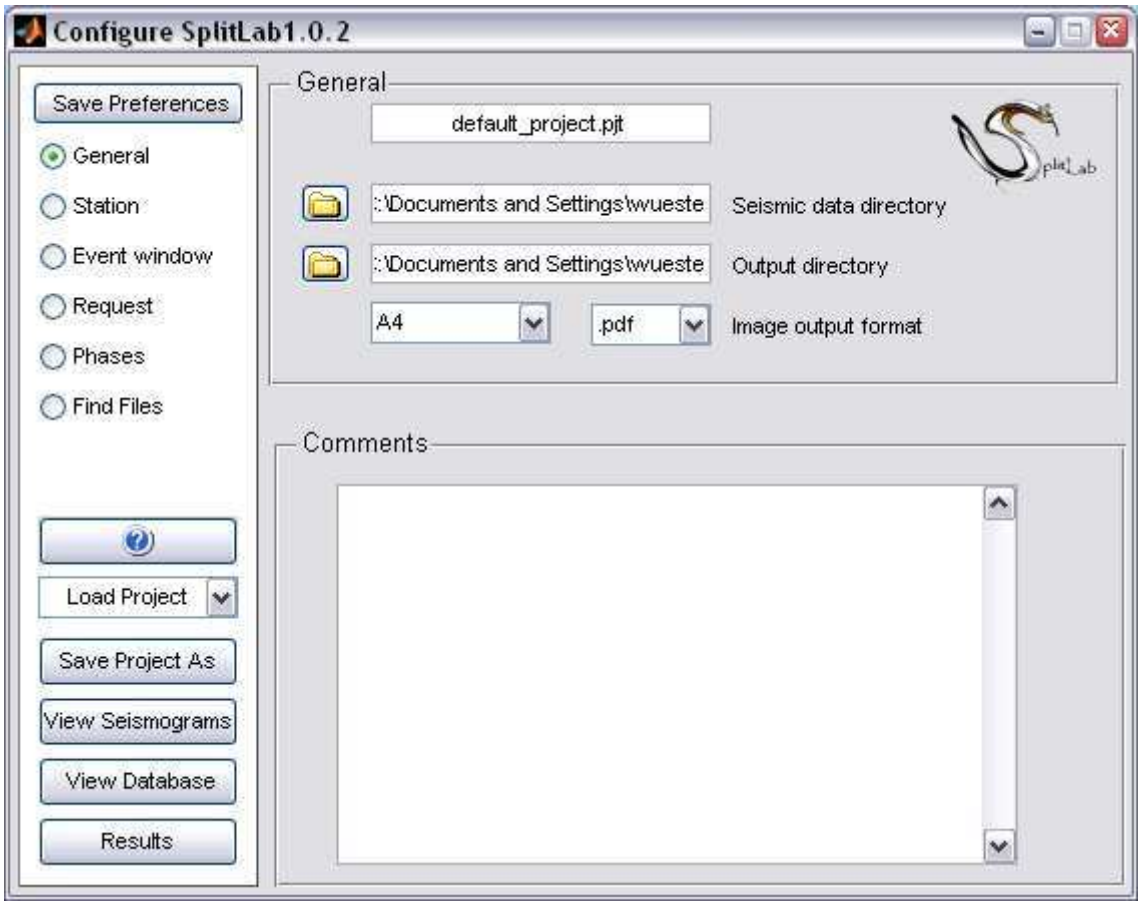

The upper window allows you to define your project name and the directories where the data are and where the output data will be stored. This allows the user to have the data ready in a directory and to store the results in another place, without affecting the data directory.

The lower part of the window allows you to store various comments related to this project.

7.3.4.2. The "Station" window:

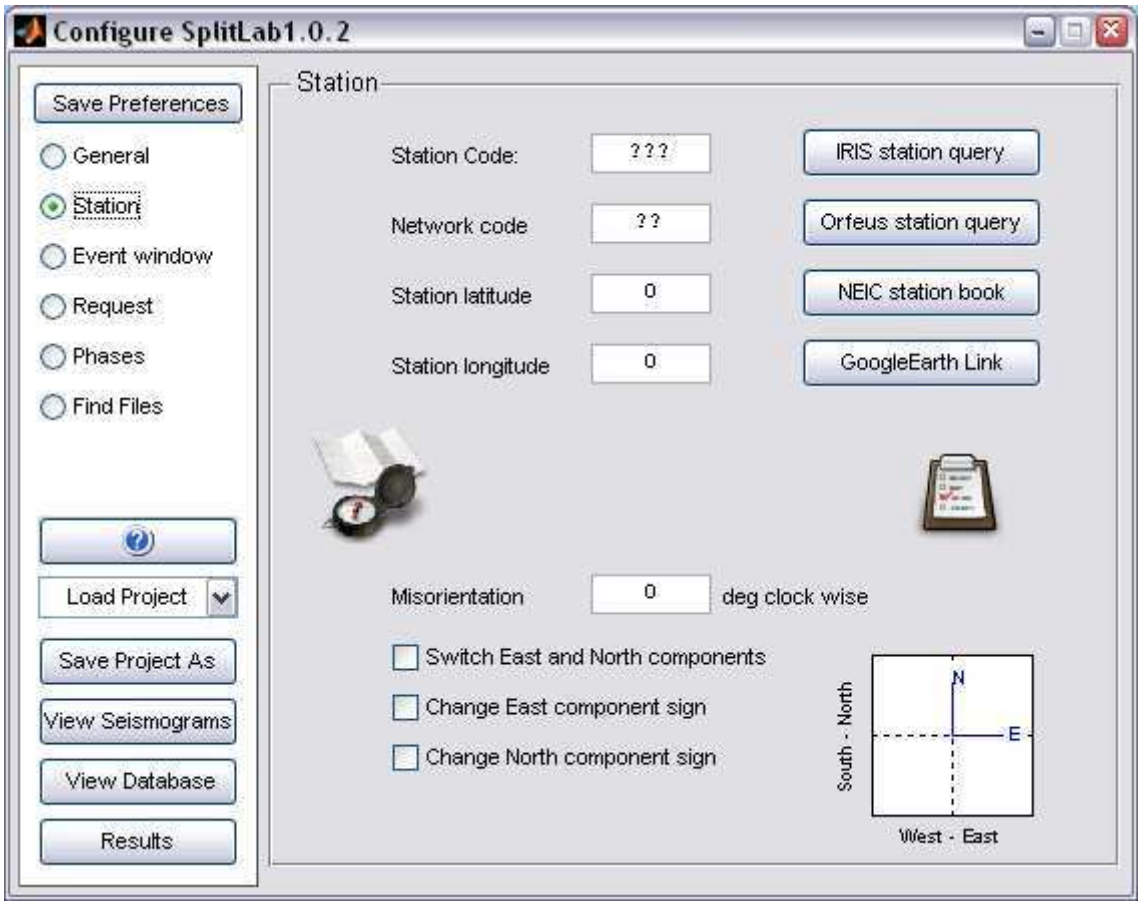

This window summarizes the information related to the station. The station *latitude* and *longitude* are absolutely necessary since they are used to select the event from the epicentral distance and to calculate the various phases travel times.

If the station has a known *misorientation*, the angle can be input in this window. This allow the user to work on true N, E and Z components and therefore, on the true radial and transverse components. Note that this operation is performed in Matlab and does thus not affect in any case your raw data.

Problems of component *signs* or *polarities* may be corrected in this window and may be combined together with the component misorientation value.

Several buttons of the right of the window provide direct Internet access to *station query tools* (such as IRIS) or to *station books* (such as NEIC). This may be useful when preparing a request, to look for instance for a stations in a given area or running during a given period.

7.3.4.3. The "Event" window:

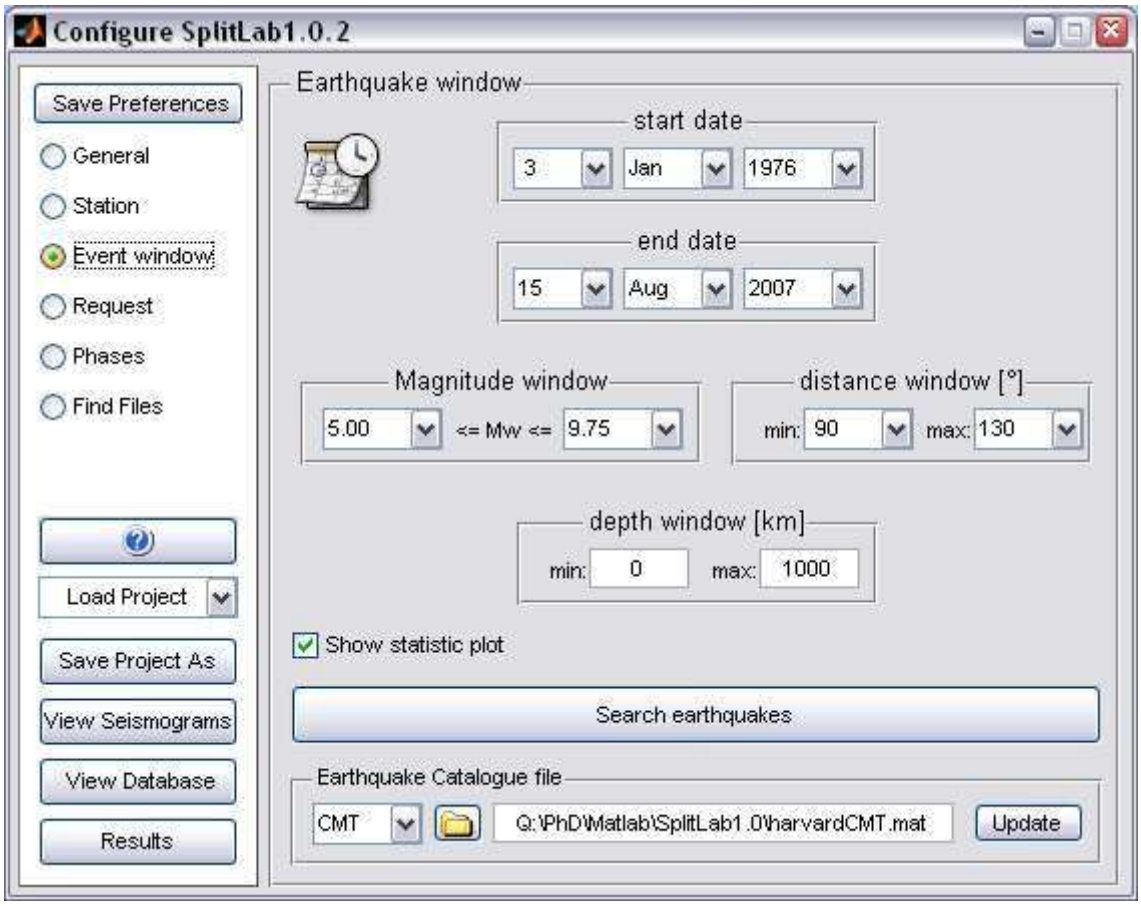

This window allows to prepare your event selection within the earthquake catalog file (NEIC or Harvard CMT) combining the *start and end dates*, the *event magnitude* (Mw), the *epicentral distance* and the *event depth*. Click on the "*Search*" button when the parameters are OK. It results (if selected) in the "*statistic plot*" that displays:

- the event location on a map preserving the true backazimuths,
- the histogram of the backazimuthal distribution, for 360º in green and for 180º in gray
- a rose diagram presenting the same backazimuthal distribution

The SplitLab package is provided with the earthquake catalog covering the period 1976 to 2006 and it may be necessary for the user to keep the local CMT or the NEIC files updated in order to search through an updated event catalog. The "*update*" button provides a way to automatically update the CMT files (in the case of the Harvard CMT format) or the information necessary to request to NEIC the data in the right format (in the case of the NEIC data format selection). Note that the NEIC catalog does not allow the calculation of the phase energy.

7.3.4.4. The "Request" window:

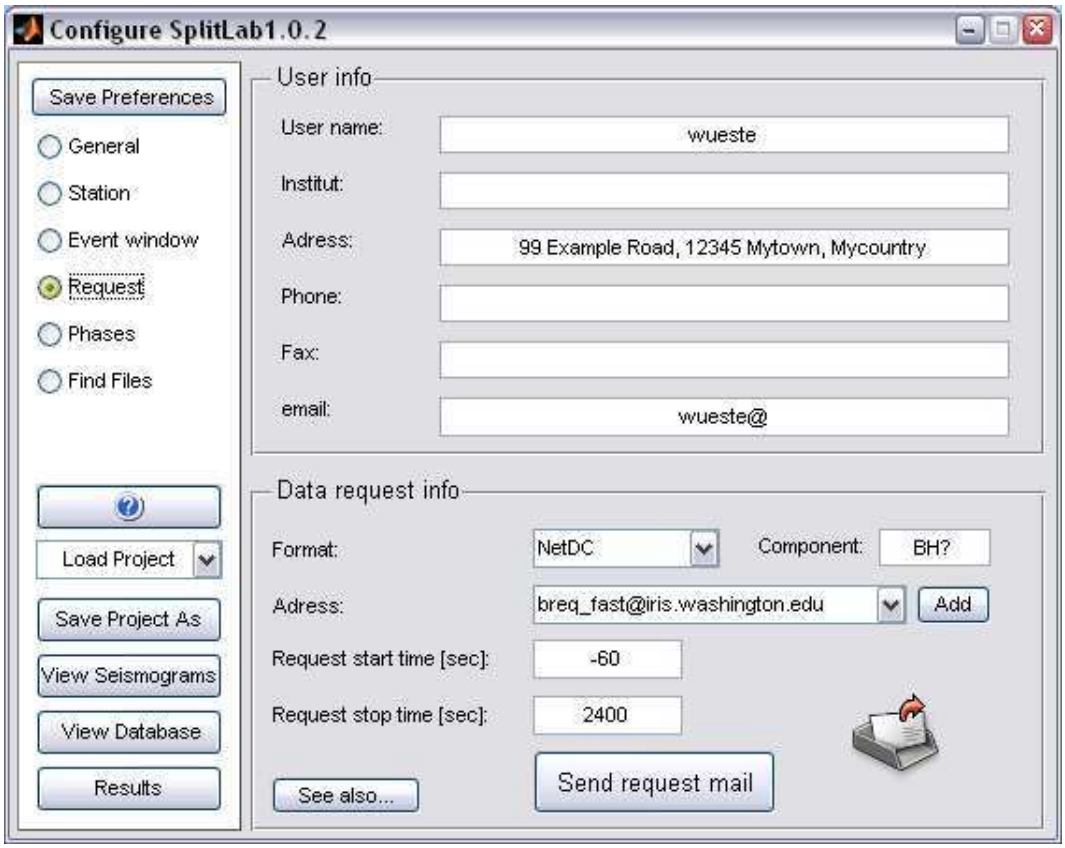

The information that you enter here will allow to prepare, format and send the request to your selected request site. In the case where you already have the data with you (for instance after a temporary deployment or coming back on old data that you already worked on), you do not have to worry about this window. If you do not have the data with you, and if you wish to request them, you have to fill the full window:

In the upper part of the window, you have to provide the information generally requested by the automatic request systems: your *name*, your *institute*, your address. Your *email* is absolutely necessary since you will be contacted by mail on the status of your request, and on the availability of the data.

In the lower part of the window, you have to choose between the various request types (*NetDC, BreqFast, AutoDRM or ASCII table*) and to the request server where the request will be sent to. You have to define the component you desire, the "*start time*" relative to the event time (0 corresponds to event time) and the *length of the seismogram* in seconds (Figure 1a). There is no way is the present version of SplitLab to prepare request relative to a phase, such as a starting time 60 seconds before a P-wave arrival… Perhaps in a future version! click "*Send request mail*" button and wait for delivery, few minutes, few hours or few days depending on the size of the request and on the activity of the servers. Multiple short requests (less than 200 events) are generally handled faster than one big.

7.3.4.5. The "Phases" window:

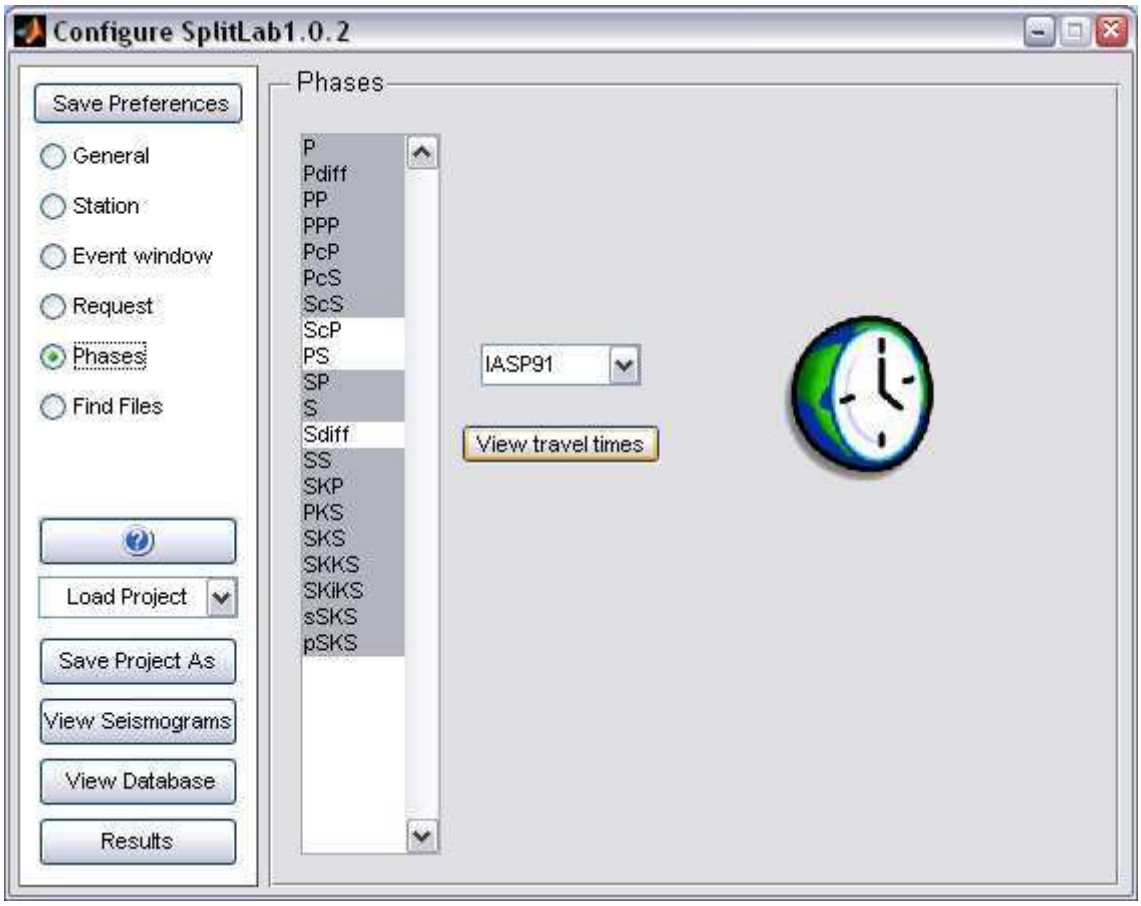

This window allows you to select the phases for which you wish to see the arrival times on your seismograms. These theoretical arrival times are calculated by using the PREM or the IASPEI91 Earth models. The "*view travel time*" button allows you to see

- the travel time of the selected phases as a function of the epicentral distance

- the travel paths through the Earth

7.3.4.6. The "Find Files" window

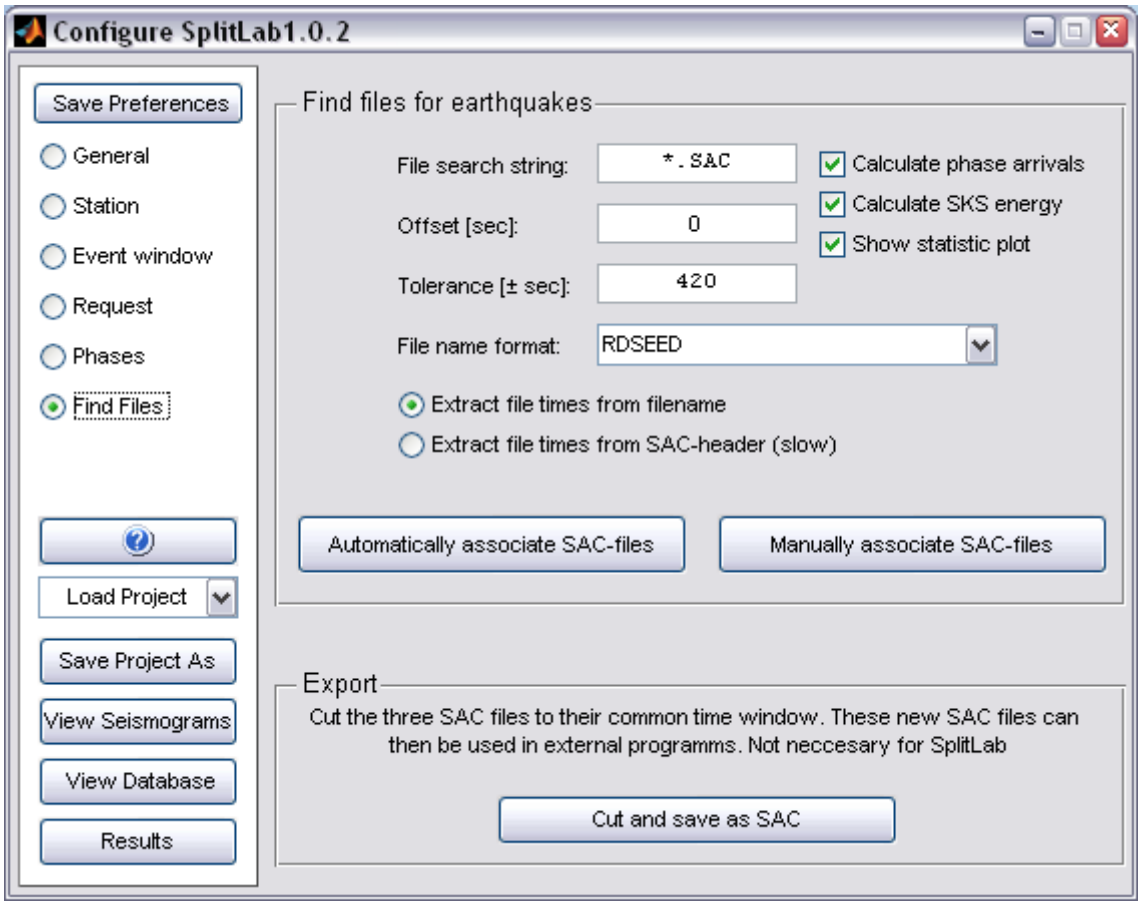

It is the final and important step that will allow you to make the link between the event list and the seismogram list that you actually have, and therefore to built a coherent and effective seismic database. In the present state of the SplitLab package, the filename format is either

- RDSEED
- SEISAN
- YYYY.MM.DD-hh.mm.ss.stn.sac.e,
- YYYY.JJJ.hh.mm.ss.stn.sac.e.
- *.e; *.n; *.z

See “Create your own Format” for more information

Note: A Java version of rdseed for Windows platforms a currently (Sep. 2006) under development by the IRIS consortium

Choose the *filename format* corresponding to your data. This is absolutely necessary to identify the seismogram components. If you selected

*.e; *.n; *.z

the last letter of the filename is used to determine the component of each file and the file start times are extracted for the SAC header. Allowed component descriptors are **`e,n,z`** or **`E,N,Z`**

find the best file *search string* that may help the program to go through the whole set of data in the directory where your data are. As well the * as the ? wildcard is possible. Be aware that files other than the expected seismic data may complicate the task. For instance, the presence of **`*.sac.r`** or **`*.sac.t`** for radial or transverse component of SAC files will not allow a right linking of events and seismograms. The safest way to make this step successful is to have the directory full of only the **`sac.e`**, **`n`** and **`z`** components.

The "*offset*" is the time duration between the event time and the starting time of your seismograms. Ideally, this offset should be identical to the "*request start time*" defined in the previous window but the data management center may have sent you data beginning later than requested. The offset value represents this difference (Figure 1b).

The "*Tolerance*" value in seconds will define the time window within which the program will try to associate a seismic file to an event file, by using either its name or the information contained in the header. It is up to the user to find the best compromise: a value too small will let orphans and a value too large will bring confusion since several files could be associated to a seismic event (Figure 77).

If the name of the sac file is (roughly) the beginning time of the seismogram, then use the "*extract time from filenames*" button else use the "*extract times from SAC headers*". This second way is slower since it has to physically open each file to read the header in order to find the begin time that will be used to connect to a given seismic event.

In the best case, the event-to-seismogram link will be created automatically by pushing the "*Automatically associate SAC files*" button. Otherwise, you can do this association manually via the "*Manually associate SAC file*" button. Anyway, at the end of the automatic association, the system may provide a list of orphan events and of seismic files that it did not succeeded to link together. This will happen when a wide event selection has been done and will be associated to a rather short existing seismic database. In that case, numerous events will not be associated to seismic files, but that is normal. Orphans may also happen when two or more events occur in a short time window, smaller than the "*tolerance window*". In that case the user may terminate manually the association. At the

end of this linking process, the seismic "*Database*" is ready for use. Do not forget to save it ("*Save Project*" button). This database can then be viewed by using the "*View Database*" button that provides the list of the events together with the global map. This database will be the starting point of the following processes such as the shear wave splitting measurements.

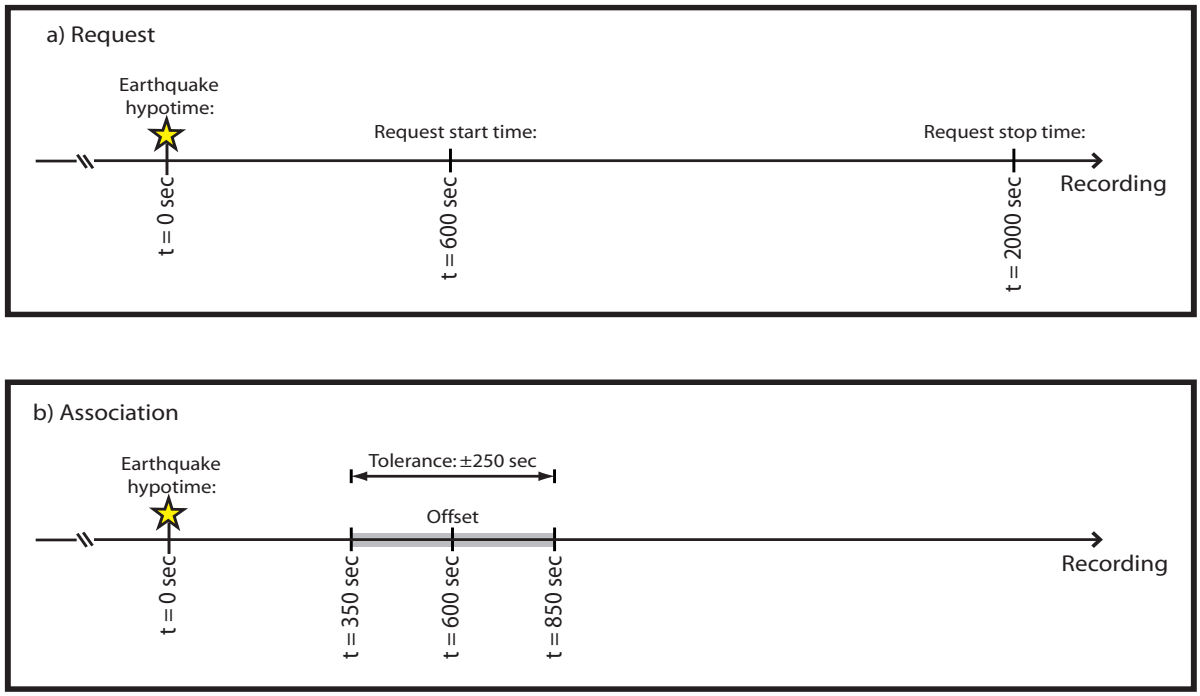

Figure 77 : (a) Definition of request start and stop time and (b) their correspondence to the file-search offset and tolerance

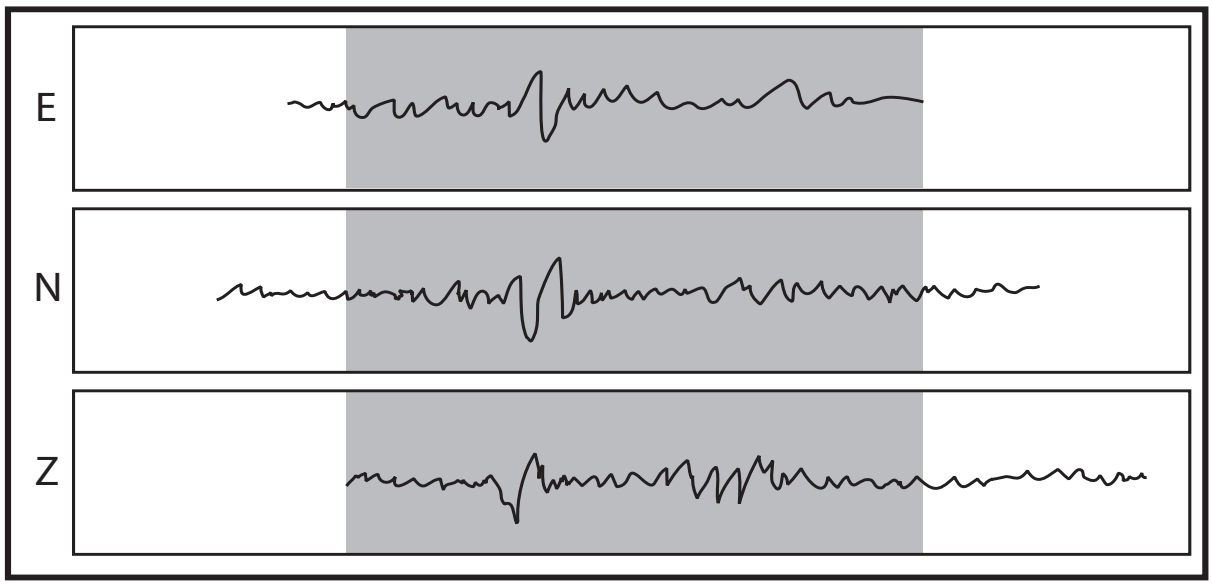

Figure 78 : The “Cut and save” button searches for the three SAC file components (East, North, Z) for their maximum common time window (here marked as gray area). Each seismogram is then cut to this time window and written to new SAC files.

The "*Cut and save as SAC*" can be used when the e, n and z components start and end at different times and therefore have different names. This button will cut the beginning of the triplet at the latest start time and the ending time at the earliest ending time of the triplet. The triplets are then saved under new names. This provides a way to export data with coherent lengths and names for other purposes than splitting measurements (Figure 78).

7.3.4.7. The “Save Preferences” button

the current configuration is saved as default Project entries for future sessions of SplitLab

7.3.4.8. The “?” button

It provides some help and information that may be useful for the user

7.3.4.9. The "Load Project" button

Allows to load a project that has been already saved.

7.3.4.10. The "Save Project As" button

Allows to save a project. It is important to save a project after having successfully finished the association between the seismograms and the events ("*Find Files*" operation).

7.3.4.11. The "View Seismograms" button

Starts the Seismogram Viewer at the beginning of the database for a newly created database. If you loaded the project, the last used database entry will be displayed.

7.3.4.12. The "View Database" button

It provides a way to select and visualize each of the seismogram from the database. The *Database* is defined as the set of seismograms that have been successfully linked to the selected events. In other words, the database is closely related to a project and a given data selection and might not contain all the SAC files the data directory.

Clicking the "*View Database*" button opens the "*Database Viewer window*".

7.3.5. The "Database Viewer" window

This window lists the events present in the database and the "*World viewer*" geographically presents the events from the database.

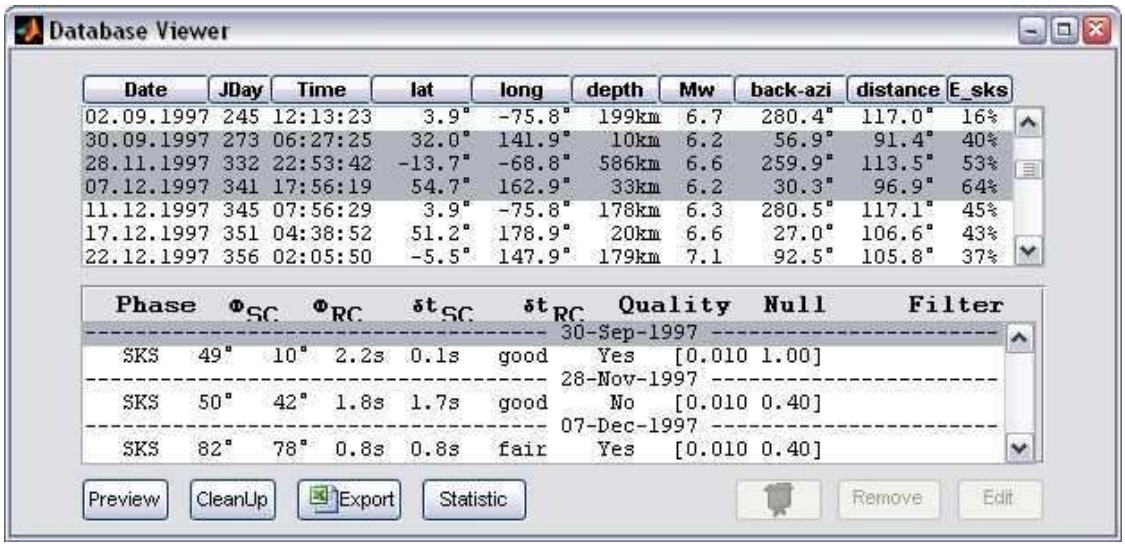

By clicking on one or several events from the list, you can visualize them as stars on the map. The user can zoom in and out on the map.

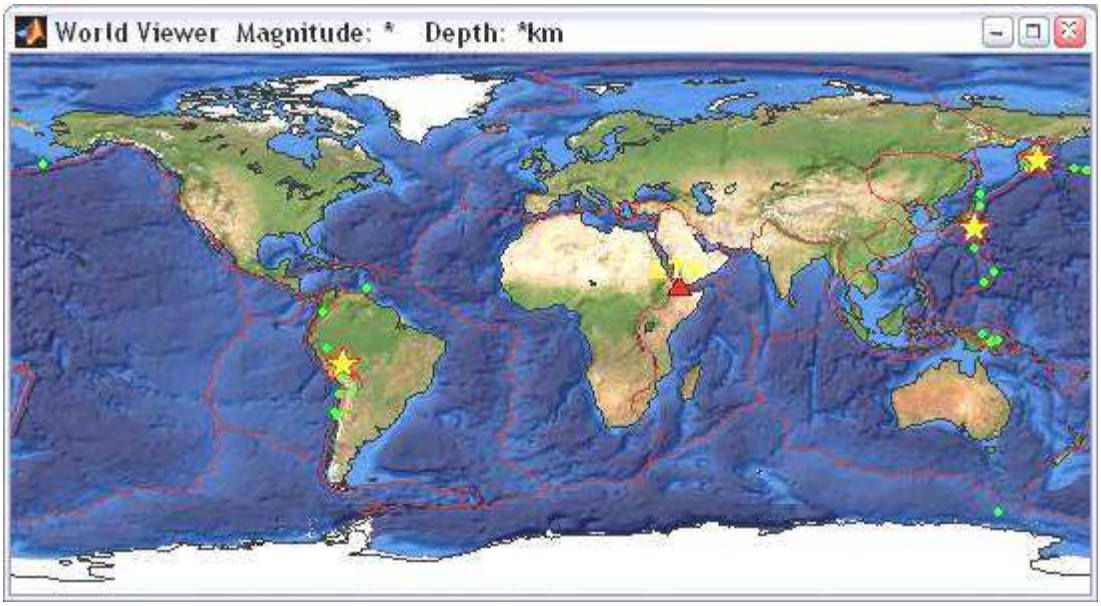

The events are sorted by date as default but you can choose your sorting criteria by clicking at the top of the column, the event distance, depth or magnitude may be useful in the process of shear wave splitting measurements.

The lower part of the window displays the shear wave splitting result(s) that have been saved for a given event. It also present some button:

The button "*view*" allows opening the "*preview*" window to see the 3 components of the selected seismogram.

The "*Cleanup*" button allows removing from the database the events on which no splitting measurements are made. After such an operation, it may be a good idea to save the project under a new name (button "*Save Project As*"), in order to keep the possibility to come back on data that did not provide splitting measurements.

The "*Export*" button allows to save the table as an Excel file.

The "*statistics*" button displays:

the event location on a map preserving the true backazimuths,

the histogram of the backazimuthal distribution,

a rose diagram presenting the same backazimuthal distribution.

The "*Presentation*" button allows to visualize the graphical results of a splitting measurement. Indeed, when the user saves a result, a copy of the graph is also saved in the output directory.

The "*Remove*" button allows the user to remove the result of a splitting measurement from the list.

The "*Edit*" button allows visualizing the numerical values associated to the splitting measurements obtained on a seismic event.

7.3.6. The "*SeismoViewer*" window

By clicking on the "*Preview*" button in the "*Database Viewer*", one accesses to the "*Preview*" window, which displays the 3 components of the selected event, together with the predicted arrival times (calculated at the "*Find Files*" stage). The data can be easily filtered through a set of prepared filters accessible through the keyboard. The list of the available filters are summarized together with their shortcuts appear by clicking on the "*?*" button at the top of the window.

The basic operations and setups are accessible by a set of buttons aligned at the top of the window:

Figure 79 : the SeismoViewer button bar offers manifold options…

The "*SAC*" button save the seismograms visible at the screen as SAC files (“SAC screenshot”). Note that only the length of the window is exported.

The "*Database*" button allows to select a seismic event through the database

The "P*rint*" button allows to print the window

The "*Toggle*" button puts and removes grids on the seismogram. By default, each seismogram is vertically scaled to the maximum value of the component.

The "*Lock*" button allows to present the 3 component at the same vertical scale

The "*System*" button allows to switch between the E-N-Z reference frame to the L-T-Q reference frame.

The "*Time table*" button allows to plot the arrival times and the travel paths of one of several seismic phases selected by the user for event present on the screen.

The "Z*oom In*" button allows to zoom into a time window defined by the user by dragging the mouse along the seismogram.

The "*Zoom Out*" button remove the zoom.

The "H*ome*" button allows to zoom directly onto a selected seismic phase, that is selected on the rolling menu at the bottom left of the window. It can be accessed also by typing on the "*home*" key (for the PC) or on the "*esc*" key for the Macintosh.

The "*Left Green Arrow*" allows to visualize the previous seismic event of the database.

The "*Particle Motion*" button presents the particle motion diagram of the 2 horizontal component (EN or QT) for the selected time window.

The "*Options*" button allows the user to select the type of shear wave splitting measurement: either by calculating the minimum energy on the transverse component or by using one of the various methods that allows to determine the minimum eigenvalues. Furthermore, the maximum delay time for the splitting measurement can be set.

The "*Right Green Arrow*" allows to visualize the next seismic event in the database.

The "*Trash*" button removes the current event from the database.

The "S*peaker*" button plays the selected time window as sounds.

The "*Camera*" button saves the actual seismogram as a graphic file.

The "*?*" button provides help on shortkeys some useful things…

7.3.7. Performing shear wave splitting measurements through SplitLab

In the "Database Viewer", select your seismic event and click on the "View" button; It is loaded in the "preview" window

Visualize your event in the geographic and seismic reference frame, use different kinds of filters and zooming options to evaluate the quality of the data and to locate the core shear phase on which you wish to make your measurement.

Select the phase-of-interest. The Phase selector can be found in the lower left corner of the SeismoViewer.

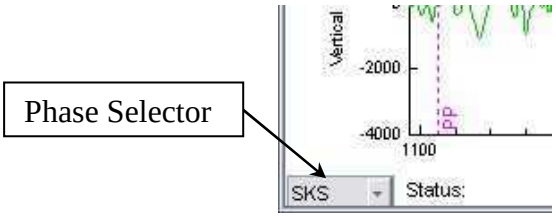

Select the time window on which you want to make the splitting measurement. The active time window will appear in gray whereas the old selection, if any, appears in yellow.

Press the "ENTER" key to start the measurement. When the measurement is finished, then appear the "Diagnostic Viewer" window that summarizes the results obtained by the different methods:

- At the top of the window is presented the radial (in blue solid) and transverse (in red dashed) components at the same vertical scale, filtered in an extended section of the previously chosen window without any correction.
- The upper horizontal panel presents a set of diagrams obtained by using the rotation-correlation method. From left to right:

The fast (blue solid) and slow (red dashed) split components corrected from the delay time. This diagram allows checking the correlation of the waveforms.

The radial (blue) and transverse (red) components corrected from the anisotropy. This allows to see if the signal on the transverse component has been well removed after correction for the best phi and dt pair.

The particle motion diagram, before (in blue) and after (in red) the anisotropy correction. In case of a good measurement, the elliptical particle motion is well linearized after the anisotropy (phi and dt) correction.

The map of the correlation coefficients showing the quality of the correlation between the fast and slow split waves for phi varying from -90 to 90° and for dt varying from 0 to 4 s

(or any other maximum delay time chosen in the SeismoViewer options Menu). Note that the program calculates the correlation for steps of 1° in phi and each sample.

1. The lower horizontal panel presents a set of diagrams obtained by using the minimum energy (or Silver and Chan) method. From left to right:
    - The fast and slow split component corrected for the best delay time.
    - The radial and transverse component corrected from the anisotropy.
    - The particle motion diagram, before (in blue) and after (in red) the anisotropy correction.
    - The map of the Energy on Transverse components or of Eigenvalue (as chosen in the Option Menu of the SeismoViewer). Here, the grid-search parameters are 2º in phi and 2 samples in time. For a 20 Hz acquisition (delta of 0.05 s between two samples), the time steps will be of 2x0.05=0.1s.
2. The results are summarized in the upper part of the window, as numerical values and the error bars for the different methods and as a polar diagram on which the fast direction is plotted with the actual backazimuth and inclination.

If you do not like the measurement, go in the "*Results*" menu and choose "*Discard*" to reprocess another time window, another phase or to test another filter. If you wish to keep this measurement, you have to choose a quality in the "*Quality*" menu, to indicate whether it is a null or not in the "*IsNull*" menu and to save it in the "*Save*" menu. Note that the quality and null information are just comments and have no role in the subsequent process. In that case, the figure is saved in the format selected in the "*configuration*" panel and the numerical results are also summarized in the "*Database Viewer*", linked to the right event. The “Result Viewer” window

7.3.7.1. The “Options”

The “ResultViewer Options” window allows to select which part of the result database you want to see:

- In the “Phases” panel select the phases of which you want to see the results
- Select, if you want the “Manual Quality” of the “Automatic Quality”. The former uses the Quality assigned to each measurement in the “Diagnostic plot” The latter determines the quality of each measurement based on the difference between th RC and SC results. See Wüstefeld & Bokelmann, (BSSA 2007) for details
- Select the Qualities you want to see: good, fair, poor

- Select if you want to see the Nulls or non-Nulls (or both)
- Automatically determined Quality includes “Weak” splitting (both RC and SC delay times are small). Select the “Weak” option to include these events in the plots and to add the delay time thresholds to detect weak as gray area in the plot.
- Select “Show Null grid” to display grid-lines in the fast axes plots. The solid grid-lines indicate where backazimuth and fast-axes coincide. The dashed grid-lines indicate a 45° difference between backazimuth and fast axes.
- The “*Fit to Model*” panel allows to calculate the theoretical backazimuthal variation of the fast axes and delay times (Savage & Silver, 1994). Set the delay time slider of second layer to “0” to see the lines for a single layer model.

7.3.7.2. The “Backazimuth distribution”

The results corresponding to the selected options are displayed for each technique (RC, SC, EV). The fast axis estimates make up the first row, the delay time estimates the second row.

7.3.7.3. The “Stereoplots”

In the third row of the result plot, stereoplots of the non-Null results are displayed. The lengths of the markers scale with the delay time, the centre of the lines correspond to backazimuth and the inclination of the wave at surface.

7.3.8. Trouble shooting

7.3.8.1. Installation problems

In case of problems please check:

The file **`classpath.txt`** You can view the file by typing in Matlab: **`edit(which('classpath.txt'))`**

This file contains the path to JAVA classes in Matlab. At the end of the file should be the proper path to the file "**`matTaup.jar`**" located by default in **`$MATLABROOT/toolbox/matTaup/lib/matTaup.jar`**

After editing classpath.txt you have to restart Matlab

The Matlab search path should contain the following folders:

SplitlabX.X.X/

SplitlabX.X.X/Tools

SplitlabX.X.X/ShearWaveSplitting

The path to the SacLab Utility

SplitlabX.X.X/SacLab

The path pointing to matTaup (usually at the end of the path)

$MATLABROOT/toolbox/mattaup

For editing the path use the command: **pathtool** or edit/create your local **startup.m** file. See the Matlab documentation for startup options

7.3.8.2. Preferences problems

During installation, SplitLab preferences are added to the Matlab environment (See the **prefdir** documentation for further details on preferences). The SplitLab Preferences contain the fields CONFIGURATION (default SplitLab project configuration), ASSOCIATIONS (figure export file types and, on non-PCs, the system command line to open the file type) and HISTORY (recently used SplitLab Projects). These preferences are only valid for the user, who installed SplitLab. However, if a new user runs SplitLab, new default preferences are automatically created for that user. In multi-user case be sure that all users have permission to the SplitLab, SacLab and matTaup path and the paths are set correctly for each user.

7.3.8.3. Create your own filename format

The association of a SAC seismogram to an event in the Database is is done in tow steps:

The finding of appropriate file start times corresponding (within a tolerance and eventually an offset) to the hypocentral time (Figure 1). This is done in the Matlab function **/Tools/getFileAndEQseconds.m**

The ordering of three matching files by component: East, North, Vertical. This ensures that in the database variable **eq.seisfile** of your project the first entry corresponds always to the East component, the second entry to the North component and the third to te Vertical. This is done in the Matlab function **/Tools/sort_components.m**

Two variables of your project configuration determine your choices:

`config.FileNameConvention` is a string corresponding to your selection in the File-Format Menu (eg 'RDSEED')

`config.UseHeaderTimes` is a logical value: 1 mean you wish to use SAC header times, and 0 means you would like to use the filename to determine the start time of the file.

Knowing all this, adding a new Filename format should now be straightforward:

edit **`/Tools/getFileAndEQseconds.m`**

go to the line which states

```
switch config.FileNameConvention
```

after this line add a new *case* statement:

```
case 'MyFormat'
```

state the positon of year, julian_day, hour, minute and second in the filename. If not all these informations are given, make sure you set the search-tolerance and search offset appropriately! Please use the existing formats as templates to your format. If your format uses day and month instead of julian_day, you have to use the «dayofyear» function, as in the 'YYYY.MM.DD-hh.mm.ss.stn.sac.e' format.

The given values have to be transformed to seconds after Jan, 1st of the corresponding year. Add something like the following:

```
FIsec  =  FISS + FIMM*60 + FIHH*3600 + (FIddd)*86400;
```

Note, that this approach omits any event close to «midnight, new year».

Save **`/Tools/getFileAndEQseconds.m`**

edit **`/Tools/sort_components.m`**

go to the line which states

```
switch config.FileNameConvention
```

after this line add a new *case* statement:

```
case 'MyFormat'
```

Define then a variable **pos** whose value corresponts to the position of the Letter in the filename which determine the Component name. For expample, if the Component corresponds to the 18th letter, use:

```
pos = 18;
```

Please use the existing formats as templates.

Save **/Tools/sort_components.m**

Finally add your format to the file format menu

edit **/private/configpanelFINDFILE.m**

find the line where the menu entries of the uicontrol are defined:

```
str = {'RDSEED' 'SEISAN', 'YYYY.JJJ.hh.mm.ss.stn.sac.e'
   'YYYY.MM.DD-hh.mm.ss.stn.sac.e'};
```

add your format to this cell array:

```
str = {'RDSEED' 'SEISAN', 'YYYY.JJJ.hh.mm.ss.stn.sac.e'
   'YYYY.MM.DD-hh.mm.ss.stn.sac.e' 'MyFormat'};
```

All entries should be in a single line! Furthermore, this entry name should be exactly the same as used before since it determines the value of the variable **config.FileNameConvention**

save **/private/configpanelFINDFILE.m**

restart **Matlab**

7.4. Electronic supplement to Null detection (Chapter 4.4)

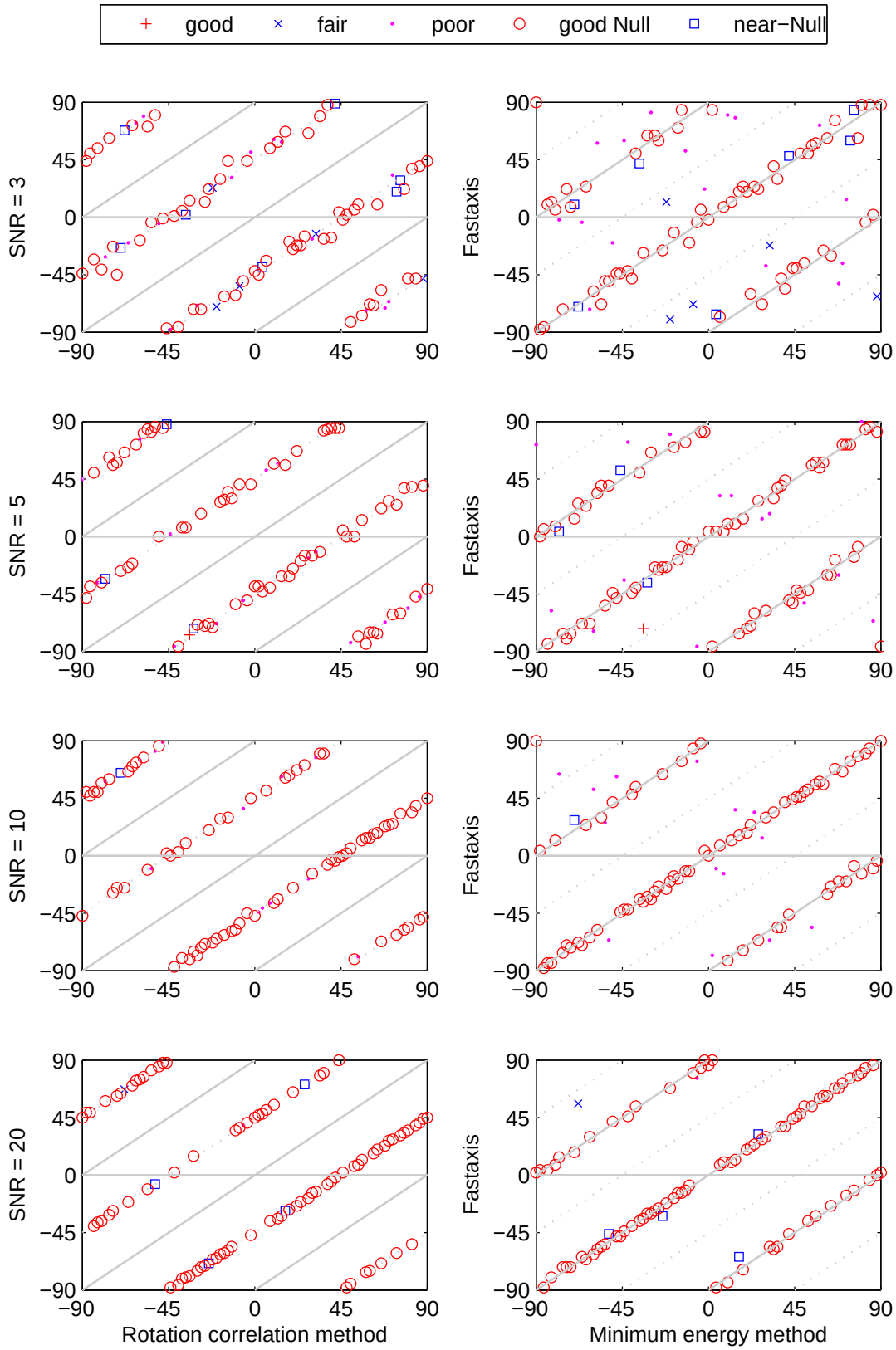

Figure B-1: Comparison of RC and SC fast axis estimates for different SNR. Model fast axis at 0° and delay time 0.0 seconds.

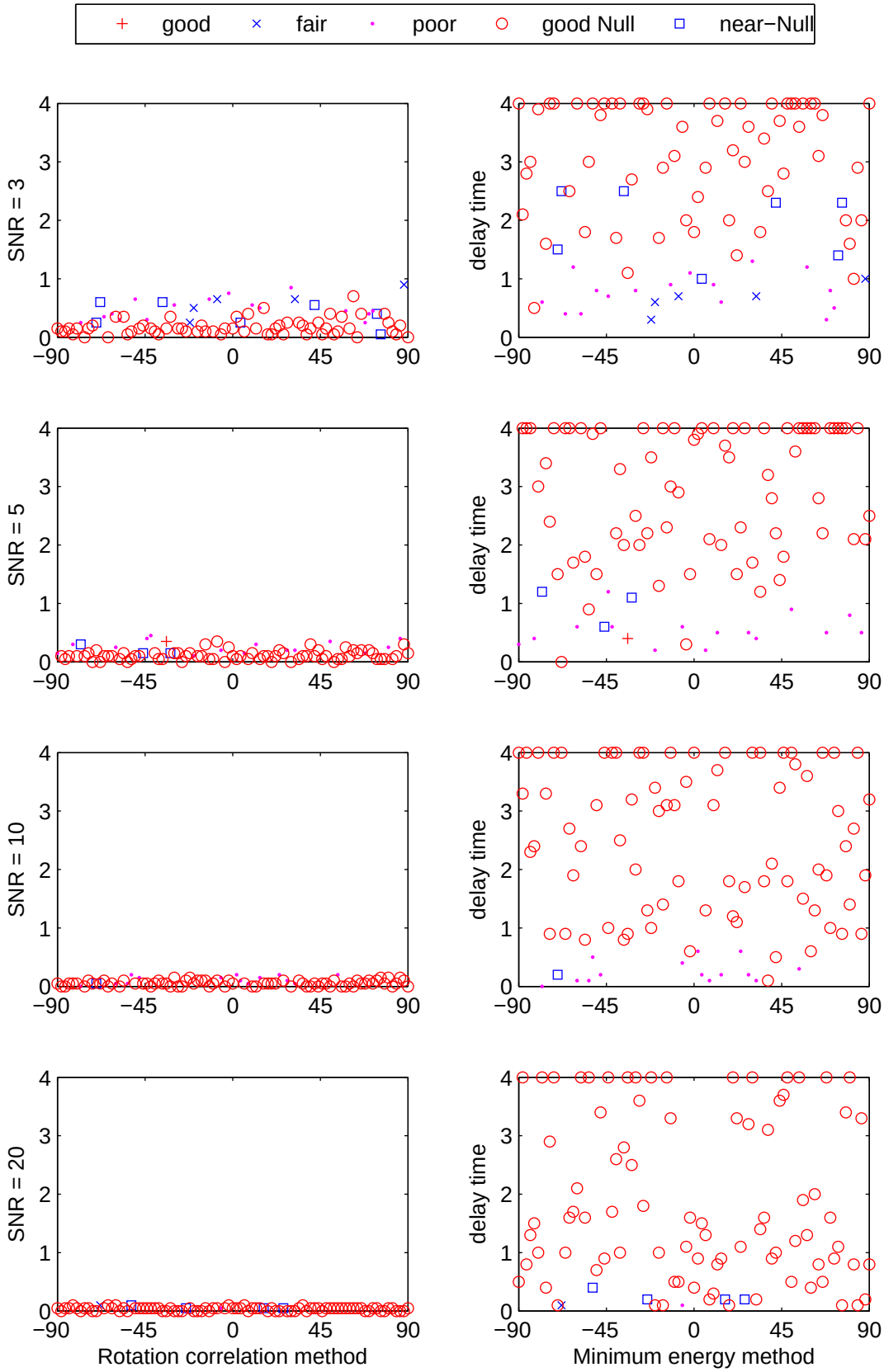

Figure B-2: Comparison of RC and SC delay time estimates for different SNR. Model fast axis at 0° and delay time 0.0 seconds.

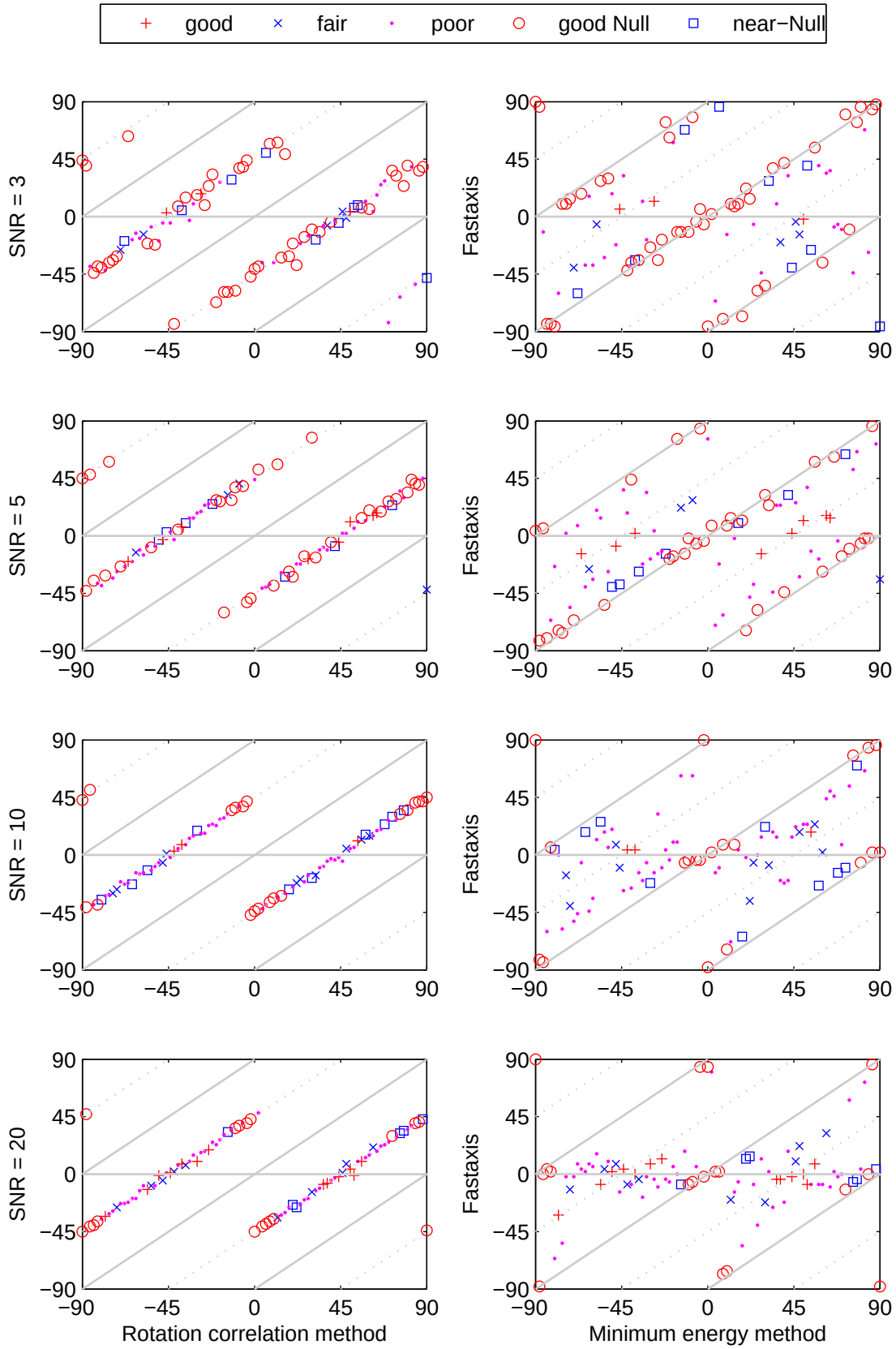

Figure B-3: Comparison of RC and SC fast axis estimates for different SNR. Model fast axis at 0° and delay time 0.5 seconds.

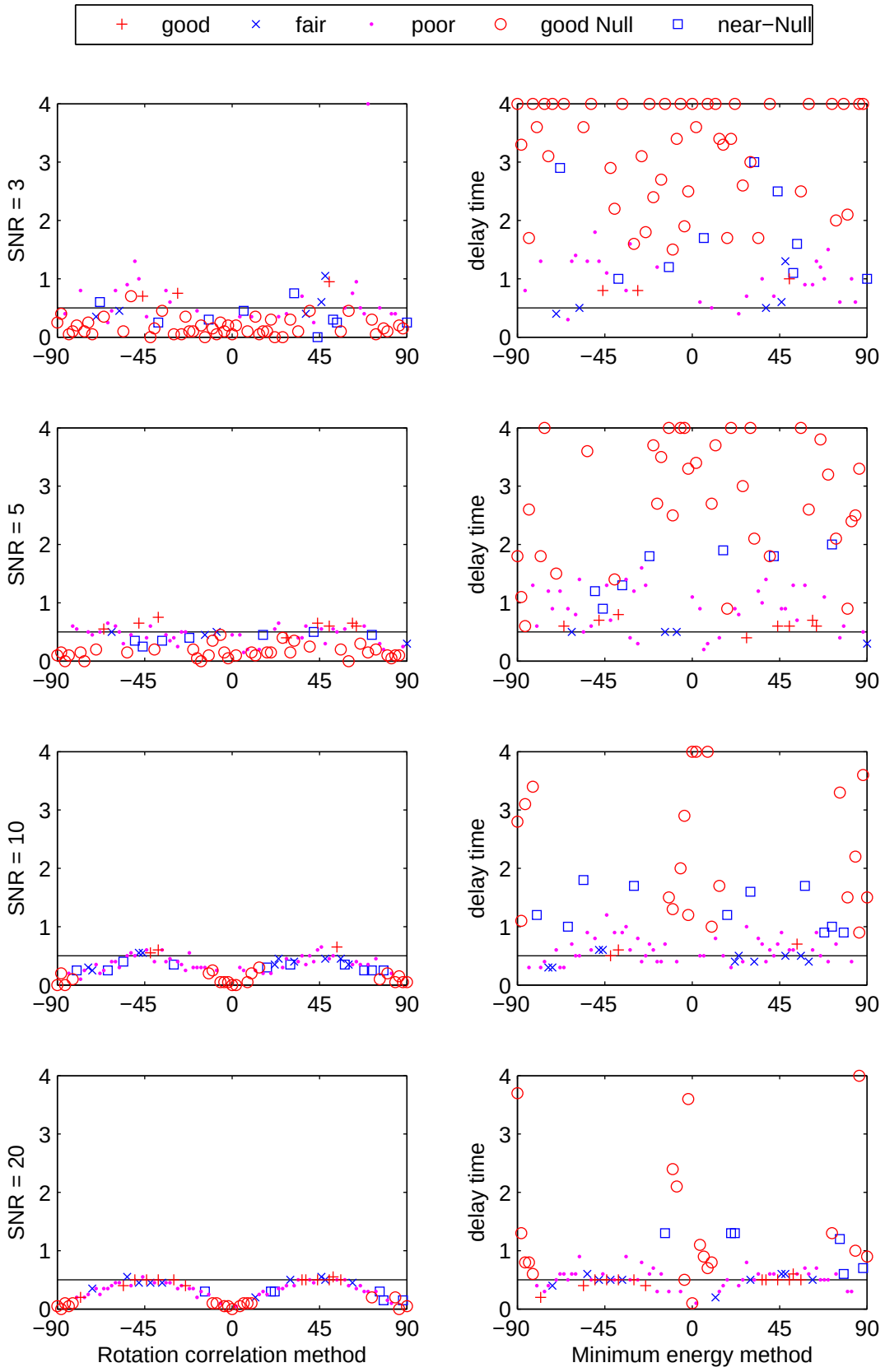

Figure B-4: Comparison of RC and SC delay time estimates for different SNR. Model fast axis at 0° and delay time 0.5 seconds.

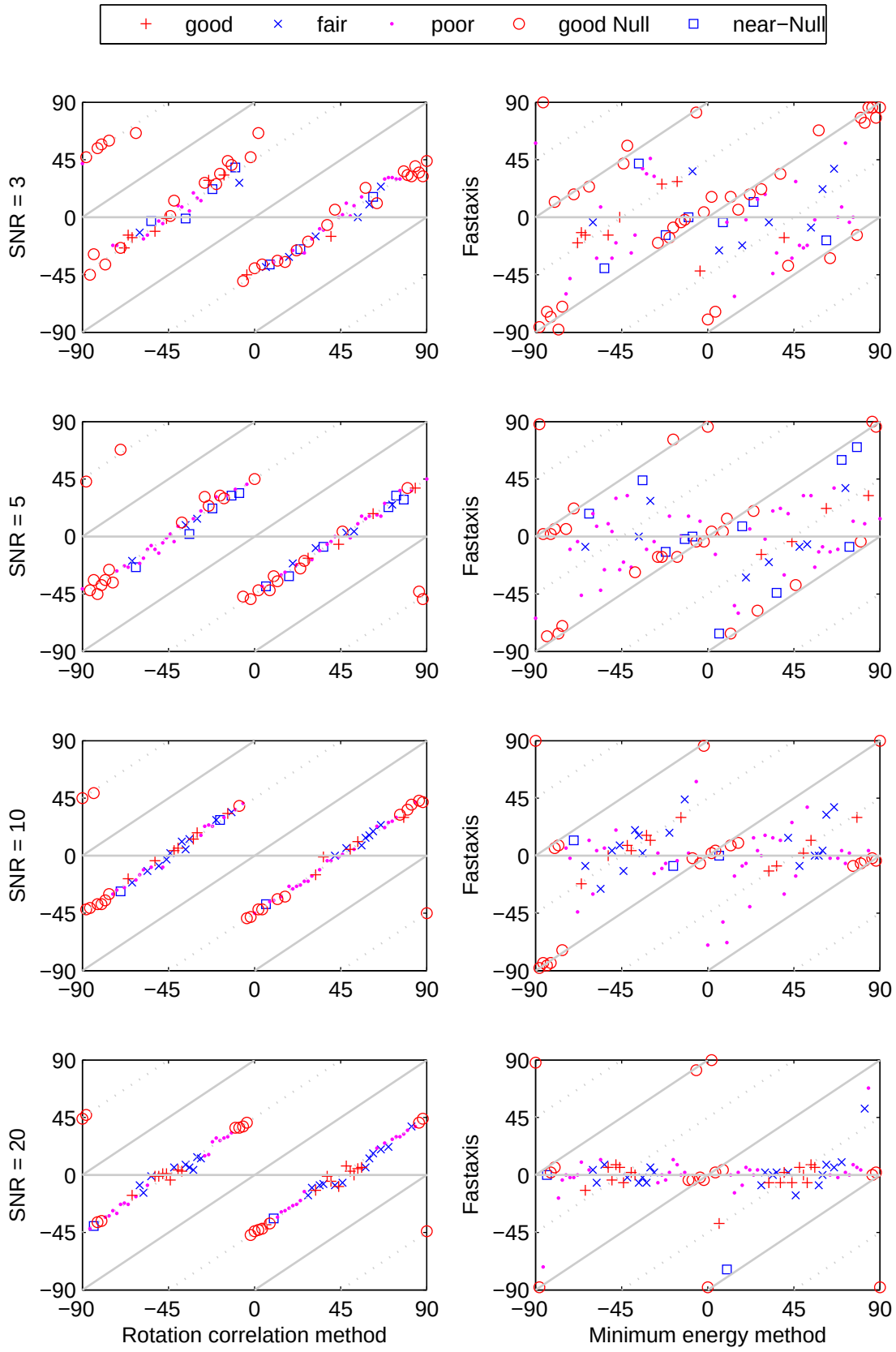

Figure B-5: Comparison of RC and SC fast axis estimates for different SNR. Model fast axis at 0° and delay time 0.7 seconds.

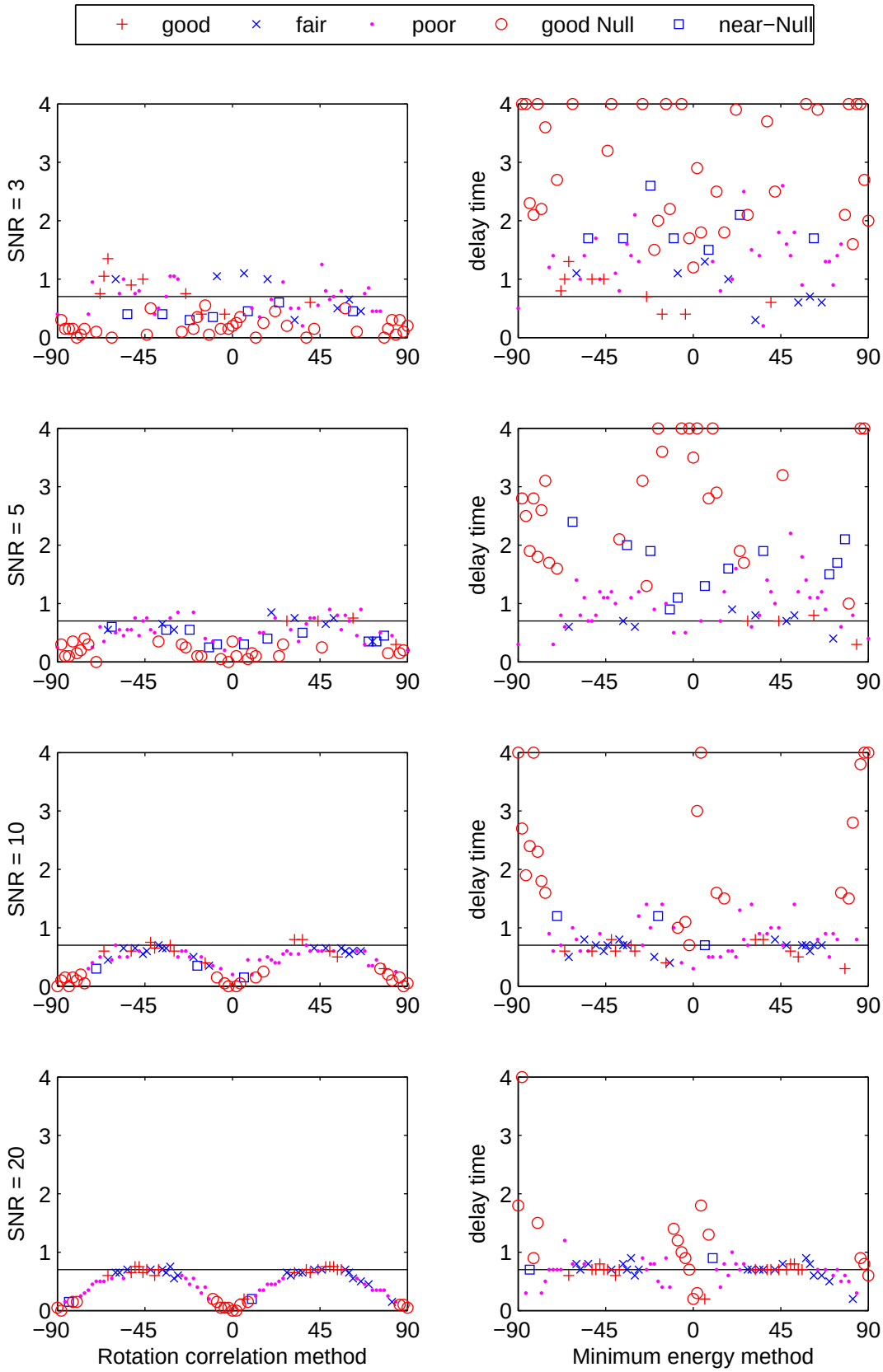

Figure B-6: Comparison of RC and SC delay time estimates for different SNR. Model fast axis at 0° and delay time 0.7 seconds.

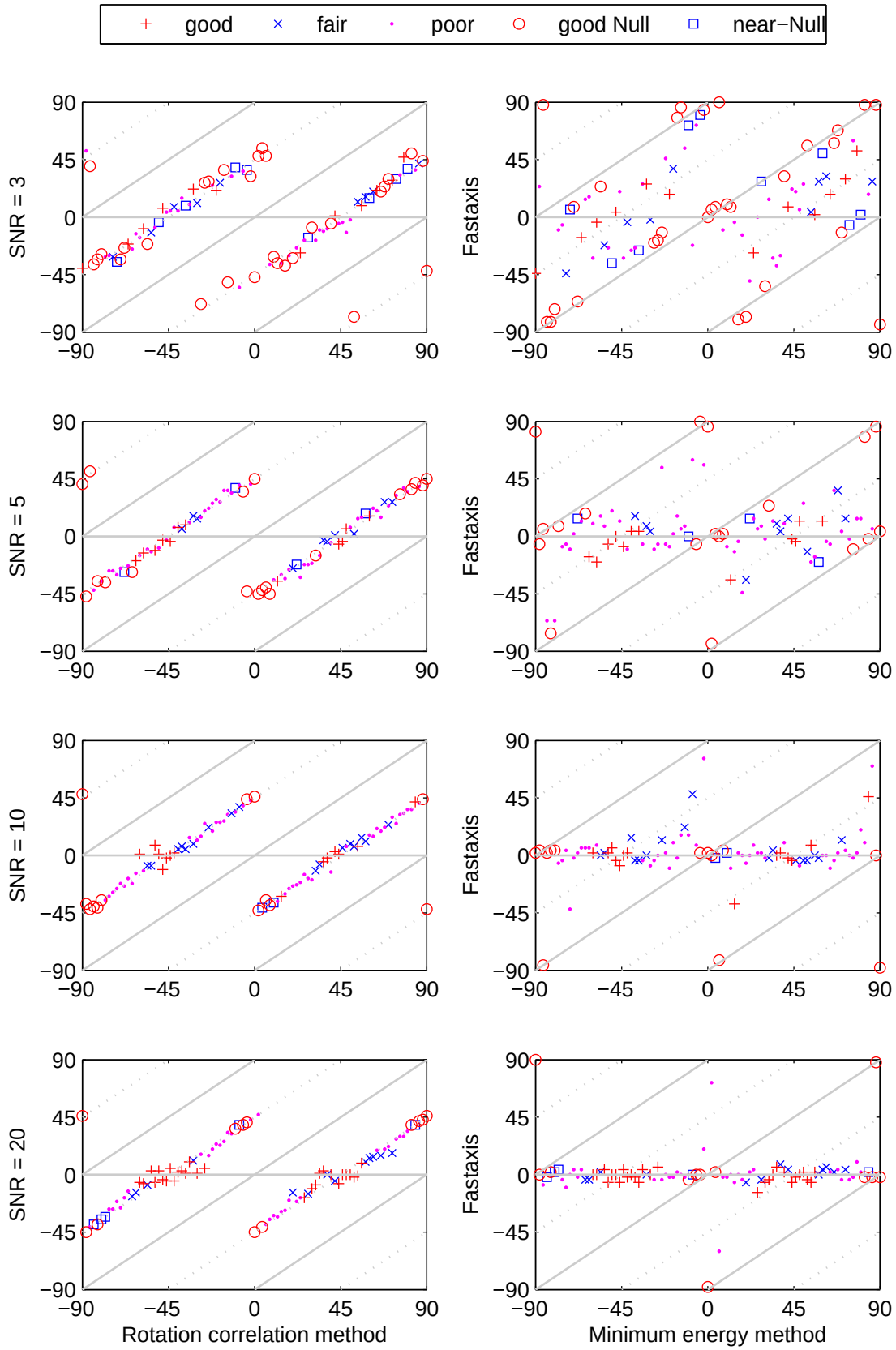

Figure B-7: Comparison of RC and SC fast axis estimates for different SNR. Model fast axis at 0° and delay time 1.0 seconds.

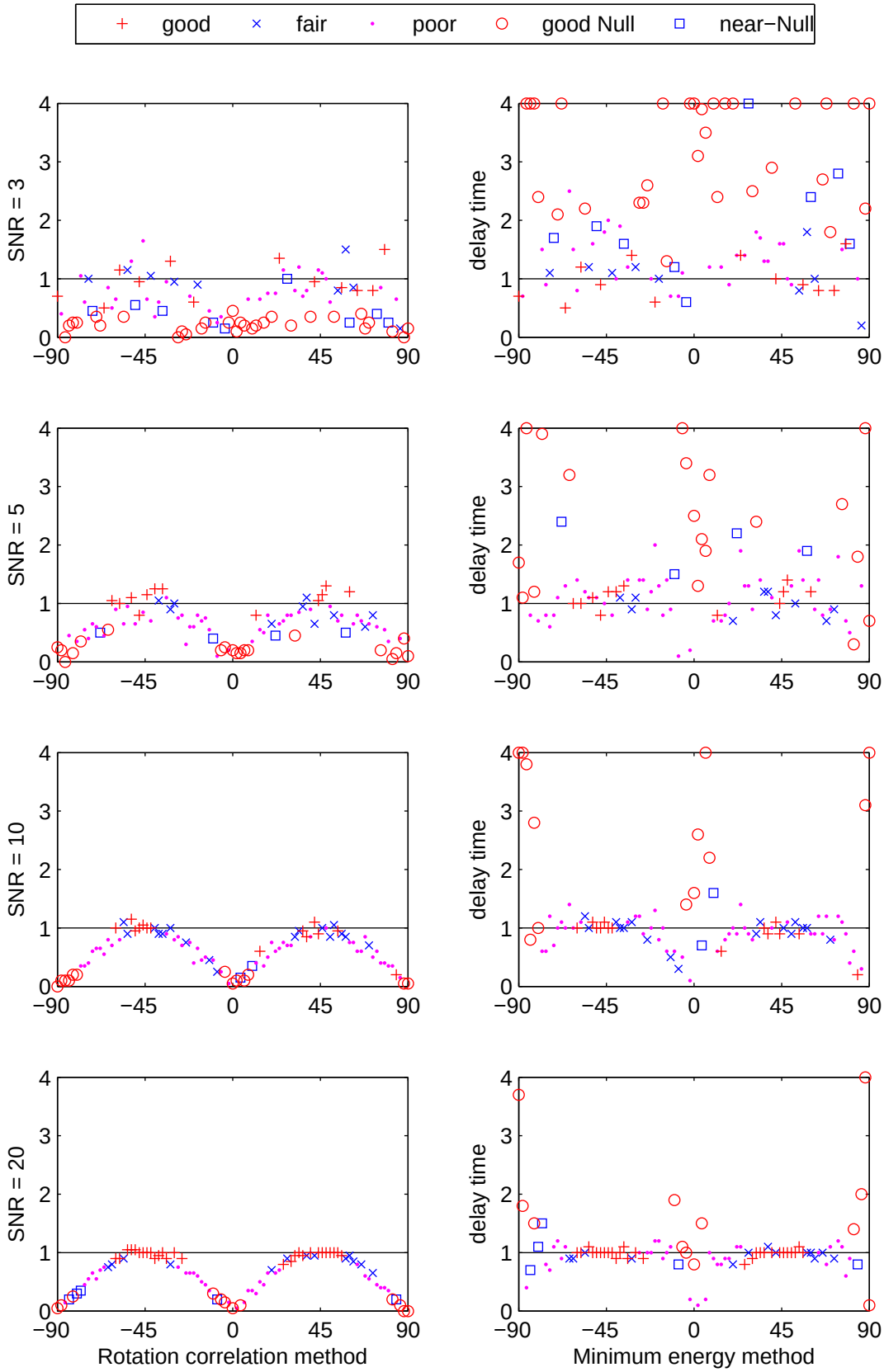

Figure B-8: Comparison of RC and SC delay time estimates for different SNR. Model fast axis at 0° and delay time 1.0 seconds.

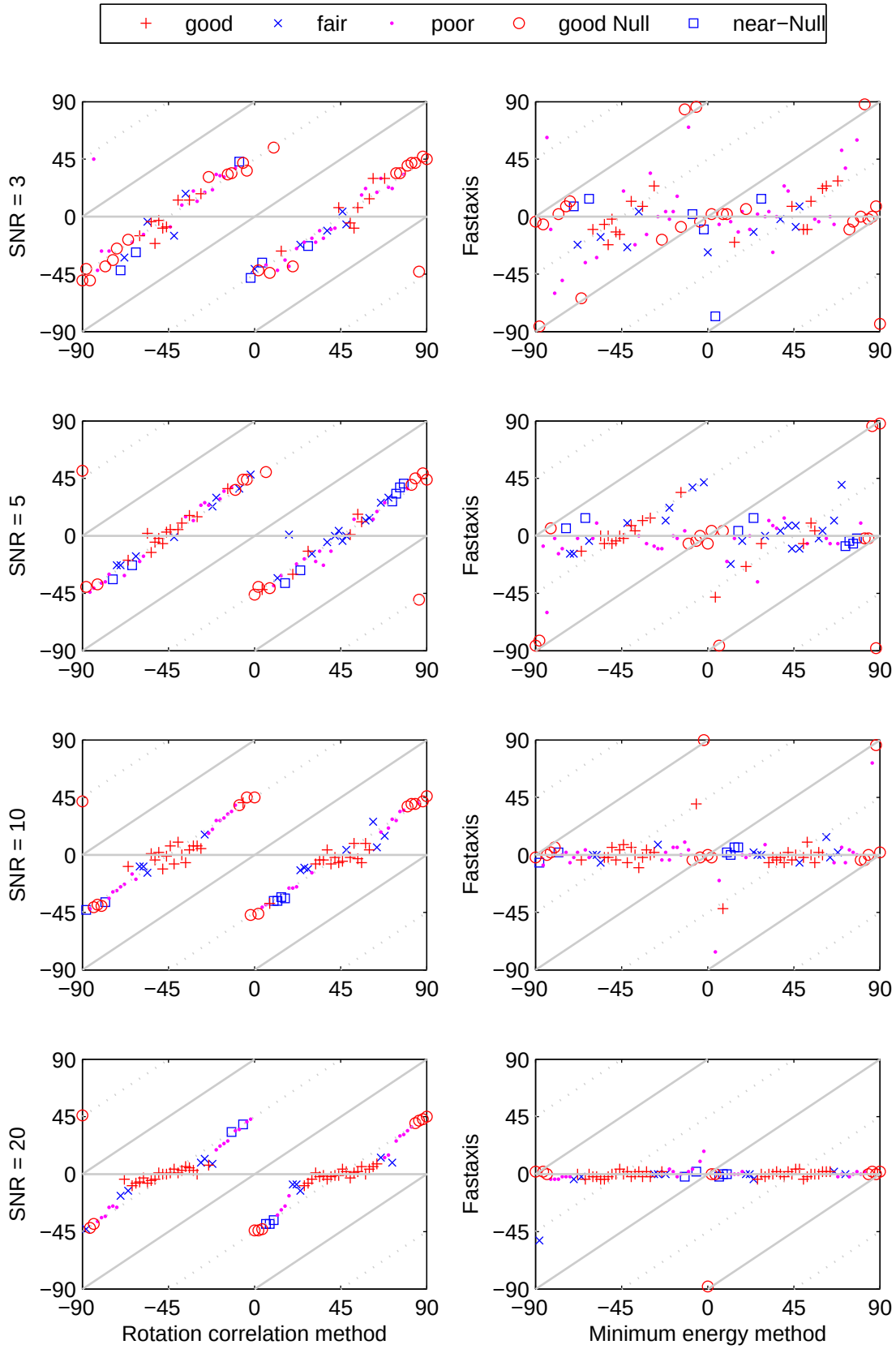

Figure B-9: Comparison of RC and SC fast axis estimates for different SNR. Model fast axis at 0° and delay time 1.3 seconds.

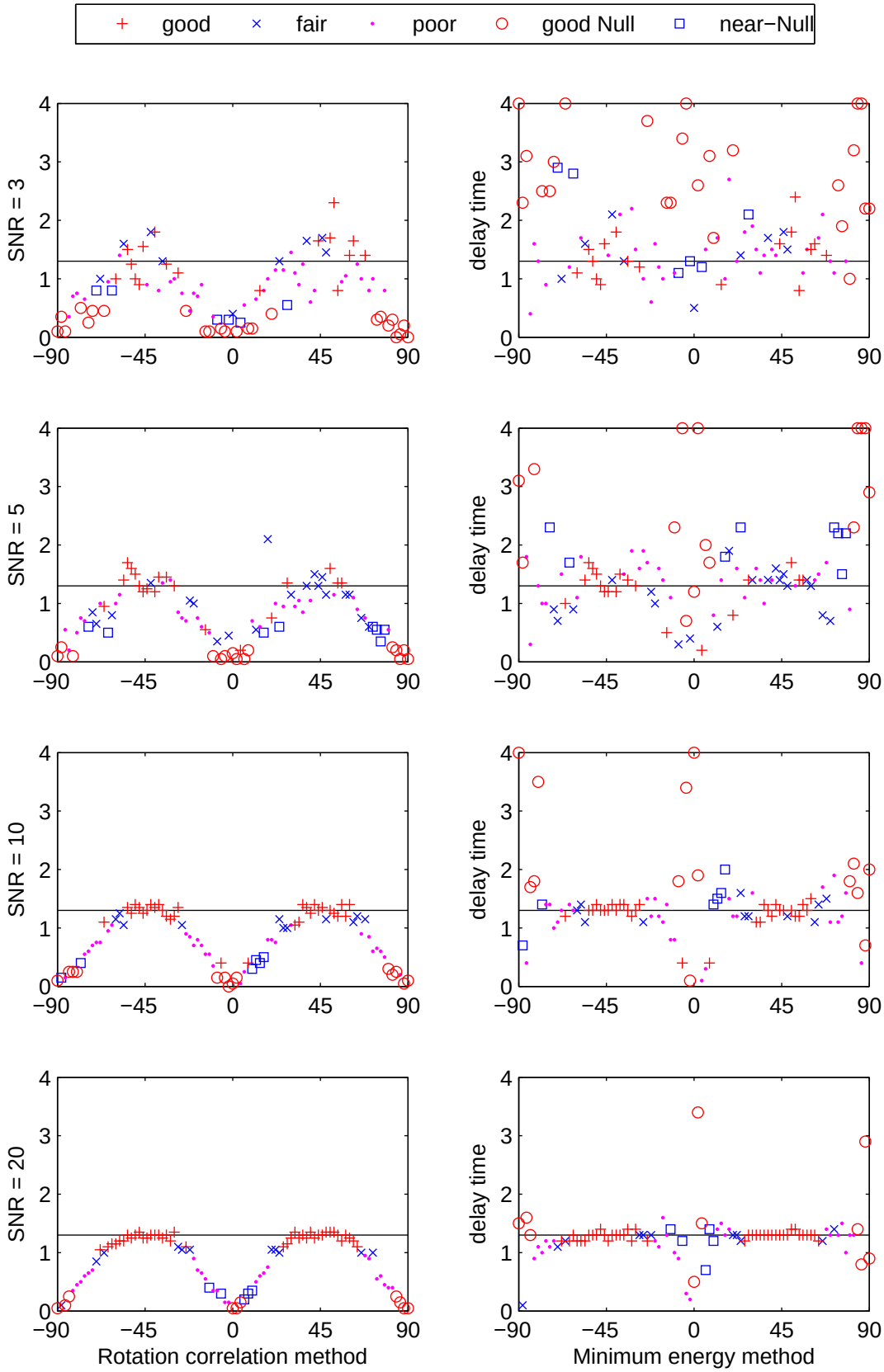

Figure B-10: Comparison of RC and SC delay time estimates for different SNR. Model fast axis at 0° and delay time 1.3 seconds.

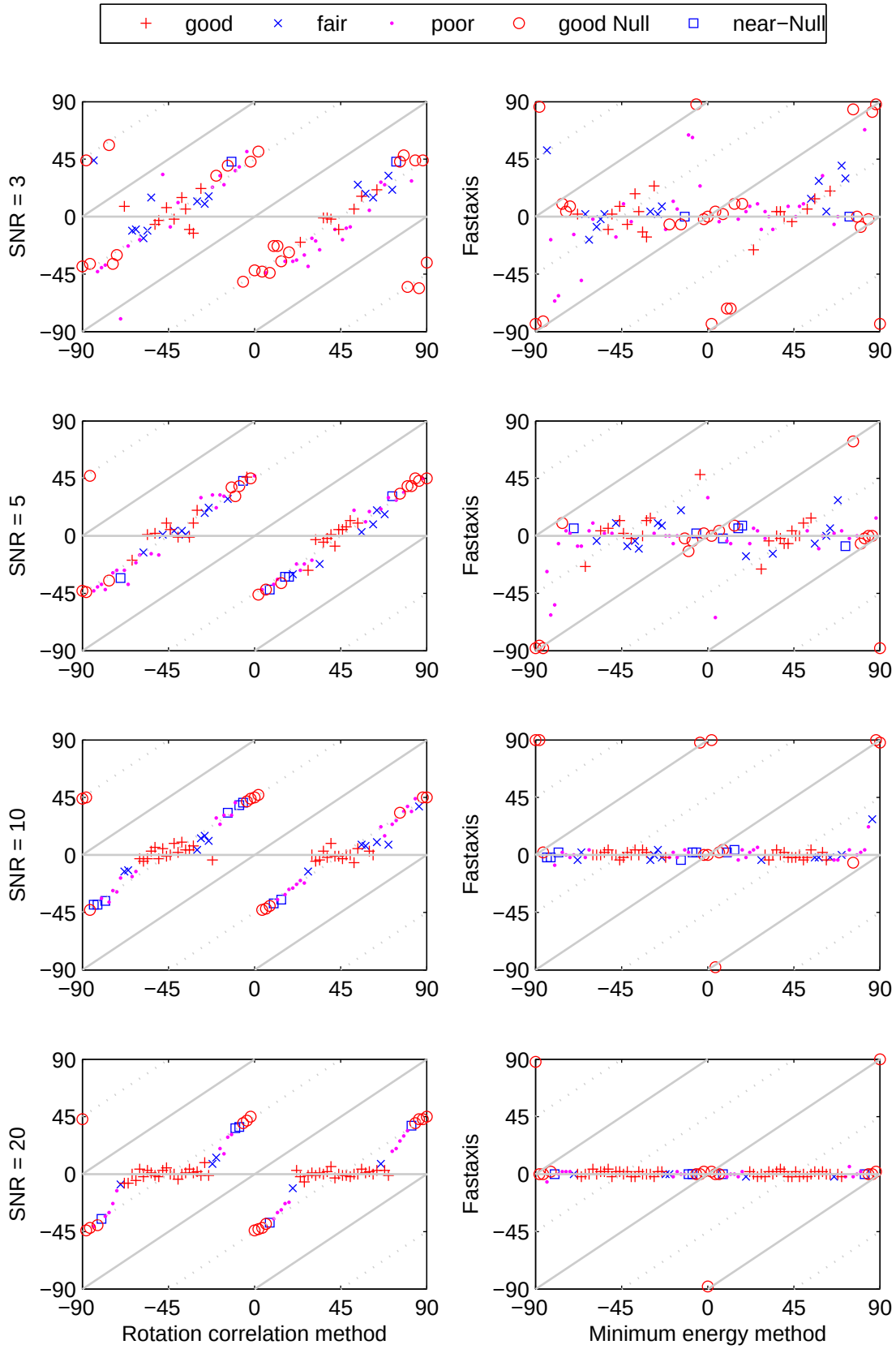

Figure B-11: Comparison of RC and SC fast axis estimates for different SNR. Model fast axis at 0° and delay time 1.5 seconds.

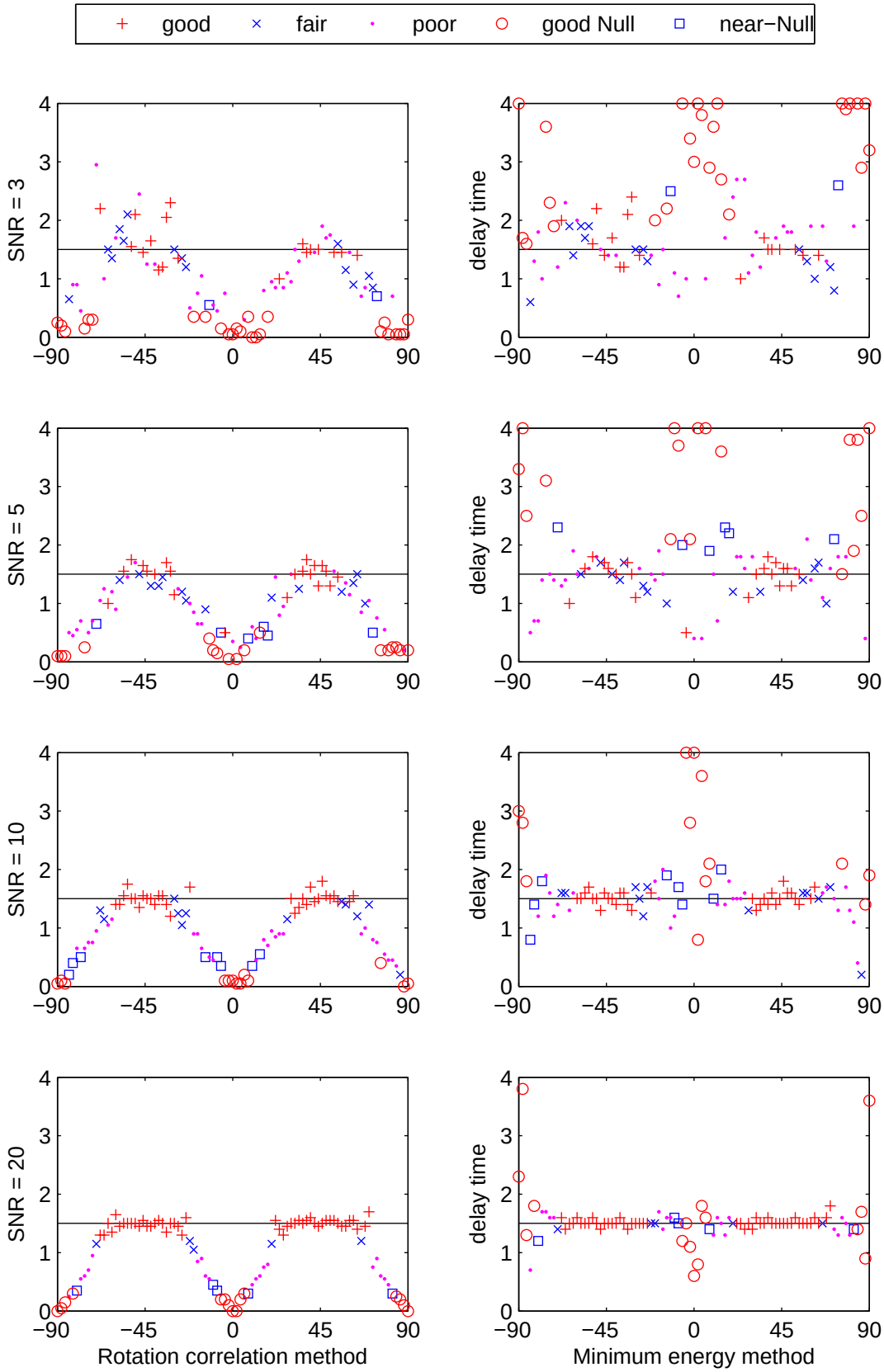

Figure B-12: Comparison of RC and SC delay time estimates for different SNR. Model fast axis at 0° and delay time 1.5 seconds.

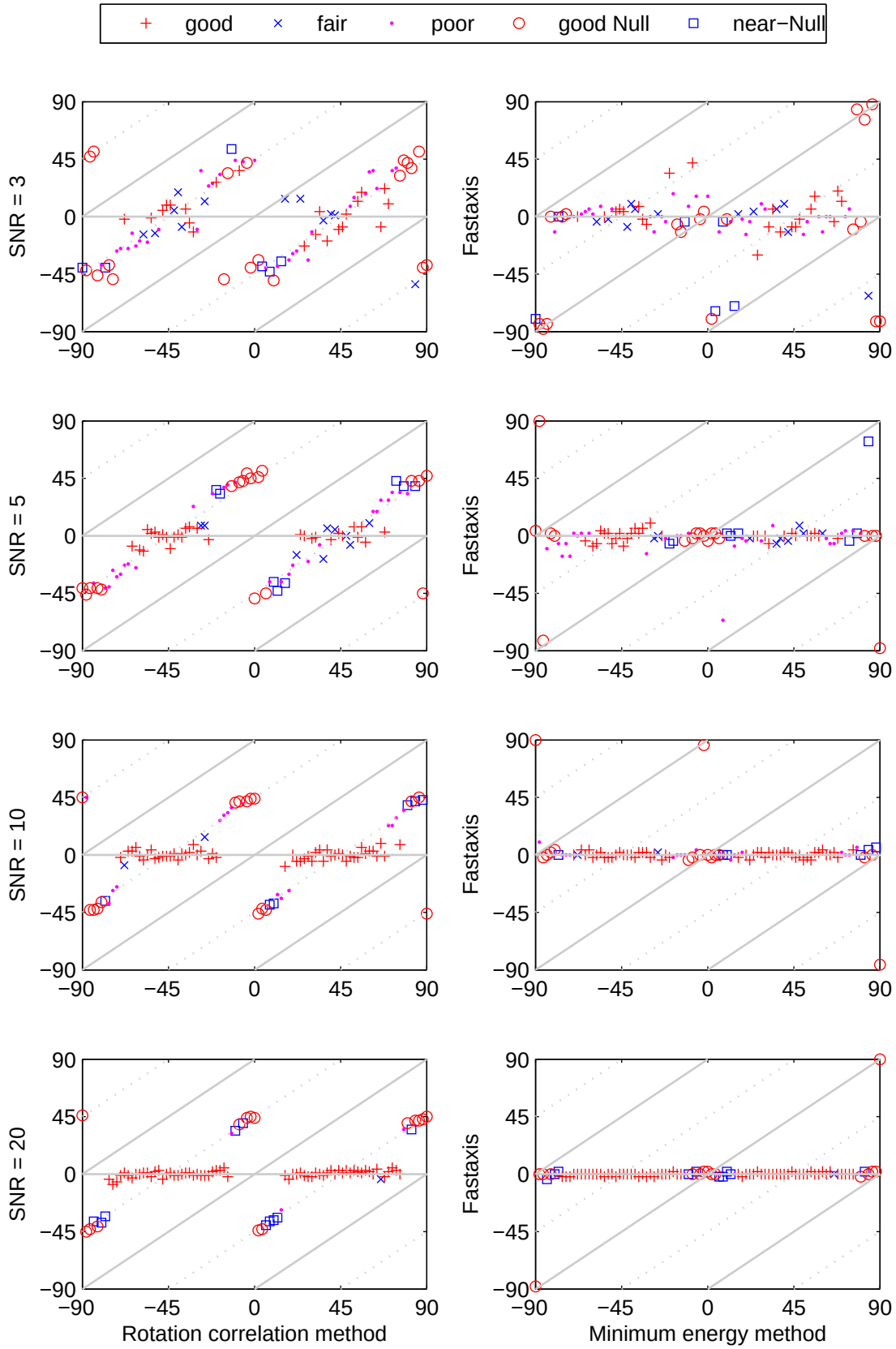

Figure B-13: Comparison of RC and SC fast axis estimates for different SNR. Model fast axis at 0° and delay time 2.0 seconds.

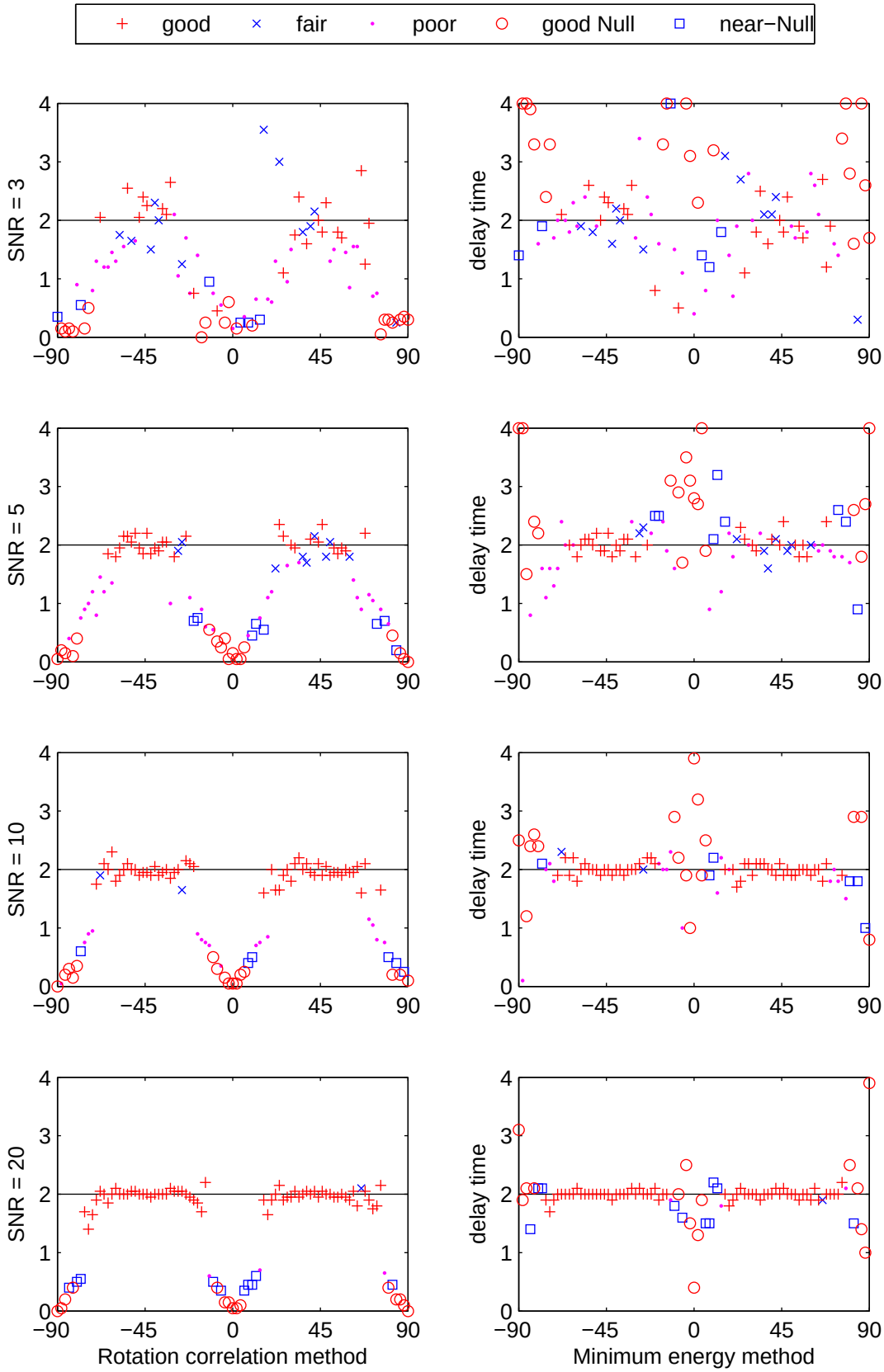

Figure B-14: Comparison of RC and SC fast axis estimates for different SNR. Model fast axis at 0° and delay time 2.0 seconds.

7.5 Table of splitting results of stations on the East European Craton

								Manual		Automatic	
Date	**Lat**	**Long**	**Bazi**	**ΦSC**	**ΦRC**	**dtSC**	**dtRC**	**isNull**	**Quality**	**IsNull**	**Quality**
Station ATK											
01-Oct-94	-17.75	167.63	86.67	88.67	46.67	4.00	0.20	Yes	fair	YES	GOOD
12-Dec-94	-17.50	-69.65	288.85	-61.15	-8.15	2.70	0.05	Yes	poor	YES	GOOD
29-May-95	-10.14	163.73	84.37	-89.63	46.37	2.90	0.08	Yes	fair	YES	GOOD
14-Jun-95	12.20	-88.35	324.61	-53.39	-81.39	0.15	0.10	Yes	good	-	POOR
24-Jun-95	-3.98	153.95	87.96	59.96	59.96	0.75	0.73	No	good	NO	GOOD
25-Jun-95	-3.28	150.37	90.28	6.28	53.28	3.05	0.48	Yes	fair	YES	GOOD
29-Jun-95	-19.46	169.24	86.68	44.68	42.68	0.40	0.38	No	fair	NO	GOOD
14-Aug-95	-4.83	151.51	90.39	84.39	48.39	3.80	0.53	Yes	fair	YES	FAIR
17-Aug-95	-5.18	153.40	89.16	-4.84	39.16	2.80	0.30	Yes	fair	YES	GOOD
26-Aug-95	-5.80	153.63	89.38	51.38	56.38	0.65	0.68	No	good	NO	GOOD
16-Sep-95	-6.31	155.25	88.46	44.46	49.46	0.65	0.65	No	fair	NO	GOOD
09-Oct-95	-21.49	170.13	87.56	25.56	42.56	0.70	0.55	Yes	poor	-	POOR
25-Feb-96	16.20	-97.96	335.40	69.40	-66.60	4.00	0.30	Yes	good	YES	GOOD
02-May-96	-4.55	154.83	87.65	45.65	46.65	0.50	0.50	No	fair	NO	GOOD
03-Jun-96	-9.31	157.17	88.94	22.94	43.94	0.95	0.65	No	fair	-	POOR
02-Aug-96	-10.77	161.45	86.59	44.59	38.59	0.40	0.38	No	fair	NO	GOOD
05-Aug-96	-20.69	-178.31	77.34	77.34	31.34	2.55	0.00	Yes	good	YES	GOOD
05-Aug-96	-2.00	-81.00	310.48	-53.52	-8.52	3.85	0.05	Yes	good	YES	GOOD
10-Aug-96	-4.94	152.13	89.99	49.99	39.99	0.75	0.75	No	poor	NO	FAIR
14-Oct-96	-7.13	155.57	88.75	60.75	36.75	0.75	0.58	No	poor	-	POOR
31-Dec-96	15.83	-92.97	330.43	-45.57	-80.57	1.00	0.45	No	fair	-	POOR
23-Jan-97	-22.00	-65.72	281.61	3.61	-46.39	4.00	0.23	Yes	fair	YES	GOOD
05-Apr-97	-6.49	147.41	94.61	66.61	45.61	0.70	0.55	No	good	-	POOR
21-May-97	-20.44	169.29	87.40	-6.60	36.40	4.00	0.15	Yes	good	YES	GOOD
22-May-97	18.68	-101.60	339.63	-24.37	-69.37	3.45	0.10	Yes	good	YES	GOOD
27-May-97	-15.21	-173.33	68.45	64.45	15.45	4.00	0.35	Yes	fair	YES	GOOD
02-Jun-97	-57.78	-25.47	222.14	44.14	72.14	3.90	0.05	Yes	poor	-	POOR
09-Jul-97	10.60	-63.49	301.48	33.48	73.48	3.65	0.05	Yes	fair	YES	GOOD
19-Jul-97	16.33	-98.22	335.69	-36.31	-72.31	1.10	0.43	Yes	fair	-	POOR
02-Sep-97	3.85	-75.75	308.58	-59.42	75.58	3.55	0.13	Yes	fair	YES	GOOD
16-Jul-98	-11.04	166.16	83.05	55.05	34.05	0.40	0.33	Yes	fair	-	POOR
04-Aug-98	-0.59	-80.39	310.65	34.65	-13.35	2.65	0.25	Yes	good	YES	GOOD
23-Aug-98	11.66	-88.04	324.09	-43.91	-82.91	0.60	0.15	Yes	good	YES	FAIR
29-Aug-98	-55.74	-27.05	224.85	38.85	78.85	2.60	0.23	Yes	good	YES	GOOD
18-Jul-99	-22.55	179.41	80.88	16.88	44.88	0.50	0.35	Yes	poor	-	POOR
Station ARU											
02-May-90	-5.62	150.15	91.80	73.80	73.80	1.50	1.45	No	good	NO	GOOD
30-May-90	-6.03	-77.27	307.74	59.74	-89.26	2.00	1.20	Yes	poor	YES	FAIR
12-Aug-90	-19.42	169.05	84.11	66.11	29.11	0.90	0.15	No	good	YES	GOOD
10-Oct-90	-19.34	-66.55	289.22	57.22	58.22	0.50	0.50	No	fair	NO	GOOD
01-Mar-91	10.80	-84.70	322.27	76.27	83.27	1.20	1.05	No	good	NO	GOOD
16-Mar-91	10.19	-85.15	322.49	80.49	-89.51	1.40	1.20	Yes	fair	-	POOR
14-Oct-91	-9.05	158.49	86.77	44.77	39.77	0.80	0.75	Yes	fair	NO	GOOD
07-Mar-92	10.20	-84.35	321.72	79.72	-82.28	1.20	1.00	No	fair	-	POOR
16-Aug-92	-5.39	146.66	94.57	70.57	75.57	1.40	1.50	No	good	NO	GOOD
30-Aug-92	-17.74	-178.77	72.04	68.04	-57.96	4.00	0.10	Yes	fair	YES	FAIR
11-Oct-92	-19.28	168.91	84.14	70.14	39.14	0.90	0.25	No	fair	-	POOR

								Manual		Automatic	
Date	**Lat**	**Long**	**Bazi**	**ΦSC**	**ΦRC**	**dtSC**	**dtRC**	**isNull**	**Quality**	**IsNull**	**Quality**
15-Oct-92	-14.45	166.63	83.05	71.05	33.05	0.80	0.20	No	good	YES	FAIR
18-Oct-92	7.12	-76.89	313.38	71.38	82.38	1.20	1.00	No	good	NO	FAIR
06-Mar-93	-10.96	164.19	83.05	73.05	38.05	1.60	0.50	Yes	good	-	POOR
16-Apr-93	-17.69	-178.88	72.11	-13.89	28.11	3.70	0.05	Yes	good	YES	GOOD
15-May-93	16.74	-98.36	337.21	71.21	-65.79	1.70	0.15	Yes	good	YES	GOOD
06-Sep-93	-4.71	153.21	88.74	70.74	71.74	1.20	1.20	No	good	NO	GOOD
10-Sep-93	14.73	-92.68	331.22	77.22	-72.78	1.40	0.55	No	good	-	POOR
22-Sep-93	-6.45	154.92	88.29	66.29	67.29	1.20	1.20	No	good	NO	GOOD
30-Sep-93	15.51	-94.71	333.39	75.39	-72.61	1.00	0.35	Yes	good	-	POOR
14-Mar-94	15.98	-92.40	331.31	79.31	-81.69	1.20	0.70	No	fair	-	POOR
15-Mar-94	11.19	-88.04	325.64	79.64	-84.36	2.30	1.65	Yes	poor	YES	FAIR
18-Apr-94	-6.49	154.92	88.31	64.31	66.31	1.00	1.05	No	good	NO	GOOD
21-Apr-94	-5.70	154.08	88.57	70.57	33.57	1.20	0.00	No	fair	YES	GOOD
23-May-94	18.31	-100.52	339.62	75.62	-62.38	1.30	0.05	Yes	fair	YES	GOOD
06-Jun-94	2.90	-76.09	310.78	76.78	-87.22	1.10	1.00	No	fair	-	POOR
01-Oct-94	-17.75	167.63	84.25	72.25	33.25	1.00	0.25	Yes	fair	YES	FAIR
27-Oct-94	-25.79	179.35	79.50	67.50	26.50	1.00	0.20	No	poor	YES	GOOD
24-Jan-95	-5.93	154.49	88.35	72.35	33.35	0.70	0.15	No	fair	YES	FAIR
16-May-95	-23.01	169.89	85.81	43.81	43.81	0.30	0.30	Yes	good	NO	GOOD
14-Jun-95	12.20	-88.35	326.27	76.27	83.27	1.40	1.15	Yes	good	NO	GOOD
24-Jun-95	-3.98	153.95	87.71	69.71	72.71	1.10	1.10	No	good	NO	GOOD
29-Jun-95	-19.46	169.24	83.97	67.97	67.97	0.90	0.90	No	good	NO	GOOD
17-Aug-95	-5.18	153.40	88.84	68.84	65.84	1.20	1.20	No	good	NO	GOOD
16-Sep-95	-6.31	155.25	87.93	65.93	68.93	0.90	0.95	No	good	NO	GOOD
21-Oct-95	16.89	-93.45	332.56	78.56	83.56	1.20	1.05	No	good	NO	GOOD
25-Feb-96	16.20	-97.96	336.70	70.70	-65.30	3.90	0.35	Yes	good	YES	GOOD
03-Mar-96	11.66	-86.86	324.65	80.65	-81.35	1.20	0.95	No	poor	-	POOR
29-Apr-96	-6.52	155.00	88.26	64.26	66.26	1.10	1.10	No	fair	NO	GOOD
02-May-96	-4.55	154.83	87.30	67.30	68.30	0.90	0.95	No	good	NO	GOOD
03-Jun-96	-9.31	157.17	88.03	70.03	37.03	1.20	0.50	No	fair	-	POOR
15-Jul-96	17.60	-100.96	339.90	73.90	-63.10	1.60	0.15	Yes	good	YES	GOOD
02-Aug-96	-10.77	161.45	85.27	59.27	48.27	0.70	0.55	No	fair	NO	FAIR
05-Aug-96	-20.69	-178.31	73.60	59.60	25.60	0.80	0.20	Yes	fair	YES	FAIR
04-Sep-96	9.36	-84.27	321.34	77.34	-79.66	1.00	0.70	No	fair	-	POOR
14-Oct-96	-7.13	155.57	88.13	70.13	48.13	1.20	0.60	No	poor	-	POOR
31-Dec-96	15.83	-92.97	331.81	71.81	-62.19	1.40	0.10	No	fair	YES	GOOD
11-Jan-97	18.22	-102.76	341.75	-20.25	-62.25	3.10	0.00	Yes	good	YES	GOOD
05-Apr-97	-6.49	147.41	94.56	68.56	69.56	1.20	1.25	No	good	NO	GOOD
22-Apr-97	11.11	-60.89	300.76	64.76	84.76	0.90	0.80	Yes	poor	-	POOR
21-May-97	-20.44	169.29	84.58	70.58	33.58	1.20	0.30	Yes	fair	YES	FAIR
22-May-97	18.68	-101.60	340.73	72.73	-61.27	1.50	0.00	Yes	good	YES	GOOD
29-Aug-97	-3.56	144.36	95.47	49.47	60.47	1.20	1.20	No	good	NO	FAIR
02-Sep-97	3.85	-75.75	310.87	72.87	75.87	1.30	1.30	No	good	NO	GOOD
14-Oct-97	-22.10	-176.77	73.13	51.13	30.13	0.40	0.25	Yes	fair	-	POOR
15-Nov-97	-15.15	167.38	82.83	-5.17	38.83	3.40	0.10	Yes	good	YES	GOOD
28-Nov-97	-13.74	-68.79	294.98	60.98	79.98	0.90	0.80	No	good	-	POOR
04-Jan-98	-22.30	170.91	84.44	68.44	41.44	0.80	0.30	Yes	fair	-	POOR
10-Jan-98	-12.03	-72.07	299.24	83.24	80.24	1.20	1.15	No	fair	NO	GOOD
10-Jan-98	14.37	-91.47	329.95	77.95	83.95	1.20	1.00	No	good	NO	GOOD
07-Jun-98	15.96	-93.78	332.62	74.62	-70.38	1.30	0.35	Yes	fair	YES	FAIR
16-Jul-98	-11.04	166.16	81.41	25.41	35.41	0.60	0.55	Yes	fair	NO	FAIR
23-Aug-98	11.66	-88.04	325.79	73.79	-86.21	1.30	0.75	No	fair	-	POOR
27-Dec-98	-21.63	-176.38	72.42	-11.58	-56.58	4.00	0.15	Yes	fair	YES	GOOD
28-Jan-99	-4.58	153.66	88.29	68.29	18.29	1.30	0.30	No	good	YES	FAIR

								Manual		Automatic	
Date	**Lat**	**Long**	**Bazi**	**ΦSC**	**ΦRC**	**dtSC**	**dtRC**	**isNull**	**Quality**	**IsNull**	**Quality**
31-Mar-99	5.83	-82.62	318.38	86.38	-80.62	1.00	1.00	No	fair	-	POOR
26-Apr-99	-1.65	-77.78	310.37	74.37	84.37	1.10	1.00	No	good	NO	FAIR
05-May-99	14.36	-94.67	333.04	75.04	-68.96	1.30	0.35	Yes	good	YES	FAIR
08-May-99	14.21	-91.94	330.36	78.36	-60.64	1.60	0.45	Yes	fair	YES	FAIR
10-May-99	-5.16	150.88	90.93	74.93	25.93	1.30	0.30	No	fair	YES	FAIR
06-Jun-99	13.90	-90.77	329.14	77.14	-60.86	1.20	0.30	No	fair	YES	FAIR
15-Jun-99	18.39	-97.44	336.72	76.72	-62.28	1.30	0.05	No	good	YES	GOOD
09-Jul-99	-6.51	154.94	88.30	66.30	81.30	1.00	1.30	No	poor	-	POOR
11-Jul-99	15.78	-88.33	327.40	75.40	85.40	1.60	1.25	No	good	NO	FAIR
26-Jul-99	-5.15	151.94	90.04	62.04	54.04	1.10	0.95	No	fair	NO	FAIR
26-Aug-99	-3.52	145.66	94.36	72.36	61.36	1.40	1.05	No	fair	NO	FAIR
28-Aug-99	-1.29	-77.55	310.31	80.31	-88.69	1.10	1.00	No	good	-	POOR
30-Sep-99	16.06	-96.93	335.67	73.67	-65.33	1.50	0.20	Yes	good	YES	GOOD
23-Oct-99	-4.81	153.41	88.63	66.63	79.63	1.10	1.20	No	good	NO	FAIR
06-Feb-00	-5.84	150.88	91.31	67.31	79.31	1.20	1.25	No	good	NO	FAIR
12-Mar-00	14.98	-92.44	331.06	83.06	-89.94	1.20	1.05	No	good	-	POOR
06-May-00	-11.30	165.43	82.19	64.19	22.19	2.00	0.40	Yes	fair	YES	GOOD
16-Jul-00	-7.75	150.92	92.35	58.35	46.35	0.60	0.55	No	poor	NO	FAIR
21-Jul-00	9.42	-85.33	322.39	78.39	-86.61	1.00	0.75	No	good	-	POOR
31-Jul-00	-16.70	174.54	77.51	31.51	33.51	0.30	0.25	Yes	poor	NO	GOOD
09-Aug-00	18.20	-102.48	341.48	75.48	-61.52	1.20	0.10	Yes	good	YES	GOOD
09-Aug-00	-15.69	167.99	82.64	54.64	41.64	0.50	0.40	Yes	fair	NO	FAIR
11-Sep-00	-15.88	-173.69	65.96	-22.04	22.96	3.10	0.00	Yes	good	YES	GOOD
26-Sep-00	-17.18	-173.93	67.02	-26.98	14.02	2.80	0.00	Yes	fair	YES	GOOD
17-Nov-00	-5.50	151.78	90.37	72.37	34.37	1.30	0.20	No	poor	YES	GOOD
18-Nov-00	-5.23	151.77	90.23	74.23	51.23	1.30	0.55	Yes	fair	-	POOR
18-Nov-00	-5.10	153.18	88.98	68.98	70.98	0.90	0.95	No	good	NO	GOOD
21-Nov-00	-5.49	152.15	90.06	74.06	79.06	1.10	1.25	No	good	NO	FAIR
23-Nov-00	-4.59	153.06	88.80	70.80	79.80	1.20	1.25	No	fair	NO	FAIR
06-Dec-00	-4.22	152.73	88.87	70.87	23.87	1.10	0.20	Yes	fair	YES	GOOD
18-Dec-00	-21.18	-179.12	74.70	60.70	27.70	0.90	0.35	No	fair	-	POOR
21-Dec-00	-5.71	151.12	91.04	69.04	83.04	1.40	1.50	No	fair	NO	FAIR
28-Dec-00	-4.05	152.31	89.12	-14.88	-59.88	2.10	0.05	Yes	fair	YES	GOOD
13-Jan-01	13.05	-88.66	326.84	66.84	-81.16	2.90	0.80	Yes	fair	YES	FAIR
19-Apr-01	-7.31	155.96	87.90	67.90	69.90	1.00	1.00	No	good	NO	GOOD
28-Apr-01	-18.06	-176.94	70.52	60.52	26.52	0.80	0.20	No	fair	YES	FAIR
29-Apr-01	18.74	-104.54	343.56	71.56	-66.44	3.10	0.10	Yes	good	YES	GOOD
20-May-01	18.82	-104.45	343.48	-4.52	27.48	0.30	0.10	Yes	good	-	POOR
29-Jun-01	-19.52	-66.25	288.81	62.81	71.81	0.60	0.60	No	good	NO	FAIR
01-Jul-01	-4.31	152.96	88.72	66.72	69.72	1.00	1.05	No	good	NO	GOOD
08-Jul-01	-6.66	152.11	90.75	66.75	71.75	1.10	1.20	No	good	NO	GOOD
28-Nov-01	15.57	-93.11	331.87	79.87	81.87	1.30	1.25	No	good	NO	GOOD
02-Jan-02	-17.60	167.86	83.96	65.96	39.96	0.90	0.40	No	fair	-	POOR
16-Jan-02	15.50	-93.13	331.87	77.87	-69.13	1.40	0.45	No	good	-	POOR
28-Feb-02	-5.68	151.26	90.91	64.91	73.91	1.30	1.35	No	good	NO	FAIR
06-Jun-02	-0.88	148.33	90.68	56.68	49.68	1.00	0.90	No	fair	NO	GOOD
16-Jun-02	8.78	-83.99	320.85	72.85	-81.15	1.20	0.70	Yes	fair	-	POOR
17-Jun-02	-12.59	166.38	82.14	-19.86	14.14	2.50	0.05	Yes	fair	YES	FAIR
30-Jun-02	-22.20	179.25	76.93	68.93	27.93	1.00	0.05	No	good	YES	GOOD
03-Jul-02	-5.03	147.34	93.80	53.80	65.80	0.90	1.05	No	good	NO	FAIR
12-Dec-02	-4.79	153.27	88.73	64.73	62.73	1.00	0.95	No	good	NO	GOOD
11-Mar-03	-4.69	153.24	88.70	70.70	39.70	1.10	0.45	No	fair	-	POOR
27-Apr-03	-20.94	169.77	84.50	66.50	26.50	4.00	0.35	Yes	fair	YES	GOOD
12-Jun-03	-5.99	154.76	88.16	66.16	60.16	0.90	0.75	No	good	NO	GOOD

								Manual		Automatic	
Date	**Lat**	**Long**	**Bazi**	**ΦSC**	**ΦRC**	**dtSC**	**dtRC**	**isNull**	**Quality**	**IsNull**	**Quality**
25-Jul-03	-1.53	149.69	89.91	69.91	69.91	1.10	1.15	No	good	NO	GOOD
27-Jul-03	-21.08	-176.59	72.23	66.23	24.23	0.80	0.10	No	good	YES	GOOD
22-Sep-03	19.78	-70.67	313.14	87.14	88.14	0.90	0.85	No	good	NO	GOOD
11-Jan-04	-36.70	53.35	184.18	68.18	50.18	0.90	0.70	No	fair	-	POOR
25-Jan-04	-16.83	-174.20	67.06	-14.94	-62.94	4.00	0.05	Yes	good	YES	GOOD
29-Apr-04	10.81	-86.00	323.53	79.53	85.53	1.20	1.10	No	fair	NO	GOOD
29-Jun-04	10.74	-87.04	324.51	72.51	87.51	1.50	0.95	No	fair	-	POOR
03-Sep-04	-15.25	-173.34	65.22	69.22	-70.78	0.40	0.05	Yes	fair	YES	GOOD
08-Oct-04	-10.95	162.16	84.77	62.77	44.77	0.70	0.50	No	good	-	POOR
20-Nov-04	13.38	-90.06	328.30	72.30	-57.70	2.30	0.25	Yes	fair	YES	GOOD
20-Nov-04	9.60	-84.17	321.33	85.33	88.33	1.30	1.30	No	poor	NO	GOOD
21-Nov-04	15.68	-61.71	303.67	49.67	78.67	0.90	0.50	Yes	fair	-	POOR
07-Feb-05	-4.53	153.19	88.65	72.65	30.65	1.30	0.30	No	good	YES	FAIR
11-Apr-05	-21.98	170.61	84.48	74.48	37.48	0.80	0.25	No	fair	-	POOR
Station KEV											
12-Jun-93	-4.38	135.05	74.48	8.48	27.48	0.30	0.20	Yes	fair	-	POOR
04-Sep-93	-9.67	122.57	88.16	86.16	42.16	3.10	0.10	Yes	good	YES	GOOD
06-Sep-93	-4.71	153.21	56.92	-5.08	1.92	0.50	0.45	No	good	NO	GOOD
29-Sep-93	0.54	121.56	85.54	-0.46	38.54	0.70	0.10	Yes	good	YES	GOOD
13-Oct-93	-5.93	146.03	64.38	60.38	16.38	3.20	0.35	Yes	good	YES	GOOD
25-May-94	-4.18	135.45	74.03	36.03	28.03	0.70	0.70	Yes	fair	NO	GOOD
13-Jul-94	-7.50	127.92	82.34	4.34	38.34	0.80	0.20	No	fair	YES	FAIR
19-Aug-94	-26.65	-63.38	260.50	74.50	-67.50	4.00	0.10	Yes	good	YES	GOOD
13-Feb-95	-1.35	127.52	80.59	2.59	35.59	1.00	0.25	Yes	fair	YES	FAIR
14-Aug-95	-4.83	151.51	58.64	2.64	-1.36	0.40	0.40	No	good	NO	GOOD
25-Dec-95	-6.94	129.18	80.95	20.95	33.95	0.40	0.35	Yes	fair	NO	FAIR
17-Feb-96	-0.59	135.87	72.42	-9.58	-62.58	1.60	0.20	Yes	good	YES	FAIR
28-Feb-96	1.73	126.10	80.87	-3.13	35.87	1.20	0.10	Yes	good	YES	GOOD
17-Mar-96	-14.70	167.30	45.35	-6.65	-0.65	0.30	0.25	No	fair	NO	GOOD
02-May-96	-4.55	154.83	55.26	37.26	9.26	0.70	0.40	Yes	fair	-	POOR
17-Jun-96	-7.14	122.59	87.24	3.24	39.24	0.90	0.10	Yes	good	YES	FAIR
05-Apr-97	-6.49	147.41	63.21	61.21	11.21	4.00	0.20	Yes	fair	YES	GOOD
05-Apr-97	-6.49	147.41	63.21	-30.79	11.21	3.20	0.20	Yes	fair	YES	GOOD
02-Sep-97	3.85	-75.75	283.29	-80.71	55.29	3.10	0.10	Yes	good	YES	GOOD
22-Dec-97	-5.49	147.87	62.44	58.44	13.44	3.10	0.25	Yes	good	YES	GOOD
06-Feb-99	-12.85	166.70	45.46	27.46	-1.54	0.60	0.30	Yes	fair	-	POOR
26-Apr-99	-1.65	-77.78	283.35	83.35	56.35	0.40	0.20	Yes	good	-	POOR
17-May-99	-5.16	152.88	57.38	33.38	9.38	0.50	0.35	Yes	fair	-	POOR
06-Feb-00	-5.84	150.88	59.58	45.58	11.58	0.80	0.30	Yes	fair	-	POOR
23-Apr-00	-28.31	-62.99	259.44	75.44	30.44	4.00	0.00	Yes	good	YES	GOOD
09-Jun-00	-5.07	152.49	57.74	41.74	10.74	0.50	0.25	Yes	fair	-	POOR
16-Nov-00	-3.98	152.17	57.73	-0.27	12.73	0.40	0.35	No	fair	NO	FAIR
09-Jan-01	-14.93	167.17	45.56	-24.44	-1.44	0.20	0.15	Yes	good	-	POOR
28-Apr-01	-18.06	-176.94	28.59	36.59	71.59	0.90	0.15	Yes	fair	YES	FAIR
25-May-01	-7.87	110.18	99.12	-82.88	51.12	4.00	0.05	Yes	good	YES	GOOD
29-Jun-01	-19.52	-66.25	266.03	76.03	31.03	1.30	0.10	Yes	fair	YES	GOOD
01-Jul-01	-4.31	152.96	57.05	23.05	11.05	0.30	0.25	No	good	NO	FAIR
11-Sep-01	-0.58	133.13	75.02	75.02	29.02	4.00	0.10	Yes	good	YES	GOOD
06-Jun-02	-0.88	148.33	60.54	54.54	9.54	2.20	0.30	Yes	good	YES	GOOD
03-Jul-02	-5.03	147.34	62.81	36.81	15.81	0.40	0.30	Yes	fair	-	POOR
10-Mar-03	1.69	127.30	79.75	79.75	34.75	3.50	0.15	Yes	good	YES	GOOD
05-May-03	0.22	127.35	80.21	74.21	32.21	2.80	0.20	Yes	fair	YES	GOOD
11-May-03	-0.99	126.94	81.01	75.01	34.01	0.20	0.05	Yes	fair	YES	FAIR

								Manual		Automatic	
Date	**Lat**	**Long**	**Bazi**	**ΦSC**	**ΦRC**	**dtSC**	**dtRC**	**isNull**	**Quality**	**IsNull**	**Quality**
26-May-03	2.35	128.85	78.07	10.07	26.07	0.60	0.40	Yes	fair	-	POOR
12-Jun-03	-5.99	154.76	55.76	-24.24	8.76	0.90	0.20	Yes	good	YES	FAIR
25-Jul-03	-1.53	149.69	59.42	-20.58	14.42	0.60	0.15	Yes	fair	YES	FAIR
27-Jul-03	-21.08	-176.59	28.86	52.86	75.86	0.60	0.40	Yes	fair	-	POOR
23-Apr-04	-9.36	122.84	87.79	3.79	41.79	0.70	0.15	Yes	good	YES	FAIR
25-Jun-04	-6.71	130.38	79.73	7.73	36.73	0.70	0.40	No	fair	-	POOR
Station KIEV											
13-Feb-95	-1.35	127.52	84.41	-89.59	-51.59	1.70	0.05	Yes	fair	YES	GOOD
02-May-95	-3.85	-76.96	280.20	-67.80	-29.80	0.90	0.30	Yes	fair	-	POOR
26-Jul-95	2.56	127.69	81.80	-78.20	-57.20	1.00	0.60	No	good	-	POOR
30-Jul-95	-23.32	-70.59	261.83	-86.17	-47.17	1.20	0.30	No	good	YES	FAIR
19-Aug-95	5.10	-75.69	284.81	20.81	-25.19	1.10	0.10	Yes	fair	YES	GOOD
14-Sep-95	16.84	-98.60	310.13	36.13	-7.87	4.00	0.15	Yes	good	YES	GOOD
03-Oct-95	-2.82	-77.90	281.61	-46.39	-28.39	0.70	0.65	No	poor	-	POOR
03-Oct-95	-2.77	-77.88	281.63	-54.37	-31.37	0.80	0.55	No	fair	-	POOR
21-Oct-95	16.89	-93.45	305.92	-42.08	-5.08	1.10	0.05	No	good	YES	GOOD
01-Nov-95	-28.96	-71.50	258.12	86.12	-52.88	1.20	0.25	Yes	fair	YES	FAIR
05-Dec-95	-9.28	125.41	91.15	-82.85	-37.85	2.50	0.10	Yes	fair	YES	GOOD
25-Dec-95	-6.94	129.18	86.69	-81.31	-44.31	0.80	0.25	No	good	-	POOR
25-Feb-96	16.20	-97.96	309.27	35.27	-8.73	3.60	0.30	Yes	good	YES	GOOD
19-Apr-96	-23.94	-70.09	261.00	-81.00	-53.00	0.80	0.40	No	good	-	POOR
02-May-96	-4.55	154.83	63.78	87.78	-67.22	0.70	0.50	No	good	-	POOR
09-Jun-96	17.44	145.46	58.89	64.89	20.89	1.60	0.00	No	fair	YES	GOOD
15-Jul-96	18.73	145.63	58.02	-19.98	20.02	0.50	0.10	No	good	YES	GOOD
05-Aug-96	-2.00	-81.00	284.64	-63.36	-29.36	1.20	0.40	No	fair	-	POOR
31-Dec-96	15.83	-92.97	304.96	-51.04	83.96	1.70	0.00	Yes	good	YES	GOOD
17-Jan-97	-8.90	123.54	92.34	10.34	-34.66	3.10	0.15	Yes	poor	YES	GOOD
23-Jan-97	-22.00	-65.72	259.23	83.23	-54.77	3.10	0.25	Yes	good	YES	GOOD
23-Apr-97	13.99	144.90	61.30	67.30	21.30	1.50	0.00	No	fair	YES	GOOD
22-May-97	18.68	-101.60	313.56	-66.44	87.56	0.30	0.20	No	fair	-	POOR
10-Aug-97	-16.01	124.33	96.45	24.45	58.45	0.80	0.35	Yes	fair	-	POOR
20-Aug-97	-41.72	80.13	143.59	-38.41	7.59	3.00	0.05	Yes	good	YES	GOOD
02-Sep-97	3.85	-75.75	284.08	-45.92	-40.92	0.70	0.65	No	good	NO	GOOD
28-Nov-97	-13.74	-68.79	267.27	-82.73	-39.73	1.30	0.25	No	good	YES	GOOD
10-Jan-98	14.37	-91.47	302.93	-41.07	-14.07	0.70	0.35	No	fair	-	POOR
21-May-98	0.21	119.58	89.58	-80.42	-37.42	2.10	0.10	Yes	fair	YES	GOOD
23-Aug-98	11.66	-88.04	298.61	-43.39	-20.39	1.00	0.55	No	good	-	POOR
02-Sep-98	5.41	126.76	80.74	-73.26	-58.26	1.00	0.75	No	good	-	POOR
28-Sep-98	-8.19	112.41	100.43	22.43	62.43	0.70	0.25	Yes	fair	-	POOR
08-Oct-98	-16.12	-71.40	267.63	-82.37	-41.37	1.30	0.25	Yes	fair	YES	GOOD
28-Oct-98	0.84	125.97	84.23	-75.77	-44.77	1.00	0.50	No	fair	-	POOR
06-Dec-98	1.25	126.20	83.79	-74.21	-60.21	1.00	0.75	No	poor	NO	FAIR
12-Aug-99	-1.72	122.46	88.57	-85.43	53.57	2.30	0.00	Yes	poor	YES	GOOD
28-Aug-99	-1.29	-77.55	282.30	-57.70	-32.70	0.70	0.40	No	good	-	POOR
15-Sep-99	-20.93	-67.28	261.14	-82.86	-57.86	0.70	0.30	No	good	-	POOR
26-Feb-00	13.80	144.78	61.51	65.51	19.51	1.10	0.15	No	fair	YES	GOOD
23-Apr-00	-28.31	-62.99	252.68	76.68	-56.32	2.00	0.10	Yes	good	YES	GOOD
12-May-00	-23.55	-66.45	258.65	-85.35	-58.35	0.90	0.35	Yes	good	-	POOR
24-Feb-01	1.27	126.25	83.74	-74.26	-35.26	1.20	0.60	No	fair	YES	FAIR
13-Apr-01	-59.72	-25.59	208.09	-49.91	84.09	2.20	0.20	No	poor	YES	GOOD
25-May-01	-7.87	110.18	101.95	25.95	61.95	0.60	0.20	Yes	fair	-	POOR
05-Jul-01	-16.09	-73.99	269.64	-48.36	-42.36	0.40	0.35	No	fair	NO	GOOD
12-Oct-01	12.69	144.98	61.99	67.99	-70.01	1.50	0.10	Yes	good	YES	GOOD

								Manual		Automatic	
Date	**Lat**	**Long**	**Bazi**	**ΦSC**	**ΦRC**	**dtSC**	**dtRC**	**isNull**	**Quality**	**IsNull**	**Quality**
16-Jan-02	15.50	-93.13	304.91	-47.09	-6.09	1.10	0.15	Yes	fair	YES	GOOD
01-Apr-02	-29.67	-71.38	257.46	-68.54	-57.54	0.40	0.35	Yes	fair	NO	FAIR
18-Apr-02	-27.53	-70.59	258.61	86.61	-45.39	2.80	0.20	Yes	fair	YES	GOOD
26-Apr-02	13.09	144.62	62.05	70.05	-72.95	1.60	0.15	No	fair	YES	GOOD
08-Sep-02	-3.30	142.95	73.28	77.28	-60.72	2.70	0.25	No	fair	YES	GOOD
12-Oct-02	-8.30	-71.74	273.18	-68.82	-35.82	0.60	0.25	No	good	-	POOR
10-Mar-03	1.69	127.30	82.66	-79.34	-70.34	1.30	1.00	No	good	NO	FAIR
05-May-03	0.22	127.35	83.54	-74.46	-60.46	1.00	0.75	No	good	NO	FAIR
09-May-03	-48.21	32.27	177.94	89.94	-45.06	2.60	0.00	Yes	good	YES	GOOD
20-Jun-03	-7.61	-71.72	273.62	-62.38	-36.38	0.50	0.30	No	good	-	POOR
18-Oct-03	0.44	126.10	84.38	-79.62	-46.62	1.50	0.55	No	fair	-	POOR
29-Apr-04	10.81	-86.00	296.47	-59.53	-14.53	3.40	0.30	Yes	good	YES	GOOD
29-Jun-04	10.74	-87.04	297.27	-44.73	-21.73	1.20	0.60	No	good	-	POOR
30-Jun-04	0.80	124.73	85.22	-66.78	-63.78	0.90	0.85	No	fair	NO	GOOD
28-Nov-04	-3.64	135.45	79.61	-82.39	-57.39	0.90	0.45	No	good	-	POOR
Station LVZ											
20-Dec-92	-6.51	130.39	87.14	21.14	32.14	1.00	0.85	No	fair	NO	FAIR
16-May-93	-15.34	-173.35	33.30	-32.70	-5.70	1.20	0.80	Yes	fair	YES	FAIR
05-Oct-93	-6.14	128.92	88.36	76.36	41.36	1.30	0.30	Yes	fair	YES	FAIR
09-Dec-93	0.48	125.98	88.59	18.59	61.59	1.30	0.30	No	good	YES	FAIR
09-Dec-93	0.43	125.89	88.69	12.69	54.69	1.50	0.20	No	fair	YES	GOOD
19-Jan-94	-3.21	136.02	80.64	4.64	49.64	2.10	0.20	Yes	fair	YES	GOOD
21-Jan-94	1.01	127.73	86.77	10.77	39.77	1.40	0.55	Yes	fair	-	POOR
13-Apr-94	-3.11	135.97	80.65	6.65	38.65	1.50	0.45	Yes	fair	-	POOR
18-Apr-94	-6.49	154.92	63.84	9.84	12.84	1.10	1.10	No	good	NO	GOOD
29-Apr-94	-28.30	-63.17	265.58	-24.42	-53.42	0.60	0.35	Yes	good	-	POOR
10-May-94	-28.50	-63.06	265.39	85.39	-53.61	4.00	0.25	Yes	good	YES	GOOD
09-Jun-94	-13.83	-67.56	276.04	-3.96	-42.96	1.60	0.30	Yes	good	YES	GOOD
13-Jul-94	-7.50	127.92	89.81	17.81	66.81	1.50	0.15	No	fair	YES	GOOD
19-Aug-94	-26.65	-63.38	266.57	-11.43	34.57	1.70	0.00	Yes	good	YES	GOOD
28-Sep-94	-5.77	110.33	105.42	-62.58	66.42	1.40	0.00	Yes	fair	YES	GOOD
13-Feb-95	-1.35	127.52	87.85	5.85	52.85	2.10	0.10	Yes	fair	YES	GOOD
16-Aug-95	-5.42	153.76	64.59	12.59	12.59	1.00	1.00	No	good	NO	GOOD
25-Dec-95	-6.94	129.18	88.43	12.43	52.43	1.60	0.40	No	good	YES	FAIR
17-Mar-96	-14.70	167.30	54.28	14.28	16.28	0.90	0.95	No	good	NO	GOOD
02-May-96	-4.55	154.83	63.25	5.25	10.25	1.10	1.00	No	good	NO	GOOD
17-Jun-96	-7.14	122.59	94.60	14.60	51.60	1.40	0.20	Yes	good	YES	FAIR
05-Apr-97	-6.49	147.41	71.11	21.11	23.11	1.40	1.35	No	good	NO	GOOD
28-Nov-97	-13.74	-68.79	277.23	-4.77	-38.77	1.00	0.35	Yes	good	-	POOR
22-Dec-97	-5.49	147.87	70.30	4.30	20.30	1.30	0.95	No	fair	-	POOR
16-Jul-98	-11.04	166.16	54.17	8.17	9.17	0.70	0.70	No	fair	NO	GOOD
06-Feb-99	-12.85	166.70	54.24	10.24	13.24	1.10	1.10	No	good	NO	GOOD
05-Apr-99	-5.59	149.57	68.70	6.70	18.70	1.40	1.20	No	good	NO	FAIR
13-Apr-99	-21.42	-176.46	38.67	-37.33	-3.33	1.40	0.40	Yes	fair	YES	FAIR
06-Feb-00	-5.84	150.88	67.53	13.53	19.53	1.30	1.30	No	good	NO	GOOD
23-Apr-00	-28.31	-62.99	265.42	-10.58	33.42	1.60	0.10	Yes	good	YES	GOOD
12-May-00	-23.55	-66.45	270.84	-13.16	-46.16	1.10	0.40	Yes	fair	-	POOR
07-Aug-00	-7.02	123.36	93.85	29.85	21.85	1.20	1.30	No	fair	NO	FAIR
16-Nov-00	-5.23	153.10	65.16	9.16	18.16	1.00	0.95	No	good	NO	FAIR
18-Nov-00	-5.23	151.77	66.45	12.45	15.45	1.00	1.00	No	good	NO	GOOD
21-Dec-00	-5.71	151.12	67.25	9.25	15.25	1.40	1.30	No	good	NO	GOOD
09-Jan-01	-14.93	167.17	54.49	-1.51	7.49	1.00	0.90	No	good	NO	FAIR
19-Oct-01	-4.10	123.91	92.23	8.23	46.23	2.30	0.25	Yes	good	YES	GOOD

								Manual		Automatic	
Date	**Lat**	**Long**	**Bazi**	**ΦSC**	**ΦRC**	**dtSC**	**dtRC**	**isNull**	**Quality**	**IsNull**	**Quality**
23-Dec-01	-9.61	159.53	60.40	30.40	19.40	0.90	0.80	No	fair	NO	FAIR
10-Oct-02	-1.76	134.30	81.71	3.71	44.71	1.90	0.55	Yes	poor	YES	FAIR
12-Dec-02	-4.79	153.27	64.84	6.84	16.84	1.40	1.30	No	good	NO	FAIR
07-Jun-03	-5.09	152.50	65.70	3.70	12.70	1.00	1.05	No	good	NO	FAIR
Station MHV											
06-Feb-00	-5.84	150.88	74.06	30.06	29.06	1.30	1.25	No	good	NO	GOOD
03-Mar-00	-7.32	128.49	93.63	25.63	55.63	0.60	0.35	No	fair	-	POOR
12-Mar-00	14.98	-92.44	311.77	31.77	-8.23	0.90	0.20	No	fair	YES	FAIR
21-Jul-00	9.42	-85.33	302.92	-55.08	-8.08	3.60	0.10	Yes	good	YES	GOOD
09-Aug-00	18.20	-102.48	321.99	-36.01	-82.01	3.70	0.05	Yes	good	YES	GOOD
16-Nov-00	-3.98	152.17	71.86	35.86	39.86	0.80	0.85	No	good	NO	GOOD
21-Dec-00	-5.71	151.12	73.78	53.78	69.78	1.20	1.55	No	fair	-	POOR
13-Jan-01	13.05	-88.66	307.59	-28.41	-4.41	0.20	0.15	Yes	good	-	POOR
20-May-01	18.82	-104.45	323.99	-34.01	-78.01	4.00	0.00	Yes	good	YES	GOOD
05-Jul-01	-16.09	-73.99	278.45	24.45	52.45	0.30	0.15	Yes	fair	-	POOR
11-Sep-01	-0.58	133.13	85.94	17.94	43.94	1.30	0.75	No	fair	-	POOR
28-Nov-01	15.57	-93.11	312.62	32.62	-3.38	0.50	0.15	Yes	fair	-	POOR
16-Jan-02	15.50	-93.13	312.61	38.61	-4.39	0.80	0.05	Yes	good	YES	GOOD
01-Apr-02	-29.67	-71.38	266.46	-9.54	-48.54	1.50	0.10	Yes	good	YES	GOOD
18-Apr-02	16.99	-100.86	320.08	44.08	84.08	3.80	0.15	Yes	poor	YES	GOOD
03-Jul-02	-5.03	147.34	76.64	40.64	47.64	1.30	1.30	No	good	NO	GOOD
22-Jan-03	18.77	-104.10	323.65	-32.35	7.65	2.00	0.20	Yes	good	YES	GOOD
25-Mar-03	-8.29	120.74	100.50	-71.50	61.50	3.20	0.25	Yes	fair	YES	GOOD
09-May-03	-48.21	32.27	183.76	17.76	66.76	2.30	0.20	Yes	fair	YES	GOOD
07-Jun-03	-5.09	152.50	72.21	36.21	38.21	0.80	0.75	No	poor	NO	GOOD
20-Jun-03	-7.61	-71.72	281.77	13.77	56.77	2.20	0.05	Yes	fair	YES	GOOD
25-Jul-03	-1.53	149.69	72.62	38.62	49.62	0.80	0.85	No	good	NO	FAIR
05-Feb-04	-3.62	135.54	85.71	21.71	48.71	1.20	0.80	Yes	fair	-	POOR
23-Apr-04	-9.36	122.84	99.40	13.40	-32.60	3.40	0.15	Yes	good	YES	GOOD
29-Apr-04	10.81	-86.00	304.19	-55.81	-9.81	4.00	0.10	Yes	good	YES	GOOD
29-Jun-04	10.74	-87.04	305.06	11.06	-7.94	0.30	0.20	Yes	fair	-	POOR
08-Oct-04	-10.95	162.16	66.94	36.94	24.94	0.80	0.70	No	good	NO	FAIR
09-Oct-04	11.42	-86.67	305.07	27.07	-5.93	1.70	0.10	Yes	poor	YES	FAIR
15-Nov-04	4.70	-77.51	293.70	1.70	-15.30	1.10	0.75	No	fair	-	POOR
20-Nov-04	9.60	-84.17	302.00	-48.00	-2.00	3.10	0.20	Yes	fair	YES	GOOD
28-Nov-04	-3.64	135.45	85.79	25.79	52.79	0.90	0.70	No	fair	-	POOR
Station NE51											
26-Jul-95	2.56	127.69	81.91	-4.09	44.91	4.00	0.00	Yes	good	YES	GOOD
14-Aug-95	-4.83	151.51	64.17	32.17	17.17	0.90	0.75	No	fair	YES	FAIR
23-Sep-95	-10.53	-78.70	280.84	0.84	-41.16	2.90	0.05	Yes	good	YES	GOOD
25-Dec-95	-6.94	129.18	85.39	39.39	33.39	0.80	0.75	No	good	NO	GOOD
31-Mar-96	-11.18	165.64	53.22	35.22	8.22	1.30	0.65	No	fair	-	POOR
17-Jun-96	-7.14	122.59	91.21	39.21	39.21	0.70	0.70	No	good	NO	GOOD
05-Apr-97	-6.49	147.41	68.82	42.82	6.82	1.40	0.80	No	fair	YES	FAIR
24-Jun-97	-1.92	127.90	83.97	49.97	28.97	0.80	0.70	No	good	-	POOR
31-Jul-97	-6.64	130.92	83.72	31.72	31.72	0.50	0.55	No	good	NO	GOOD
22-Dec-97	-5.49	147.87	67.90	33.90	16.90	1.20	1.05	No	fair	-	POOR
10-Jan-98	14.37	-91.47	304.07	-55.93	77.07	4.00	0.00	Yes	good	YES	GOOD
28-Sep-98	-8.19	112.41	100.50	40.50	41.50	0.80	0.80	No	good	NO	GOOD
Station NE52											
30-Jul-95	-23.32	-70.59	264.36	-59.64	-61.64	0.80	0.85	No	good	NO	GOOD

								Manual		Automatic	
Date	**Lat**	**Long**	**Bazi**	**ΦSC**	**ΦRC**	**dtSC**	**dtRC**	**isNull**	**Quality**	**IsNull**	**Quality**
03-Aug-95	-23.13	-70.60	264.49	-31.51	-77.51	1.40	1.25	Yes	fair	-	POOR
23-Sep-95	-10.53	-78.70	278.90	2.90	-38.10	0.60	0.10	Yes	fair	YES	GOOD
25-Dec-95	-6.94	129.18	84.56	-19.44	-56.44	0.60	0.20	Yes	fair	-	POOR
17-Jun-96	-7.14	122.59	90.27	86.27	-50.73	2.30	0.10	Yes	good	YES	GOOD
05-Aug-96	-2.00	-81.00	285.55	-62.45	-31.45	0.90	0.30	Yes	fair	-	POOR
23-Jan-97	-22.00	-65.72	261.19	-88.81	-59.81	1.40	0.45	Yes	fair	-	POOR
23-Apr-97	13.99	144.90	60.30	-33.70	10.30	4.00	0.05	Yes	good	YES	GOOD
Station NE53											
30-Jul-95	-23.32	-70.59	261.81	25.81	38.81	0.30	0.25	Yes	fair	NO	FAIR
02-Aug-95	-23.15	-70.58	261.92	79.92	39.92	3.80	0.20	Yes	good	YES	GOOD
19-Aug-95	5.10	-75.69	283.15	-86.85	36.15	4.00	0.30	No	poor	YES	FAIR
01-Nov-95	-28.96	-71.50	258.56	80.56	-54.44	4.00	0.05	Yes	good	YES	GOOD
25-Dec-95	-6.94	129.18	83.83	11.83	37.83	0.30	0.15	No	good	-	POOR
28-Feb-96	1.73	126.10	81.37	-4.63	39.37	1.00	0.05	Yes	fair	YES	GOOD
19-Apr-96	-23.94	-70.09	261.00	85.00	43.00	1.60	0.00	Yes	good	YES	GOOD
17-Jun-96	-7.14	122.59	89.39	85.39	33.39	4.00	0.10	Yes	fair	YES	GOOD
12-Aug-96	-0.27	125.09	83.35	3.35	37.35	0.30	0.10	Yes	good	-	POOR
10-Aug-97	-16.01	124.33	93.33	81.33	27.33	2.80	0.05	Yes	poor	YES	FAIR
26-Sep-97	-5.39	128.99	83.08	1.08	42.08	0.50	0.10	Yes	fair	YES	GOOD
15-Oct-97	-30.93	-71.22	256.90	0.90	37.90	0.80	0.30	Yes	fair	-	POOR
28-Nov-97	-13.74	-68.79	266.49	56.49	33.49	0.30	0.25	No	good	-	POOR
03-Mar-00	-7.32	128.49	84.63	4.63	37.63	0.70	0.20	Yes	poor	YES	FAIR
03-Apr-00	4.08	125.61	80.44	86.44	-51.56	0.70	0.10	Yes	good	YES	GOOD
04-May-00	-1.11	123.57	85.08	-0.92	38.08	0.50	0.05	Yes	good	YES	GOOD
12-May-00	-23.55	-66.45	258.44	22.44	41.44	0.20	0.20	No	fair	-	POOR
07-Aug-00	-7.02	123.36	88.69	-13.31	25.69	2.20	0.10	Yes	fair	YES	GOOD
Station NE54											
23-Apr-97	13.99	144.90	56.79	-59.21	-74.21	0.60	0.45	No	fair	-	POOR
22-May-97	18.68	-101.60	309.28	-60.72	80.28	3.90	0.00	Yes	fair	YES	GOOD
31-Jul-97	-6.64	130.92	80.37	-61.63	-55.63	0.60	0.60	No	good	NO	GOOD
Station NE55											
14-Sep-95	16.84	-98.60	310.39	-47.61	-2.61	2.20	0.10	Yes	good	YES	GOOD
28-Oct-97	-4.37	-76.68	279.77	-66.23	-31.23	1.30	0.45	Yes	fair	-	POOR
21-Jul-00	9.42	-85.33	295.35	-48.65	-18.65	0.60	0.30	Yes	good	-	POOR
07-Aug-00	-7.02	123.36	91.74	-78.26	-31.26	1.80	0.10	Yes	good	YES	GOOD
09-Aug-00	18.20	-102.48	314.33	-49.67	87.33	1.80	0.10	Yes	good	YES	GOOD
28-Sep-00	-0.22	-80.58	285.57	-36.43	-27.43	0.80	0.80	No	good	NO	FAIR
Station NE56											
09-Jun-96	17.44	145.46	60.34	-65.66	-63.66	0.90	0.90	Yes	good	NO	GOOD
17-Jun-96	-7.14	122.59	93.69	-50.31	-46.31	0.60	0.60	No	good	NO	GOOD
22-Aug-96	-7.12	123.28	93.18	-40.82	-35.82	0.70	0.75	No	good	NO	GOOD
23-Jan-97	-22.00	-65.72	258.98	84.98	-53.02	2.90	0.25	Yes	good	YES	GOOD
28-Nov-97	-13.74	-68.79	267.37	-42.63	-36.63	0.50	0.50	No	fair	NO	GOOD
28-Sep-98	-8.19	112.41	101.77	-50.23	-33.23	0.50	0.40	No	good	-	POOR
Station OBN											
25-Mar-90	9.89	-84.89	301.75	17.75	-15.25	0.70	0.30	Yes	good	-	POOR
08-May-90	6.95	-82.64	298.30	-29.70	-11.70	0.80	0.65	No	poor	-	POOR
24-May-90	-7.36	120.33	99.31	-60.69	-37.69	0.80	0.50	No	fair	-	POOR
31-May-90	17.25	-100.75	319.03	-32.97	15.03	1.50	0.05	Yes	good	YES	GOOD

								Manual		Automatic	
Date	**Lat**	**Long**	**Bazi**	**ΦSC**	**ΦRC**	**dtSC**	**dtRC**	**isNull**	**Quality**	**IsNull**	**Quality**
23-Jun-90	-0.63	146.44	73.84	23.84	31.84	0.70	0.60	No	poor	NO	FAIR
18-Aug-90	-40.21	78.25	148.76	50.76	9.76	1.50	0.10	Yes	fair	YES	GOOD
02-Sep-90	-0.12	-80.24	292.45	-23.55	-15.55	0.50	0.50	No	fair	NO	FAIR
17-Oct-90	-10.99	-70.78	277.96	-24.04	-23.04	0.90	0.85	No	fair	NO	GOOD
05-Apr-91	-5.95	-77.09	286.40	-17.60	-23.60	0.60	0.50	No	fair	NO	GOOD
04-May-91	9.49	-82.47	299.46	-44.54	-12.54	0.70	0.35	Yes	fair	-	POOR
17-May-91	-4.38	142.62	79.22	49.22	36.22	0.80	0.65	No	fair	NO	FAIR
24-May-91	-16.48	-70.72	274.47	-11.53	-14.53	0.80	0.80	No	good	NO	GOOD
23-Jun-91	-26.82	-63.40	261.50	-64.50	-50.50	0.20	0.20	Yes	good	NO	FAIR
07-Mar-92	10.20	-84.35	301.44	49.44	87.44	1.60	0.65	Yes	poor	-	POOR
04-May-92	-6.72	130.14	90.94	-83.06	57.94	3.10	0.10	Yes	fair	YES	GOOD
30-May-92	14.51	-92.90	310.93	16.93	-2.07	0.30	0.20	Yes	fair	-	POOR
14-Jul-92	-4.71	125.43	93.63	-68.37	-42.37	0.30	0.10	Yes	fair	-	POOR
02-Aug-92	-0.90	127.59	89.68	3.68	49.68	2.00	0.10	Yes	fair	YES	GOOD
02-Aug-92	-7.12	121.72	98.04	-53.96	-40.96	0.50	0.40	No	good	NO	FAIR
13-Aug-92	-6.13	148.92	74.84	-1.16	40.84	2.00	0.55	Yes	poor	YES	FAIR
16-Aug-92	-5.39	146.66	76.36	14.36	28.36	0.40	0.35	Yes	fair	NO	FAIR
15-Oct-92	-14.45	166.63	63.56	69.56	-68.44	0.40	0.05	Yes	good	YES	GOOD
18-Oct-92	-6.29	130.22	90.62	4.62	52.62	1.40	0.00	Yes	good	YES	GOOD
18-Oct-92	7.12	-76.89	293.45	-20.55	-16.55	0.60	0.65	No	fair	NO	GOOD
20-Jan-93	-7.24	128.60	92.50	16.50	48.50	0.40	0.15	Yes	good	-	POOR
15-Mar-93	-26.79	-70.91	267.45	81.45	-56.55	3.20	0.15	Yes	fair	YES	GOOD
15-May-93	16.74	-98.36	316.70	-17.30	1.70	0.50	0.40	Yes	fair	-	POOR
24-May-93	-23.22	-66.64	266.59	-17.41	-47.41	0.70	0.30	Yes	fair	-	POOR
12-Jun-93	-4.38	135.05	85.54	37.54	45.54	0.70	0.70	No	fair	NO	FAIR
11-Jul-93	-25.35	-70.18	267.93	87.93	39.93	4.00	0.00	Yes	poor	YES	GOOD
04-Sep-93	-9.67	122.57	98.81	-49.19	-40.19	0.40	0.35	No	good	NO	FAIR
06-Sep-93	-4.71	153.21	70.26	-7.74	27.26	0.60	0.15	No	good	YES	FAIR
10-Sep-93	14.73	-92.68	310.84	-45.16	-1.16	1.00	0.10	Yes	good	YES	GOOD
12-Sep-93	13.81	-90.47	308.49	28.49	-9.51	0.90	0.25	Yes	poor	YES	FAIR
29-Sep-93	-42.57	-18.43	219.44	-8.56	10.44	1.30	1.20	No	poor	-	POOR
30-Sep-93	15.51	-94.71	312.96	-49.04	86.96	1.40	0.00	Yes	good	YES	GOOD
05-Oct-93	-6.14	128.92	91.60	-76.40	64.60	4.00	0.50	Yes	poor	YES	GOOD
10-Jan-94	-13.31	-69.39	275.36	-10.64	-14.64	0.90	0.85	No	fair	NO	GOOD
19-Jan-94	-3.21	136.02	84.06	10.06	46.06	1.30	0.50	No	fair	-	POOR
14-Mar-94	15.98	-92.40	311.16	-46.84	-0.84	1.90	0.05	Yes	good	YES	GOOD
13-Apr-94	-3.11	135.97	84.04	24.04	44.04	0.60	0.50	No	good	-	POOR
10-May-94	-28.50	-63.06	260.03	-13.97	-54.97	1.00	0.10	Yes	good	YES	GOOD
23-May-94	18.31	-100.52	319.25	51.25	6.25	3.10	0.10	Yes	good	YES	GOOD
31-May-94	7.43	-72.06	289.56	-20.44	2.56	0.90	0.95	No	good	-	POOR
04-Jun-94	-10.77	113.42	106.87	-43.13	-34.13	0.40	0.35	No	fair	NO	FAIR
06-Jun-94	2.90	-76.09	290.50	-9.50	-24.50	0.70	0.60	No	good	-	POOR
15-Jun-94	-10.41	113.54	106.58	-15.42	-37.42	0.50	0.45	No	good	-	POOR
04-Jul-94	14.94	-97.32	315.02	-36.98	1.02	0.50	0.10	Yes	good	YES	GOOD
24-Jul-94	-10.72	113.33	106.92	-29.08	-31.08	0.50	0.50	No	fair	NO	GOOD
04-Aug-94	-6.32	131.54	89.55	9.55	53.55	1.20	0.20	No	fair	YES	GOOD
19-Aug-94	-26.65	-63.38	261.61	-16.39	-53.39	0.50	0.10	Yes	good	YES	GOOD
12-Dec-94	-17.50	-69.65	272.91	78.91	-61.09	2.50	0.15	Yes	fair	YES	GOOD
13-Feb-95	-1.35	127.52	89.99	9.99	52.99	1.00	0.20	No	fair	YES	GOOD
19-Mar-95	-4.15	135.09	85.37	7.37	48.37	1.90	0.30	Yes	good	YES	GOOD
14-May-95	-8.40	125.08	96.04	-53.96	-35.96	0.30	0.25	Yes	fair	-	POOR
14-Jun-95	12.20	-88.35	305.88	-36.12	-7.12	0.30	0.15	Yes	good	-	POOR
24-Jun-95	-3.98	153.95	69.19	9.19	23.19	0.20	0.15	Yes	good	NO	FAIR
30-Jul-95	-23.32	-70.59	269.73	-18.27	-52.27	0.50	0.25	Yes	good	-	POOR

								Manual		Automatic	
Date	**Lat**	**Long**	**Bazi**	**ΦSC**	**ΦRC**	**dtSC**	**dtRC**	**isNull**	**Quality**	**IsNull**	**Quality**
14-Aug-95	-4.83	151.51	71.83	-8.17	31.83	1.70	0.25	Yes	fair	YES	GOOD
18-Sep-95	-6.95	128.90	92.08	8.08	54.08	0.90	0.00	No	fair	YES	GOOD
03-Oct-95	-2.77	-77.88	288.91	-31.09	-24.09	0.50	0.50	No	fair	NO	GOOD
21-Oct-95	16.89	-93.45	312.47	30.47	-0.53	0.40	0.15	Yes	good	-	POOR
25-Dec-95	-6.94	129.18	91.85	9.85	53.85	0.80	0.00	No	fair	YES	GOOD
02-May-96	-4.55	154.83	68.73	-5.27	20.73	0.50	0.20	Yes	good	-	POOR
05-Aug-96	-2.00	-81.00	292.08	-31.92	-20.92	0.50	0.50	No	good	NO	FAIR
22-Aug-96	-7.12	123.28	96.77	-71.23	-29.23	1.20	0.25	No	good	YES	FAIR
17-Jan-97	-8.90	123.54	97.58	-70.42	-33.42	1.00	0.25	No	fair	YES	FAIR
23-Jan-97	-22.00	-65.72	266.69	-67.31	-44.31	0.30	0.25	Yes	good	-	POOR
22-May-97	18.68	-101.60	320.34	-37.66	7.34	1.60	0.05	Yes	good	YES	GOOD
10-Aug-97	-16.01	124.33	101.11	-32.89	-28.89	0.50	0.45	No	fair	NO	GOOD
02-Sep-97	3.85	-75.75	290.72	-13.28	-31.28	0.80	0.70	No	good	-	POOR
28-Nov-97	-13.74	-68.79	274.59	-11.41	47.59	0.90	0.10	No	good	-	POOR
03-Apr-98	-8.15	-74.24	282.63	-13.37	-28.37	0.70	0.55	No	good	-	POOR
20-Apr-98	18.52	-101.20	319.93	51.93	-82.07	2.20	0.05	Yes	good	YES	GOOD
07-Jun-98	15.96	-93.78	312.35	-31.65	-1.65	0.20	0.10	Yes	good	-	POOR
04-Aug-98	-0.59	-80.39	292.32	-37.68	-13.68	0.60	0.50	No	good	-	POOR
23-Aug-98	11.66	-88.04	305.35	-50.65	-4.65	1.70	0.15	Yes	good	YES	GOOD
08-Oct-98	-16.12	-71.40	275.27	-12.73	-48.73	0.80	0.35	No	good	-	POOR
26-Apr-99	-1.65	-77.78	289.45	-28.55	-14.55	0.50	0.55	No	good	NO	FAIR
15-Jun-99	18.39	-97.44	316.58	-83.42	-87.42	0.00	0.00	Yes	good	-	POOR
28-Aug-99	-1.29	-77.55	289.45	-24.55	-16.55	0.50	0.55	No	good	NO	FAIR
15-Sep-99	-20.93	-67.28	268.68	-15.32	-52.32	0.70	0.20	No	good	YES	FAIR
03-Mar-00	-7.32	128.49	92.63	-79.37	-33.37	3.00	0.05	Yes	fair	YES	GOOD
12-Mar-00	14.98	-92.44	310.74	36.74	-10.26	1.60	0.10	Yes	good	YES	GOOD
23-Apr-00	-28.31	-62.99	260.11	-17.89	-55.89	0.60	0.10	Yes	good	YES	GOOD
12-May-00	-23.55	-66.45	266.21	-15.79	-49.79	0.60	0.20	Yes	fair	-	POOR
07-Aug-00	-7.02	123.36	96.65	-55.35	-44.35	0.50	0.45	No	good	NO	FAIR
09-Aug-00	18.20	-102.48	320.94	52.94	-82.06	3.40	0.05	Yes	good	YES	GOOD
12-Aug-00	-3.07	136.11	83.91	23.91	50.91	0.60	0.50	No	good	-	POOR
21-Aug-00	-53.02	-45.97	228.86	-29.14	17.86	1.30	0.20	No	poor	YES	GOOD
28-Sep-00	-0.22	-80.58	292.69	-55.31	-14.31	1.60	0.40	No	poor	YES	FAIR
09-Jan-01	-14.93	167.17	63.33	61.33	-72.67	3.70	0.30	Yes	fair	YES	GOOD
16-Feb-01	-7.16	117.49	101.52	-38.48	-38.48	0.50	0.45	No	good	NO	GOOD
19-Jun-01	-22.74	-67.88	267.93	-10.07	-55.07	1.10	0.10	Yes	poor	YES	GOOD
29-Jun-01	-19.52	-66.25	268.78	-15.22	-50.22	0.70	0.25	No	good	-	POOR
05-Jul-01	-16.09	-73.99	277.49	-4.51	-41.51	1.00	0.30	No	fair	-	POOR
11-Sep-01	-0.58	133.13	84.94	20.94	44.94	1.00	0.70	No	good	-	POOR
22-Sep-01	3.87	-75.97	290.92	-7.08	26.92	1.10	1.25	No	poor	-	POOR
28-Nov-01	15.57	-93.11	311.59	-18.41	-3.41	0.20	0.15	Yes	fair	-	POOR
16-Jan-02	15.50	-93.13	311.58	15.58	-5.42	0.20	0.15	Yes	good	-	POOR
19-Mar-02	-6.49	129.90	91.00	-79.00	57.00	3.80	0.20	Yes	fair	YES	GOOD
16-Jun-02	8.78	-83.99	300.41	-45.59	-12.59	0.60	0.25	Yes	fair	-	POOR
20-Sep-02	-1.68	134.23	84.66	14.66	43.66	1.20	0.60	No	good	-	POOR
10-Oct-02	-1.48	134.11	84.65	24.65	29.65	0.90	0.80	No	good	NO	GOOD
12-Oct-02	-8.30	-71.74	280.40	-11.60	-34.60	0.70	0.45	No	fair	-	POOR
21-Jan-03	13.63	-90.77	308.67	42.67	84.67	3.50	0.00	Yes	good	YES	GOOD
27-Apr-03	-8.19	-71.59	280.34	-55.66	-48.66	0.50	0.45	No	fair	NO	GOOD
05-May-03	0.22	127.35	89.23	-84.77	51.23	2.10	0.10	Yes	fair	YES	GOOD
20-Jun-03	-7.61	-71.72	280.79	-21.21	-32.21	0.70	0.60	No	fair	NO	FAIR
27-Jul-03	-20.13	-65.18	267.51	-16.49	-59.49	0.90	0.20	Yes	fair	YES	FAIR
29-Jun-04	10.74	-87.04	304.04	-37.96	-5.96	0.50	0.30	Yes	fair	-	POOR
15-Nov-04	4.70	-77.51	292.69	-19.31	-5.31	0.80	0.85	No	good	NO	FAIR

								Manual		Automatic	
Date	**Lat**	**Long**	**Bazi**	**ΦSC**	**ΦRC**	**dtSC**	**dtRC**	**isNull**	**Quality**	**IsNull**	**Quality**
02-Mar-05	-6.53	129.93	91.00	9.00	51.00	1.20	0.15	Yes	fair	YES	GOOD
21-Mar-05	-24.98	-63.47	262.85	-19.15	-48.15	0.50	0.15	Yes	poor	-	POOR
Station PUL											
16-Jul-98	-11.04	166.16	63.17	49.17	11.17	1.20	0.15	Yes	fair	YES	GOOD
04-Aug-98	-0.59	-80.39	293.34	-68.66	63.34	4.00	0.00	Yes	good	YES	GOOD
23-Aug-98	11.66	-88.04	306.38	-55.62	-13.62	3.50	0.05	Yes	good	YES	GOOD
03-Apr-99	-16.66	-72.66	276.93	-87.07	-42.07	4.00	0.20	Yes	good	YES	GOOD
05-Apr-99	-5.59	149.57	75.05	53.05	29.05	1.10	0.70	No	fair	-	POOR
15-Jun-99	18.39	-97.44	317.61	19.61	2.61	0.20	0.15	Yes	good	-	POOR
28-Aug-99	-1.29	-77.55	290.46	-65.54	69.46	2.10	0.05	Yes	good	YES	GOOD
15-Sep-99	-20.93	-67.28	269.58	83.58	36.58	1.20	0.05	Yes	good	YES	GOOD
12-Mar-00	14.98	-92.44	311.77	-50.23	84.77	3.60	0.00	Yes	good	YES	GOOD
23-Apr-00	-28.31	-62.99	260.95	64.95	41.95	0.30	0.15	No	good	-	POOR
12-May-00	-23.55	-66.45	267.10	75.10	37.10	0.50	0.10	No	good	YES	GOOD
21-Jul-00	9.42	-85.33	302.92	-59.08	-15.08	4.00	0.05	Yes	good	YES	GOOD
09-Aug-00	18.20	-102.48	321.99	43.99	-87.01	0.50	0.00	Yes	good	YES	GOOD
16-Nov-00	-5.23	153.10	71.77	31.77	26.77	0.80	0.80	No	good	NO	GOOD
18-Nov-00	-5.23	151.77	72.93	32.93	23.93	1.10	1.05	No	fair	NO	FAIR
09-Jan-01	-14.93	167.17	64.62	46.62	12.62	1.00	0.50	No	fair	-	POOR
20-May-01	18.82	-104.45	323.98	-36.02	-82.02	4.00	0.00	Yes	good	YES	GOOD
16-Jan-02	15.50	-93.13	312.61	-47.39	-3.39	2.40	0.05	Yes	good	YES	GOOD
08-Sep-02	-3.30	142.95	79.36	57.36	32.36	0.80	0.45	No	fair	-	POOR
23-Apr-04	-9.36	122.84	99.40	43.40	42.40	0.60	0.55	No	good	NO	GOOD
Station SUW											
25-Feb-96	16.20	-97.96	304.54	-59.46	75.54	3.90	0.45	Yes	good	YES	GOOD
28-Feb-96	1.73	126.10	78.48	-65.52	-69.52	0.70	0.75	No	good	NO	GOOD
02-May-96	-4.55	154.83	56.69	-63.31	-70.31	1.10	1.05	No	good	NO	GOOD
09-Jun-96	17.44	145.46	53.89	-80.11	76.89	0.60	0.65	No	good	-	POOR
17-Jun-96	-7.14	122.59	86.60	-51.40	-54.40	0.50	0.55	No	fair	NO	GOOD
16-Jul-96	1.02	120.25	83.67	-68.33	-54.33	0.60	0.50	Yes	good	NO	FAIR
05-Aug-96	-2.00	-81.00	280.39	-73.61	58.39	2.70	0.20	Yes	good	YES	GOOD
31-Dec-96	15.83	-92.97	300.24	-49.76	-6.76	1.00	0.10	No	fair	YES	GOOD
23-Jan-97	-22.00	-65.72	255.80	81.80	29.80	2.10	0.05	Yes	fair	YES	GOOD
11-Mar-97	7.74	127.65	73.76	-22.24	-67.24	3.20	0.15	Yes	good	YES	GOOD
09-May-97	13.20	144.70	56.66	-77.34	-73.34	0.50	0.60	No	fair	-	POOR
22-May-97	18.68	-101.60	308.79	-83.21	87.79	0.50	0.45	No	good	-	POOR
25-Jul-97	-30.46	-71.91	254.63	-83.37	-56.37	0.40	0.30	Yes	fair	-	POOR
02-Sep-97	3.85	-75.75	279.49	39.49	59.49	0.50	0.40	No	fair	-	POOR
26-Sep-97	-5.39	128.99	80.27	-73.73	-26.73	0.90	0.50	No	fair	-	POOR
15-Oct-97	-30.93	-71.22	253.78	67.78	-57.22	4.00	0.25	Yes	fair	YES	FAIR
28-Nov-97	-13.74	-68.79	263.39	-80.61	-82.61	1.00	1.05	No	good	NO	GOOD
11-Dec-97	3.93	-75.79	279.57	51.57	46.57	0.40	1.75	No	fair	-	POOR
03-Apr-98	-8.15	-74.24	271.18	-48.82	-44.82	0.20	0.20	Yes	good	NO	GOOD
21-May-98	0.21	119.58	84.69	-57.31	-56.31	0.40	0.40	No	good	NO	GOOD
07-Jun-98	15.96	-93.78	300.97	-61.03	-17.03	3.00	0.15	Yes	good	YES	GOOD
23-Aug-98	11.66	-88.04	293.95	7.95	-26.05	0.50	0.25	Yes	good	-	POOR
02-Sep-98	5.41	126.76	75.82	-50.18	-59.18	0.50	0.50	No	good	NO	FAIR
28-Sep-98	-8.19	112.41	95.45	87.45	-45.55	2.40	0.15	Yes	fair	YES	GOOD
28-Sep-98	3.84	126.41	77.01	-70.99	-58.99	0.50	0.45	No	good	NO	FAIR
08-Oct-98	-16.12	-71.40	263.98	-76.02	-43.02	0.80	0.45	Yes	fair	-	POOR
29-Nov-98	-2.07	124.89	81.69	-26.31	-54.31	1.10	0.60	Yes	good	-	POOR
03-Apr-99	-16.66	-72.66	264.63	-33.37	-54.37	0.40	0.35	Yes	fair	-	POOR

								Manual		Automatic	
Date	**Lat**	**Long**	**Bazi**	**ΦSC**	**ΦRC**	**dtSC**	**dtRC**	**isNull**	**Quality**	**IsNull**	**Quality**
05-Apr-99	-5.59	149.57	62.31	-69.69	-76.69	0.80	0.80	No	good	NO	GOOD
26-Apr-99	-1.65	-77.78	277.94	21.94	56.94	0.40	0.20	No	fair	-	POOR
17-May-99	-5.16	152.88	58.92	-63.08	-82.08	1.10	0.85	No	fair	-	POOR
18-Jun-99	5.51	126.64	75.86	-80.14	-82.14	0.60	0.65	No	good	NO	GOOD
12-Aug-99	-1.72	122.46	83.48	-54.52	-51.52	0.50	0.45	No	fair	NO	GOOD
28-Aug-99	-1.29	-77.55	277.96	33.96	61.96	0.30	0.25	No	fair	-	POOR
15-Sep-99	-20.93	-67.28	257.69	-88.31	-42.31	1.10	0.15	No	good	YES	GOOD
30-Sep-99	16.06	-96.93	303.62	-62.38	75.62	3.30	0.45	Yes	fair	YES	GOOD
06-Feb-00	-5.84	150.88	61.22	-74.78	-61.78	0.90	0.90	No	good	NO	FAIR
26-Feb-00	13.80	144.78	56.29	80.29	-59.71	0.80	0.50	No	poor	-	POOR
03-Apr-00	4.08	125.61	77.52	-68.48	-63.48	0.60	0.60	No	good	NO	GOOD
23-Apr-00	-28.31	-62.99	249.63	83.63	49.63	1.40	0.00	No	fair	YES	FAIR
04-May-00	-1.11	123.57	82.21	-71.79	-58.79	0.60	0.45	No	good	NO	FAIR
12-May-00	-23.55	-66.45	255.35	85.35	-60.65	0.90	0.20	Yes	good	YES	FAIR
21-Jul-00	9.42	-85.33	290.49	18.49	-28.51	3.10	0.05	Yes	good	YES	GOOD
08-Nov-00	7.04	-77.83	283.03	23.03	65.03	2.60	0.05	Yes	fair	YES	GOOD
21-Dec-00	-5.71	151.12	60.91	-71.09	-80.09	1.00	1.05	No	good	NO	FAIR
25-May-01	-7.87	110.18	97.05	87.05	-49.95	1.70	0.10	No	fair	YES	GOOD
26-Jun-01	-17.75	-71.65	263.14	-16.86	-52.86	1.30	0.25	Yes	fair	YES	FAIR
29-Jun-01	-19.52	-66.25	257.79	87.79	-43.21	1.10	0.10	No	fair	YES	GOOD
01-Jul-01	-4.31	152.96	58.37	-71.63	-79.63	1.00	1.00	No	good	NO	FAIR
05-Jul-01	-16.09	-73.99	266.05	-9.95	39.05	2.80	0.20	Yes	good	YES	GOOD
11-Sep-01	-0.58	133.13	73.97	-78.03	-65.03	0.30	0.25	Yes	fair	NO	FAIR
28-Nov-01	15.57	-93.11	300.22	-47.78	-6.78	1.00	0.15	Yes	fair	YES	GOOD
16-Jan-02	15.50	-93.13	300.19	-47.81	-14.81	0.90	0.15	No	fair	YES	FAIR
01-Apr-02	-29.67	-71.38	254.82	84.82	-58.18	1.10	0.30	Yes	fair	YES	FAIR
26-Apr-02	13.09	144.62	56.78	-73.22	-84.22	0.60	0.55	No	good	NO	FAIR
10-Jun-02	10.98	140.69	61.19	-60.81	-79.81	0.60	0.55	No	fair	-	POOR
16-Jun-02	8.78	-83.99	289.03	-72.97	-28.97	4.00	0.10	Yes	good	YES	GOOD
08-Sep-02	-3.30	142.95	67.03	-32.97	-74.97	3.00	0.75	Yes	good	YES	FAIR
10-Oct-02	-1.76	134.30	73.66	-52.34	-68.34	0.60	0.55	No	fair	-	POOR
12-Oct-02	-8.30	-71.74	269.06	-78.94	-39.94	0.60	0.15	No	fair	YES	FAIR
10-Mar-03	1.69	127.30	77.52	-74.48	-66.48	0.70	0.60	No	good	NO	FAIR
05-May-03	0.22	127.35	78.33	-65.67	-62.67	0.60	0.60	No	good	NO	GOOD
26-May-03	6.76	123.71	77.52	-76.48	-48.48	0.60	0.40	No	fair	-	POOR
20-Jun-03	-7.61	-71.72	269.46	-80.54	-40.54	3.20	0.15	Yes	fair	YES	GOOD
23-Apr-04	-9.36	122.84	87.74	-64.26	-47.26	0.50	0.35	No	fair	-	POOR
30-Jun-04	0.80	124.73	80.14	-61.86	-65.86	0.60	0.60	No	fair	NO	GOOD
15-Feb-05	4.76	126.42	76.47	-79.53	-77.53	0.60	0.55	No	poor	NO	GOOD
02-Mar-05	-6.53	129.93	80.17	-83.83	-55.83	0.40	0.20	Yes	fair	-	POOR
13-Jun-05	-19.99	-69.20	259.78	-14.22	-59.22	4.00	0.15	Yes	good	YES	GOOD
26-Sep-05	-5.68	-76.40	274.42	2.42	-42.58	4.00	0.10	Yes	good	YES	GOOD
25-Aug-06	-24.32	-66.89	255.18	85.18	33.18	1.80	0.15	Yes	fair	YES	GOOD
Station TRTE											
04-Sep-96	9.36	-84.27	292.75	-69.25	-28.25	1.00	0.10	Yes	fair	YES	GOOD
23-Jan-97	-22.00	-65.72	260.03	-29.97	-60.97	0.80	0.50	Yes	fair	-	POOR
05-Apr-97	-6.49	147.41	66.44	-63.56	-56.56	1.60	1.55	No	fair	YES	FAIR
22-May-97	18.68	-101.60	311.95	-52.05	81.95	1.60	0.05	Yes	fair	YES	GOOD
02-Sep-97	3.85	-75.75	282.65	-25.35	-38.35	0.60	0.60	No	good	NO	FAIR
28-Nov-97	-13.74	-68.79	267.33	-34.67	-45.67	0.90	0.80	No	good	NO	FAIR
03-Apr-98	-8.15	-74.24	275.05	-16.95	-31.95	1.00	0.70	No	good	-	POOR
30-Aug-98	17.09	148.13	54.67	-17.33	14.67	1.10	0.55	No	fair	-	POOR
28-Oct-98	0.84	125.97	81.67	85.67	-43.33	2.10	0.10	Yes	good	YES	GOOD

								Manual		Automatic	
Date	**Lat**	**Long**	**Bazi**	**ΦSC**	**ΦRC**	**dtSC**	**dtRC**	**isNull**	**Quality**	**IsNull**	**Quality**
03-Apr-99	-16.66	-72.66	268.95	-15.05	-46.05	1.90	0.55	No	fair	-	POOR
17-May-99	-5.16	152.88	60.59	-27.41	4.59	1.10	0.00	Yes	good	YES	FAIR
18-Jun-99	5.51	126.64	78.68	76.68	35.68	1.50	0.00	Yes	good	YES	GOOD
28-Aug-99	-1.29	-77.55	281.55	-20.45	-31.45	0.80	0.75	No	good	NO	FAIR
21-Dec-99	-6.84	105.56	103.07	-6.93	-56.93	1.10	0.45	No	fair	-	POOR
12-Mar-00	14.98	-92.44	302.45	-25.55	-2.55	0.40	0.30	No	fair	-	POOR
23-Apr-00	-28.31	-62.99	254.00	-44.00	-56.00	0.60	0.50	No	good	NO	FAIR
21-Jul-00	9.42	-85.33	293.69	-16.31	-27.31	0.30	0.30	Yes	fair	NO	FAIR
25-May-01	-7.87	110.18	99.68	-40.32	-38.32	0.20	0.20	No	fair	NO	GOOD
16-Jan-02	15.50	-93.13	303.28	27.28	-18.72	1.10	0.15	Yes	fair	YES	GOOD
08-Sep-02	-3.30	142.95	68.90	72.90	-67.10	1.50	0.15	Yes	good	YES	GOOD
12-Oct-02	-8.30	-71.74	272.82	-31.18	-53.18	0.80	0.70	No	good	-	POOR
10-Mar-03	1.69	127.30	80.09	2.09	41.09	1.00	0.25	No	fair	YES	FAIR

RESUME en français

La mesure du déphasage des ondes de cisaillement offre la possibilité de caractériser l'anisotropie sismique présente dans les différentes couches de la Terre, qui résulte généralement des orientations préférentielles des minéraux anisotropes induites par la déformation. Le nouveau logiciel SplitLab présenté dans cette thèse, simplifie le traitement des données depuis la requête des données jusqu'à la masure de déphasage et l'interprétation des résultats. La comparaison de trois techniques indépendantes pour mesurer ce déphasage permet de quantifier la qualité des résultats et de détecter automatiquement les mesures sans déphasage apparent. Ce critère est appliqué aux mesures de déphasages des ondes SKS enregistrées en 16 stations situées sur le Craton Est Européen. Les résultats indiquent que les directions rapides reflètent les structures anciennes, qui constituent le Craton Est Européen. En outre, les directions rapides dans le Sud-ouest s'alignent avec la bordure du craton et sont en continuité avec la tendance générale définie par les stations éloignées du Craton. Les stations dans les unités externes de l'Oural montrent des directions rapides perpendiculaires à la tendance générale de la chaîne de montagne.

TITRE en anglais

Methods and applications of shear-wave splitting: The East European Craton

RESUME en anglais

The method of shear-wave splitting provides a unique possibility to identify seismic anisotropy, which is a result of the preferred orientations of the anisotropic minerals by deformation. The novel software SplitLab, presented in this thesis, simplifies the data processing. The comparison of three independent techniques makes it possible to associate an objective quality to the results and also to define a criterion to automatically detect events without splitting (“Nulls”). This criterion is applied to shear-wave splitting measurements at 16 stations located on the East European Craton. The results indicate that the fast directions reflect the ancient blocks, which constitute the East European Craton. The fast directions in south-west are aligned with the margin of the craton and continue the general tendency of off-craton stations. The stations in the Ural foredeep show fast directions perpendicular to the general tendency of the mountain chain. Various indicators give reason to assume lithospheric origins of anisotropy

DISCIPLINE Géophysique

MOTS-CLES

anisotropie, craton, Matlab, déphasages des ondes de cisaillement, Europe de l'est

INTITULE ET ADRESSE DE L'U.F.R. OU DU LABORATOIRE :

Geosciences Montpellier
5, Place Eugene Batallion, Bât 22
34095 Montpellier